Theory and Application of Left-Handed Metamaterials

by

Joe Pacheco, Jr.

S. B., Electrical Science and Engineering
Massachusetts Institute of Technology, June 2000
M. Eng., Electrical Engineering and Computer Science
Massachusetts Institute of Technology, June 2000

Submitted to the Department of Electrical Engineering and Computer Science
in partial fulfillment of the requirements for the degree of

Doctor of Philosophy

at the

MASSACHUSETTS INSTITUTE OF TECHNOLOGY

February 2004

Author . . . .
Department of Electrical Engineering and Computer Science
January 16, 2004

Certified by . . . .
Jin A. Kong
Professor of Electrical Engineering
Thesis Supervisor

Accepted by . . . .
Arthur C. Smith
Professor of Electrical Engineering
Chairman, Department Committee on Graduate Students

Theory and Application of Left-Handed Metamaterials

by

Joe Pacheco, Jr.

Abstract

Materials with simultaneously negative permittivity and permeability over a certain frequency band were first studied by Veselago in 1968, who termed such media left-handed (LH) due to the LH triad formed by the electric field vector, the magnetic field vector, and the phase propagation vector. However, since no such naturally occurring materials were known, Veselago's work laid dormant for nearly 30 years. Recently though, a composite material, also known as a metamaterial, consisting of the periodic arrangment of metallic rods and split-rings has been shown to exhibit left-handed properties. Because the dimension of the rods and rings that makeup the metamaterial are small compared to the wavelength of interest, it is possible to approximately describe their bulk electromagnetic properties using an effective permittivity and an effective permeability. In this thesis, the properties and potential applications of LH media are explored. In addition, various tools are presented for the purpose of characterizing metamaterial designs.

Before studying their metamaterial realization, the basic properties of propagation, radiation, and scattering through homogeneous LH media are studied. Many of the basic properties of LH media are in constrast to those typically encountered in right-handed media. For example, using a rigourous plane wave analysis of propagation and transmission into a dispersive LH medium from a RH medium, it is shown that power refracts at a negative angle, without violating causality. Second, the perfect lens concept is studied through a Green's function analysis. It is shown that under the perfect lens requirement, that a single source outside a LH media slab will generate two perfect images. Interestingly though, the time-averaged power flow inside the slab forms a sink. However, it is shown that while the introduction of loss eliminates this behavior, the lens becomes imperfect. It is seen that even a small amount of loss can destroy the imaging properties of the LH media lens. In terms of scattering, the Mie solution for plane wave scattering by a LH medium sphere is examined. It is shown that where applicable, care must be taken in choosing the appropriate algebraic signs of the wavenumbers in the evaluation of the Mie coefficients. In addition, it is then shown that a sphere composed of a LH medium will focus incoming energy into a spot inside the sphere. Finally, because the metamaterials studied in this thesis are anisostropic, the effects of aniostropy on reflection and transmission are examined.

Next, various tools for understanding and characterizing left-handed metamaterials are presented. First, the accuracy of approximate analytic models of the rods and split-rings is investigated by using two-dimensional FD-TD simulations to compare transmission charac-

teristics. It is shown that the rods tend to agree more favorably with their analytic model than the split-rings do. Next, in order to better understand the behavior of the rods and rings separately, numerical simulations of rods (or rings) embedded in homogeneous magnetic (or electric) plasma media were performed. Using the transmission characteristics, it is shown that in order to obtained left-handed features, the plasma in the immediate vicinity of the rods or rings needed to be removed, which shows that the electromagnetic fields surrounding metamaterial are not homogeneous. To further verify left-handed features, a phase-tracking method is used to retrieve the bulk index of refraction. In addition to the phase-tracking retrieval method, a more precise retrieval method that utilizes the complex S-parameter results is also investigated. Using this method, and S-parameters results from three-dimensional FD-TD and MoM simluations, it is shown that metamaterials composed of rods and split-rings can be characterized by a negative permittivity and negative permeability.

Next, two potential applications of LH media are explored. The first application is to use left-handed media as a radar absorber. These absorbers are designed by using a genetic algorithm, which determines a set of material parameters and layer thicknesses that minimizes the reflected power over a given frequency bandwidth or angular swath. In the design process, the frequency dispersive bulk media Drude and Lorentz models were used to model the ring and rod metamaterials. It is shown that LH media can be used to reduce the backscatter RCS, although its applicability is somewhat limited.

The second application explored is that of using metamaterials in the design of a lightweight directive antenna substrate. By Snell's law, if a source is embedded in a substrate that has a small index of refraction compared to air, its source rays will be transmitted near the normal of the substrate. Since left-handed metamaterials are frequency dispersive, there exists a frequency where its index of refraction is zero. Unaltered, the metamaterial will have a narrowband of operation where it is highly directive. In order to design a wideband directive antenna, the plasma and resonant frequencies of the metamaterials are adjusted to achieve minimum beamwidth. Additionally, it is found that certain anisotropic metamaterials, which in practice are simpler to build, will actually perform better in terms of beamwidth than their isotropic counterparts. In conjunction, the perfomance tradeoffs between beamwidth, gain, and substrate thickness are dicussed.

Thesis Supervisor: Jin A. Kong
Title: Professor of Electrical Engineering

Acknowledgments

It has been a long time since I first left my home state of Texas to make the long trek out to this far northeast corner of the country, farther than I ever imagined myself going. After being here for nearly eight years, I have met and interacted with so many people who have greatly influenced and shaped both my emotional and academic state. I would like to sincerely thank each and everyone of them.

First and foremost, I would like to wholeheartedly thank Prof. Kong for his encouragement and guidance throughout my tenure as a graduate student at the Massachusetts Institute of Technology. Through his enthusiastic lectures I not only learned the fundamentals of electromagnetics, but more importantly, how to efficiently problem solve. Furthermore, by working with him on numerous projects, technical and non-technical, I learned to how to negotiate, how to lead, and in general how to effectively communicate with a wide variety of people.

I am also indebted to Dr. Robert Atkins of M.I.T. Lincoln Laboratory for his continuous support throughout my graduate student career and his encouragement to study electromagnetics. I am grateful to him for allowing me the freedom to pursue research topics of my own choice. He was always willing to take the time to provide valuable advice and direction on both technical and non-technical topics alike.

I would also like to thank the current and former scientists in Prof. Kong's research group on campus for their valuable technical discussions and feedback during group meetings. In particular, I would like to acknowledge Dr. Tomasz Grzegorczyk, Dr. Fernando Teixeira, Dr. Eric Yang, and Dr. Yan Zhang for their expertise and guidance without which this thesis would not have been possible. I am also appreciative of Prof. David Staelin who served on both my thesis and RQE committees and of Prof. Markus Zahn for serving on my RQE committee.

To all the current and former graduate students that I have met here during our time together in Prof. Kong's group, namely Chi O. Ao, Benjamin B. Barrowes, Henning Braunisch, James Chen, Xudong Chen, Fuwan Gan, Jie Lu, Christopher D. Moss, Madhusudhan Nikku, Sang-Hoon Park, Zachary Thomas, Elana Wang, Bae-Ian Wu, Beijia Zhang, and

Yan Zhang. Thanks for your friendship and valuable discussions. The best of luck to all of you, especially those who are still making their way through the maze of graduate school. I wish you all the best.

To all my friends, who have seen me hide out in my office for way too long, thanks for reminding me that there is much more to life than equations and numbers. To my apartmentmate David Dunmeyer, thanks for making sure I was always fed, properly entertained, and for reminding me not to take life so seriously. To Venetia Chan, Al Chen, Julie Wertz-Chen, Shonna Coffey, Lucy Fang, Chris Salthouse, Steve Sell, Ilva Wilson, thanks for being there and helping me become my independent self. I sincerely hope our friendships last a lifetime.

Finally, and perhaps most importantly I would like to thank my family for their unwavering support. Mom, Dad, without you, I certainly would not be where I am today. Even though for the better part of the last eight years, I've lived a couple thousand miles away, it has always felt like you were right here next to me. You've always had such tremendous faith in me and never failed to remind me that I can do anything I set my mind to even when I most doubted myself. Thank you so much. This thesis is for you. I love you very much.

Para mi familia

Dios creó el Burro y le dijo

Serás Burro,

Trabajarás incansablemente de sol a sol cargando bolsas en el lomo,

Comerás pasto,

No tendrás inteligencia y vivrás 50 años,

Serás Burro.

El Burro contestó,

Seré burro pero vivir 50 años es demasiado,

Dame nada mas 20 años.

Dios se le concedió.

Never look back. – Chicho

Contents

List of Figures

14

15

16

17

18

19

List of Tables

Chapter 1

Introduction

In the last few years, there has been an increased interest in the scientific community in the study of metamaterials. Metamaterials are a class of composite materials artificially constructed to exhibit exceptional properties not readily found in nature. In particular, there has been high level interest in studying materials which can be characterized by simultaneously negative permittivity and permeability over a certain frequency band. This type of medium was originally studied by Veselago [1] in 1968, who termed such media left-handed (LH) due to the LH triad formed by the $\overline{E}$, $\overline{H}$, and $\overline{k}$ vectors. In his work, Veselago showed that LH media have a number of unique properties such as a negative index of refraction and the ability to support backward waves. However, since no such naturally occurring materials were known, Veselago's work lay dormant for nearly 30 years. Recently though, with the advent of the first LH metamaterial [2–4], there has been a renewed interest in this area. This thesis examines various aspects of LH media and metamaterials including their fundamental properties, their characterization and design, and their application to directive antenna and RCS reduction problems.

The study and application of electromagnetic wave propagation and scattering begins of course with Maxwell's equations, which relate the electric and magnetic fields through a coupled set of space and time dependent differential equations, or equivalently, integral

equations. Of primary importance in applying Maxwell's equations is the identification of the known sources and the properties of the surrounding media in the region of interest. Sources generate fields and waves which propagate through media and scatter at boundaries between two different types of media. Media are incorporated into the field theory through the use of the constitutive relations. Because Maxwell's equations form a macroscopic theory, a medium described by a certain set of constitutive relations is considered homogeneous. The validity of this assumption depends on the dimension, with respect to the wavelength of interest, of the smallest particles comprising the medium. For example, to the naked eye, water appears completely homogeneous when in fact it is composed of many discrete H_2O molecules. However, to observe and understand the refraction of visible light through water, it is enough to use a *macroscopic* analysis where the water is characterized by an effective index of refraction. However, if one were interested in understanding the internal mechanisms at the molecular level, a *microscopic* analysis would be needed where details of the molecule configuration and distribution would be modeled.

A similar situation arises in the case of LH metamaterials. As will be discussed in detail in Section 1.1, metamaterials are a composite material composed of elements that are small compared to the wavelength of interest and can therefore be analyzed from both macroscopic and microscopic points of view. The macroscopic viewpoint is taken in order to gain a better understanding of the bulk material properties, such as the negative index of refraction. The microscopic approach is taken in order to gain a better understanding of the internal mechanisms which will enable the design and characterization of metamaterials for specific applications.

Also, note that throughout this thesis, for the sake of clarity, a left-handed (LH) medium shall refer to a homogeneous body whose permittivity and permeability's real parts are both negative, whereas the term right-handed (RH) media shall refer to a homogeneous body whose permittivity and permeability's real parts are not both negative. Furthermore, the terminology "LH metamaterial" shall refer to a composite material that exhibits LH medium properties on average over a specific frequency band.

1.1 Background

In order to be characterized as an LH metamaterial, a metamaterial must have an effective permittivity and permeability that are simultaneously negative over some frequency band. As shown in [1], electromagnetic waves will propagate in such a medium since the real parts of the permittivity and permeability are of the same algebraic sign; however, waves will not propagate in a medium where the permittivity and permeability are of the opposite algebraic sign. Using this principle, the first step in the creation of LH metamaterials was to create metamaterials that restricted propagation at certain frequency bands due to either a negative permittivity or a negative permeability. Then under the assumption of minimal coupling and if the stop-bands of each could be made to overlap, LH metamaterials could be constructed by combining those types of metamaterials [5].

Historically, the first step taken in the development of LH metamaterials was the design of a composite material that has an effective negative permittivity over some frequency band. One approach used to achieve this property at microwave frequencies, studied by Pendry in [2], is to use a periodic collection of metallic rods, which he showed behaves as a plasma medium when the electric field vector is aligned with the rods. As Pendry showed, the plasma frequency, below which the effective permittivity is negative, depends on the spacing and radius of the rods. Of course, such a medium is inherently anisotropic, and it is necessary to use a mesh of criss-crossing wires to achieve a more isotropic medium [6].

Next, in order to create a medium with an effective negative permeability, Pendry proposed various magnetic resonant structures such as an array of cylinders, a capacitative array of sheets wound on cylinders, and an array of "swiss roll" capacitors [3]. For each structure, Pendry made an approximate analysis of the field distribution assuming the magnetic field vector was aligned along the axis of the cylinders, and he found that the effective permeability could be described by a resonant model, which exhibits a negative permeability over a certain frequency range. Qualitatively, this effect can be understood via Lenz's law wherein a magnetic field which opposes the change due to the incident magnetic field

is generated. The opposing magnetic field will be of the opposite sign leading to a negative permeability. Currently, most work in the area of LH metamaterials has focused on the study of the capacitative array of sheets wound on cylinders design, also known as the split-ring resonator (SRR) design. Such designs where the magnetic field is forced to be aligned with the axis of the cylinders are anisotropic, and as Pendry proposed, also in [3], a more isotropic medium can be created by placing thin split-ring disks in three perpendicular directions. Other designs for creating a more isotropic negative permeability medium have also been suggested in [7] and [8]. Additionally, Pendry later proposed some variations on the SRR design, and scaled the design so that it operates at IR frequencies [9, 10].

It is worth also worth mentioning that various studies on the bianisotropy of the rings have been done by Marques [11, 12]. In his work, Marques argues that a while a magnetic field incident upon the ring does indeed induce a magnetic moment, it can also induce an electric moment. Thus, a magnetic field incident on the ring particle polarizes both the electric and magnetic field, meaning that it is bianisotropic. In order to eliminate the effects of bianisotropy, it is suggested that the inner ring be a ring equal in size to the outer ring in an edge-coupled configuration. In this configuration, the induced electric dipole moments on each ring would cancel while the induced magnetic dipole moments would add, leaving the desired negative permeability features of the ring intact. Related to the work of Marques is the recent use of omega particles as a left-handed metamaterial [13]. Omega particles, originally pioneered by the work of Engheta's group at the University of Pennsylvania [14] are, as their name implies, metallic inclusions shaped in the form of the Greek symbol omega (Ω); essentially a combination of a broken rod and a split-ring. Omega particles were one of the first material known to exhibit chiral properties. For left-handed metamaterial applications, researchers have used the edge-coupled approach suggested by Marques to eliminate the bianisotropy of the omega particles making them useful candidates for many new metamaterial applications [13].

Returning back to the original concentric split-ring designs, these composite structures were were first combined by Smith *et al* [5] to create a metamaterial made up of periodic rods

and periodic SRRs that had left-handed properties. Physically, the medium was built by first printing a thin sheet of metal in the shape of circular split rings on one side of the dielectric substrate. The printed dielectric was then placed adjacent to a set of relatively large metallic posts. Since the metamaterials constructed were expected to be highly anisotropic, the initial experiments studied only the transmission properties of the metamaterial for a specific polarization and incident angle. However, this requirement was later relaxed to allow the incident wave to be any angle within one plane by creating a metamaterial with a set of SRRs and a set of parallel rods in two perpendicular planes [15].

In order to test if the rod/SRR composite metamaterial is left-handed, Smith *et al* studied the transmission through metamaterials with only metallic rods and with only SRRs using both numerical and experimental techniques. The basis of the study was that if one could show that propagation does not occur in a metamaterial that theoretically has an effective negative permittivity but an effective positive permeability, and vice versa, but does occur in a medium where both are theoretically negative, then it is possible to conclude that the composite material is left-handed. Indeed, their results showed that a metamaterial containing only SRRs has a stop band characteristic while a metamaterial containing only rods has a high-pass characteristic. However, when both the rings and rods are present, a pass band appears near where the stop band for the SRRs once was, which Smith *et al* claimed meant that propagation was allowed at those frequencies due to fact that the permittivity and permeability were both negative [5].

Because it is possible that a coupling effect between the rings and rods creates a metamaterial whose effective permittivity and permeability are both positive, transmission characteristics alone cannot definitively prove that such metamaterials are left-handed. A more definitive characterization method, used by Smith *et al* in [16], was to numerically calculate the average electromagnetic fields inside a metamaterial structure. Then by using the definition given by Pendry in [3], Smith *et al* determined the effective permittivity and permeability by calculating the ratio between the $\overline{D}_{\mathrm{avg}}$ and $\overline{E}_{\mathrm{avg}}$ fields and the $\overline{B}_{\mathrm{avg}}$ and $\overline{H}_{\mathrm{avg}}$ fields, respectively. The results obtained not only showed that the effective permittivity and

permeability were both negative over a certain frequency band, but they also confirmed the permittivity and permeability models previously derived by Pendry in [2, 3].

Although the above method works well in conjunction with numerical simulations where one can easily obtain the field quantities at every position in space, an alternate method is needed for experimental proof. One method, which relies on the correlation between the index of refraction, permittivity, and permeability is a Snell's law experiment where the index of refraction is measured directly. As discussed by Veselago [1] and rigorously demonstrated by Smith *et al* [17], a medium with negative permittivity and permeability will have a negative index of refraction. Thus, if a certain metamaterial was measured to have a negative index of refraction, then it can be concluded that both the permittivity and permeability are negative. The first experimental demonstration in this manner was performed by Shelby *et al* wherein the authors placed a prism shaped metamaterial structure in a parallel-plate waveguide [4]. In the experiment, an X-band microwave beam was launched into one end of the waveguide, 1 m from the backside of the prism sample, and the resulting angular radiation pattern of the transmitted beam that was refracted by the prism's slanted side was recorded. Shelby *et al* observed a negative angle refraction near 10.5 GHz, which corresponded to a index of $n = -2.7 \pm 0.1$.

The setup created by Shelby *et al* had many features that needed to be carefully tuned, such as the gap between the top of the parallel plate and the rods, which made it difficult to repeat for quite some time. For this reason among others, some researchers have questioned the validity of the experimental results [18], as well as the fundamental theoretical properties of LH media [19–21].

In particular, Valanju *et al* claimed that the presence of dispersion prevents power transmitted at a RH medium-LH medium interface from refracting at a negative angle [19]. However, Valanju *et al* drew their conclusions based solely on the electric field, inferring the direction of the power flow from the normal of the phase front based on an erroneous definition of the group velocity. In [22], Smith *et al* refute the position of Valanju *et al* by demonstrating that the group velocity vector must always be parallel to the phase velocity

vector in an isotropic medium, contrary to the conclusion reported by Valanju *et al.* Simultaneously, the controversy was addressed by Pacheco *et al* in [23] from the point of view of power propagation. As discussed in detail in Section 2.2, the authors demonstrate, through explicit calculation of the time and space dependent Poynting vector, that the power of a multi-frequency wave transmitted into a frequency dispersive LH material refracts at a negative angle [23]. Additional work using time-domain numerical techniques by other authors has confirmed these conclusions by showing that due to the dispersion and initially large bandwidth of the incident pulse, there is a setup time before which the transmitted beam is inhomogeneous, but after which a homogeneous negatively refracted beam emerges [24].

Another debate in the literature concerned the concept of the perfect lens, which was first introduced by Pendry [25]. In his paper, Pendry showed that a slab with material parameters of $\epsilon = -\epsilon_o$ and $\mu = -\mu_o$ perfectly focuses a source placed in front of an LH slab. However, Garcia *et al* [21] claim that a perfect lens cannot theoretically exist because if it did, it would require infinite energy generation; however this claim was later refuted by Gómez-Santos [26] who introduced an intrinsic time scale in the time evolution of subwavelength (including perfect) resolution to remove the problem of divergences claimed in [21]. Although the debate has not been concluded, others have begun to focus on more practical issues such as the effects of dispersion and absorption on the creation of near-perfect lens [27–30]. For instance, it has been observed that in the presence of absorption, the image created by a LH slab is not stationary but actually oscillates along the central axis of propagation on the time scale of the source frequency. Thus, the net effect in the near field is the appearance of a collimated beam rather than an image of the source.

While the above work concerned the theoretical aspects of the debate, other researchers have questioned the experimental proof of the existence of LH metamaterials. For example, Valanju *et al* claimed that the observation by Shelby *et al* [4] of negative refraction was really just near-field diffraction effects [19]. Additionally, Garcia *et al* said that they believed the effects of losses in [4] were understated. They claimed that if they were fully taken into account, they would make the distinction between right-handed and left-handed

metamaterials difficult because the transmitted electromagnetic wave would be very inhomogeneous [18].

In order to overcome these criticisms, more experimental work was needed. As mentioned above, the results by Shelby *et al* were difficult to reproduce due to the sensitivity of the placement of the metamaterial inside the waveguide. In order to eliminate the issue of the gap between the metamaterial and the waveguide, a group at Boeing Phantom Works measured the transmission and angle of refraction through the metamaterials using a free-space configuration. In order to avoid diffraction effects, focused beams were used to illuminate the metamaterial. Their work confirmed that the rod/SRR metamaterial had transmission bands characteristic of left-handed materials [31] as well as a negative index of refraction [32]. Simultaneously, a group at the MIT Media Laboratory managed to reproduce the results of Shelby *et al* using the original parallel-plate waveguide configuration [33]. The parallel-plate configuration experiment was also later repeated successfully by a group at Zhejiang University [34]. In addition to the transmission and Snell's law prism experiments, other methods for experimentally demonstrating that a metamaterial is left-handed have been proposed [35–39]. Recently, some of these proposed experimental configurations, such as the lateral shift of a Gaussian beam and the propagation through a loaded T-junction, have been realized and have successfully demonstrated the left-handed properties of certain metamaterials [34].

Because the free-space experiments done by the Boeing team focused on far-field measurements, they helped to refute the claims that the original measurements were just near-field effects. However, it is true that the metamaterials created so far are very lossy, a fact which has prompted researchers to study the origins of loss in the metamaterials [40], as well as exploring new designs. One other approach, where the loss is low compared to the rod/SRR design, uses a transmission line (TL) network. This method, pioneered by a group at the University of Toronto, is based on the principle of using a two-dimensional lumped element transmission line network to create a high-pass filter, which supports backward waves [41–46]. With the appropriately chosen configuration, they show that the effective

permittivity and permeability are negative. The advantage of this approach is that the TL can possess some left-handed properties over a very wide bandwidth while not suffering from the same losses as the rod/SRR designs. However, the main disadvantage is that while the transmission line approach reproduces some of the same phenomena as LH metamaterials, it is a fundamentally different approach which cannot be applied in the same way as the rods and SRRs.

Yet another approach to generate negative refractive index materials is to use photonic band gap structures (PBG) [47–49]. PBGs are periodic structures, typically constructed from high dielectric materials [50], that, as their name implies, exhibit frequency band gaps where electromagnetic waves cannot propagate. In addition, the dispersion relations describing the propagating modes, also known as Bloch or Floquet modes, are nonlinear and can in some cases lead to negative refraction. However, because the group velocity and phase vectors are not parallel, the negative refraction behavior in PBGs is different from ideal LH media, which has a permeability and permittivity that are negative and isotropic so that the velocity and phase vectors are exactly anti-parallel.

Since one of the goals in the proposed thesis is to develop metamaterials that can be used in a wide variety of applications such as antennas and radar absorbers, the type of metamaterials that will be studied are the rod and SRR structures. Compared to the TL approach, the rod/SRR structures can easily be used in a wide variety of microwave engineering applications. In addition, compared to PBGs, at the present time it is currently easier to implement rod/SRR structures in applications, because it is easier to create simple uniaxial or even isotropic materials, whereas PBG structures are in general highly anisotropic with complex dispersion relations.

1.2 Thesis Work

As mentioned previously, there are two general viewpoints for modeling left-handed metamaterials: microscopic and macroscopic. Both of these methods are employed in this thesis.

The macroscopic approach is used to gain a fundamental understanding of the principles of left-handed media as well as to gauge the potential of left-handed metamaterials for two applications. In order to connect the theory to the physical realization, various tools for the characterization of metamaterials are introduced. The input to these tools is of course data obtained from numerical simulations of the microscopic structure. In the following, the contributions of this thesis are briefly outlined.

The purpose of Chapter 2 is understand the fundamental electromagnetic properties of propagation, radiation, and scattering in the presence of left-handed media. The main contribution in this chapter is to provide a solid understanding of the effects of dispersion on the refraction of a wave from a right-handed medium into a left-handed medium. As discussed above, this topic has received much attention in the recent literature due to the controversial paper by Valanju *et al* [19] who asserted that negative refraction is not theoretically possible. In this chapter, this claim is disputed by performing a rigorous analysis of the power flow. Other topics covered in this chapter include an in-depth study of the perfect lens and the associated difficulties of achieving perfect focusing, scattering from left-handed media spheres, and the effects of anisotropy on Gaussian beam propagation through a slab of an indefinite medium.

The purpose of Chapter 3 is to study the microscopic structure of left-handed metamaterials and methods of characterization. The contribution of the first half of this chapter is to provide an understanding of the mechanisms needed for the generation of left-handed properties. In particular, it is shown that a rod metamaterial embedded in a homogeneous magnetic plasma medium cannot function as a left-handed metamaterial nor can a split-ring metamaterial that is embedded in a homogeneous electric plasma medium. This result, termed the "problem of left-handed materials" by Pokrovsky and Efros [20] means that in combining rods and split-rings together to form a left-handed metamaterials, it is essential that there be regions within the metamaterial that are right-handed; however, the overall material can in general still effectively be treated as a left-handed material. The contribution in this section is to isolate the regions within the metamaterial that need a right-handed

medium background. Additionally, a modified form of the phase-tracking method is presented, which allows the extraction of the bulk index of refraction from the field distribution within the metamaterial. In addition to the phase-tracking retrieval method, a more precise retrieval method that utilizes the complex S-parameter results is investigated. Using this method, and S-parameters results from three-dimensional FD-TD and MoM simulations, it is shown that metamaterials composed of rods and split-rings can be characterized by a negative permittivity and negative permeability.

The final two chapters are concerned with addressing the potential applications of left-handed materials. Although these materials are still in their infancy of development, a number of applications have already been proposed. These include perfect and near-perfect lens [25, 29, 30, 51], backward wave devices [52, 53], novel Cerenkov detectors [54], high speed interconnects in integrated circuits [55], subwavelength cavity resonators [56], and multiplexing devices [37].

The first application considered is to use left-handed metamaterials as radar absorbers. The motivation behind this work was to investigate the potential benefits of being able to design an absorber with a materials that have negative permittivity and/or negative permeability. In designing the coatings, a genetic algorithm optimization method is used to determine the parameters of the Drude and Lorentz models, which are used to characterize the current generation of left-handed metamaterials. For single frequency applications, it is found that there is no advantages to using right-handed versus left-handed materials. On the other hand, for wideband applications, it seen that the sharp resonance of the Lorentz models limits the maximum bandwidth achievable. Despite these drawbacks, metamaterials do have the advantage of being light-weight and frequency tunable. Thus, for applications requiring light-weight coatings, left-handed metamaterials offer a viable alternative.

The second application investigated is the use metamaterials in the design of a light-weight directive antenna substrate. It is well known that by Snell's law, if a source is embedded in a substrate that has a small index of refraction compared to air, its source rays will be transmitted near the normal of the substrate. In the past, antennas have been

designed using this concept; however, they have been limited to narrowband operation. It is the purpose of this chapter to use left-handed metamaterials, which have frequency dispersive magnetic and electric properties, to design a wideband directive antenna. The fact that metamaterials are extremely light-weight is added benefit. Furthermore, one of the main contributions in this chapter is an understanding of the role that anisotropy plays in controlling the beamwidth. It will be shown that certain anisotropic metamaterials, which in practice are simpler to fabricate, will actually perform better in terms of beamwidth than their isotropic counterparts. In conjunction, the performance trade-offs between beamwidth, gain, and substrate thickness are discussed.

Chapter 2

Propagation, radiation, and scattering in left-handed media

2.1 Introduction

In this chapter, the fundamental electromagnetic properties of propagation, radiation, and scattering in the presence of left-handed media will be considered. Throughout this chapter, all media are assumed to be homogeneous and, except for Section 2.5, isotropic. Before considering more complex phenomena, it is useful to review the simple concept of wave propagation in a source-free unbounded medium. For such a medium, propagating waves obey the frequency domain Maxwell's curl equations, which are given by,

$$\nabla \times \overline{E}(\overline{r}) \;=\; i\omega\mu(\omega)\overline{H}(\overline{r}) \tag{2.1}$$

$$\nabla \times \overline{H}(\overline{r}) \;=\; -i\omega\epsilon(\omega)\overline{E}(\overline{r}) \tag{2.2}$$

where $\epsilon(\omega)$ and $\mu(\omega)$ are the frequency dependent permittivity and permeability. For plane wave solutions of the form $e^{i\overline{k}\cdot\overline{r}}$, Maxwell's equations become,

$$\overline{k} \times \overline{E}(\overline{r}) = \omega\mu(\omega)\overline{H}(\overline{r}) \tag{2.3}$$

$$\overline{k} \times \overline{H}(\overline{r}) = -\omega\epsilon(\omega)\overline{E}(\overline{r}) \tag{2.4}$$

where $\overline{k}$ is the wave propagation vector. As discussed in Chapter 1, media with simultaneously negative permittivity and permeability were first studied by the Russian scientist, Veselago, who termed such media left-handed [1]. The origin of this terminology is due to the fact, as evident from (2.3), that the $\overline{E}$, $\overline{H}$, and $\overline{k}$ vectors form a left-handed system when both ϵ and μ are negative. Note that if only μ is negative, then the wave propagation vector becomes imaginary, and it no longer possible define the handedness of the system. The other unique property of left-handed materials is their ability to support backward waves, which are waves whose power propagates in the opposite direction of their phase. For example, consider an electric field that is polarized along the $\hat{p}$ direction. From Maxwell's equations and Poynting theorem, the power flow direction may be calculated as follows,

$$\overline{E} = \hat{p}\, e^{i\overline{k}\cdot\overline{r}} \tag{2.5}$$

$$\overline{H} = \frac{1}{\omega\mu}\left(\overline{k} \times \hat{p}\right)e^{i\overline{k}\cdot\overline{r}} \tag{2.6}$$

$$\Rightarrow \langle\overline{S}\rangle = \Re\left\{\overline{E} \times \overline{H}^*\right\} = \frac{1}{\omega\mu}\,\hat{p} \times \left(\overline{k} \times \hat{p}\right)$$

$$= (\hat{p}\cdot\hat{p})\overline{k} - (\hat{p}\cdot\overline{k})\overline{k}$$

$$= \frac{\overline{k}}{\omega\mu} \tag{2.7}$$

where $\Re$ is the real operator and $\hat{p}\cdot\overline{k} = 0$ is due to Gauss' law. The result shows that the time-averaged Poynting vector will be in the opposite direction of the phase propagation vector when ϵ and μ are both negative. With this simple result, an entire new field in electromagnetics has opened up. The remainder of this chapter and indeed much of this

thesis is devoted to the study of the consequences of ϵ and μ being simultaneously negative.

2.2 Reflection and transmission at a RH-LH boundary

As Veselago showed in [1], non-dispersive media cannot be left-handed, or in other words, a medium can only have a negative permittivity and permeability for a finite frequency band. In order to understand the implications of this property, the first part of this work examines the effects of dispersion in the transmission of a plane wave from a right-handed medium (RHM: $\epsilon > 0$, $\mu > 0$) to a frequency dispersive left-handed medium (LHM: $\epsilon(\omega) < 0$, $\mu(\omega) < 0$ for some ω), which are both homogeneous and isotropic.

In particular, Valanju *et al* claimed in [19] that the presence of dispersion prevents power transmitted at a RH-LH interface from refracting at a negative angle. In their work, Valanju *et al* drew their conclusions based solely on the electric field, inferring the direction of the power flow from the normal of the phase front based on an erroneous definition of the group velocity. The confusion arises from the presence of an interference pattern in the transmitted LH medium region, whose apparent motion is in the direction of positive refraction. However, it is well known that the direction of power flow for both non-dispersive and dispersive media is determined by the Poynting vector, which is not necessarily parallel to the normal of the phase front [57].

In this section, this confusion is explained by explicitly calculating the time and space dependent electric and magnetic fields in order to determine the Poynting vector. In order to account for the dispersion, two types of signal spectra are considered. The first consists of two discrete frequencies, while the second is Gaussian. Explicit expressions for the time-domain fields are obtained, from which the time averaged Poynting vectors and hence power flow vectors are calculated. For each case, it will be shown that the apparent direction of motion of the interference pattern is not the direction of power propagation, and that the power is negatively refracted.

2.2.1   Dirac Delta Function Spectrum

In order to study the effect of dispersion on the direction of power propagation, we consider the transmission of an incident field, composed of many frequencies, from an isotropic non-dispersive region into an isotropic dispersive region as shown in Fig. 2-1. The total TE polarized incident electric field is constructed as a weighted sum of plane waves, and is given by,

$$E_{0y}(\overline{r}, t) = \int_{-\infty}^{\infty} d\omega \; A(\omega) e^{i\phi_0(\overline{r},\omega) - i\omega t}, \tag{2.8}$$

where $A(\omega) = \alpha(\omega) + \alpha^*(-\omega)$ is the signal spectrum, $k_x(\omega) = k_0 \sin\theta_i$, $k_{0z}(\omega) = k_0 \cos\theta_i$, $k_0 = \omega\sqrt{\mu_0 \epsilon_0}$, and $\phi_\ell(\overline{r}, \omega) = k_x(\omega)x + k_{\ell z}(\omega)z$, with ℓ referring to region 0 or 1. With this formulation, the transmitted electric field in region 1 is given by,

$$E_{1y}(\overline{r}, t) = \int_{-\infty}^{\infty} d\omega \; A(\omega) T(\omega, \theta_i) e^{i\phi_1(\overline{r},\omega) - i\omega t}, \tag{2.9}$$

where $T(\omega, \theta_i)$ is the frequency and angle dependent transmission coefficient given by,

$$T(\omega, \theta_i) \;\; = \;\; \frac{2\mu_1 k_{0z}}{\mu_1 k_{0z} + \mu_0 k_{1z}}, \tag{2.10}$$

and

$$k_{1z}(\omega) \;\; = \;\; \sigma\sqrt{\omega^2 \mu_1(\omega)\epsilon_1(\omega) - k_x^2(\omega)}, \tag{2.11}$$

where $\sigma = +1$ for RHM and $\sigma = -1$ for LHM. This choice of sign ensures power propagates away from the surface in the $+\hat{z}$ direction rather than from infinity [55]. From the electric field, we can calculate the magnetic field which is given by,

$$H_{1z}(\overline{r}, t) = \int_{-\infty}^{\infty} d\omega \; \frac{k_x(\omega)}{\omega\mu_1(\omega)} A(\omega) T(\omega, \theta_i) e^{i\phi_1(\overline{r},\omega) - i\omega t}, \tag{2.12}$$
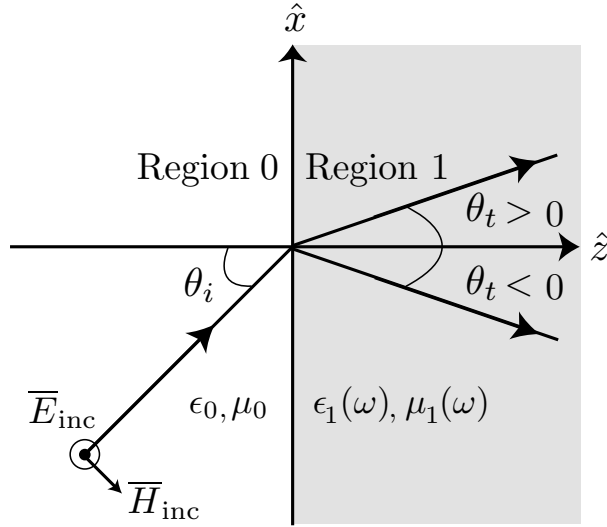
Figure 2-1: Half-space problem geometry: A TE polarized incident wave is transmitted from a non-dispersive region (0) into a dispersive region (1). Arrows shown here indicate power flow direction.

where for brevity we list only H_{1z}, noting that H_{1x} can be calculated in a similar manner.

In order to study the effects of dispersion, an incident field composed of two slightly separated frequencies with the following spectrum,

$$\alpha(\omega) \quad = \quad \frac{E_0}{2}\left[\delta(\omega - \omega_1) + \delta(\omega - \omega_2)\right] \tag{2.13}$$

is introduced where E_0 is the real-valued amplitude, $\omega_2 - \omega_1 = \delta\omega$, and $|\delta\omega/\omega_1| \ll 1$. From (2.9), we can find the expression for the time and space dependent transmitted electric field,

$$E_{1y}(\overline{r}, t) = E_0\left[\cos\psi_1 + \cos\psi_2\right], \tag{2.14}$$

where $\psi_j = \phi_1(\overline{r}, \omega_j) - \omega_j t$, with $j = 1, 2$. Note that, here we consider the lossless case and let $T(\omega, \theta_i) = 1$ for the simplicity of derivation. Later in this section we will consider a more rigorous derivation that includes the transmission coefficient. To proceed with the

Poynting vector calculation, we first determine the magnetic field, which is given by

$$H_{1z}(\overline{r}, t) = E_0 \left[\frac{k_x(\omega_1) \cos \psi_1}{\omega_1 \mu_1(\omega_1)} + \frac{k_x(\omega_2) \cos \psi_2}{\omega_2 \mu_1(\omega_2)} \right], \tag{2.15}$$

where again for brevity we list only H_{1z}. To find the power flow direction, we calculate the time and space dependent Poynting vector, given by, $\overline{S}_1(\overline{r}, t) = \overline{E}_1(\overline{r}, t) \times \overline{H}_1(\overline{r}, t)$, yielding

$$
\begin{aligned}
S_{1x}(\overline{r}, t) &= E_{1y}(\overline{r}, t) H_{1z}(\overline{r}, t) \\
&= E_0^2 \frac{k_x(\omega_1)}{\omega_1 \mu_1(\omega_1)} \cos^2 \psi_1 + E_0^2 \frac{k_x(\omega_2)}{\omega_2 \mu_1(\omega_2)} \cos^2 \psi_2 \\
&\quad + E_0^2 \left[\frac{k_x(\omega_1)}{\omega_1 \mu_1(\omega_1)} + \frac{k_x(\omega_2)}{\omega_2 \mu_1(\omega_2)} \right] \cos \psi_1 \cos \psi_2,
\end{aligned} \tag{2.16}
$$

where we note that a similar calculation for S_{1z} can also be done. In order to determine the power propagation direction, we calculate the time average value of the time dependent Poynting vector by integrating (2.16) and a similar expression for S_{1z} over a period T, which is chosen to be the period of the combined signal, i.e. it is the common period of the frequencies $\omega_1 + \omega_2$ and $\omega_1 - \omega_2$. Integrating, we find that the cross terms average to zero if $\omega_1 \neq \omega_2$ yielding,

$$< \overline{S}_1(\overline{r}, t) > = \frac{E_0^2}{2} \left[\frac{\overline{k}_1(\omega_1)}{\omega_1 \mu_1(\omega_1)} + \frac{\overline{k}_1(\omega_2)}{\omega_2 \mu_1(\omega_2)} \right], \tag{2.17}$$

where $\overline{k}_1(\omega) = \hat{x} k_x(\omega) + \hat{z} k_{1z}(\omega)$. From this expression, we see that the power flow will be in the average direction of the two single frequencies. Thus, depending on the values of $\mu_1(\omega_1)$, $\mu_1(\omega_2)$, $\epsilon_1(\omega_1)$, and $\epsilon_1(\omega_2)$ the wave will refract at either a positive or a negative angle. In the case that both the permittivities and permeabilities at each frequency are negative, the wave will refract at a negative angle.

We will now consider two specific simple examples. The first example is the transmission of a wave with two frequency components at $f_1 = 10.5$ GHz and $f_2 = 11.5$ GHz ($\omega = 2\pi f$) where we take the permittivity for region 1 to be different for each frequency, yet both

positive, while the permeability remains fixed and positive such that in this example, both regions are RHM. The second example is the case of transmission from a RHM to a LHM where we again take the permittivity for region 1 to be different for each frequency, yet both negative, while the permeability remains fixed and negative. Fig. 2-2(a) for the first example and Fig. 2-2(b) for the second example show, at a specific time, the resulting $\hat{x}$-component of the Poynting vector, overlayed with black colored arrows that indicate the overall direction of the vector. Clearly, in the case of the RHM-RHM interface, the $\hat{x}$-component of the Poynting vector is positive, while in the RHM-LHM case the $\hat{x}$-component is negative. Hence, as can be seen from the arrows, $\theta_t > 0$ for the RHM-RHM interface and $\theta_t < 0$ for the RHM-LHM interface. Note that calculation of the Poynting vector for subsequent times shows that the time-averaged S_x component remains positive for the RHM-RHM case and negative for the RHM-LHM case, as predicted by (2.17).

Note, however, that in both cases an interference pattern is formed whose normal vectors are not in the direction of the respective power flows. This interference is a result of the fact that the waves for each frequency are refracted at different angles. From the above calculations we see that, contrary to the conclusions in [19], the normal vectors of these interference fronts do not indicate the power flow direction.

2.2.2 Gaussian Spectrum

Next, in order to more rigorously model a physically realizable narrowband signal, we consider an incident field with a normalized Gaussian signal spectrum,

$$\alpha(\omega) \;\; = \;\; \frac{E_0}{\sqrt{4\pi(\delta\omega)^2}} \exp\left[-\frac{(\omega-\omega_0)^2}{(\delta\omega)^2}\right], \tag{2.18}$$

where as before E_0 is the real-valued amplitude, and $|\delta\omega/\omega_0| \ll 1$. The time-domain expressions for the fields given in (2.9) and (2.12) involve the evaluation of integrals that can be dealt with using a standard expansion method. Note that, by conjugate symmetry, we need only integrate the portion of the spectrum centered at ω_0. A generic form of the
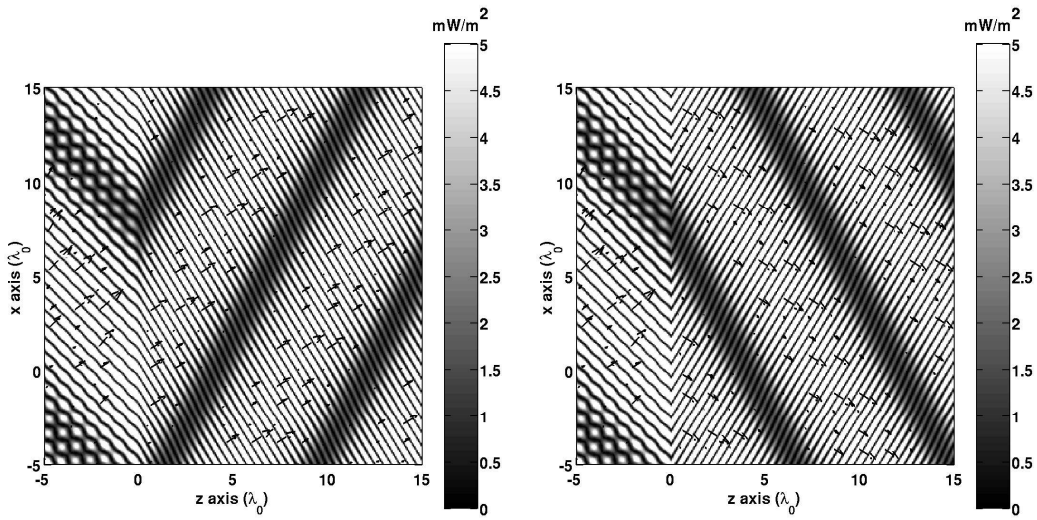
(a) RHM-RHM interface, negative slope: $\epsilon_{1r}(\omega_1) = 2$, $\epsilon_{1r}(\omega_2) = 1.5$ and $\mu_{1r}(\omega_1) = \mu_{1r}(\omega_2) = 1$

(b) RHM-LHM interface, positive slope: $\epsilon_{1r}(\omega_1) = -2$, $\epsilon_{1r}(\omega_2) = -1.5$, and $\mu_{1r}(\omega_1) = \mu_{1r}(\omega_2) = -1$

Figure 2-2: Interference pattern of the magnitude of the Poynting vector ($|\overline{S}|$) overlayed with arrows indicating the direction at a specific time for a wave incident at $\theta_i = 45°$ composed of two discrete frequencies, $f_1 = 10.5$ GHz and $f_2 = 11.5$ GHz. The figures illustrate that the normal to the interference front does not necessarily point in the same direction as the Poynting vector. Nb: λ_0 corresponds to the wavelength of the mean frequency.

integral is given by,

$$I = \int_{-\infty}^{\infty} \mathrm{d}\omega \ f(\omega)e^{i\gamma(\omega)} = \int_{-\infty}^{\infty} \mathrm{d}\omega \ e^{g(\omega)}, \tag{2.19}$$

where $g(\omega) = i\gamma(\omega) + \ln[f(\omega)]$ and the principle branch of the logarithm function is taken. To evaluate this integral, the argument to the exponential, $g(\omega)$, is expanded in a Taylor series about ω_0 to second order to yield,

$$I = \sqrt{\frac{2\pi}{g''(\omega_0)}} \exp\left[g(\omega_0) - \frac{[g'(\omega_0)]^2}{2g''(\omega_0)}\right]. \tag{2.20}$$

Note that, in the case of non-dispersive media, the second order Taylor series expansion is exact. For dispersive media, this approximation holds as long as the signal spectrum $\alpha(\omega)$ spans only a linear portion of the dispersion curve, which is true outside the region of resonance, under the condition $|\delta\omega/\omega_0| \ll 1$. Note that there is no loss of generality by limiting the spectrum in this manner since group velocity and power flow direction are determined by considering the local slope of the dispersion curve [58].

In order to apply this method to determine the fields in region 1, we specify the following definitions of $g(\omega)$, depending on the field component examined:

$$g_{E_{1y}}(\omega) = -\frac{(\omega - \omega_0)^2}{(\delta\omega)^2} + \ln[T(\omega)]$$
$$+i(k_x(\omega)x + k_{1z}(\omega)z - \omega t), \tag{2.21a}$$

$$g_{H_{1x}}(\omega) = -\frac{(\omega - \omega_0)^2}{(\delta\omega)^2} + \ln[T(\omega)] + \ln\left[\frac{k_{1z}(\omega)}{\omega\mu_1(\omega)}\right]$$
$$+i(k_x(\omega)x + k_{1z}(\omega)z - \omega t), \tag{2.21b}$$

$$g_{H_{1z}}(\omega) = -\frac{(\omega - \omega_0)^2}{(\delta\omega)^2} + \ln[T(\omega)] + \ln\left[\frac{k_x(\omega)}{\omega\mu_1(\omega)}\right]$$
$$+i(k_x(\omega)x + k_{1z}(\omega)z - \omega t), \tag{2.21c}$$

where the definition of $g_{H_{1x}}$ is based on a integral expression for H_{1x} that has been derived but not listed.

As an example, we consider the following dispersion relations given by Shelby *et al* [4],

$$\frac{\mu_1(\omega)}{\mu_0} = 1 - \frac{\omega_{mp}^2 - \omega_{mo}^2}{\omega^2 - \omega_{mo}^2 + i\gamma\omega}, \tag{2.22a}$$

$$\frac{\epsilon_1(\omega)}{\epsilon_0} = 1 - \frac{\omega_{ep}^2 - \omega_{eo}^2}{\omega^2 - \omega_{eo}^2 + i\gamma\omega}, \tag{2.22b}$$

where ω_{mo} is the magnetic resonance frequency, ω_{mp} is the magnetic plasma frequency, ω_{eo} is the electric resonance frequency, ω_{ep} is the electric plasma frequency, and γ is the damping frequency. Explicit analytical expressions for the electric and magnetic fields are derived from the use of (2.20) and (2.21), but are not listed for the sake of brevity.

To proceed with a numerical evaluation of the electric and magnetic fields, the parameters reported in [4] are used, except with $\gamma = 0$ in order to suppress losses for the purpose of illustration. The incident wave is chosen to have a Gaussian spectrum centered at $f_0 = 10.5$ GHz with $\delta f = 10$ Hz, and is incident at $\theta_i = 45°$. From the resulting time-domain electric and magnetic fields, the Poynting vector is calculated. Fig. 2-3 shows the S_{1x} and S_{1z} components as a function of time for one typical spatial point in the LHM region. The dot-dashed curve shows that the $\hat{x}$-component of the power is indeed always negative indicating a negative angle of refraction. Specifically, this angle can be calculated by applying,

$$\theta_t = \tan^{-1}\left[\frac{< S_{1x}(t) >}{< S_{1z}(t) >}\right]. \tag{2.23}$$

In the example shown in Fig. 2-3, θ_t is found to be approximately $-11.12°$. For comparison, note that at the center frequency, $\epsilon_{1r}(\omega_0) \approx -12.88$ and $\mu_{1r}(\omega_0) \approx -1.04$, which corresponds to an index of refraction $n(\omega_0) \approx -3.67$ and a refraction angle of $\theta_t \approx -11.12°$. Hence, comparing these two values we conclude that dispersion does not preclude refraction at a negative angle in accordance with Snell's law. It should be noted that the power plotted in Fig. 2-3 is not strictly periodic since a continuum of frequencies is used; however, this fact does not affect the conclusion that the power is refracted at a negative angle.
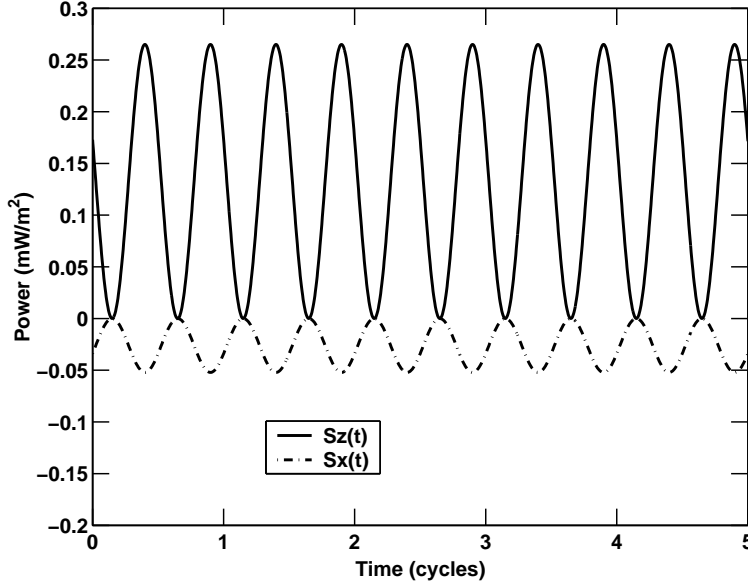
Figure 2-3: S_{1x} and S_{1z} at one typical spatial point in the LHM region as a function of time. Center frequency is $f_0 = 10.5$ GHz with $\delta f = 10$ Hz. Parameters used were those reported in [4], $f_{mp} = 10.95$ GHz, $f_{mo} = 10.05$ GHz, $f_{ep} = 12.8$ GHz, $f_{eo} = 10.3$ GHz, except $\gamma = 0$. Refraction angle is found to be $\theta_t \approx -11.12°$.

In addition to their group velocity argument, Valanju *et al* also claimed in [19] that negative refraction was not possible because it violated causality. However, their argument fails to consider two important points. First, at a RHM-RHM interface with the index of refraction great than one, points on a single phase front in the incident region can all be mapped to the same phase front in the transmitted region; however, this is not the case for a RHM-LHM interface. Instead, the points along the incident phase fronts are each mapped to different backward propagating phase fronts in the LHM. Second, in the case of a single frequency signal, for which constant phase front arguments apply, it is always possible to form new backward propagating phase fronts due to the negative phase property of LHM in conjunction with the fact that the wave exists for all time and space. Considering these two points, we see that waves can refract at negative angles while maintaining a finite velocity.

On the other hand, the interference fronts of a multi-frequency signal are indeed dis-

torted at an RHM-LHM interface since its different frequency components are refracted at different angles. In the case of two discrete frequencies, examples of two distorted interference patterns are shown in Fig. 2-2. Valanju *et al* argue that these distorted interference patterns move and carry power perpendicularly to the interference front, which happens to be at a positive angle in the case considered in Fig. 2-2(b). In actuality, each point on the interference front moves in the direction of power flow (downward and to the right in Fig. 2-2(b)). The apparent upward movement is due to the combined effects of semi-infinite extent, the periodicity of the interference pattern and its slanted angle. Indeed, a spatially finite extent signal such as a Gaussian beam, which can be represented by a collection of plane waves [35, 36], will also propagate downwards in this case since each plane wave component will refract negatively. The combined effects listed above along with the exact analytical calculation of the power flow presented in this section demonstrate that conclusions based solely on the apparent motion of the interference fronts are misguided.

In conclusion, we have calculated the power flow of a wave transmitted from a non-dispersive right-handed medium into two types of dispersive media, RHM and LHM. In particular, we have shown that negative refraction is possible for multi-frequency signals by explicit calculation of the Poynting vector in LHM. Using two discrete frequencies, we have shown that the direction of the time-averaged Poynting vector is in the average direction of the time-averaged Poynting vectors for each frequency treated separately, implying that negative refraction is possible. Using a Gaussian signal spectrum, we have confirmed this conclusion after also determining the power refraction angle to be negative, without violating causality. The angle of refraction was found to be in agreement with that predicted by Snell's law, with the LHM having a negative index of refraction.

2.3   Radiation of a source in the presence of an LH slab

Next, the effects of loss on the perfect lens, originally proposed by Pendry [25] will be ana-
lyzed. Although the Kramers-Kronig relations require a dispersive medium to be lossy [59],
it is beneficial to first consider the ideal lossless case as Pendry originally did when he an-
alyzed the transmission of a plane or evanescent wave through a LH slab with a relative
permittivity and permeability of $\epsilon_r = -1$ and $\mu_r = -1$ at a single frequency. Using an infi-
nite series solution, where each term represents an additional reflection or transmission at
one of the two boundaries, Pendry determined that propagating as well as evanescent waves
are perfectly reconstructed in terms of phase and amplitude in the transmitted region. In
particular, evanescent waves were found to grow exponentially inside the LH medium slab.
However, in Pendry's method, certain assumptions were made about the sign of the trans-
verse wave component inside the LH medium. To avoid the ambiguity in the choice of sign,
Zhang *et al* [60] and Kong [61] used a more general approach, which used the boundary
conditions to determine the amplitudes of the forward and backward propagating (or in the
case of evanescent decaying or growing) terms. As with Pendry's solution, their solution
also showed that evanescent modes grow inside the slab.

While individually growing evanescent modes do not pose any mathematical difficulties,
issues of convergence arise in the case of computing the image of an ideal source. To compute
the image of a current source, both Zhang *et al* [60] and Kong [61] use the Green's function
methodology where a separate spatial Fourier integral is used to express the fields in each
region due to the source. However, under the perfect lens condition when the source is
located from the slab at a distance less than half the slab thickness, the Fourier integrals
can become exponentially divergent rendering them unintegrable. Previous work avoided
this issue by restricting the choice of source position and slab thickness, but it is clearly an
issue of fundamental theoretical importance. As will be shown, it is possible to obtain a
closed form solution that satisfies the necessary boundary conditions by using the principle
of analytic continuation; however, due to the lossless nature of the LH medium, this solution

may not be unique. By introducing a small amount of loss into the LH medium, the integral expressions for the fields become well defined and convergent, and can be uniquely computed using numerical integration techniques. In this work, the amount of loss introduced into the slab will be varied in order to better understand the perfect lens effect. The limiting case of the lossless solution will be examined.

2.3.1 Theoretical Formulation

In this section, the radiation of a source located below a LH medium slab is examined. As discussed earlier, this work stems from the idea of using LH media to create a perfect lens first proposed by Pendry in [25], where he analyzed the case of individual plane wave or evanescent components propagating through a LH medium slab. In this work, however, the radiation of an ideal source in the presence of an LH slab will be considered. Because an ideal source can be decomposed into a set of plane waves and evanescent waves, some of Pendry's work will be repeated; however, the main difference will be the difficulties encountered when summing all the wave components.

Consider an infinite line source located at the position $z = 0$ in region 0 as shown in Fig. 2-4. The region above the source in medium 0 is denoted as 0+ while the region below the source in medium 0 is denoted as 0−. Similarly, as will become clear later, regions 1 and 2 are also divided into plus and minus regions which correspond to the regions above and below the images of the original source. In the following work, regions 0 and 2 will always be taken to be RH media whereas region 1 can be either right-handed or left-handed.

For an infinite electric line source polarized in the $\hat{x}$-direction, the electric and magnetic fields take the following general form,

$$E_{\ell x} = \int_{-\infty}^{\infty} dk_y \left[A_\ell e^{ik_{\ell z}z} + B_\ell e^{-ik_{\ell z}z} \right] e^{ik_y y}, \qquad (2.24a)$$

$$H_{\ell y} = \int_{-\infty}^{\infty} dk_y \frac{k_{\ell z}}{\omega \mu_\ell} \left[A_\ell e^{ik_{\ell z}z} - B_\ell e^{-ik_{\ell z}z} \right] e^{ik_y y}, \qquad (2.24b)$$

$$H_{\ell z} = \int_{-\infty}^{\infty} dk_y \frac{-k_y}{\omega \mu_\ell} \left[A_\ell e^{ik_{\ell z}z} + B_\ell e^{-ik_{\ell z}z} \right] e^{ik_y y}, \qquad (2.24c)$$
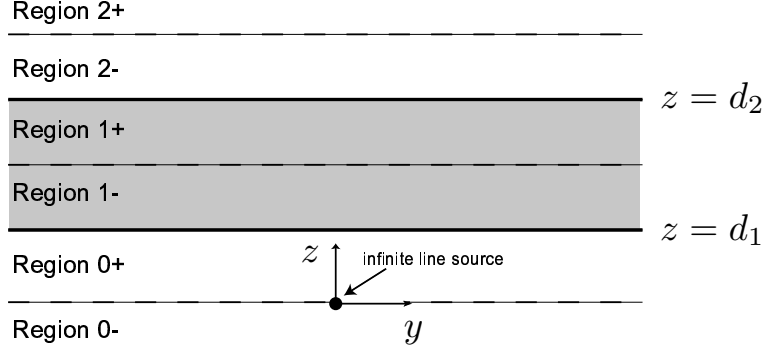
Figure 2-4: Geometry for studying radiation of an ideal source through a LH slab.

where $k_y^2 + k_{\ell z}^2 = k_\ell^2$. For RH media regions, the A_ℓ coefficients correspond to upward propagating wave components and the B_ℓ coefficients correspond to downward propagating wave components; however, for a LH medium region, the reverse is true since the power and phase are anti-parallel in isotropic LH media.

Because the source is located in region 0, the coefficients, $A_{0\pm}$ and $B_{0\pm}$ must take the following form,

$$A_{0-} = 0, \tag{2.25a}$$

$$B_{0-} = (1+R)E_{lin}, \tag{2.25b}$$

for $z \leq 0$ and

$$A_{0+} = E_{lin}, \tag{2.26a}$$

$$B_{0+} = RE_{lin}, \tag{2.26b}$$

for $z \geq 0$ with the source amplitude spectrum given by,

$$E_{lin} = -\frac{\omega\mu_0 I}{4\pi k_{0z}}. \tag{2.27}$$

Note that because region 0 is unbounded from below, only downward propagating scattered field components were included in the coefficients. Similarly, because region 2 is unbounded from above, only upward propagating field components will be included (*i.e.*, $A_2 = T$, $B_2 = 0$). In contrast, because region 1 is bounded from both above and below, both upward and downward propagating wave components are included.

In order to solve for the unknown coefficients, the boundary conditions for the E_x and H_y fields at $z = d_1$ and $z = d_2$ are used. Matching these fields across the boundaries yields the following system of equations,

$$A_{0+}e^{ik_{0z}d_1} + B_{0+}e^{-ik_{0z}d_1} \;=\; A_1 e^{ik_{1z}d_1} + B_1 e^{-ik_{1z}d_1} \tag{2.28}$$

$$A_{0+}e^{ik_{0z}d_1} - B_{0+}e^{-ik_{0z}d_1} \;=\; p_{01}^{TE}\left[A_1 e^{ik_1 z d_1} - B_1 e^{-ik_{1z}d_1} \right] \tag{2.29}$$

$$A_1 e^{ik_{1z}d_2} + B_1 e^{-ik_{1z}d_2} \;=\; T e^{ik_{2z}d_2} \tag{2.30}$$

$$A_1 e^{ik_{1z}d_2} - B_1 e^{-ik_{1z}d_2} \;=\; p_{12}^{TE} T e^{ik_{2z}d_2} \tag{2.31}$$

where

$$p_{01}^{TE} \;=\; \frac{\mu_0 k_{1z}}{\mu_1 k_{0z}} \tag{2.32}$$

$$p_{12}^{TE} \;=\; \frac{\mu_1 k_{2z}}{\mu_2 k_{1z}}. \tag{2.33}$$

The system can be rewritten as,

$$A_{0+}e^{ik_{0z}d_1} \;=\; \frac{1}{2}(1 + p_{01}^{TE})\left[A_1 e^{ik_{1z}d_1} + R_{01} B_1 e^{-ik_{1z}d_1} \right] \tag{2.34}$$

$$B_{0+}e^{-ik_{0z}d_1} \;=\; \frac{1}{2}(1 + p_{01}^{TE})\left[R_{01} A_1 e^{ik_{1z}d_1} + B_1 e^{-ik_{1z}d_1} \right] \tag{2.35}$$

$$A_1 e^{ik_{1z}d_2} \;=\; \frac{1}{2}(1 + p_{12}^{TE}) T e^{ik_{2z}d_2} \tag{2.36}$$

$$B_1 e^{-ik_{1z}d_2} \;=\; \frac{1}{2}(1 + p_{12}^{TE}) R_{12} T e^{ik_{2z}d_2} \tag{2.37}$$

where R_{01} and R_{12} are the TE Fresnel reflection coefficients given by,

$$R_{01} = \frac{1 - p_{01}^{TE}}{1 + p_{01}^{TE}} = \frac{\mu_1 k_{0z} - \mu_0 k_{1z}}{\mu_1 k_{0z} + \mu_0 k_{1z}} \tag{2.38}$$

$$R_{12} = \frac{1 - p_{12}^{TE}}{1 + p_{12}^{TE}} = \frac{\mu_2 k_{1z} - \mu_1 k_{2z}}{\mu_2 k_{1z} + \mu_1 k_{2z}} \tag{2.39}$$

Solving for the amplitudes of the field components in each region yields,

$$T = \frac{4 \, E_{lin} \, e^{ik_{0z}d_1} e^{ik_{1z}(d_2 - d_1)} e^{-ik_{2z}d_2}}{\left(1 + p_{01}^{TE}\right)\left(1 + p_{12}^{TE}\right)\left(1 + R_{01}R_{12}e^{i2k_{1z}(d_2 - d_1)}\right)}, \tag{2.40}$$

$$A_1 = \frac{2 \, E_{lin} \, e^{-i(k_{1z} - k_{0z})d_1}}{\left(1 + p_{01}^{TE}\right)\left(1 + R_{01}R_{12}e^{i2k_{1z}(d_2 - d_1)}\right)}, \tag{2.41}$$

$$B_1 = \frac{2 \, R_{12} \, E_{lin} \, e^{-i(k_{1z} - k_{0z})d_1} e^{i2k_{1z}d_2}}{\left(1 + p_{01}^{TE}\right)\left(1 + R_{01}R_{12}e^{i2k_{1z}(d_2 - d_1)}\right)}, \tag{2.42}$$

$$R = \frac{B_{0+}}{A_{0+}} = e^{i2k_{0z}d_1} \frac{R_{01} + R_{12}e^{i2k_{1z}(d_2 - d_1)}}{\left(1 + R_{01}R_{12}e^{i2k_{1z}(d_2 - d_1)}\right)}, \tag{2.43}$$

As discussed before, the difficulties involved in calculating the images of the source arises when performing the integration of all the evanescent wave components for the particular case when $\epsilon_0 = -\epsilon_1 = \epsilon_2$ and $\mu_0 = -\mu_1 = \mu_2$. For this case, it follows that $k_{0z} = -k_{1z} = k_{2z}$, where we define $k_{0z} = k_{0z}' + ik_{0z}''$, with $k_{0z}' > 0$ and $k_{0z}'' > 0$. Upon substitution of these values into (2.40)–(2.43) the coefficients become $R = 0$, $T = E_{lin}e^{-ik_{0z}[2(d_2 - d_1)]}$, $A_1 = E_{lin}e^{i2k_{0z}d_1}$, and $B_1 = 0$. It should also be noted that the formulation is independent of the choice of sign for k_{1z}. In other words, if one defines k_{1z} such that $k_{1z} = k_{0z}$, then the R and T coefficients remain the same; however, the values for the A_1 and B_1 coefficients are swapped, i.e., $A_1 = 0$, $B_1 = E_{lin}e^{i2k_{0z}d_1}$, but the resulting integral expressions for the electric field in each region remain unchanged and are given by,

$$E_{0-x} = \int_{-\infty}^{\infty} dk_y E_{lin} \left[e^{-ik_{0z}z} \right] e^{ik_y y}, \tag{2.44a}$$

$$E_{0+x} = \int_{-\infty}^{\infty} dk_y E_{lin} \left[e^{ik_{0z}z} \right] e^{ik_y y}, \tag{2.44b}$$

$$E_{1x} = \int_{-\infty}^{\infty} dk_y E_{lin} e^{-ik_{0z}(z-2d_1)} e^{ik_y y}, \tag{2.44c}$$

$$E_{2x} = \int_{-\infty}^{\infty} dk_y E_{lin} e^{-ik_{0z}(z-2(d_2-d_1))} e^{ik_y y}. \tag{2.44d}$$

Because $R = 0$, the field in region 0 is due entirely to the source and will radiate as a cylindrical wave. Because the integral expressions for regions 1+ and 2- have the same functional form as for region 0, the fields in regions 1+ and 2- will be perfect images of the source albeit centered at $z = 2d_1$ and $z = 2(d_2 - d_1)$. However, note that because $k''_{0z} > 0$, the integral in (2.44c) is divergent for $z > 2d_1$ (region 1+) and the integral in (2.44d) is divergent for $z < 2(d_2 - d_1)$ (region 2-) leaving the fields in these regions undefined. Yet if loss is added to the permittivity and/or permeability of the LH medium region, it can be shown that all of the integral expressions are convergent.

2.3.2 Source-sink-source solution

Despite the difficulties in evaluating the above integrals for the case when $\epsilon_0 = -\epsilon_1 = \epsilon_2$ and $\mu_0 = -\mu_1 = \mu_2$, it is possible to directly find a closed form solution to Maxwell's equations that satisfy the boundary and radiation conditions. This solution, termed the source-sink-source for reasons that will be explained shortly, takes the form,

$$E_{\ell x} = \frac{-\omega\mu_0 I}{4} H_0^{(1)}(k_0 \rho_\ell) \tag{2.45}$$

$$H_{\ell y} = -\frac{iIk\mu_0}{4\mu_\ell} \left(\frac{z - z_\ell}{\rho_\ell} \right) H_1^{(1)}(k_0 \rho_\ell) \tag{2.46}$$

$$H_{\ell z} = \frac{iIk\mu_0}{4\mu_\ell} \left(\frac{y}{\rho_\ell} \right) H_1^{(1)}(k_0 \rho_\ell) \tag{2.47}$$

where $\rho_\ell \hat{\rho}_\ell = \hat{z}(z - z_\ell) + \hat{y}y$ and $H_m^{(1)}$ is the Hankel function of the first kind of the mth order. The image points are located at $y = 0$, $z_\ell = \{0, 2d_1, 2(d_2 - d_1)\}$. By direct evaluation, it can be noted that this solution satisfies Maxwell's equations, all boundary conditions, and radiation conditions. For this solution the time-averaged Poynting vectors follows as,

$$< \overline{S}_\ell > \quad = \quad \hat{\rho}_\ell \frac{\omega \mu_0^2 |I|^2}{16\pi \mu_\ell \rho_\ell}. \tag{2.48}$$

This solution is shown in Fig. 2-5 where the magnitude and direction of the time averaged Poynting vector is plotted. As can be seen, on average power flows away from the original source and its image in region 2, whereas the average power flows toward the image point that is in region 1. As unusual as this solutions seems, it is mathematically correct albeit possibly non-unique; however, because this is a steady state solution, it may not be possible to observe it in either a physical experiment or a numerical time-domain simulation due to the long time it may take to reach steady state. Recently, there have been a number of efforts to more precisely understand this phenomena using time-domain simulations [24, 27, 28]. In these simulations the material properties of the slab are accounted for by using the Drude and/or Lorentz model to include the effects of dispersion. For example, in [24], the authors report that the dispersion of the media introduces a setup time before which the wave transmitted through the slab is inhomogeneous instead of negatively refracted. This setup time is of course due to the fact that at early times, the bandwidth of the signal is much larger than the bandwidth over which the material is left-handed. This fact has also been studied in detail by using spectrogram analysis techniques [62], where the authors show that the higher frequency components, which give rise to the inhomogeneity of the transmitted wave, indeed are the first to arrive. Only after these components have dissipated are the negative index effects apparent.

Compounded on this time-domain aspect are two further complications that prohibit observation of the source-sink-source solution. First, the slab considered above is assumed to be infinitely long along the tangential direction, which is of course an impossibility to

realize either in practice or a numerical simulation. Secondly, the calculation relied on the assumption of a perfectly homogeneous material, which is not experimentally realizable.

2.3.3 Numerical Study

The above source-sink-source result is only obtainable for the perfectly lossless case at a single frequency; however, in order to understand the more practical cases the effects of mismatch and loss will be studied. To consider more physical values of ϵ and μ that can approximately form a perfect lens, it is necessary to numerically evaluate the integrals presented above. One of the difficulties in evaluating these integrals is that the coefficients tend to grow in magnitude and oscillate rapidly up to a critical k_y at which point they begin to decrease so that the integrand converges. The rapid oscillations and large magnitudes in combinations with finite precision computing making it difficult to accurately compute the integrals. For the following examples, the integrals were evaluated using an adaptive Simpson's method. The maximum level of refinement, (*i.e.*, the smallest separation in k_y between two function evaluations) was chosen as 10^{-10}. Finer refinements were also tried, but led to numerical instabilities, due to finite computer precision. Thus, unfortunately, with a finite level of refinement, it is not possible to evaluate the integrals for slab whose material parameters are arbitrarily close to the perfect lens solution.

In the first set of examples, rather than introducing loss, the imperfection is due to slight deviations from the perfect lens condition of impedance matching along with $n = -1$. Fig. 2-6 shows the distribution of the electric field at the focal plane $z = 2(d_2 - d_1)$ in region 2. Compared to an ideal image, which has an infinitesimal resolution, the three cases shown have a relatively wide spatial extent. As can be seen, there is slight improvement as the index of refraction moves closer to the ideal solution of $n = -1$; however, the convergence is slow. For the case when $n = -1.0001$, the distribution of the Poynting vector in the area near the source is plotted in Fig. 2-7. In comparison to the perfect image solution, note the presence of strong surfaces waves. Also, from the vectors, it can be seen that the power from the source is essentially channeled along a straight line from the source. Finally, according

to the plot, it seems that the power vector creates swirl-type pattern in the slab region; however, one must be careful not to draw any conclusions based on this region where the magnitude of the power is relatively small. In these regions, even a small inaccuracy in the computation of the spatial Fourier integrals can lead to erroneous results.

In the next example, a small amount of loss will be introduced into a slab which would otherwise satisfy the perfect lens requirement. Fig. 2-8 shows the resulting electric field distribution at the focal plane. As expected, as the amount of loss is reduced the resolution at the image point becomes better, although as in the previous example, convergence toward the ideal solution is extremely slow. In addition, for the smallest amount of loss for which the Fourier integrals were able to numerically converge, the Poynting vector and magnitude distribution are shown in Fig. 2-9. As in the previous example, the imperfection introduces a collimation effect in which the power in channeled along a straight line from the source. However, note in this case that the amplitude of the surface waves has lessened, due in part to the absorption inside the slab.
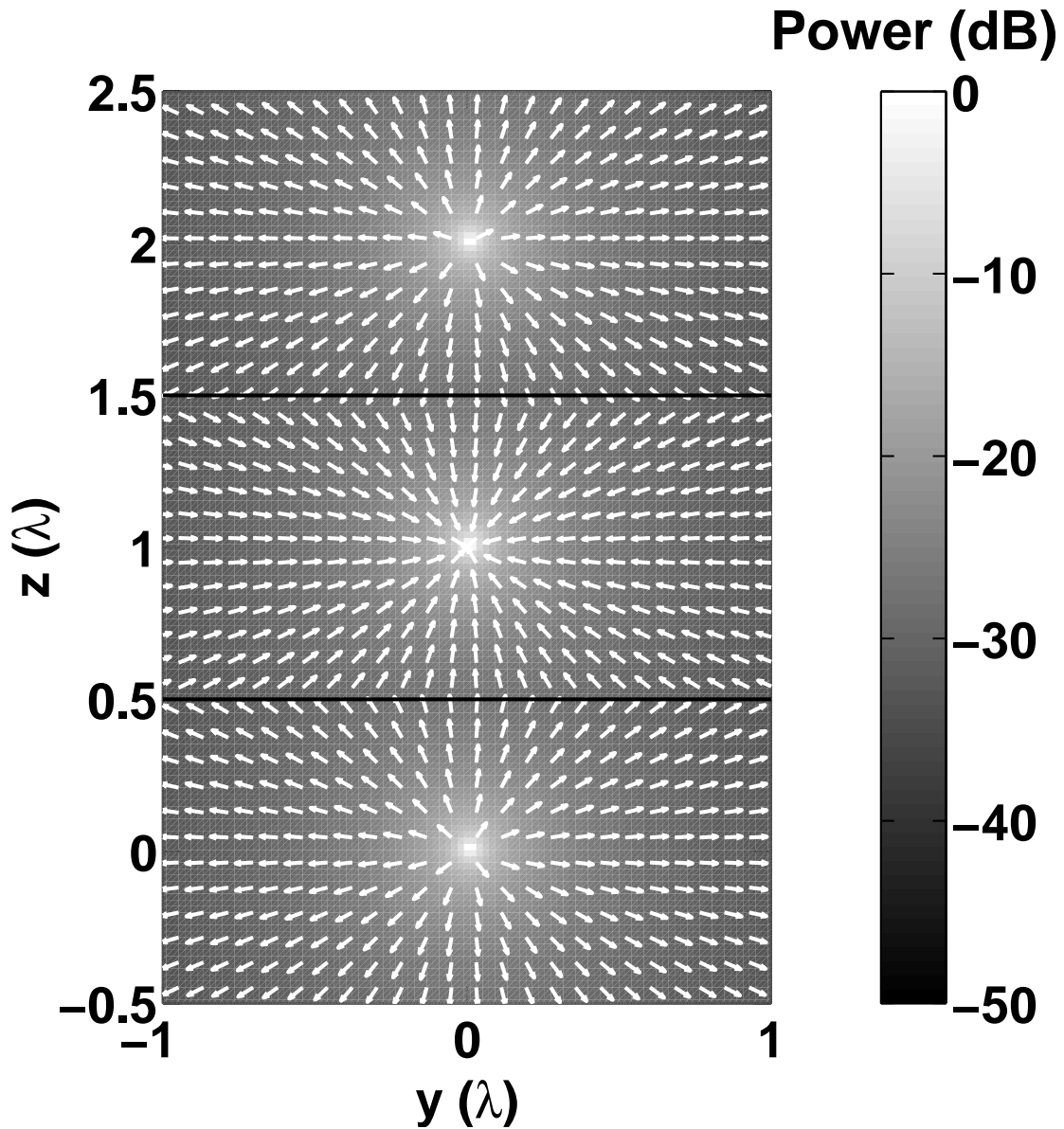
Figure 2-5: Time averaged Poynting vector magnitude and direction for the source-sink-source solution for a slab with an index of refraction of $n = -1$. Slab dimensions are $d_1 = 0.5\lambda$, and $d_2 = 1.5\lambda$.
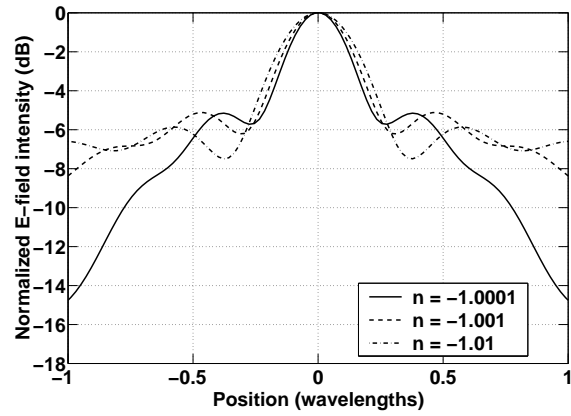
(a) Regular view
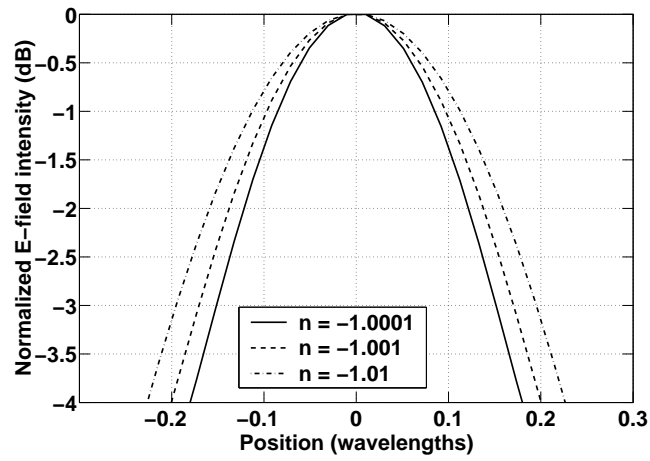
(b) Zoomed view

Figure 2-6: Plot of electric field intensity at the focal plane $z = 2(d_2 - d_1)$ for three lossless but slightly mismatched slabs. Slab dimensions are, $d_1 = 0.5\lambda$, and $d_2 = 1.5\lambda$.
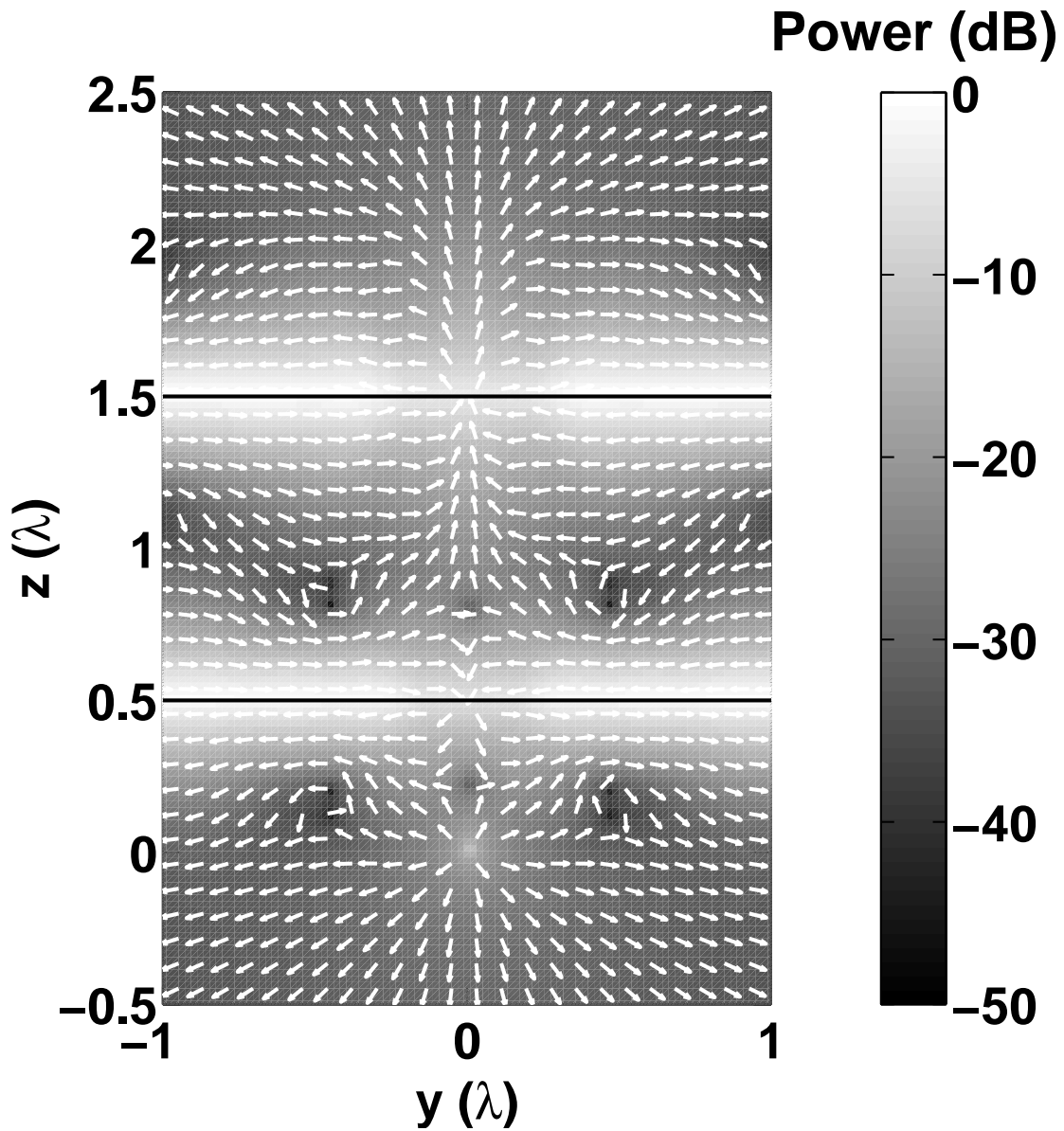
Figure 2-7: Time averaged Poynting vector magnitude and direction for slab with an index of refraction $n = -1.0001$. Slab dimensions are $d_1 = 0.5\lambda$, and $d_2 = 1.5\lambda$.
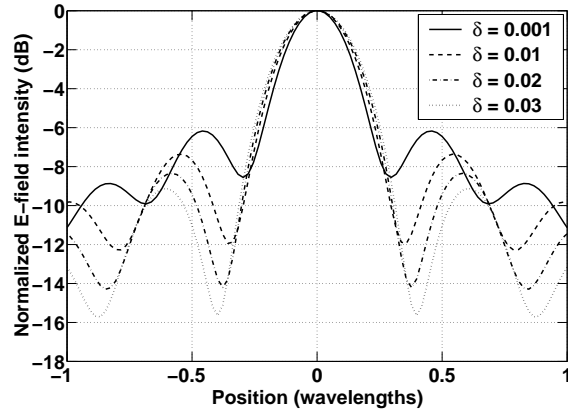
(a) Regular view
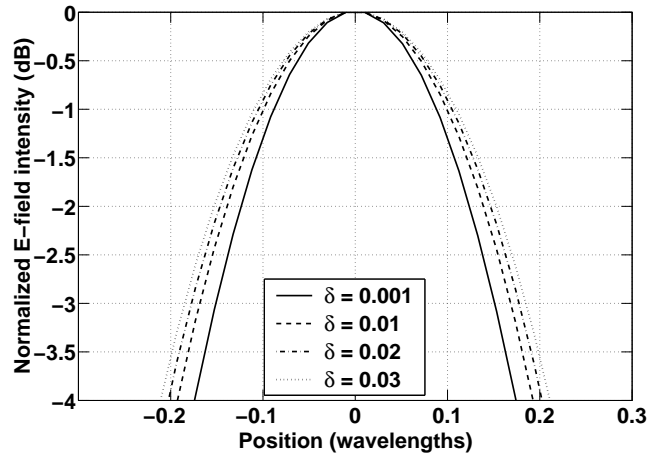
(b) Zoomed view

Figure 2-8: Plot of electric field intensity at the focal plane $z = 2(d_2 - d_1)$ for different levels of loss. The relative permittivities and permeabilities used were $\epsilon_r = -1 + i\delta = -1 + i\delta$. For these cases, $d_1 = 0.5\lambda$, and $d_2 = 1.5\lambda$.
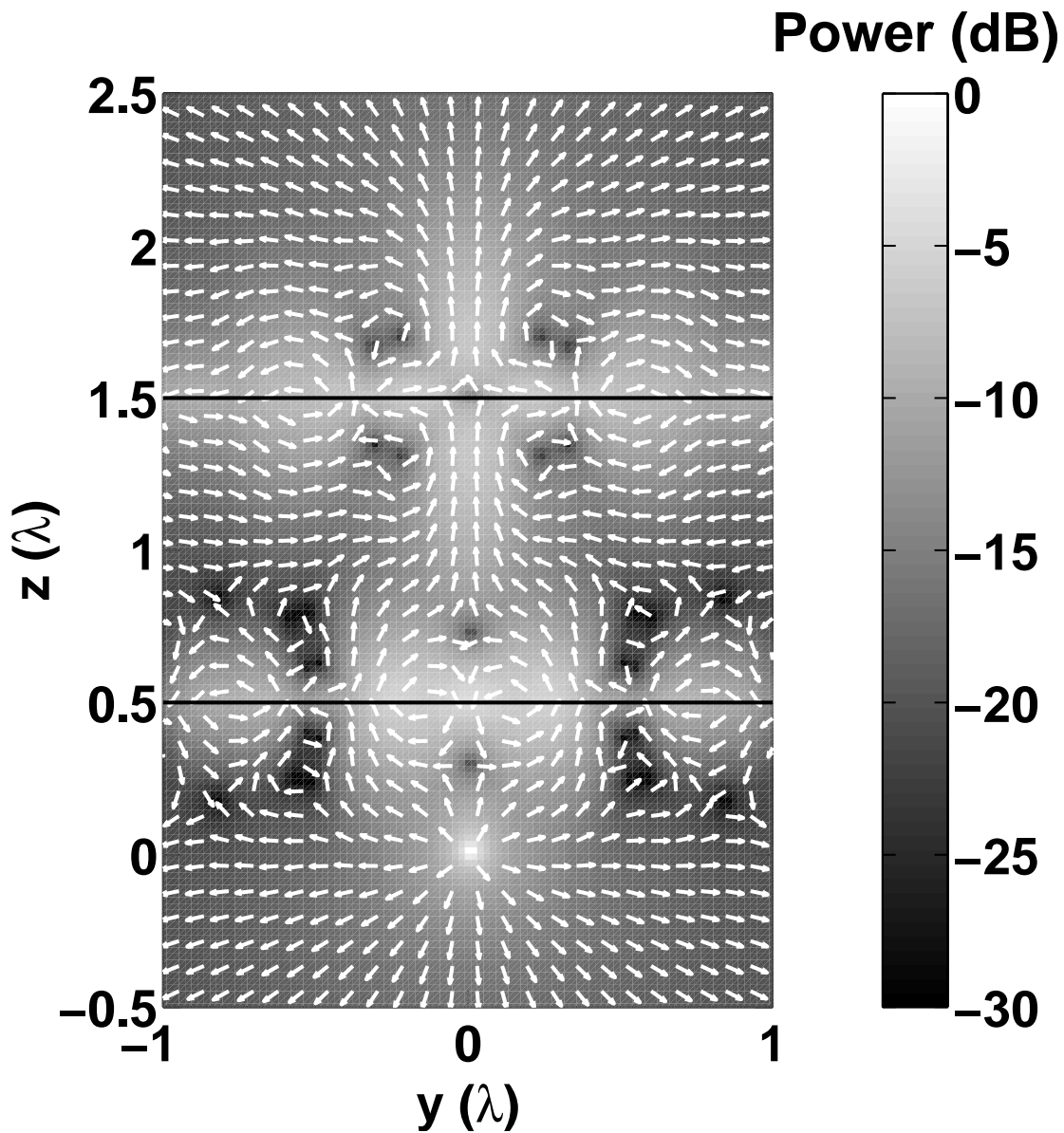
Figure 2-9: Time averaged Poynting vector magnitude and direction for slab with a relative permittivity of $\epsilon_r = -1 + i0.001$ and a relative permeability of $\mu_r = -1 + i0.001$. Slab dimensions are $d_1 = 0.5\lambda$, and $d_2 = 1.5\lambda$.

2.4 Scattering from isotropic LH media spheres

Next, in order to better understand the properties and potential applications of left-handed materials, the scattering of electromagnetics waves in the presence of LH media will be studied. Recently, some preliminary work by the author as well as other researchers has been on the scattering from spheres and infinite cylinders composed of LH media [63–67]. While these problems have already been solved and analyzed for the case of RH media, it is necessary to repeat the derivations for LH media, in order to understand the subtleties that arise, such as the ambiguity of wavenumber. For example, in the case of scattering from spheres, it has been found that the Mie scattering coefficients presented in many textbooks can only be used with one choice of the sign of the wavenumber. A more general formulation independent of the sign choice will be presented in this section. Using these re-derived scattering coefficients, the field distribution within a LHM sphere will be examined.

Consider a sphere of radius a located at the origin of the coordinate system, composed of a medium with permittivity ϵ_s and permeability μ_s. Let the incident wave be of the form,

$$\overline{E} = \hat{x}E_0 e^{\mathrm{i}kz} = \hat{x}E_0 e^{\mathrm{i}kr\cos\theta} \tag{2.49}$$

which can be expressed via the wave transform in terms of a collection of spherical waves as,

$$e^{\mathrm{i}kr\cos\theta} = \sum_{n=0}^{\infty} (-\mathrm{i})^{-n}(2n+1)j_n(kr)P_n(\cos\theta) \tag{2.50}$$

where j_n is the spherical Bessel function and P_n is the Legendre function. For example, the E_r component of the incident field can be represented as,

$$
\begin{aligned}
E_r &= E_0 \sin\theta\cos\phi\, e^{\mathrm{i}kr\cos\theta} \\
&= \frac{\mathrm{i}E_0\cos\phi}{(kr)^2} \sum_{n=1}^{\infty} (-\mathrm{i})^{-n}(2n+1)\hat{J}_n(kr)P_n^1(\cos\theta)
\end{aligned}
\tag{2.51}
$$

where $\hat{C}_n$ is the Ricatti-Bessel function, which is defined as,

$$\hat{C}_n(kr) \equiv kr c_n(kr) \tag{2.52}$$

where $c_n(kr)$ is the spherical Bessel $(c = j)$ or Hankel $(c = h)$ function of order n. To proceed, the incident wave is further decomposed using Debeye potentials into its spherical TM and TE components as follows,

$$\pi_e = \frac{E_0 \cos \phi}{\omega \mu r} \sum_{n=1}^{\infty} \frac{(-\mathrm{i})^{-n}(2n+1)}{n(n+1)} \hat{J}_n(kr) P_n^1(\cos \theta), \tag{2.53a}$$

$$\pi_m = -\frac{E_0 \sin \phi}{kr} \sum_{n=1}^{\infty} \frac{(-\mathrm{i})^{-n}(2n+1)}{n(n+1)} \hat{J}_n(kr) P_n^1(\cos \theta), \tag{2.53b}$$

where the fields are given in terms of the potentials as,

$$\overline{A} = \overline{r} \pi_e \tag{2.54}$$

$$\overline{H} = \nabla \times \overline{A} = \hat{\theta} \frac{1}{\sin \theta} \frac{\partial}{\partial \phi} \pi_e - \hat{\phi} \frac{\partial}{\partial \theta} \pi_e, \tag{2.55}$$

for the TM component, and

$$\overline{Z} = \overline{r} \pi_m \tag{2.56}$$

$$\overline{E} = \nabla \times \overline{Z} = \hat{\theta} \frac{1}{\sin \theta} \frac{\partial}{\partial \phi} \pi_m - \hat{\phi} \frac{\partial}{\partial \theta} \pi_m, \tag{2.57}$$

for the TE component. Using this general approach, the scattered fields in terms of the potentials are given by,

$$\pi_e^s = \frac{E_0 \cos \phi}{\omega \mu r} \sum_{n=1}^{\infty} a_n \hat{H}_n^{(1)}(kr) P_n^1(\cos \theta) \tag{2.58a}$$

$$\pi_m^s = -\frac{E_0 \sin \phi}{kr} \sum_{n=1}^{\infty} b_n \hat{H}_n^{(1)}(kr) P_n^1(\cos \theta). \tag{2.58b}$$

Similarly, the internal fields in terms of the potentials are given by

$$\pi_e^i = \frac{E_0 \cos\phi}{\omega\mu_s r} \sum_{n=1}^{\infty} c_n \hat{J}_n(k_s r) P_n^1(\cos\theta) \tag{2.59a}$$

$$\pi_m^i = \frac{-E_0 \sin\phi}{k_s r} \sum_{n=1}^{\infty} d_n \hat{J}_n(k_s r) P_n^1(\cos\theta). \tag{2.59b}$$

Using the above and enforcing continuity of the E_θ fields at $r = a$, yields the following two equations,

$$\frac{k}{\mu\epsilon}\left[g_n \hat{J}_n'(ka) + a_n \hat{H}_n^{(1)\prime}(ka)\right] = \frac{k_s}{\mu_s \epsilon_s} c_n \hat{J}_n'(k_s a), \tag{2.60}$$

$$\frac{1}{k}\left[g_n \hat{J}_n(ka) + b_n \hat{H}_n^{(1)}(ka)\right] = \frac{1}{k_s} d_n \hat{J}_n(k_s a). \tag{2.61}$$

Similarly, enforcement of the H_θ boundary condition leads to an additional set of independent equations,

$$\frac{1}{\mu}\left[g_n \hat{J}_n(ka) + a_n \hat{H}_n^{(1)}(ka)\right] = \frac{1}{\mu_s} c_n \hat{J}_n(k_s a), \tag{2.62}$$

$$\frac{1}{\mu}\left[g_n \hat{J}_n'(ka) + b_n \hat{H}_n^{(1)\prime}(ka)\right] = \frac{1}{\mu_s} d_n \hat{J}_n'(k_s a). \tag{2.63}$$

Solving (2.60) and (2.62) for a_n and c_n, which are the coefficients for the TM part of the wave, yields,

$$a_n = \frac{(-\mathrm{i})^{-n}(2n+1)}{n(n+1)} \cdot \frac{k\epsilon_s \hat{J}_n(k_s a)\hat{J}_n'(ka) - k_s \epsilon \hat{J}_n(ka)\hat{J}_n'(k_s a)}{k_s \epsilon \hat{H}_n^{(1)}(ka)\hat{J}_n'(k_s a) - k\epsilon_s \hat{J}_n(k_s a)\hat{H}_n^{(1)\prime}(ka)}, \tag{2.64}$$

$$c_n = \frac{(-\mathrm{i})^{-n}(2n+1)}{n(n+1)} \cdot \frac{k\epsilon_s \mu_s \left(\hat{J}_n(ka)\hat{H}_n^{(1)\prime}(ka) - \hat{J}_n'(ka)\hat{H}_n^{(1)}(ka)\right)}{k\epsilon_s \mu \hat{J}_n(k_s a)\hat{H}_n^{(1)\prime}(ka) - k_s \epsilon\mu \hat{H}_n^{(1)}(ka)\hat{J}_n'(k_s a)}$$

$$= \frac{(-\mathrm{i})^{-n}(2n+1)}{n(n+1)} \cdot \frac{\mathrm{i}k\epsilon_s \mu_s}{k\epsilon_s \mu \hat{J}_n(k_s a)\hat{H}_n^{(1)\prime}(ka) - k_s \epsilon\mu \hat{H}_n^{(1)}(ka)\hat{J}_n'(k_s a)}. \tag{2.65}$$

where the Wronskian relation for spherical Bessel functions were used. Similarly, solving

(2.61) and (2.63) for b_n and d_n, which are the coefficients for the TE part of the wave, yields,

$$b_n = \frac{(-i)^{-n}(2n+1)}{n(n+1)} \cdot \frac{k\mu_s\hat{J}_n(k_sa)\hat{J}'_n(ka) - k_s\mu\hat{J}_n(ka)\hat{J}'_n(k_sa)}{k_s\mu\hat{H}_n^{(1)}(ka)\hat{J}'_n(k_sa) - k\mu_s\hat{J}_n(k_sa)\hat{H}_n^{(1)'}(ka)}, \qquad (2.66)$$

$$d_n = \frac{(-i)^{-n}(2n+1)}{n(n+1)} \cdot \frac{k_s\mu_s\left(\hat{J}_n(ka)\hat{H}_n^{(1)'}(ka) - \hat{J}'_n(ka)\hat{H}_n^{(1)}(ka)\right)}{k\mu_s\hat{J}_n(k_sa)\hat{H}_n^{(1)'}(ka) - k_s\mu\hat{H}_n^{(1)}(a)\hat{J}'_n(k_sa)}$$

$$= \frac{(-i)^{-n}(2n+1)}{n(n+1)} \cdot \frac{ik_s\mu_s}{k\mu_s\hat{J}_n(k_sa)\hat{H}_n^{(1)'}(ka) - k_s\mu\hat{H}_n^{(1)}(ka)\hat{J}'_n(k_sa)}. \qquad (2.67)$$

Making use of the analytic properties of the Ricatti-Bessel functions, it can be shown that the following symmetries hold,

$$a_n(-k_s) = a_n(k_s) \qquad (2.68a)$$

$$b_n(-k_s) = b_n(k_s) \qquad (2.68b)$$

$$c_n(-k_s) = (-1)^{n+1}c_n(k_s) \qquad (2.68c)$$

$$d_n(-k_s) = (-1)^{n}d_n(k_s) \qquad (2.68d)$$

so that the potentials in (2.59a) and (2.59b) are independent of the choice for the sign of k_s. Thus, the formulation presented here is independent of the sign choice of k_s and avoids the ambiguity in other formulations (*e.g.*, eqn. 6.1.21 in [59]) that require an explicit choice of sign depending on whether the medium is left-handed or right-handed.

To illustrate the unique effects of a sphere composed of a left-handed medium, the electric field distribution inside the sphere as well as in the surrounding region is computed. The first example is the scattering due to a plane wave impinging upon a sphere composed of a $n = -1$ medium with a radius of $a = 2\lambda_0$. The resulting pattern, shown in Fig. 2-10, is that the fields create a focal point inside the sphere on the side of the sphere nearest to the incident wave direction. This is due to the fact that the plane waves are negatively
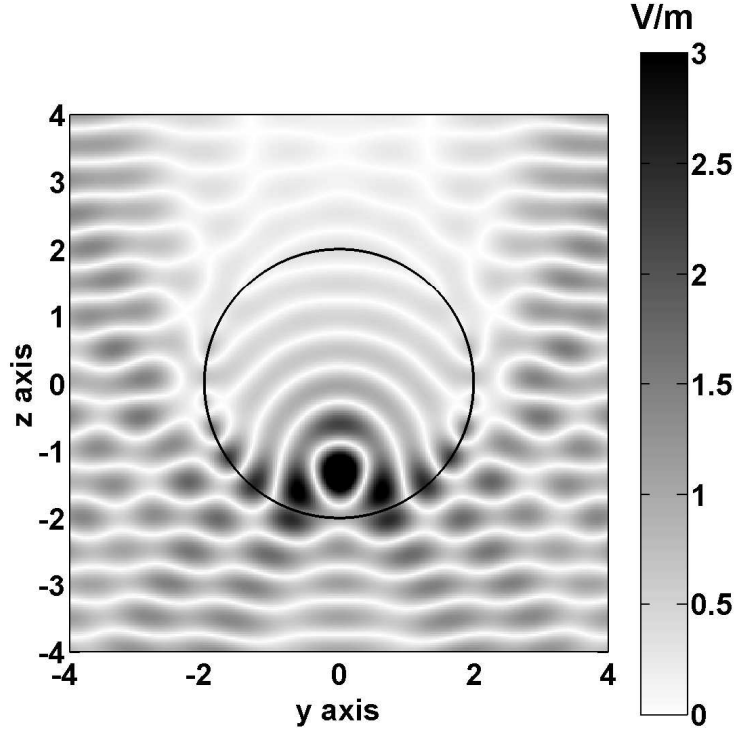
Figure 2-10: Magnitude of E_x total field (scattered + incident) of the incident plane wave $\overline{E} = \hat{x}e^{ikz}$ impinging upon a sphere of $n = -1$ with a radius of $a = 2\lambda_0$

refracted at each of the tangent planes of the sphere. To illustrate this point further, the scattering from a right-handed medium sphere and a left-handed medium sphere, whose indices of refraction are the same in magnitude, is compared. As can be seen in Fig. 2-11, the right-handed sphere produces a focal point in the forward scattering direction, while the left-handed sphere produces a focal inside the sphere.

While these results are interesting, their usefulness remains to be seen especially since, although not presented here, the far-field radiation patterns of a RH versus LH sphere are very similar.
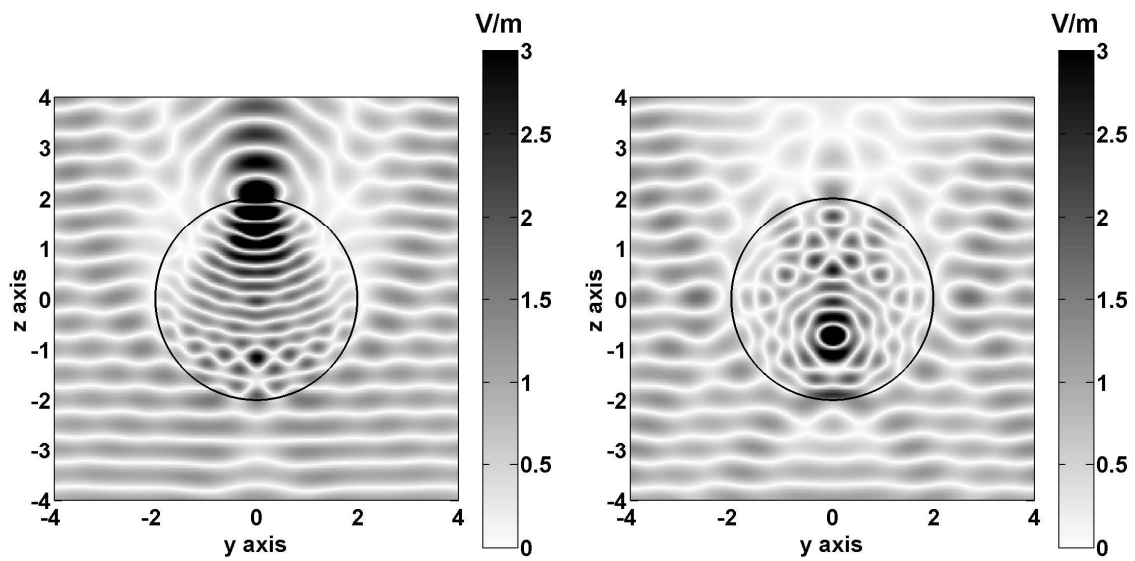
(a) RHM sphere: $n = 3.2$ (b) LHM sphere: $n = -3.2$

Figure 2-11: Comparison of the magnitudes of E_x total field (scattered + incident) of the incident plane wave $\overline{E} = \hat{x}e^{ikz}$ impinging upon a RHM and LHM sphere both with $|n| = \sqrt{3.2}$ with a radius of $a = 2\lambda$

2.5   Anisotropic indefinite media

Up to this point, all the left-handed media in this thesis were isotropic; however, as will become clearer in the next chapter, left-handed metamaterials are in general anisotropic. For examples, the rods respond to an electric field that is polarized along their lengthwise direction whereas the rings respond to a magnetic field that is polarized parallel to their axis. Because of the importance of this effect, there has already been much work published in the literature. For example, in [52], the guidance conditions for a dielectric waveguide composed of a uniaxial medium which has some of the components being negative are presented. For a similar type of medium [68] studies the effect on the half-space reflection and transmission coefficients of material components. In [69], each of the possible combinations of a permittivity and permeability tensors with positive and negative components are classified according to the type of propagation that they support [69]. In that work, the author terms such media as "indefinite" due to the fact that the material tensors are neither positive definite or negative definite. Expanding upon this work, it is shown in [70] that a bilayer of indefinite media can be used to construct low-, high-, and bandpass spatial filters, which possess the ability to select specific spatial components from a source. Finally, in [71], the effect of anisotropy on the perfect lens is studied using the finite difference time domain method. It is shown that the perfect lens requires an isotropic left-handed medium.

In this section, the basic properties of anisotropic indefinite media are discussed. In particular, one of the goals of the chapter is to provide an understanding how negative refraction may occur at the interface of an indefinite medium and a right-handed medium. Such phenomena have been numerically and experimentally observed by studying the refraction of a beam through a prism shaped anisotropic metamaterial [72]. At first, such a conclusion may seem unusual, but as will be shown, through the use of Gaussian beam propagation results, such phenomena is possible.

2.5.1 Dispersion relations for anisotropic LH media

The dispersion relation of a medium with arbitrary permittivity and permeability tensors can be represented by [59],

$$\det\left[\overline{k}\times\overline{\overline{I}}\cdot\overline{\overline{\mu}}^{-1}\cdot\overline{k}\times\overline{\overline{I}}+\omega^2\overline{\overline{\epsilon}}\right]=0 \qquad (2.69)$$

where $\overline{k}$, $\overline{\overline{I}}$, $\overline{\overline{\mu}}$, and $\overline{\overline{\epsilon}}$ are the wave propagation vector, unit tensor, permeability tensor, and permittivity tensor, respectively. In order to study a few special cases, the material tensors will be assumed diagonal, that is they will take the form,

$$\overline{\overline{\epsilon}}=\begin{pmatrix} \epsilon_x & 0 & 0 \\ 0 & \epsilon_y & 0 \\ 0 & 0 & \epsilon_z \end{pmatrix}, \qquad (2.70)$$

and

$$\overline{\overline{\mu}}=\begin{pmatrix} \mu_x & 0 & 0 \\ 0 & \mu_y & 0 \\ 0 & 0 & \mu_z \end{pmatrix}. \qquad (2.71)$$

Using these tensors and assuming that the electric field has only one component along the y direction, the dispersion relation given in (2.69) can be simplified as,

$$k_z^2=\epsilon_y\mu_x\omega^2-\frac{\mu_x}{\mu_z}k_x^2 \qquad (2.72)$$

where k_x and k_z are the two non-zero $\overline{k}$ components of a wave polarized along the y direction. From (2.72), the cutoff frequency, $k_x=k_c$ for which k_z becomes exactly zero is can be determined as,

$$k_c=\omega\sqrt{\epsilon_y\mu_z} \qquad (2.73)$$

	Media conditions		Propagation
Cutoff	$\epsilon_y \mu_x > 0$	$\mu_x/\mu_z > 0$	$k_x < k_c$
Anti-cutoff	$\epsilon_y \mu_x < 0$	$\mu_x/\mu_z < 0$	$k_x > k_c$
Never cutoff	$\epsilon_y \mu_x > 0$	$\mu_x/\mu_z < 0$	All real k_x
Always cutoff	$\epsilon_y \mu_x < 0$	$\mu_x/\mu_z > 0$	No real k_x

Table 2.1: Conditions on components of the permittivity and permeability tensor components for propagation of a TE polarized electromagnetic wave [69].

The conditions for the various types of cutoff, as originally published in [69], are given in Table 2.1. Fig. 2-12 illustrates one example of each of these types of dispersions. For example, in Fig. 2-12(d), the y component of the permittivity and the x of the permeability are negative yielding a medium with no spatial cutoff.

2.5.2 Transmission and reflection from planar layered indefinite media

So far in this thesis, the formulations presented have been for only isotropic layered media; however, as seen discussed above metamaterials are anisotropic. Because one of the goals of this thesis is to use LH metamaterials in microwave engineering applications, it is of interest to have a general formulation for left-handed anisotropic layered media. For this purpose, in this section, the formulation for determining the field distribution within an arbitrary layered planar media will be addressed using the formulation given by Chew in [73]. In Chew's formulation, a matrix equation is derived for the tangential field components, which is converted to an eigenvalue problem upon substitution of general plane wave solutions.

(a) Cutoff

(b) Anti-Cutoff

(c) Always Cutoff

(d) Never Cutoff
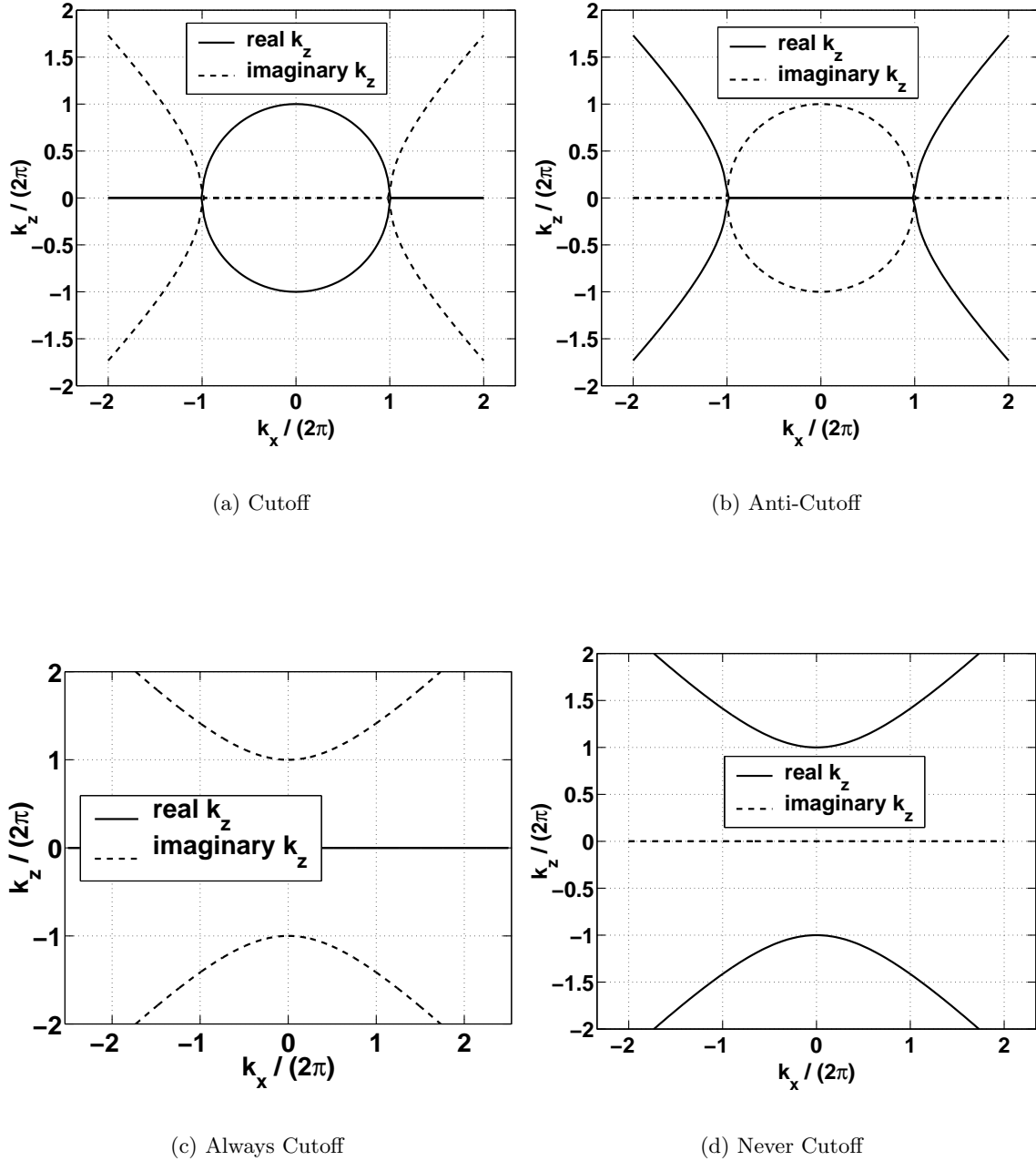
Figure 2-12: Typical example of the k-surface from each of the four classes of indefinite media.

Formulation

The formulation begins by writing Maxwell's equations in the following matrix form,

$$\nabla \times \begin{pmatrix} \overline{E}_s \\ \overline{E}_z \end{pmatrix} = \mathrm{i}\omega \begin{pmatrix} \overline{\overline{\mu}}_{ss} & \overline{\overline{\mu}}_{sz} \\ \overline{\overline{\mu}}_{zs} & \overline{\overline{\mu}}_{zz} \end{pmatrix} \begin{pmatrix} \overline{H}_s \\ \overline{H}_z \end{pmatrix} \tag{2.74}$$

$$\nabla \times \begin{pmatrix} \overline{H}_s \\ \overline{H}_z \end{pmatrix} = -\mathrm{i}\omega \begin{pmatrix} \overline{\overline{\epsilon}}_{ss} & \overline{\overline{\epsilon}}_{sz} \\ \overline{\overline{\epsilon}}_{zs} & \overline{\overline{\epsilon}}_{zz} \end{pmatrix} \begin{pmatrix} \overline{E}_s \\ \overline{E}_z \end{pmatrix} \tag{2.75}$$

where we let

$$\nabla = \nabla_s + \hat{z}\frac{\partial}{\partial z} \tag{2.76}$$

Expanding out the matrix equation and separating by components yields,

$$\frac{\partial}{\partial z}\hat{z} \times \overline{E}_s = \mathrm{i}\omega\overline{\overline{\mu}}_{ss} \cdot \overline{H}_s + \mathrm{i}\omega\overline{\overline{\mu}}_{sz} \cdot \overline{H}_z - \nabla_s \times \overline{E}_z \tag{2.77}$$

$$\nabla_s \times \overline{E}_s = \mathrm{i}\omega\overline{\overline{\mu}}_{zs} \cdot \overline{H}_s + \mathrm{i}\omega\overline{\overline{\mu}}_{zz} \cdot \overline{H}_z \tag{2.78}$$

and by duality we can find,

$$\frac{\partial}{\partial z}\hat{z} \times \overline{H}_s = -\mathrm{i}\omega\overline{\overline{\epsilon}}_{ss} \cdot \overline{E}_s - \mathrm{i}\omega\overline{\overline{\epsilon}}_{sz} \cdot \overline{E}_z - \nabla_s \times \overline{H}_z \tag{2.79}$$

$$\nabla_s \times \overline{H}_s = -\mathrm{i}\omega\overline{\overline{\epsilon}}_{zs} \cdot \overline{E}_s - \mathrm{i}\omega\overline{\overline{\epsilon}}_{zz} \cdot \overline{E}_z. \tag{2.80}$$

From here we can use (2.77) and (2.79) to eliminate $\overline{E}_z$ and $\overline{H}_z$ from (2.78) and (2.80) by writing them in terms of $\overline{E}_s$ and $\overline{H}_s$ as follows:

$$\overline{E}_z = -\frac{1}{\mathrm{i}\omega}\kappa_{zz}\nabla \times \overline{H}_s - \kappa_{zz}\overline{\overline{\epsilon}}_{zs} \cdot \overline{E}_s \tag{2.81}$$

$$\overline{H}_z = \frac{1}{\mathrm{i}\omega}\nu_{zz}\nabla \times \overline{E}_s - \nu_{zz}\overline{\overline{\mu}}_{zs} \cdot \overline{H}_s. \tag{2.82}$$

In order to apply this method to a multi-layered geometry, it is convenient to take

advantage of the phase-matching principle and express each field component in the form,

$$f(\overline{r}) = f(z) \ e^{\mathrm{i}\overline{k}_s \cdot \overline{r}_s} \tag{2.83}$$

where $\overline{k}_s$ is the tangential wave propagation vector. Next, by making use of (2.83), elimi-
nating $\overline{E}_z$ and $\overline{H}_z$ from (2.78) and (2.80), and cross multiplying by $-\hat{z}$, we obtain:

$$
\begin{aligned}
\frac{d}{dz}\overline{E}_s &= \left[\left(-\mathrm{i}\omega\hat{z} \times \overline{\overline{\mu}}_{ss}\cdot\right) + \left(\mathrm{i}\omega\hat{z} \times \overline{\overline{\mu}}_{sz} \cdot \overline{\overline{\mu}}_{zs} \cdot \nu_{zz}\cdot\right) - \left(\frac{\mathrm{i}\hat{z}}{\omega} \times \overline{k}_s \times \kappa_{zz}\overline{k}_s\times\right) \right] \overline{H}_s \\
&\quad + \left[\left(-\mathrm{i}\hat{z} \times \overline{\overline{\mu}}_{sz} \cdot \nu_{zz}\overline{k}_s\times\right) - \mathrm{i}\hat{z} \times \overline{k}_s \times \kappa_{zz} \cdot \overline{\overline{\epsilon}}_{zs}\cdot \right] \overline{E}_s \tag{2.84} \\
\frac{d}{dz}\overline{H}_s &= \left[\left(\mathrm{i}\omega\hat{z} \times \overline{\overline{\epsilon}}_{ss}\cdot\right) - \left(\mathrm{i}\omega\hat{z} \times \overline{\overline{\epsilon}}_{sz} \cdot \overline{\overline{\epsilon}}_{zs} \cdot \kappa_{zz}\cdot\right) + \left(\frac{\mathrm{i}\hat{z}}{\omega} \times \overline{k}_s \times \nu_{zz}\overline{k}_s\times\right) \right] \overline{E}_s \\
&\quad + \left[\left(-\mathrm{i}\hat{z} \times \overline{\overline{\epsilon}}_{sz} \cdot \kappa_{zz}\overline{k}_s\times\right) - \mathrm{i}\hat{z} \times \overline{k}_s \times \nu_{zz} \cdot \overline{\overline{\mu}}_{zs}\cdot \right] \overline{H}_s \tag{2.85}
\end{aligned}
$$

These state equations can then formulated in matrix notation as:

$$\frac{d}{dz}\left(\begin{array}{c} \overline{E}_s \\ \overline{H}_s \end{array}\right) = \left(\begin{array}{cc} \overline{\overline{\Pi}}_{11} & \overline{\overline{\Pi}}_{12} \\ \overline{\overline{\Pi}}_{21} & \overline{\overline{\Pi}}_{22} \end{array}\right)\left(\begin{array}{c} \overline{E}_s \\ \overline{H}_s \end{array}\right) \tag{2.86}$$

where $\overline{\overline{\Pi}}_{ij}$ are 2×2 matrices obtained from (2.84) and (2.85). The determination of these
matrices can be facilitated by noting the following matrix form of the cross product:

$$\overline{a} \times \overline{b} = \left(\begin{array}{ccc} 0 & -a_z & a_y \\ a_z & 0 & -a_x \\ -a_y & a_x & 0 \end{array}\right)\left(\begin{array}{c} b_x \\ b_y \\ b_z \end{array}\right) \tag{2.87}$$

If we then enlarge all matrices to a size of 3×3 by appropriate zero-padding, we can use the
matrix form for cross products to find the elements of $\overline{\overline{\Pi}}$ by applying a few matrix products.

To solve the state equation, (2.86), we assume solutions of form:

$$\overline{V}_\ell = \overline{V}_{s\ell} \ e^{\mathrm{i}k_{\ell z}z} \tag{2.88}$$

which allows the formulation of the following eigenvalue problem

$$\left(\overline{\overline{\Pi}} - \mathrm{i}k_{\ell z}\overline{\overline{I}}\right)\overline{V}_{s\ell} = 0 \tag{2.89}$$

Note that the eigenvalues and eigenvectors lead to the development of Type I and Type II waves, equivalent to those determined by the kDB method [59].

After solving the eigenvalue problem for each region, we have the following general solution form for each region:

$$\overline{V}_\ell = A_{\ell 1}\,\overline{a}_{\ell 1}\,e^{\mathrm{i}k_{\ell z}^{(1)}z} + A_{\ell 2}\,\overline{a}_{\ell 2}\,e^{\mathrm{i}k_{\ell z}^{(2)}z} + A_{\ell 3}\,\overline{a}_{\ell 3}\,e^{\mathrm{i}k_{\ell z}^{(3)}z} + A_{\ell 4}\,\overline{a}_{\ell 4}\,e^{\mathrm{i}k_{\ell z}^{(4)}z} \tag{2.90}$$

where $\overline{a}_{\ell i}$ are the eigenvectors and A_i are the unknown coefficients to be solved for by matching boundary conditions. In matrix form, $\overline{V}_\ell$ can be expressed as:

$$\overline{V}_\ell(z) = \overline{\overline{a}}_\ell \cdot e^{\mathrm{i}\overline{\overline{k}}_{\ell z}z} \cdot \overline{A} \tag{2.91}$$

where $\overline{\overline{a}}_\ell$ is a 4×4 matrix whose columns contain each of the four eigenvectors, $\overline{\overline{k}}_{\ell z}$ is a diagonal matrix containing the corresponding eigenvalues, and $\overline{A}$ is 4×1 column vector containing the coefficients. Also, note that we can determine a propagator matrix, $P(z, z')$ that expresses the fields at z in terms of those at z', which is given by:

$$\begin{aligned}
\overline{V}(z) &= \overline{\overline{a}} \cdot e^{\mathrm{i}\overline{\overline{k}}_{\ell z}(z-z')} \cdot \overline{\overline{a}}^{-1} \cdot \overline{V}(z') \tag{2.92} \\
&= \overline{\overline{P}}(z, z') \cdot \overline{V}(z) \tag{2.93}
\end{aligned}$$

In order to facilitate the matching of boundary conditions, it is convenient to define the order of $\overline{\overline{a}}$, $\overline{\overline{k}}_z$, and $\overline{A}$ such that A_1 and A_2 correspond to up-going $(+\hat{z})$ waves and A_3 and A_4 correspond to down-going $(-\hat{z})$ waves. Then assuming that the incident field originates in region zero and propagates in the positive z direction, one can relate the coefficients for

region zero by defining a reflection matrix,

$$\begin{pmatrix} A_{01} \\ A_{02} \end{pmatrix} = \overline{\overline{R}} \cdot \begin{pmatrix} A_{03} \\ A_{04} \end{pmatrix} \tag{2.94}$$

which implies that

$$\overline{A}_0 = \begin{pmatrix} \overline{\overline{R}} \\ \overline{\overline{I}} \end{pmatrix} \begin{pmatrix} A_{03} \\ A_{04} \end{pmatrix} . \tag{2.95}$$

Similarly in the transmitted region the coefficients can be expressed in terms of a transmission matrix,

$$\overline{A}_t = \begin{pmatrix} \overline{\overline{0}} \\ \overline{\overline{T}} \end{pmatrix} \begin{pmatrix} A_{03} \\ A_{04} \end{pmatrix} \tag{2.96}$$

where the fact that $A_{t1} = A_{t2} = 0$ was used.

The boundary conditions at each of the N interfaces are given by:

$$V_0(-z_0) \;=\; V_1(-z_0) = P_1(-z_0, -z_1)V_1(-z_1) \tag{2.97}$$

$$V_1(-z_1) \;=\; V_2(-z_1) = P_2(-z_1, -z_2)V_2(-z_2) \tag{2.98}$$

$$\vdots$$

$$V_N(-z_N) \;=\; V_{N+1}(-z_N) = P_{N+1}(-z_N, -z_{N+1})V_{N+1}(-z_N) \tag{2.99}$$

so that a matrix equation for $\overline{\overline{R}}$ and $\overline{\overline{T}}$ can be found,

$$\begin{pmatrix} \overline{\overline{R}} \\ \overline{\overline{I}} \end{pmatrix} = e^{i\overline{\overline{k}}_{0z}z_0} \cdot \overline{\overline{a}}_0^{-1} \cdot \overline{\overline{L}} \cdot \overline{\overline{a}}_{N+1} \cdot e^{-i\overline{\overline{k}}_{(N+1)z}z_N} \begin{pmatrix} \overline{\overline{0}} \\ \overline{\overline{T}} \end{pmatrix} \tag{2.100}$$

where

$$\overline{\overline{L}} = P_1(-z_0, -z_1) \cdot P_2(-z_1, -z_2) \cdots P_N(-z_{N+1}, -z_N) \tag{2.101}$$

Note that the definitions of $\overline{\overline{R}}$ and $\overline{\overline{T}}$ are not necessarily unique, but can be made unique by normalizing the eigenvectors $\overline{a}_{\ell i}$ [73]. Alternatively, we can formulate the solution in a different way without the need of defining reflection and transmission matrices. In this method, the propagator matrix is used to directly relate the field coefficients of the incident region to those of the transmission region,

$$\overline{\overline{a}}_0 \cdot e^{-i\overline{k}_{0z}} \cdot \begin{pmatrix} A_{01} \\ A_{02} \\ A_{03} \\ A_{04} \end{pmatrix} = \overline{\overline{L}} \cdot \overline{\overline{a}}_{N+1} \cdot e^{-ik_{N+1}z_N} \begin{pmatrix} A_{(N+1)1} \\ A_{(N+1)2} \\ A_{(N+1)3} \\ A_{(N+1)4} \end{pmatrix} \tag{2.102}$$

In this system of equations, there are four equations, but 8 unknowns. To solve, we need to assume amplitudes for the incident plane wave components, A_{03} and A_{04}; also, as usual, in the transmitted region, there are no up-going waves, thus $A_{(N+1)1} = A_{(N+1)2} = 0$.

In the case where the multi-layer structure is terminated by a perfectly electric conducting ground plane the formulation is altered due to the different boundary condition at the interface, say $-z_N$, and can be written in the form,

$$V_N(-z_N) = \begin{pmatrix} 0 \\ 0 \\ H_x \\ H_y \end{pmatrix} \tag{2.103}$$

where H_x and H_y are the magnetic fields on the surface of the metal. The overall equation

to solve then becomes,

$$
\bar{\bar{a}}_0 \cdot e^{-i\bar{k}_{0z}} \cdot \begin{pmatrix} A_{01} \\ A_{02} \\ A_{03} \\ A_{04} \end{pmatrix} = \bar{\bar{L}} \cdot \begin{pmatrix} 0 \\ 0 \\ H_x \\ H_y \end{pmatrix} \tag{2.104}
$$

where the unknowns are H_x, H_y, A_{01}, and A_{02}.

Gaussian beam propagation results

In this section, the propagation of a Gaussian beam through a various slabs of indefinite media will be examined. The Gaussian beam is generated by summing a weighted collection of plane waves as illustrated by the following integral for the E_y field component [36],

$$
E_y = \int dk_x \; e^{ik_x x + ik_z z} \; \psi(k_x) \tag{2.105}
$$

where ψ is the weighting function given by,

$$
\psi(k_x) = \frac{g}{2\sqrt{\pi}} e^{-\frac{g^2}{4}(k_x - k_{ix})^2} \tag{2.106}
$$

with g being the width factor.

In Fig. 2-13, the propagation of a Gaussian beam through a isotropic LH medium slab is shown. In this case, the phase propagation vector and time-averaged Poynting vector are anti-parallel. This can be seen from the fact that the dispersion relation for an isotropic LH medium is a unit circle just as free space. However, the power direction is reversed due to the negative permittivity and permeability. Thus, inside the slab a backward exists with a phase that propagates toward the incidence plane. The backward phase has been verified by incorporating the $e^{-i\omega t}$ time dependence into a field animation, which clearly showed the phase propagating opposite to that of the phase in the incident region.

Figure 2-13: Propagation of a Gaussian beam from free space through an isotropic left-handed slab (indicated by solid lines at $z = -5$ and $z = 0$) with $\epsilon_r = \mu_r = -1$ The solid white arrows indicate the direction of the time-averaged Poynting vector while the broad strips show the electric field pattern.

In Fig. 2-14, the propagation of a Gaussian beam through an anisotropic medium of the always-propagating type is shown. In this case, the tangential permittivity (y) and permeability (x) components are both negative while the perpendicular (z) permeability component is positive, *i.e.*,

$$\bar{\bar{\epsilon}} = \epsilon_o \begin{pmatrix} 1 & 0 & 0 \\ 0 & -1 & 0 \\ 0 & 0 & 1 \end{pmatrix} \qquad \bar{\bar{\mu}} = \mu_o \begin{pmatrix} -1 & 0 & 0 \\ 0 & 1 & 0 \\ 0 & 0 & 1 \end{pmatrix}. \qquad (2.107)$$

The illustration in Fig. 2-14 shows that part of the incident beam is reflected due to mismatch, and part of it is transmitted through the slab at a positive angle. It should be noted
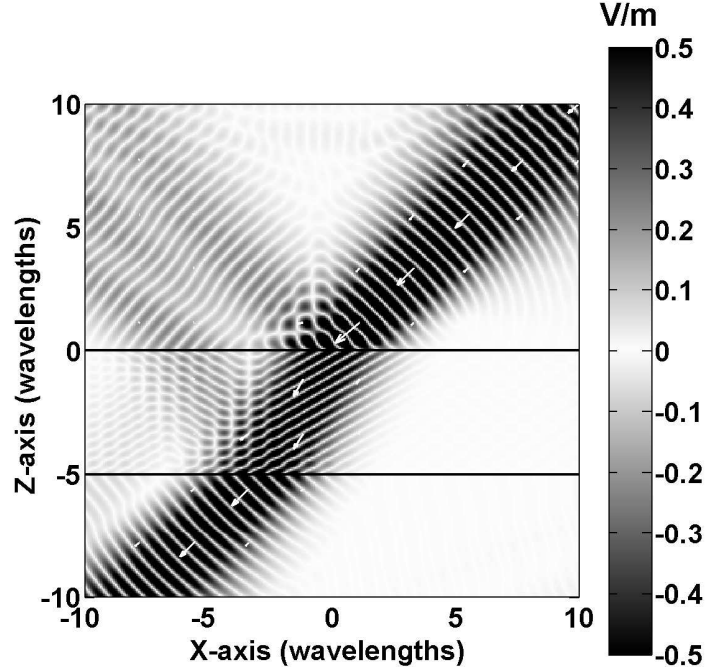
Figure 2-14: Propagation of a Gaussian beam from free space through an anisotropic slab (indicated by solid lines at $z = -5$ and $z = 0$) with $\epsilon_{ry} = \mu_{rx} = -1$ and $\mu_{rz} = 1$ (see k-surface plotted in Fig. 2-12(d)). The solid white arrows indicate the direction of the time-averaged Poynting vector while the broad strips show the electric field pattern.

in this case that the Poynting vector and phase vector inside the slab are not aligned. This can be seen from the dispersion relation. For a non-zero k_x, the normal to the k-surface and the phase vector are skew and in opposite directions. Thus, the wave inside the medium is indeed a backward wave, but it is not a negatively refracted wave. Again, as before the backward nature of the phase predicted by the dispersion relation has been verified by including in the time dependence and observing a field animation.

Next, in Fig. 2-15, the propagation of a Gaussian beam through an anisotropic medium of the always-cutoff type is shown. In this case, the roles of the permeability components

(x and z) are reversed, *i.e.*,

$$\overline{\overline{\epsilon}} = \epsilon_o \begin{pmatrix} 1 & 0 & 0 \\ 0 & -1 & 0 \\ 0 & 0 & 1 \end{pmatrix} \qquad \overline{\overline{\mu}} = \mu_o \begin{pmatrix} 1 & 0 & 0 \\ 0 & 1 & 0 \\ 0 & 0 & -1 \end{pmatrix}. \tag{2.108}$$

However, because this medium corresponds to the always cutoff type, it acts as similar to a plasma medium, whereby the incident wave would totally be reflected were this a half-space configuration. Due to the finite thickness of the slab, there is of course a small amount of energy that propagates through the slab. Still, the waves inside the slab are evanescent meaning that the time-averaged Poynting vector is zero, which makes it difficult to discuss about such concepts as backward waves.

Still, none of the above results have explained the fact that a negatively refracted beam has been observed in anisotropic metamaterial prism configurations. However, the key difference between the above simulations and the prism experiment is that the wave is incident normal to the first interface, meaning that only one component of the permittivity and permeability needs to be negative. Once inside the prism, the wave propagates as if it were inside a isotropic LH medium since it only "sees" the negative components of the material tensors. However, the question is, what happens at the second interface of the prism which is tilted with respect to the direction of propagation? To answer this question, use of the rotated media model introduced by Smith *et al* in [72] will be used. In order to solve the analytically intractable problem of propagation through a prism structure, a solvable half-space problem (see Fig. 2-16) is created which approximates that of the true configuration to first order by neglecting higher order reflections inside the prism.

The rotated media model begins by taking the original material tensor, generically denoted below as Λ, and applying a rotation operation to it, as follows,

$$\text{rot}_\theta \, \overline{\overline{\Lambda}} = Q \, \overline{\overline{\Lambda}} \, Q^{-1} \tag{2.109}$$
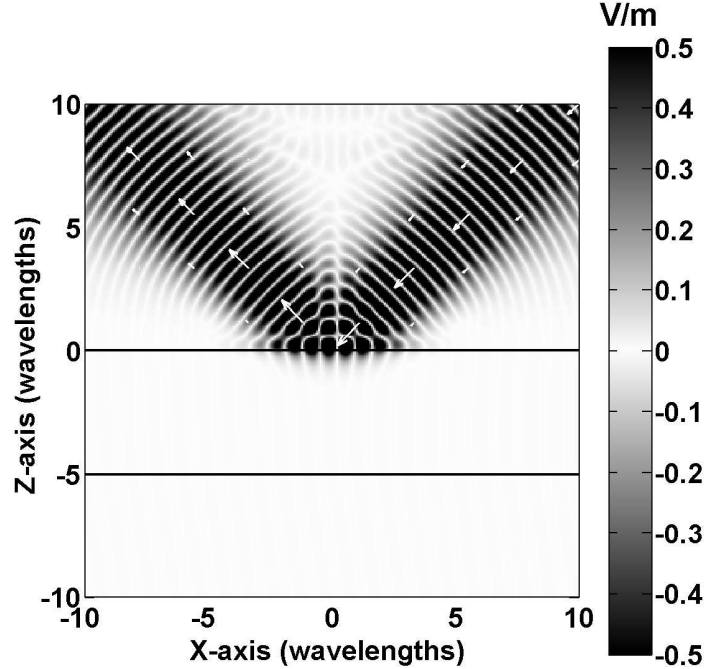
Figure 2-15: Propagation of a Gaussian beam from free space through an anisotropic slab (indicated by solid lines at $z = -5$ and $z = 0$) with $\epsilon_{ry} = \mu_{rz} = -1$ and $\mu_{rx} = 1$ (see k-surface plotted in Fig. 2-12(b)). The solid white arrows indicate the direction of the time-averaged Poynting vector while the broad strips show the electric field pattern.

where

$$Q = \begin{pmatrix} \cos\theta & 0 & \sin\theta \\ 0 & 1 & 0 \\ -\sin\theta & 0 & \cos\theta \end{pmatrix}. \tag{2.110}$$

The degree of rotation is chosen such that the principle axis of the material tensor lies along the direction of propagation, which corresponds to the slant angle of the prism.

In the following example, the prism will assumed to have a slant angle of $15°$ and the original (non-rotated) material tensor will be of the always propagating type, as in (2.107).
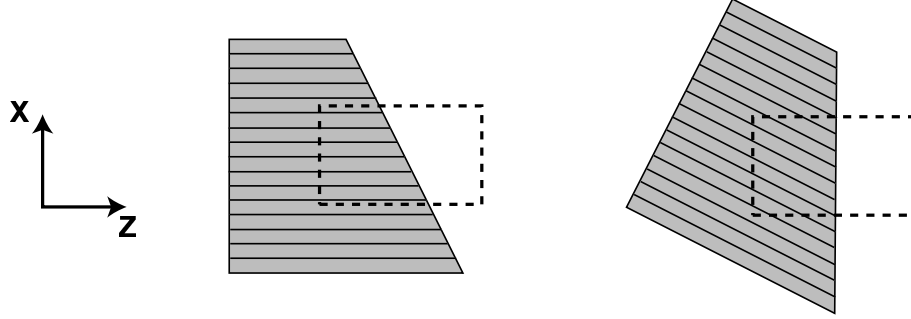
Figure 2-16: Diagram of setup for original prism experiment and rotated prism. The solid lines inside the prism indicate the direction of propagation within the prism. Perpendicular to these lines is the direction of the LH material component (x). The dashed box indicates the region of interest.

Upon applying the rotation matrix the permittivity tensor remains unchanged,

$$\overline{\overline{\epsilon}} = \epsilon_o \begin{pmatrix} 1 & 0 & 0 \\ 0 & -1 & 0 \\ 0 & 0 & 1 \end{pmatrix}, \tag{2.111}$$

while the permeability tensor becomes

$$\overline{\overline{\mu}} = \text{rot}_{15} \left\{ \mu_o \begin{pmatrix} -1 & 0 & 0 \\ 0 & 1 & 0 \\ 0 & 0 & 1 \end{pmatrix} \right\} = \mu_o \begin{pmatrix} -\sqrt{3}/2 & 0 & 1/2 \\ 0 & 1 & 0 \\ 1/2 & 0 & \sqrt{3}/2 \end{pmatrix}. \tag{2.112}$$

The resulting dispersion relation and beam propagation pattern are shown in Fig. 2-17 and Fig. 2-18. As can be seen, the power is negatively refracted from the "prism" medium into freespace. For this specific angle of incidence the Poynting vector and phase vector are anti-parallel as in isotropic case due to the fact that the normal to the k-surface and phase vector are aligned. For any other angle this is not true, although there does exist a small range of angles centered about the rotation angle, $15°$, for which there is negatively refracted power. For these angles, though, the phase and Poynting vectors are not aligned.
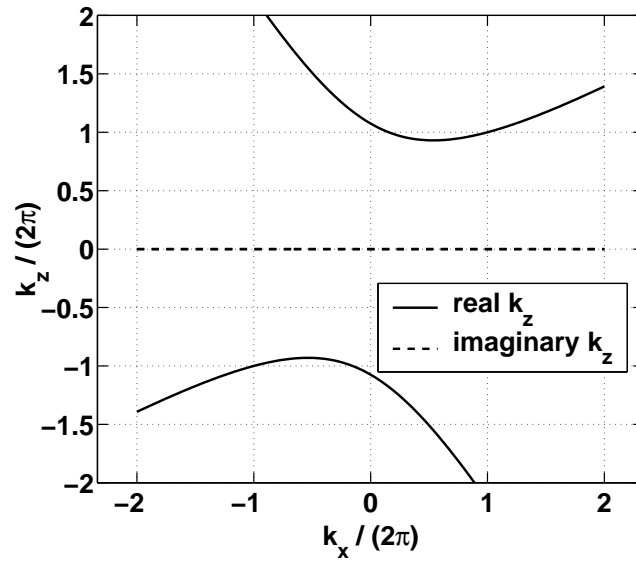
Figure 2-17: Dispersion relation for an anisotropic medium with $\epsilon_{ry} = \mu_{rx'} = -1$ and $\mu_{rz'} = 1$ The primes indicate that the material tensor has been rotated about y axis by 15°. The solid white arrows indicate the direction of the time-averaged Poynting vector while the broad strips show the electric field pattern.
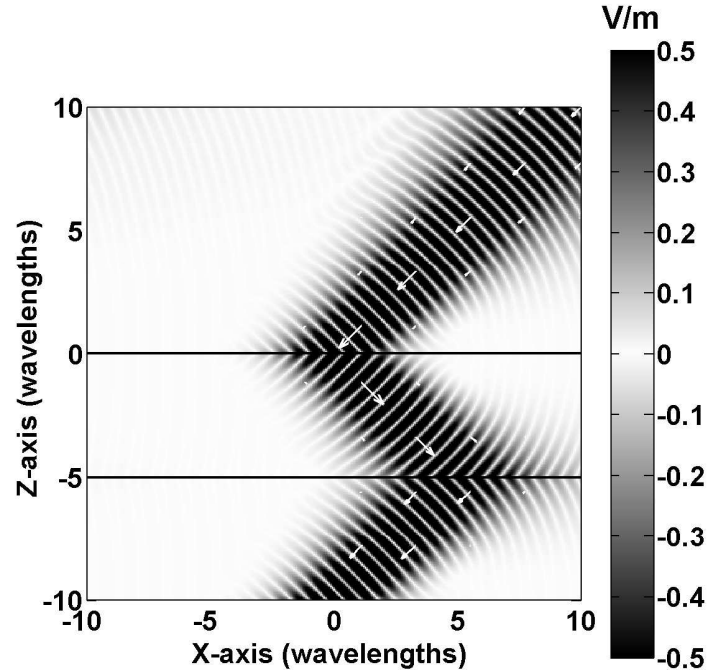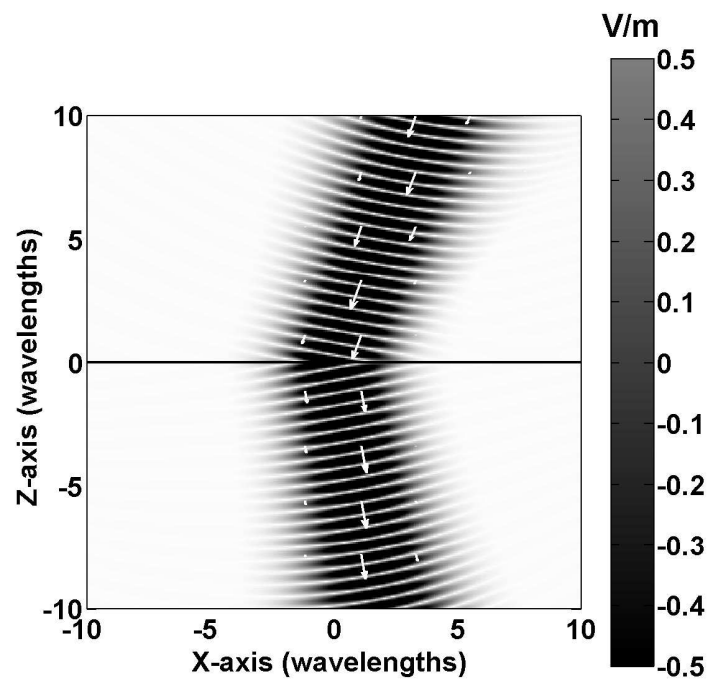
Figure 2-18: Propagation of a Gaussian beam from free space through an anisotropic slab (indicated by solid lines at $z = -5$ and $z = 0$) with $\epsilon_{ry} = \mu_{rx'} = -1$ and $\mu_{rz'} = 1$ (see k-surface in Fig. 2-17). The primes indicate that the material tensor has been rotated about y axis by $15°$. The solid white arrows indicate the direction of the time-averaged Poynting vector while the broad strips show the electric field pattern.

2.6   Summary

In summary, this chapter has discussed the fundamental properties of propagation, radiation, and scattering in the presence of left-handed media. It was seen by plane wave analysis, that neither causality nor any other physical law prevents negative refraction from occurring at the interface of a RH medium and a dispersive LH medium. Secondly, the perfect lens concept was studied using a two-dimensional Green's function analysis. It is shown that under the perfect lens requirement, that two perfect images of source outside a LH media slab are formed. Interestingly though, the time-averaged power flow inside the slab seemingly forms a sink. However, it was shown that while the introduction of loss eliminates this conundrum, the lens becomes imperfect. It was also shown that even a small amount of loss can significantly destroy the imaging properties of the LH media lens. In terms of scattering, the Mie solution for plane wave scattering by a LH medium sphere is examined. It was shown that while applicable, care must be taken in choosing the appropriate signs of the wavenumbers in the evaluation of the Mie coefficients. In addition, it is then shown that a sphere composed of a LH medium will focus incoming energy into a spot inside the sphere. Finally, because the metamaterials are in general anisotropic, the effects of anisotropy on reflection and transmission of a Gaussian beam were examined.

Chapter 3

Characterization of left-handed metamaterials

3.1 Introduction

While a fundamental understanding of LH media is important, of practical importance is the development of metamaterials that behave as LH media. In development of metamaterials, there are two aspects that must be addressed. The first is the question of being able to characterize a given material as a right-handed or left-handed material. The second aspect that must be addressed is how to achieve a design that meets the specifications for some particular application in terms of operating frequency, bandwidth, and loss. Both the design and characterization aspects go hand in hand as design approaches invariably rely on characterization methods. In this chapter, various tools that can be used in the characterization of metamaterials will be discussed.

With the recent interest in metamaterials, there have been a number of approaches in the past, both experimental and theoretical (or numerical). The focus of this work will be techniques which can be readily applied to numerical simulation results. Originally, transmission characteristics alone were used to determine if a material exhibited LH properties [5], with-

out specific characterization of the permittivity and permeability. Theoretically, a medium will only support propagating waves if the real part of both the permittivity and permeability are of the same algebraic sign. Thus, if a transmission band appears when both the rings and rods are present, but does not occur with either independently, then it is possible the material is behaving as a LH metamaterial at that frequency band. While the conclusion in [5] that the SRRs exhibit a negative permeability is based on the fact that the rods are known to have negative permittivity at certain frequencies, the amount of coupling between the two structures is unknown. Therefore, the appearance of the transmission band alone does not confirm this conclusion and further proof is needed. Additionally, the presence of a transmission band does not give any indication of the exact values of the permittivity and permeability, thus, more robust methods are needed.

3.2 Left-handed metamaterials models

As discussed in Section 1.1, currently left-handed metamaterials are constructed by creating a periodic arrangement of rods and split-rings. In this section, some of the basic metamaterials models currently used to model the rods and split-rings will be discussed.

3.2.1 Analytic models

In the literature the most common models for the relative effective permittivity and permeability for left-handed metamaterials used are the Drude [27] and Lorentz models [4]. The forms of these models are,

$$\text{Drude} \;=\; 1 - \frac{\omega_p^2}{\omega^2 + \mathrm{i}\gamma\omega} \tag{3.1}$$

$$\text{Lorentz} \;=\; 1 - \frac{\omega_p^2 - \omega_o^2}{\omega^2 - \omega_o^2 + \mathrm{i}\gamma\omega} \tag{3.2}$$

where ω_p, ω_o, and γ are the plasma, resonant, and damping frequencies, respectively, of the model. Examples curves of these models are shown in Fig. 3-1.

(a) Drude model   (b) Lorentz model
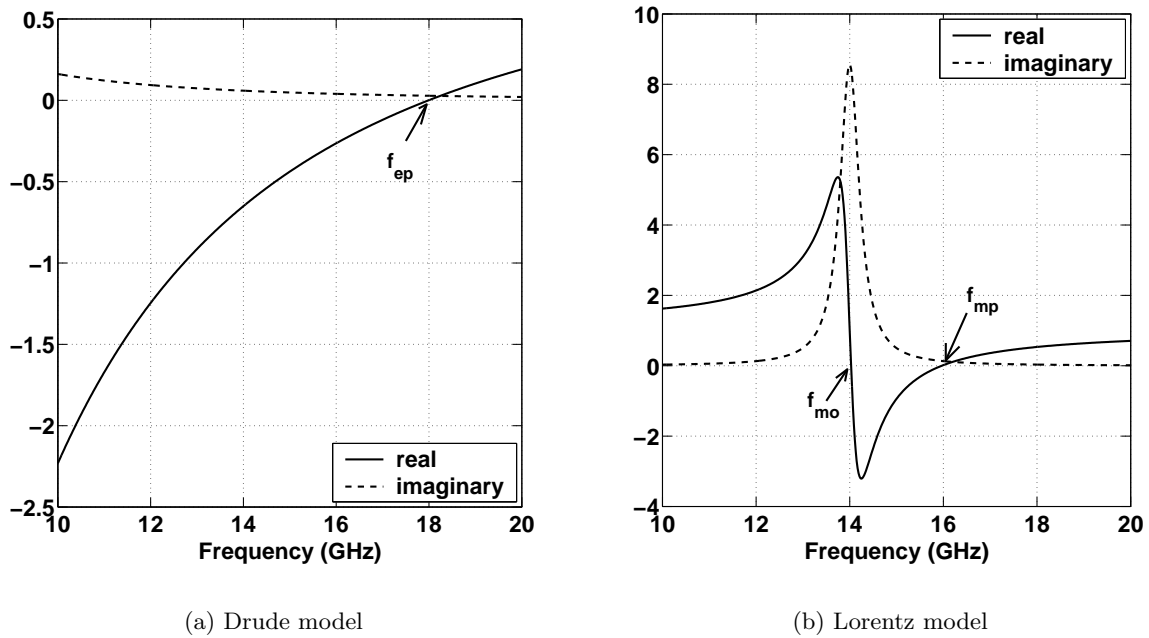
Figure 3-1: Example of typical left-handed metamaterial dispersion models. Drude: $f_p = 18$ GHz, $\Gamma = 0.5$ GHz. Lorentz: $f_o = 14$ GHz, $f_p = 16$ GHz, $\gamma = 0.5$ GHz. Note, damping frequencies are exaggerated for the purposes of illustration.
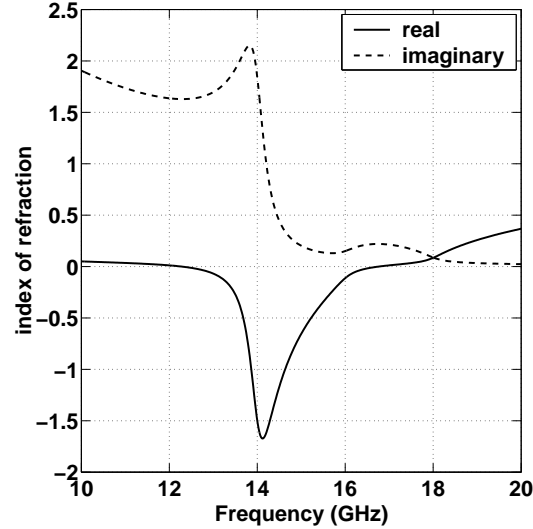
Figure 3-2: Example of index of refraction profile for a rod and ring metamaterial. Assuming a rod/SRR design, the permittivity follows the Drude model, whereas the permeability follows the Lorentz model. Parameters used are the same as in Fig. 3-1.

Typically, the rods, which contribute primarily to the effective permittivity, are characterized by the Drude model, although in some cases where there are gaps in the rods (*e.g.*, waveguide implementations where good electrical contact is not usually achieved), the Lorentz model is more appropriate [4]. In the case when the permittivity follows the Drude model and the permeability follows the Lorentz model, the material has an effective index of refraction with a negative real part between the resonant and plasma frequency of the rings only if the plasma frequency of the rods is greater than the plasma frequency of the rings. Fig. 3-2 shows one example of the index of refraction for such a medium.

3.2.2 Comparison with numerical results

In order to use the analytical models presented above, the plasma and resonant frequencies need to be estimated by either theoretical, numerical, or experimental means. It is the purpose of this section to compare the prediction of theory with numerical simulation results, specifically, the reflection and transmission coefficients. The slab configuration under study
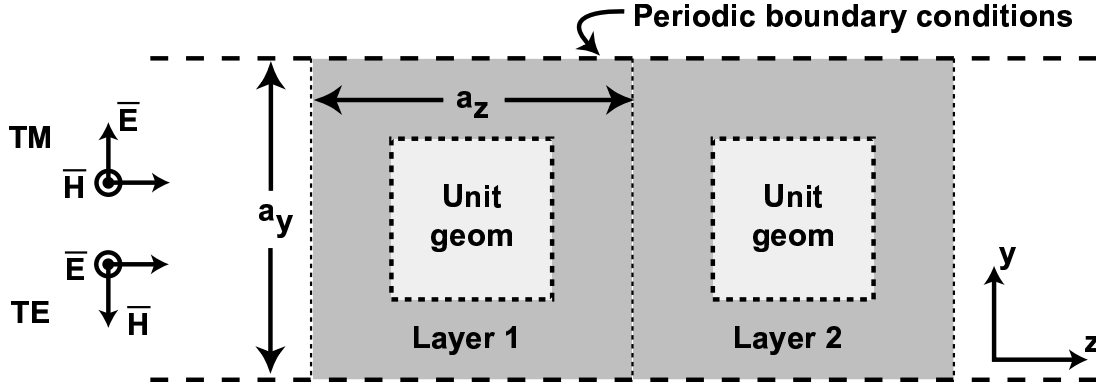
Figure 3-3: Periodic arrangement of two-dimensional unit cells as simulated by the FDTD method. The unit cell is repeated for a finite number of layers (2 shown in figure) along the x direction. Each layer is infinitely repeated along the $\hat{y}$ direction using a periodic boundary condition.

is shown in Fig. 3-3. In this two-dimensional setup, the cells are infinitely repeated along the $\hat{y}$ direction separated by the lattice constant a_y whereas there are a finite number of layers along the $\hat{x}$ direction separated by the lattice constant a_x. Depending on the geometry (rods or rings), either a TE or TM polarized incident wave will be used.

Rods

As discussed above, the rods can be characterized by using the Drude model. A very rough understanding of this fact can be obtained by treating relating the plasma frequency of the rods to the cutoff frequency of a waveguide. In a parallel plate waveguide, frequencies with wavelengths that are larger than twice the separation distance are cutoff. However, in the case of rods, some of these lower frequencies can propagate through since there is more freespace area in rods configuration than in the waveguide configuration. Nevertheless, the waveguide configuration gives an upper bound on the effective plasma frequency of the system. However, a more precise model has been formulated by Pendry *et al* in [2] wherein the authors show that the rod medium is the equivalent of a plasma medium albeit with electrons of a higher effective mass. It should be noted that other models
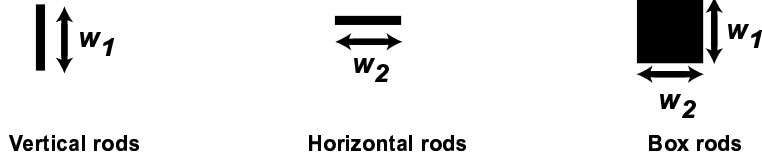
Figure 3-4: Three types of rod configurations that were simulated. The vertical and horizontal configurations are theoretically infinitesimally thin lines, but in practice, they are modeled as one unit cell using the FDTD method.

are available that predict similarly behavior albeit with different estimates of the effective plasma frequency [74]. In [2], the equivalent plasma of the rod medium was given as,

$$\omega_p^2 = \frac{n_{\text{eff}} e^2}{\epsilon_0 m_{\text{eff}}} = \frac{2\pi c_0^2}{a^2 \ln(a/r)} \tag{3.3}$$

where c_0 is speed of light in the host medium, r is the effective rod radius, and a is the lattice constant. Furthermore, by accounting for the finite conductivity of the metallic rods, the damping frequency of the equivalent plasma medium can be estimated such that the final effective permittivity is given by,

$$\epsilon_{\text{eff}} = 1 - \frac{\omega_p^2}{\omega \left(\omega + \mathrm{i}\epsilon_0 a^2 \omega_p^2 / \pi r^2 \sigma \right)}, \tag{3.4}$$

where σ is the conductivity of the metal. In the above theoretical treatment, the rods were assumed to be cylindrical; however, because curved surfaces are difficult to model using a Cartesian coordinate system based FD-TD method, the rods simulated here will be one the of the three types shown in Fig. 3-4.

Fig. 3-5 shows the reflected and transmitted power through a 2-layer geometry composed of the three different rod configurations. Also shown is the transmission and reflection for a homogeneous slab composed of an electric plasma medium with a plasma frequency of 13.82 GHz, which was calculated using (3.4). As can be seen, the effective medium model matches the numerical results for the vertically and horizontally rods oriented quite well. The differences in the case of the box shaped rods can be attributed to the larger area of

this design. In the calculation of the plasma frequency, the effective radius used for the configuration needs to be larger than the effective radius for the vertical and horizontal rod configurations.

(a) Reflected power   (b) Transmitted power
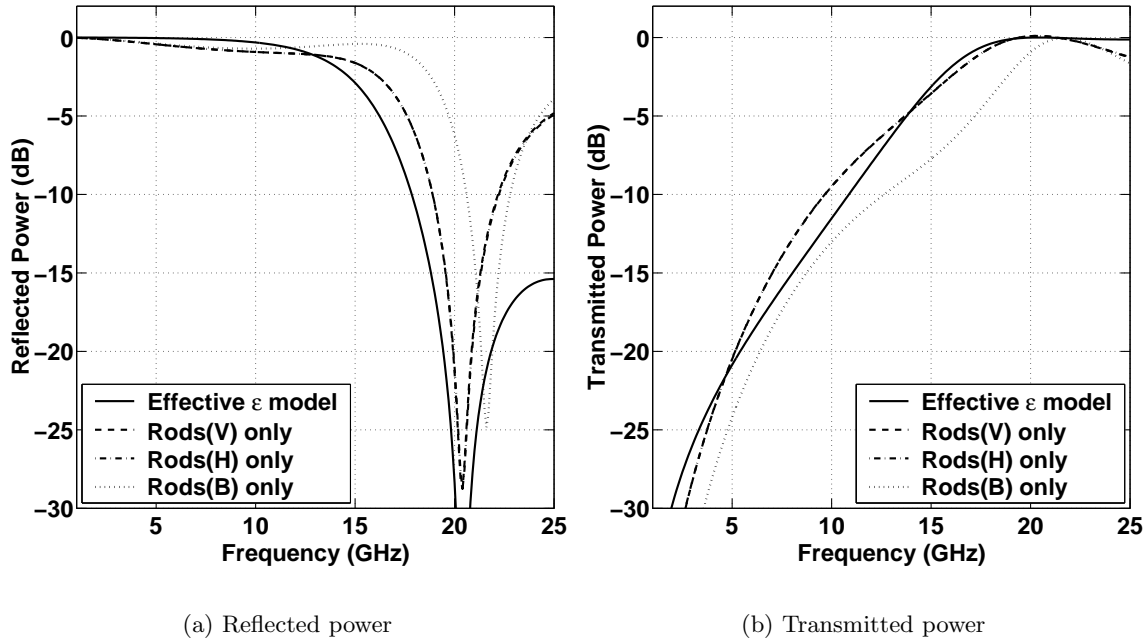
Figure 3-5: Comparison of reflected and transmitted power for three different rod configurations (shown in Fig. 3-4) compared to that predicted by an effective permittivity model. For $w_1 = w_2 = 0.25$ mm, the predicted plasma frequency is 13.82 GHz. Nb: reflection and transmission curves for vertical and horizontal rods significantly overlap.

Split-ring resonators

On the other hand, the behavior of the the split-ring resonators (SRR), is much more difficult to capture through an effective medium concept. The majority of the work in characterizing the SRR was originally done by Pendry *et al* [3, 10], where they proposed and studied the two ring designs investigated in this thesis.

The first ring design considered is the concentric ring structure, which was theoretically
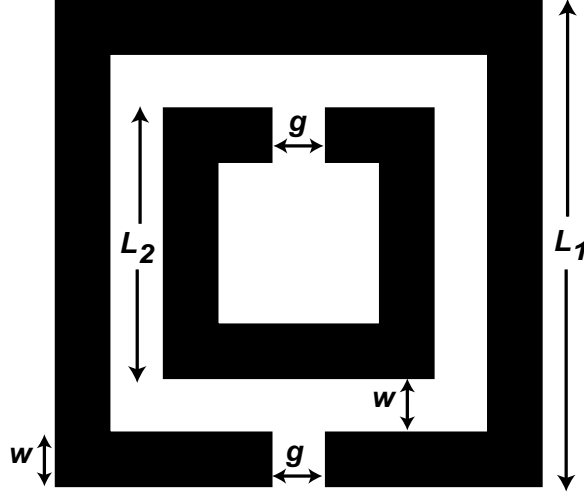
Figure 3-6: Unit cell geometry for concentric ring design

studied in [3] and experimentally characterized in [5, 15]. The unit cell geometry is shown in Fig. 3-6. The key features of the design are the gaps in the inner and outer rings which serve to set up the necessary charge distribution and the spacing between the inner and outer ring, which contributes to the capacitance of the ring. The overall area of the two rings contributes to the inductance of the structures. With the combined LC effects, Pendry showed that the effective permeability (for the circular version of the split-ring design) takes the form,

$$\mu_{\text{eff}} = 1 - \frac{\pi r^2}{a^2} \left[1 + i \frac{2}{\omega \sigma r \mu_0} \right]^{-1} \tag{3.5}$$

where r is the radius of the outer ring, d is the separation between the rings, a is the lattice constant, and σ is the conductivity of the metal. Note that when applying this formula to the geometry shown in Fig. 3-6, an effective radius is taken such that the area of a circle with such a radius matches the area of the square.

As with the rods, the transmission of a plane wave through a periodic 2-layer structure is simulated using the 2D FDTD method. Fig. 3-7 shows the results of such a simulation and compares the results to those analytically calculated using the effective permeability

model described above. In constrast to the effective medium models of the rods, the effec-

(a) Reflected power   (b) Transmitted power
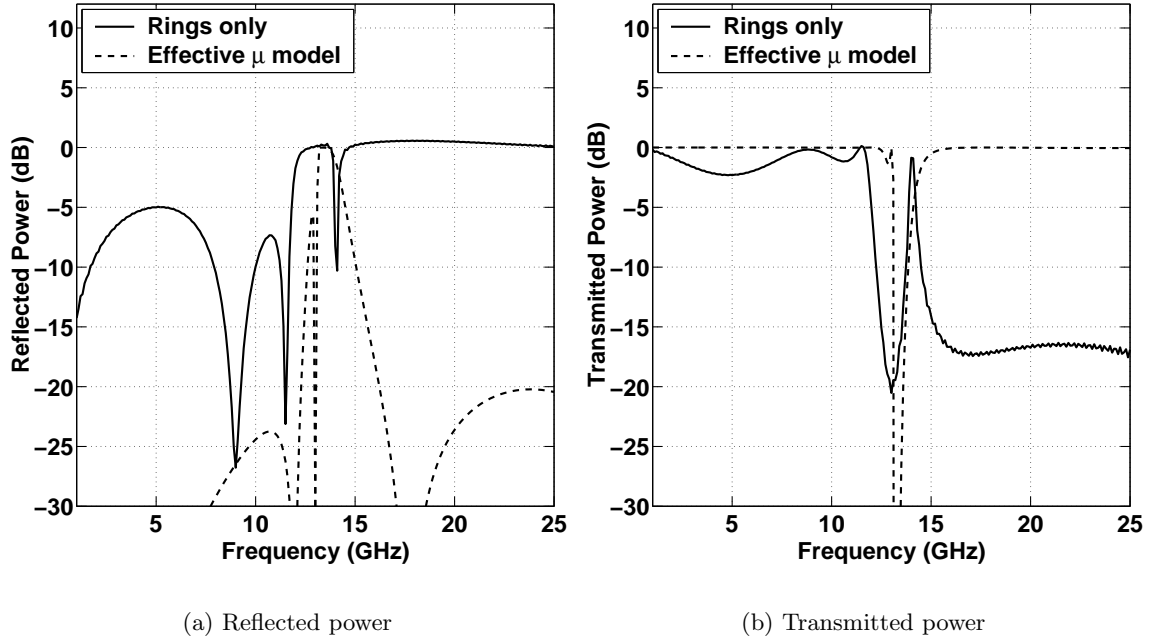
Figure 3-7: Comparison of the numerically simulated reflected and transmitted power through a two layer concentric ring structure to that predicted by the effective permeability model. The parameters used were $a_x = a_y = 5$ mm, $L_1 = 1.52$ mm, $L_2 = 2.52$ mm, $g = 0.50$ mm, and $w = 0.25$ mm [16].

tive medium model does not accurately predict the reflection and transmission coefficients. Rather, it seems to only capture the resonance effect of the rings that occurs around 14 GHz for this particular design simulated. This mismatch in Fig. 3-7 between the FDTD simulation and the analytic model can in part be attributed to the fact that the simulated ring was square rather than circular as originally studied by Pendry in [3]. Still, although there is significant disagreement, the model gives a rough estimate of the resonant frequency, which can be useful in design.

In addition to the original split-ring resonator design analyzed above, there have been other designs including the adjacent ring design proposed by O'Brien *et al* in [10], which is
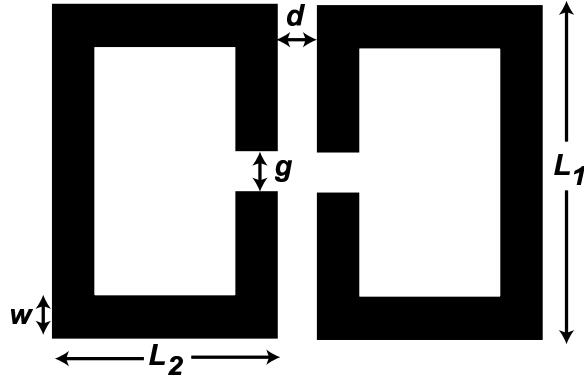
Figure 3-8: Unit cell geometry for adjacent ring design

shown in Fig. 3-8. It should be noted that the dimensions presented in [10] were designed to have the ring resonate at infrared frequencies; however, as used in this thesis, the design was scaled for microwave frequencies and studied in combination with periodic rods for potential use in left-handed metamaterials [75]. It has also recently been experimentally studied and shown to be less lossy than the concentric ring design while also having left-handed properties [34].

As shown in Fig. 3-8, the notable difference between this design and that of the concentric SRR design is that the two split rings are placed adjacent to each other rather than concentrically. Hence, the main capacitive areas are along the inner vertical section of the rings. It should be pointed out that the both circular and rectangular version of this ring were discussed in [10]; however, even in the circular design, the inner sections of the ring were vertical. The circular designed allows for a simpler analytic analysis whereas as the rectangular design is easier to model numerically. For the circular model, O'Brien *et al* found that the effective permeability takes the following form,

$$\mu = 1 - \frac{f'\omega^2}{\omega^2 - \omega_0^2 + \mathrm{i}\Gamma\omega} \tag{3.6}$$

where

$$f' = \frac{L_g}{L_g + L_i}f \tag{3.7}$$

$$\omega_0^2 = (L_g + L_i)^{-1}C^{-1} \tag{3.8}$$

and

$$\Gamma = \frac{L_i}{L_g + L_i}\gamma. \tag{3.9}$$

In the above expressions, C is the capacitance between the rings, while L_g and L_i are the inductances of the structure due to the geometry and impedance, respectively. These parameters are given by,

$$C = \frac{\epsilon_0(L_1 - g)}{4d} \tag{3.10}$$

$$L_g = \mu_o\pi R_{\text{eff}}^2 \tag{3.11}$$

$$L_I = \frac{2\pi R_{\text{eff}}}{\epsilon_0\omega_p^2 d} \tag{3.12}$$

where the effective radius, R_{eff}, is defined such that $\pi R_{\text{eff}}^2 = (L_1 - 2w)^2$.

As with the concentric ring design, the transmission and reflection properties of the rings in freespace were simulated using the FDTD method. As shown in Fig. 3-9, the model accurately predicts the resonant frequency, and approximately matches the observed reflection and transmission coefficients for frequencies near this resonance. In fact, the match is much more accurate than the case of the concentric ring design, where it was only possible to estimate the resonant frequency. This is probably due to the fact that in this design the main capacitive effect is between the inner two parallel section of the rings making it easier to more accurately calculate the inductance and capacitance of this structure.

(a) Reflected power

(b) Transmitted power
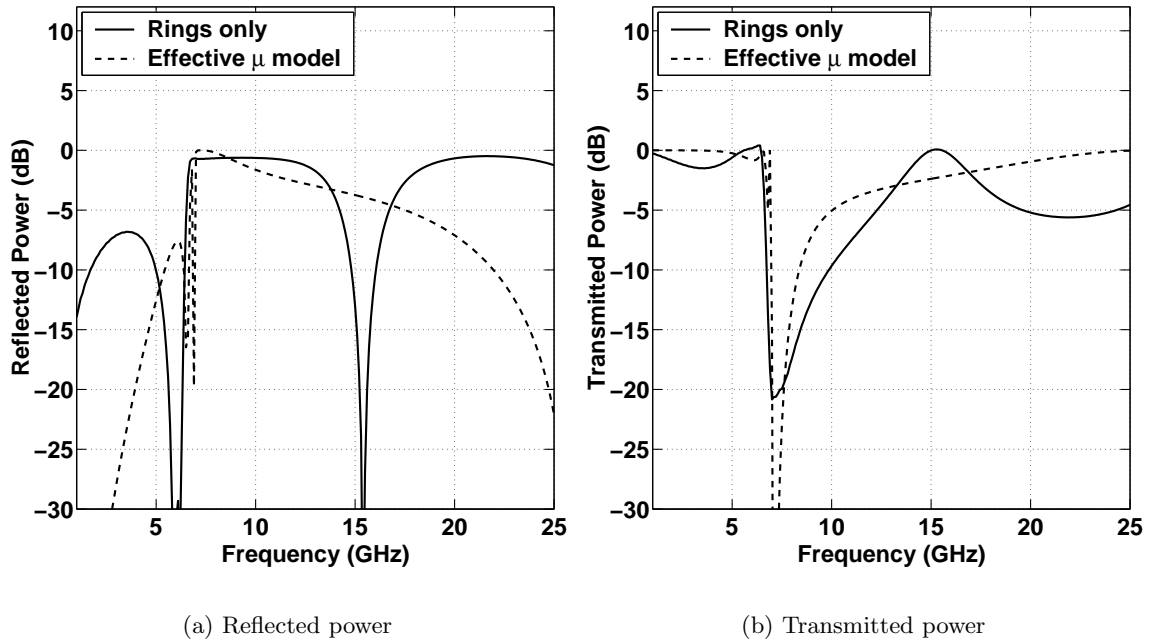
Figure 3-9: Comparison of the numerically simulated reflected and transmitted power through a two layer adjacent ring structure to that to that predicted by the effective permeability model. Parameters used were $L_1 = 3.25$ mm, $L_2 = 2.25$ mm, $g = w = s = 0.25$ mm [75].

3.3 FDTD simulation of SRRs in homogeneous electric plasma media

In this section, the theoretically predicted negative permittivity and negative permeability for the rods and rings will be tested by embedding them in homogeneous electric and magnetic plasma media, respectively. While it not possible to realize this in an experimental setup, it is possible to do so in a numerical simulation, *e.g.*, embedding a split-ring resonator (SRR) in a homogeneous electric plasma. Because the permittivity is analytically known to be negative at all frequencies less than the predetermined plasma frequency, transmission through such a multi-layer slab below the plasma frequency would be a good indication of left-handed properties, meaning that the rings can be characterized by an effective negative permeability. Still, it must be noted that the SRR structures have an intrinsic effective permittivity [76] combined with the background permittivity may yield an effective right-handed medium. To overcome this uncertainty, the field distribution inside the slab is also studied.

3.3.1 Modeling of dispersive materials using the FDTD

In order to simulate the metallic rods or rings embedded in a homogeneous plasma, the two-dimensional finite difference-time domain (FDTD) method will be used. As shown in Fig. 3-3, periodic boundary conditions will be used to model an infinite row of two-dimensional rods or rings. The formulation for being able to embed a SRR in electric plasma medium is described below. The formulation for the dual case of embedding a rod in a magnetic plasma medium is analogous and is not shown for brevity. Note that for simplicity of implementation, the Drude model will be used both for the homogeneous background electric and magnetic plasma frequencies. Specifically, the Drude model for the

permittivity [27] is given by,

$$\epsilon \ = \ \epsilon \left(1 - \frac{\omega_{pe}^2}{\omega(\omega + i\gamma)} \right) \tag{3.13}$$

where ω_{pe} is the plasma frequency of the medium and γ is the damping frequency. In order to incorporate the dispersion of the plasma medium into the time-domain FDTD method, a current term must be added to the set of unknowns [77]. The formulation begins with the frequency domain version of the 2D TM Maxwell's equations, which are given by,

$$i\omega\mu H_z \ = \ \partial_x E_y - \partial_y E_x \tag{3.14a}$$

$$-i\omega\epsilon E_x + J_x \ = \ \partial_y H_z \tag{3.14b}$$

$$-i\omega\epsilon E_y + J_x \ = \ -\partial_x H_z. \tag{3.14c}$$

Upon making use of (3.13), Maxwell's equations for a source-free region become

$$i\omega\mu H_z \ = \ \partial_x E_y - \partial_y E_x \tag{3.15a}$$

$$-i\omega\epsilon E_x + \frac{i\omega_p^2}{\omega + i\gamma}\epsilon E_x \ = \ \partial_y H_z \tag{3.15b}$$

$$-i\omega\epsilon E_y + \frac{i\omega_p^2}{\omega + i\gamma}\epsilon E_y. \ = \ -\partial_x H_z \tag{3.15c}$$

While the medium is source free, the introduction of the plasma medium generates an induced current which is related to the electric field as follows,

$$J_x \ = \ \frac{i\omega_p^2}{\omega + i\gamma}\epsilon_x E_x \tag{3.16a}$$

$$J_y \ = \ \frac{i\omega_p^2}{\omega + i\gamma}\epsilon_y E_y \tag{3.16b}$$

Substituting (3.16) into (3.15) and converting the equations into the time domain yields the following coupled space and time dependent differential equations,

$$\partial_t \mu H_z = \partial_y E_x - \partial_x E_y \tag{3.17a}$$

$$\partial_t \epsilon E_x + J_x = \partial_y H_z \tag{3.17b}$$

$$\partial_t \epsilon E_y + J_y = -\partial_x H_z \tag{3.17c}$$

$$\partial_t J_x + \gamma J_x = \epsilon \omega_p^2 E_x \tag{3.17d}$$

$$\partial_t J_y + \gamma J_y = \epsilon \omega_p^2 E_y. \tag{3.17e}$$

These equations can then be discretized using the standard central differencing scheme [78, 79]. For example, if the magnetic field and currents are placed in the center of the cell and the electric fields along the edges of the cell, the update difference equations for the E_x and J_x components are given by,

$$
\begin{aligned}
E_x\left(n+\frac{1}{2}, i, j+\frac{1}{2}\right) = {} & E_x\left(n-\frac{1}{2}, i, j+\frac{1}{2}\right) \\
& + \frac{2\Delta_t}{[\epsilon_x(i, j+1) + \epsilon_x(i, j)]} \left\{ \frac{1}{\Delta} [H_z(n, i, j+1) - H_z(n, i, j)] \right. \\
& \left. -\frac{1}{2} [J_x(n, i, j+1) + J_x(n, i, j)] \right\}
\end{aligned} \tag{3.18a}
$$

$$
\begin{aligned}
J_x(n+1, i, j) = {} & \left(\frac{1 - \frac{1}{2}\gamma\Delta t}{1 + \frac{1}{2}\gamma\Delta t}\right) J_x(n, i, j) \\
& + \frac{\epsilon_x(i,j)\omega_{exp}^2\Delta t}{1 + \frac{1}{2}\gamma\Delta t}\left(\frac{1}{2}\right)\left[E_x\left(n+\frac{1}{2}, i, j+\frac{1}{2}\right) + E_x\left(n+\frac{1}{2}, i, j-\frac{1}{2}\right)\right]
\end{aligned} \tag{3.18b}
$$

where Δ and Δt are the spatial and temporal discretizations, respectively.

With the dispersion of the permittivity now included in the FDTD update equations, the transmission and reflection coefficients can be obtained for SRRs embedded in a homogeneous electric plasma medium. The reflection and transmission coefficients are calculated by averaging the fields over a contours in front and behind the layered structure of interest.
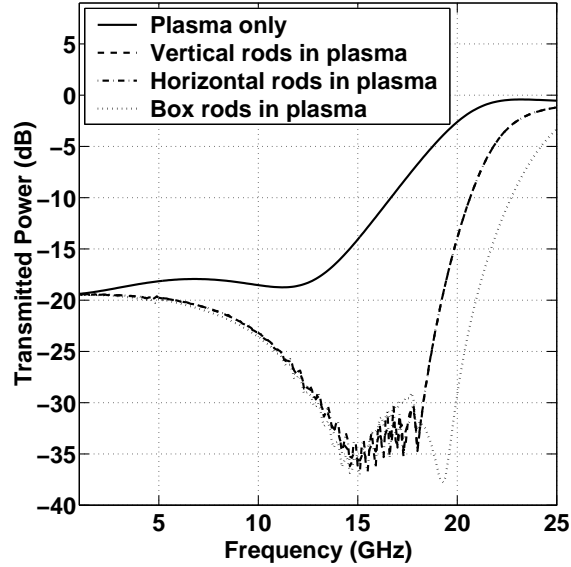
Figure 3-10: Transmission through a two layer structure consisting of metallic rods embedded in a homogeneous magnetic plasma medium. The plasma medium implemented is that based on the Drude model with a plasma frequency of 18 GHz and damping frequency of 100 MHz.

As noted before, a similar FDTD formulation can be derived for modeling a set of rods embedded in a homogeneous magnetic plasma.

3.3.2   Simulation Results

Rods embedded in a magnetic plasma

In the first example, a 2-layer periodic set of metallic rods embedded in a homogeneous magnetic plasma medium is simulated. The plasma medium implemented is that based on the Drude model with a plasma frequency of 18 GHz and a damping frequency of 100 MHz. The results for the three different types of rod configurations in the plasma as well as transmission through the plasma alone are shown in Fig. 3-10. As can be seen, there are no transmission bands below the plasma frequency of the background medium indicating the rods are not functioning with a negative permittivity.

At first glance, such a result does not seem to be consistent with the results shown in

Fig. 3-11, which matched the theoretically predicted negative permittivity. An explanation for this phenomena can be found in a recent paper by Pokrovsky *et al* [20] wherein the authors show that a periodic metallic structure embedded in a negative magnetic medium $(\mu(\omega) < 0)$, such as a collection of rods in a magnetic Lorentz medium can not support left-handed modes. By duality, as will be shown later in this section, one could imagine that the case of a set of split-ring resonators embedded in a homogeneous electric plasma medium also is not capable of supporting left-handed modes. In each case, the surrounding medium changes the effective medium properties of the periodic metallic structure. For example, it is well understood that a collection of rods embedded in dielectric substrate will have a different plasma frequency from the same set of rods in freespace. The difference is simply due to the fact that wavelength inside the dielectric is different than freespace. Similarly, by placing metallic structures inside a negative permittivity or negative permeability medium, capacitive effects are converted into inductive effects. In the case of the rods embedded in the magnetic plasma, the inductive effects, which are normally relied upon [2], for yield an effective electric plasma medium, are no longer present thus preventing transmission.

In order to overcome this problem, one solution is to remove sections of the corresponding homogeneous plasma in regions near the metallic structure. This solution was motivated by a similar concept suggested by N. Engheta [80] in order to restore the resonant behavior of a SRR embedded in a homogeneous electric plasma medium (see next section). By removing these sections, is will be shown that the structure on average exhibit left-handed behavior; however, the fields near the structures can behave in a variety of other ways.

Since it is unclear from the analysis in [20] how the plasma surrounding the metallic metamaterial in the immediate vicinity of the rods will affect their behavior, various sized areas where the plasma is removed will be considered, as diagrammed in Fig. 3-11. Because the behavior of the vertical, horizontal, and box shaped rods is so similar, only the case of the vertical rods embedded in the plasma medium will be presented, although simulations of all three cases where carried out and noted to have similar results.

Fig. 3-12 shows the transmission results for two different values of d. In each case, a
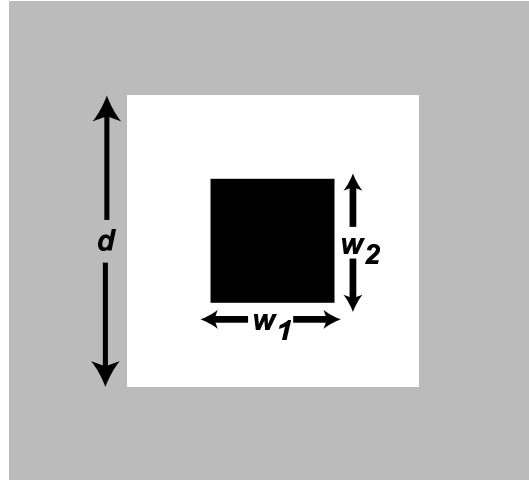
Figure 3-11: Top view of geometry for simulating a periodic collection of metallic rods embedded in a homogeneous magnetic plasma medium. Gray scale area corresponds to plasma, and white area corresponds to freespace.

simulation of the plasma medium alone with gaps was performed in order to ensure that the background plasma medium was still functioning as a high-pass filter, which is seen to be true (note dashed curves). Next, by examining the transmission curve of the rods embedded in the modified background, transmission bands appear near 15.2 GHz for $d = 0.5$ mm and near 13.5 GHz for $d = 1.0$ mm. The fact that the transmission peak in (a) is above the predicted plasma frequency of the rods alone may be partially explained by noting that wavelength of the surrounding medium is smaller than that of freespace. Even in this case where the background medium is known exactly, as discussed in Chapter 1, a transmission band is not conclusive evidence for left-handed behavior, especially since in this situation the plasma frequency of the rods embedded in the medium appears to have shifted from that of the rods in freespace. In order to better characterize the material properties, the fields surrounding the structures need to be analyzed. As reported by Moss *et al* in [81], one method is to examine the slope of points of common phase, or phase-tracking. For example,

(a) Local transmission peak at 15.2 GHz

(b) Local transmission peak at 13.5 GHz
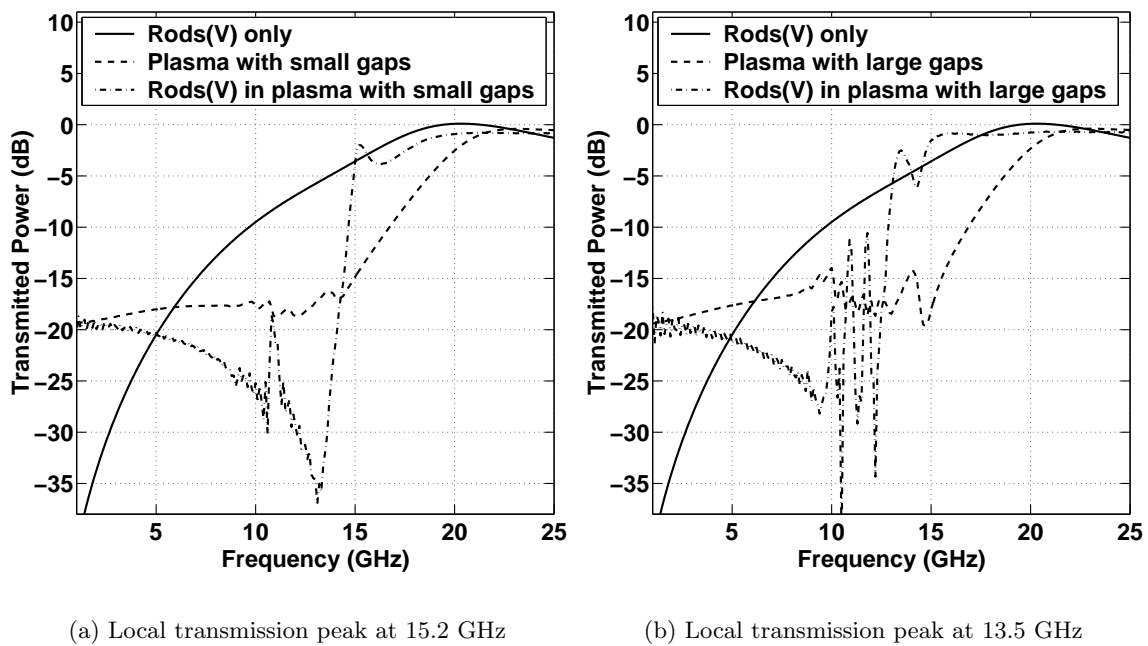
Figure 3-12: Transmission through rods embedded in a background plasma medium with gaps near the rods. In (a), the freespace area is of size 0.5×0.5mm^2, whereas in (b), the area is 1.0×1.0mm^2. In (a) a local transmission peak where the metamaterial could potentially be left-handed occurs at 15.2 GHz, whereas in (b) it occurs at 13.5 GHz.

consider the following space and time dependent wave,

$$E_z = \cos(kx - \omega t) \tag{3.19}$$

where $k = n(\omega)k_o(\omega)$ is the wavenumber of the medium which depends on the index of refraction $n(\omega)$ at frequency ω. For this wave, points of constant phase plotted on a space-time $k_o x$ *vs.* ωt graph will have a slope of n. If the slope of the curve is negative, one can conclude that the wave is traveling through a left-handed media. Based on the previously shown reflection and transmission curves, it is of interest to obtain a space-time plot of the electric field for the 15.2 GHz frequency component, which is shown in Fig. 3-13. In order to observe the most uniform field, the spatial position cut is taken lengthwise along the direction of propagation at a position near the boundary of the unit cell, *i.e.*, between two rows of rods along the $\hat{y}$ direction.

Based on these results and the negative slope of the points of constant phase, it seems that the material is left-handed at these particular frequencies. However, the major assumption in this approach is that there is only one wave inside the medium. In general, and in particular in the case of transmission through a slab in freespace, there are two waves co-existing, a forward and backward propagating wave, such as,

$$E_z = A\cos(kx - \omega t) + B\cos(kx + \omega t) \tag{3.20}$$

where A and B are the coefficients of the forward and backward waves, respectively. In this case, points of constant phase of E_z do not generally correspond to points of constant phase for either the forward nor backward propagating wave component. However, as a general rule of thumb, it can be noted that the sign of the slope of constant phase of the total field corresponds to the sign of the slope of the term with the larger coefficient. For example, if $|A| > |B|$, then observation of a positive slope indicates a positive index of refraction ($n > 0$) and a negative slope indicates that of a LHM. The reverse is true when $|B| > |A|$.
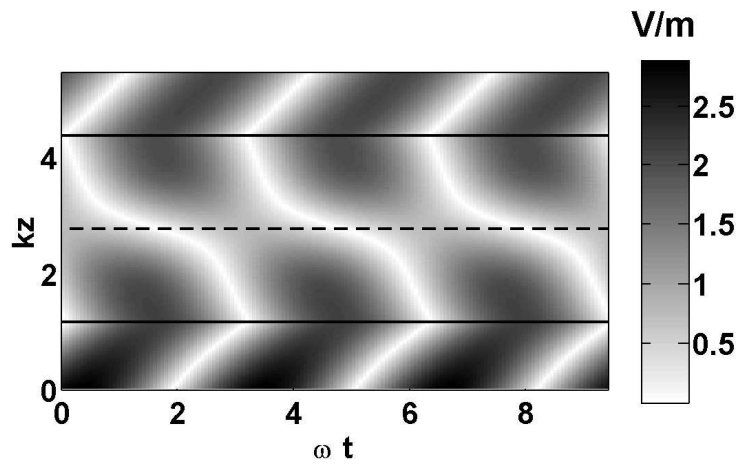
(a) Small gap ($d = 0.5$ mm): at 15.2 GHz
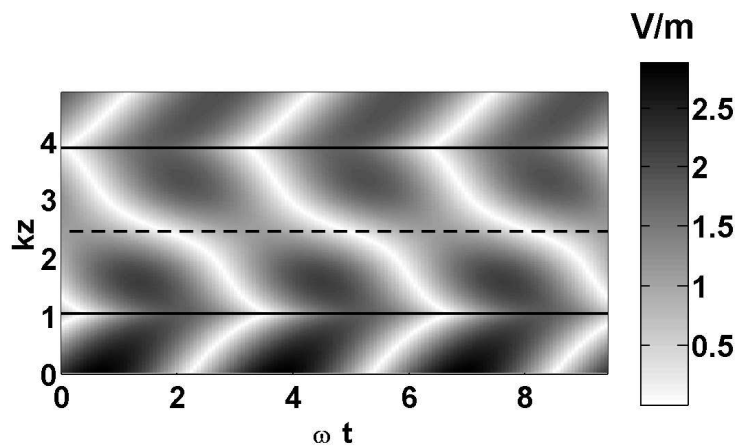
(b) Large gap ($d = 1.0$ mm): at 13.5 GHz

Figure 3-13: Space-time plots of FDTD simulated E-field magnitude of rods embedded in modified plasma background medium. The spatial position shown is a cut taken above the rods near the boundary of the unit cell, *i.e.*, between two rows of rods along the $\hat{y}$ direction.

Note that in cases when $|A| \sim |B|$, the resulting interference pattern does not exhibit phase with a clear slope making a visual inspection more difficult.

Additionally, there is another ambiguity which is that a given solution $A = A_0$, $B = B_0$, and $n = n_0$ yields the same distribution of fields as the solution $A = B_0$, $B = A_0$, and $n = -n_0$. Luckily, however, for a passive media it is always possible to distinguish between solutions by associating the wave inside the medium whose power is propagating in the same direction of the incident wave with the larger of the two coefficients, A and B. In particular, if the the larger coefficient is defined to be A, then if this wave component has a positively propagating phase component, the medium is right-handed, but if this wave component has a negatively propagating phase component, the medium is left-handed.

Using the fields generated by the FDTD simulations, it is possible to extract the coefficients A and B as well as the index of refraction. In order to determine the unknown coefficients and index of refraction, a non-linear least squares curve fitting method is used. Applying this technique to the previously generated FDTD data, the index of refraction within the medium was found to be negative in both the cases of the small gap and the large gap. For comparison Fig. 3-14 shows the corresponding analytically generated space-time plots of the E-field magnitude. As can be seen, the results compare favorably, reproducing not only the slope of the points of constant phase but the interference pattern as well.

So far, the distribution of the fields within and around the vicinity of the metallic components has not been discussed. It must be noted that rods are only expected to behave as an electric plasma medium on average, *i.e.*, the Drude model represents the effective permittivity. Indeed, as shown in Fig. 3-15, the field distribution along the center of the unit cell are distorted with respect to the results of Fig. 3-15. This is due to the presence of the air gap as well as the fields on the metallic rods, for which the electric field is always zero.
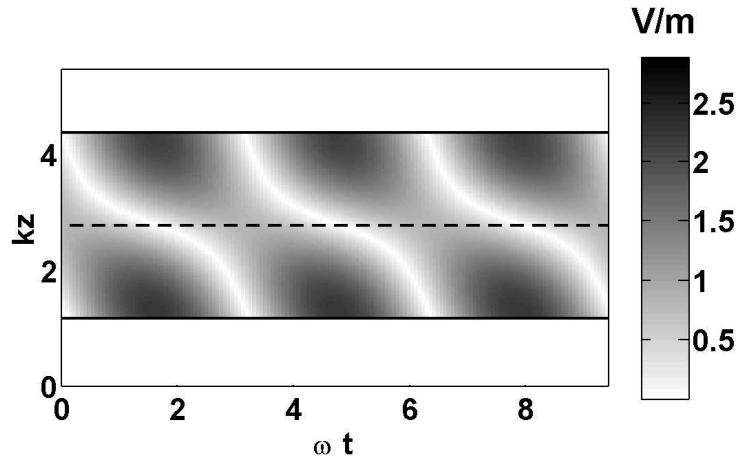
(a) Small gap: $A = 0.63 - i0.14, B = -0.22 - i0.05, n = -1.05 + i0.04$
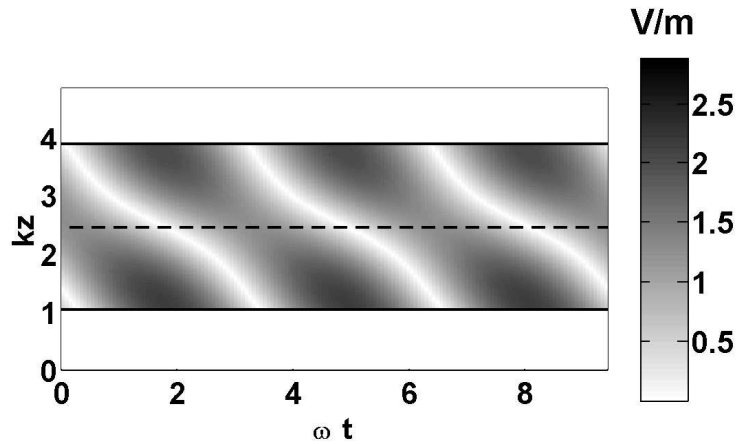
(b) Large gap: $A = 0.71 + i0.01, B = -0.14 - i0.03, n = -1.22 + i0.05$

Figure 3-14: Space-time plots of analytically calculated E-field magnitude of rods embedded in modified plasma background medium. Figure (a) approximately reproduces the Fig. 3-13(a) and figure (b) Fig. 3-13(b). Note, fields only analytically reproduced for the region inside the metamaterial medium.
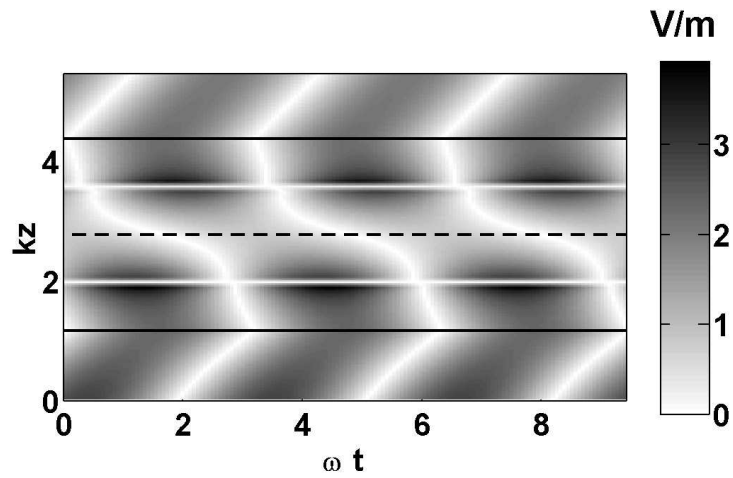
(a) Sgap at 15.2 GHz
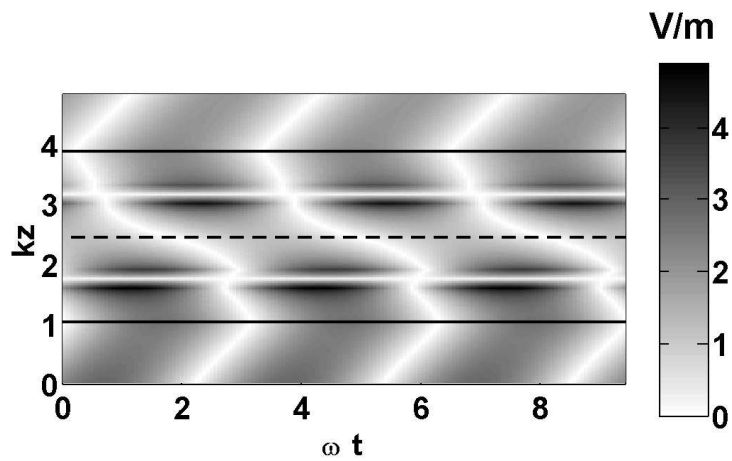
(b) Lgap at 13.5 GHz

Figure 3-15: Space-time plots of FDTD simulated E-field magnitude of rods embedded in modified plasma background medium. The spatial position shown is a cut taken through the center of the unit cell.

Concentric split-rings embedded in an electric plasma

In the next example, a 2-layer structure composed of the concentric SRR will be analyzed. Fig. 3-16 shows the behavior of transmitted power as a function of frequency for the ring embedded in a fully homogeneous electric plasma. For comparison, the first curve shows the expected notch filter behavior of the SRR in freespace which has a resonance around approximately 13 GHz. The second curve shows the transmitted power for a homogeneous electric plasma alone. The plasma follows the Drude model with a plasma frequency of 18 GHz and a damping frequency of 100 MHz. In this curve, it is apparent that the plasma acts as a high-pass filter inhibiting transmission below 18 GHz. Ignoring interaction effects, we might expect a ring structure embedded in the plasma structure to have a transmission band near 13 GHz; however as the third curve shows, this is not true.

As with the rods embedded in the plasma medium, the explanation for this phenomena is do the reversal of the capacitative and inductive effects. As before, in order to observe a transmission band, which could lead to a possible LH band, sections of the plasma are removed as shown in Fig. 3-17. The motivation for removing these section of plasma is to restore the capacitance between the inner and outer ring [80]. With a plasma in-between the rings rather than a normal dielectric, the capacitative effect becomes an inductive effect. Because in geometries A and B there is no plasma in the regions where the capacitance would be the largest, it is expected to yield larger transmissions, whereas this is less likely for geometry C.

In order to ensure that any transmission band observed is due to the presence of the rings and plasma and not just a reduced area of plasma, the plasma with freespace gaps is also simulated. Fig. 3-18 shows the transmission results for each of the three different cases with and without the SRR structure. The transmission through SRRs in freespace are also included for comparison. In geometry A, a transmission band near 16.3 GHz appears, a frequency below the plasma frequency of the background medium, which without the rings has a significantly lower transmission value. A similar type of transmission band

Figure 3-16: Transmitted power for a 2-cell structure consisting of the rings alone (solid), a homogeneous electric plasma ($f_{ep} = 18$ GHz) only (dashed), and the rings embedded in the homogeneous electric plasma (dashed-dotted)

appears in the results for geometry B; however, in this case the transmission band is near to 15.3 GHz, closer to the resonance of the ring predicted by theory. In case C, the results show no transmission band, which is an indication that the rings are no longer behaving in the typical resonant fashion. as they would in a freespace environment. In order to verify left-handed behavior in geometries A and B, space-time plots are used. Fig. 3-19 and Fig. 3-20 show the corresponding plots for cuts taken along the direction of propagation at the boundary and at the center of the unit cell, respectively. In addition, for the data near the boundary, the index of refraction retrieval method described previously is used to show that the indices of refraction are indeed negative. The values are listed in the caption of Fig. 3-19. Note, in the case of the cut along the center of the cell, the presence of the rings

(a) Geometry A

(b) Geometry B

(c) Geometry C
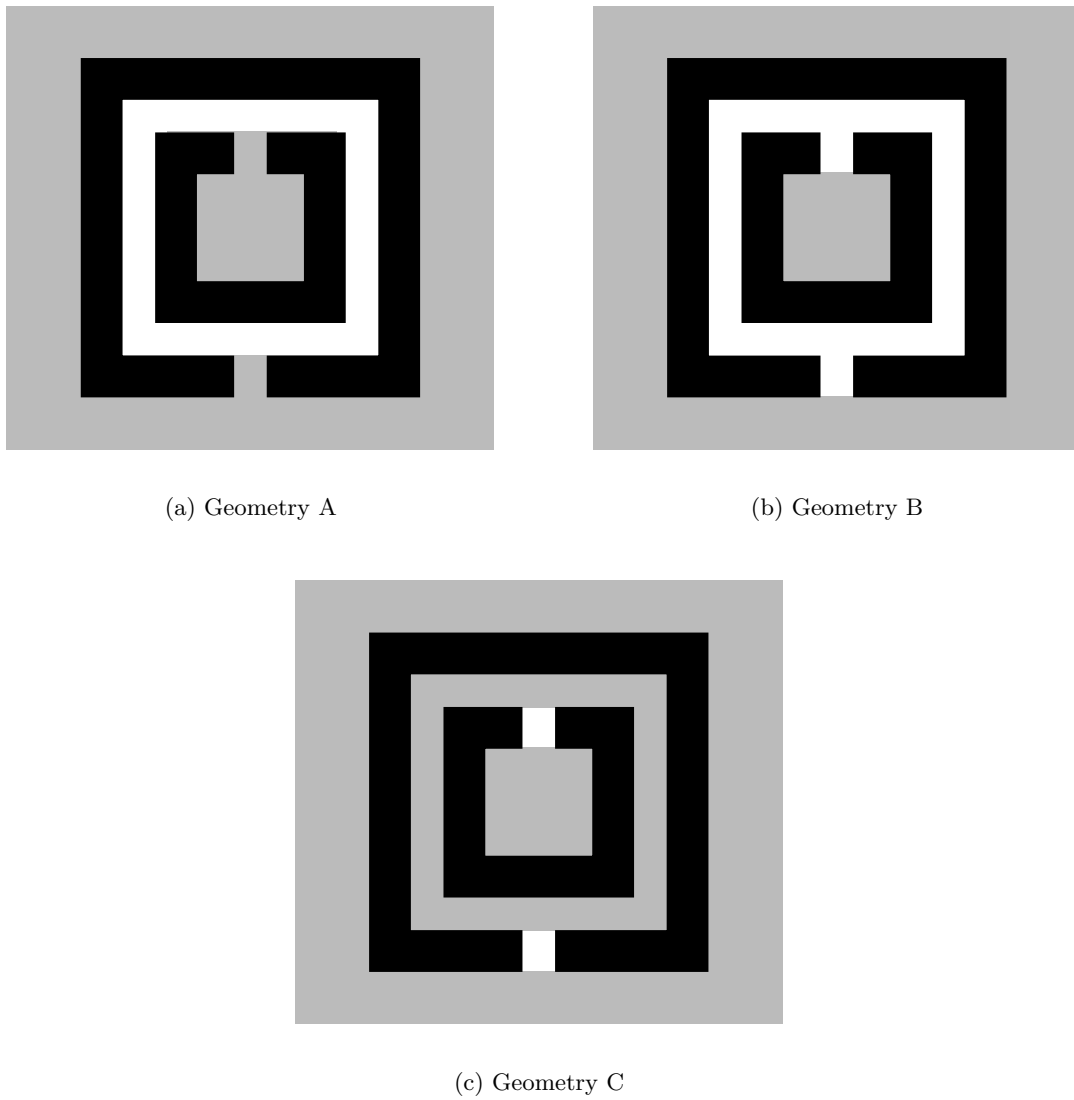
Figure 3-17: Geometries *A-C* show varying levels of surrounding plasma removed for the concentric ring design. Gray scale areas represents regions of homogeneous electric plasma, whereas black represents metal, and white indicates freespace.

strongly distorts the field. In particular, due to the resonance, the fields are relatively large at the center of the cells when compared to the fields near the boundary of the unit cell.
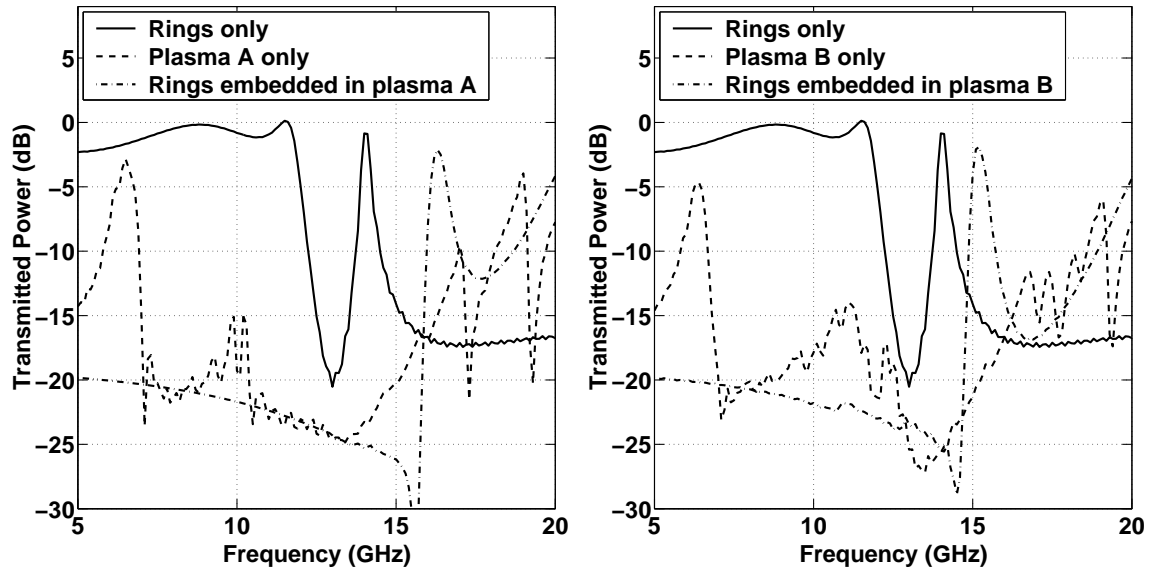
(a) Geometry A

(b) Geometry B
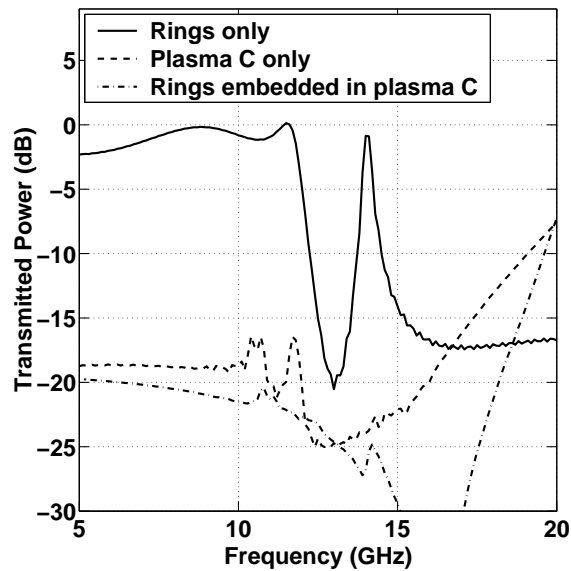
(c) Geometry C

Figure 3-18: Transmission through a 2-layer concentric ring design embedded in a plasma corresponding to the configurations shown above in geometries *A-C*. In cases A and B, there is a transmission band near the resonance frequency of the ring, which indicates a possible LH band.
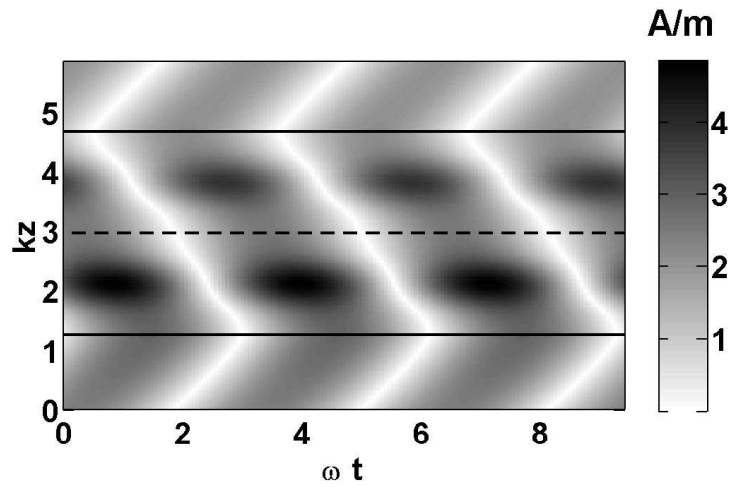
(a) Geometry A at 16.3 GHz
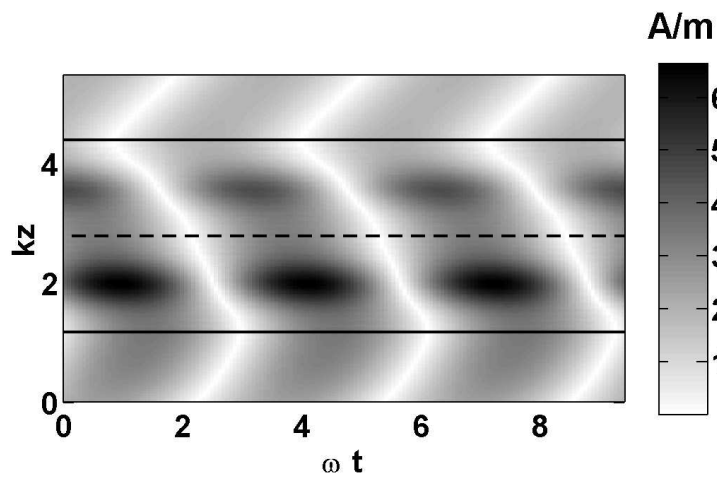
(b) Geometry B at 15.3 GHz

Figure 3-19: Space-time plots of FDTD simulated H-field magnitude of SRRs embedded in modified plasma background medium. The spatial position shown is a cut taken at the boundary of the unit cell, along the $\hat{y}$ direction. Retrieved parameters are: (a) $A = 1.11 - \mathrm{i}0.87, B = -0.04 + \mathrm{i}0.06, n = -0.77 + \mathrm{i}0.05$ (b) $A = 1.33 - \mathrm{i}1.01, B = -0.19 + \mathrm{i}0.22, n = -0.76 + \mathrm{i}0.05$
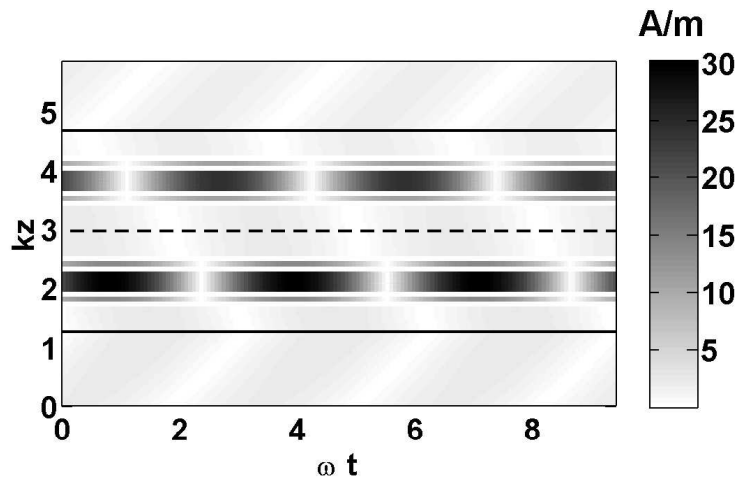
(a) Geometry A at 16.3 GHz
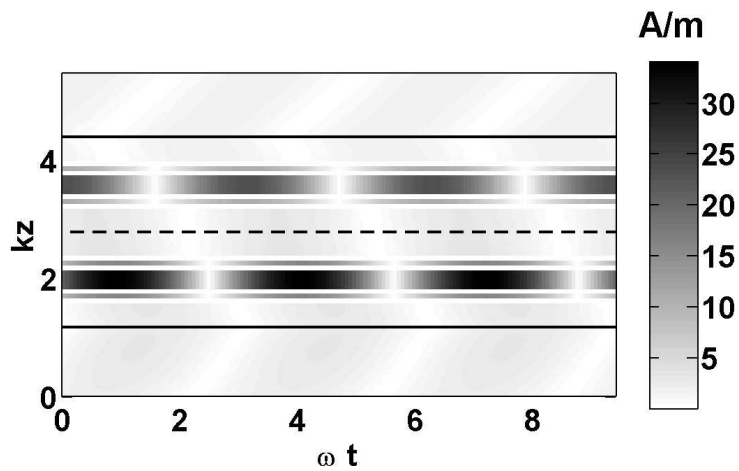
(b) Geometry B at 15.3 GHz

Figure 3-20: Space-time plots of FDTD simulated H-field magnitude of SRRs embedded in modified plasma background medium. The spatial position shown is a cut taken through the center of the unit cell along the $\hat{y}$ direction.

Adjacent split-rings embedded in an electric plasma

The final geometry to be investigated using the hybrid approach of embedding the metallic structure in a plasma medium is the adjacent split-ring design. As was done in the previous two cases, propagation through a 2-layer geometry is simulated using the periodic 2D FDTD method. The background medium again is a homogeneous electric plasma implemented using the Drude model with a plasma frequency of 18 GHz, and a damping frequency of 100 MHz. Fig. 3-21 shows the results for the rings with and without the plasma as well as the plasma, where it can been seen that as in the case of the concentric ring design that no transmission bands are observed below the plasma frequency of the background medium. Again, the capacitive effects normally needed for generating the resonance response of the rings is not present due to the plasma in the spacing between the two rings. As in the previous two examples, in order to restore the capacitive effects and possibly observe a left-handed transmission bands, various sections of plasma from the unit cell were removed as shown in Fig. 3-22.

Based on the previous results, one might expect for geometry A to fail because the displacement current is only allowed to flow through the gaps, meaning current is confined to within one ring. Indeed, as shown in Fig. 3-23(a), no transmission band is observed below the plasma frequency. In order for current to flow between the two rings, a positive material needs to be inserted in the vertical spacing between the rings as in geometry B. As shown in Fig. 3-23(b), a possible LHM transmission band appears near 14 GHz. However, the passband is still below -5 dB, whereas the results for transmission through geometry C, shown in Fig. 3-23(c), shows a more obvious transmission band at approximately 12.5 GHz. In the final plot, Fig. 3-23(d), the results for geometry D are shown where it is evident that there is significant transmission in the presence of the modified background plasma alone without the rings present, making it impossible to draw any conclusion on the behavior of the rings for this case.

In order to verify left-handed behavior in geometries B and C, space-time plots are again
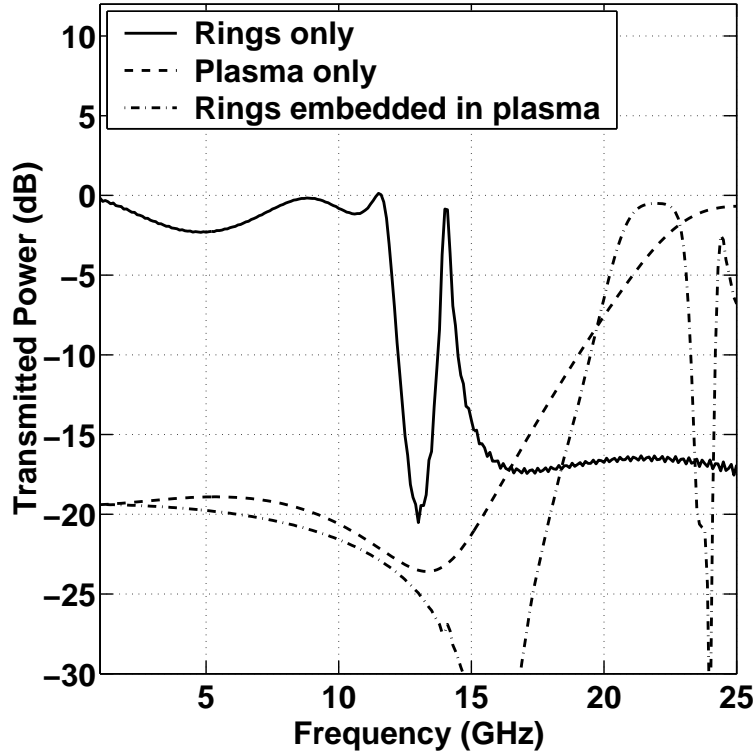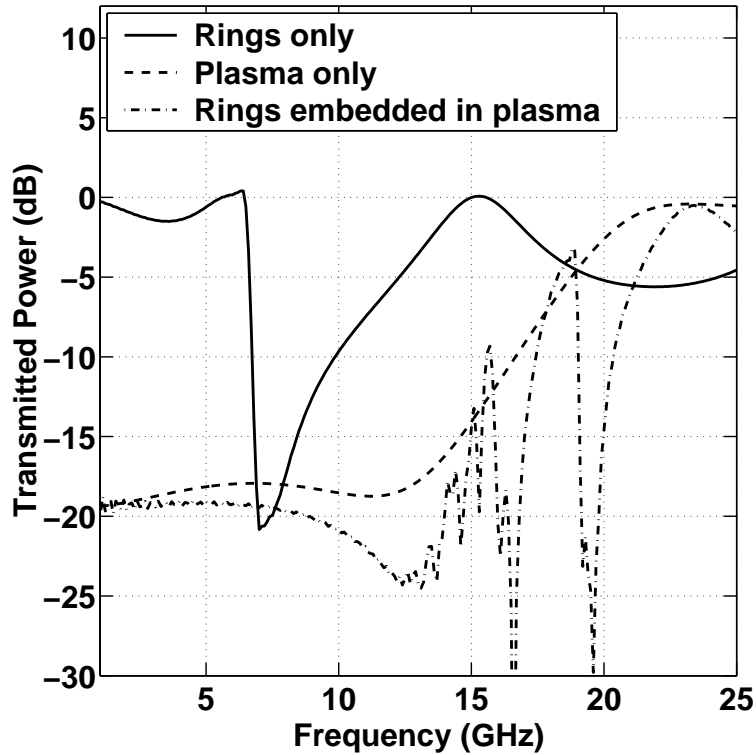
Figure 3-21: Transmitted power for a 2 cell structure consisting of the rings alone (solid), a homogeneous electric plasma ($f_{ep} = 18$ GHz) only (dashed), and the rings embedded in the homogeneous electric plasma (dashed-dotted)

used. Fig. 3-24 and Fig. 3-25 show the corresponding plots for cuts taken along the direction of propagation at the boundary and at the center of the unit cell, respectively. For the data near the boundary, the index of refraction retrieval method is used to show that the indices of refraction are indeed negative. The values are listed in the caption of Fig. 3-24. Note, in the case of the cut along the center of the cell, the presence of the rings strongly distorts the field. In particular, due to the resonance, the fields are relatively large at the center of the cells when compared to the fields near the boundary of the unit cell. In contrast to the concentric ring design, the fields along the center of the cell are large throughout the majority of the propagation direction. This is simply due to the large fractional area occupied by the adjacent rings, *i.e.*, the fields are large when inside the rings.

(a) Geometry A

(b) Geometry B

(c) Geometry C

(d) Geometry D
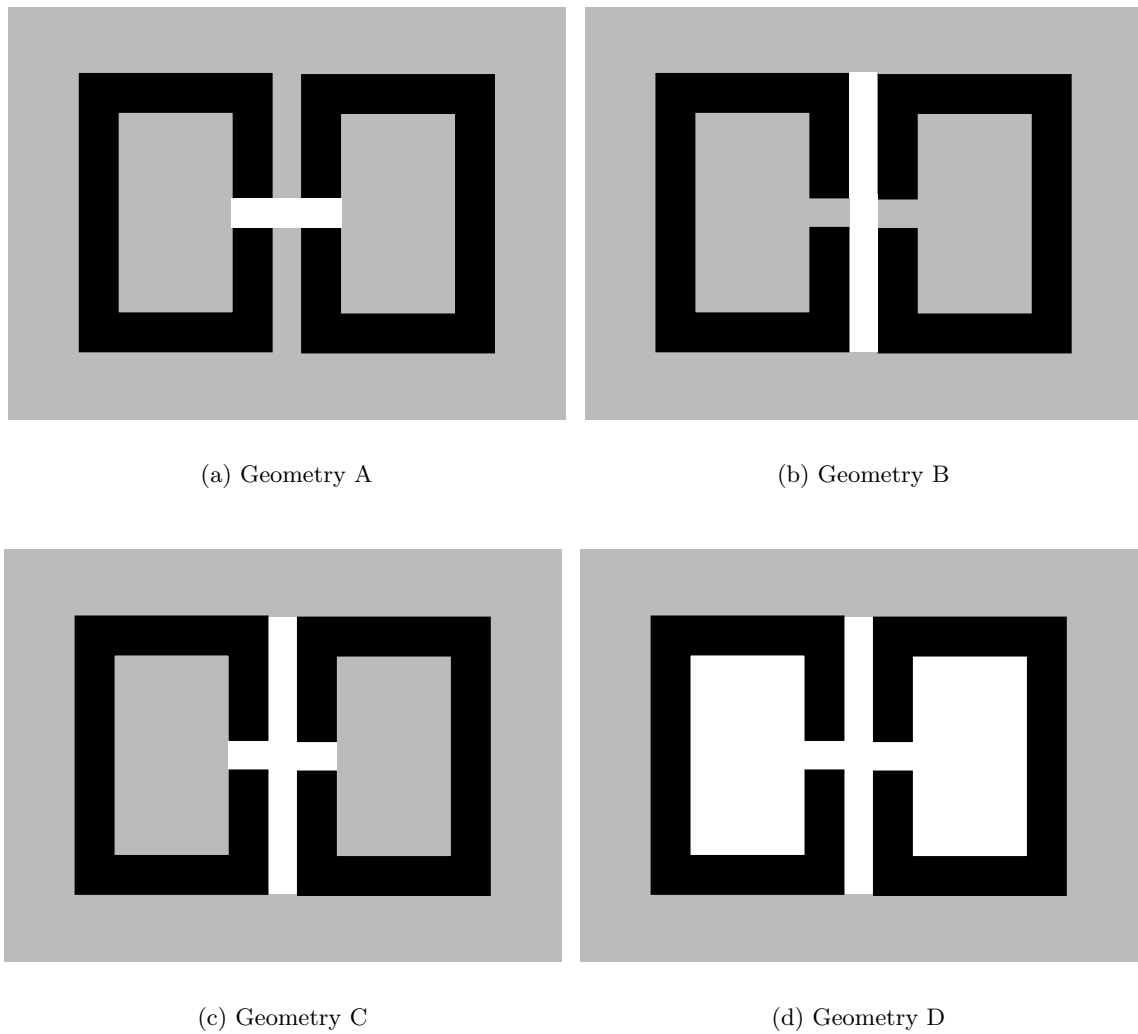
Figure 3-22: Geometries *A-D* show varying levels of plasma removed for the adjacent ring design. The color gray represents regions of homogeneous electric plasma, whereas black represents metal, and white indicates freespace.

(a) Geometry A

(b) Geometry B

(c) Geometry C
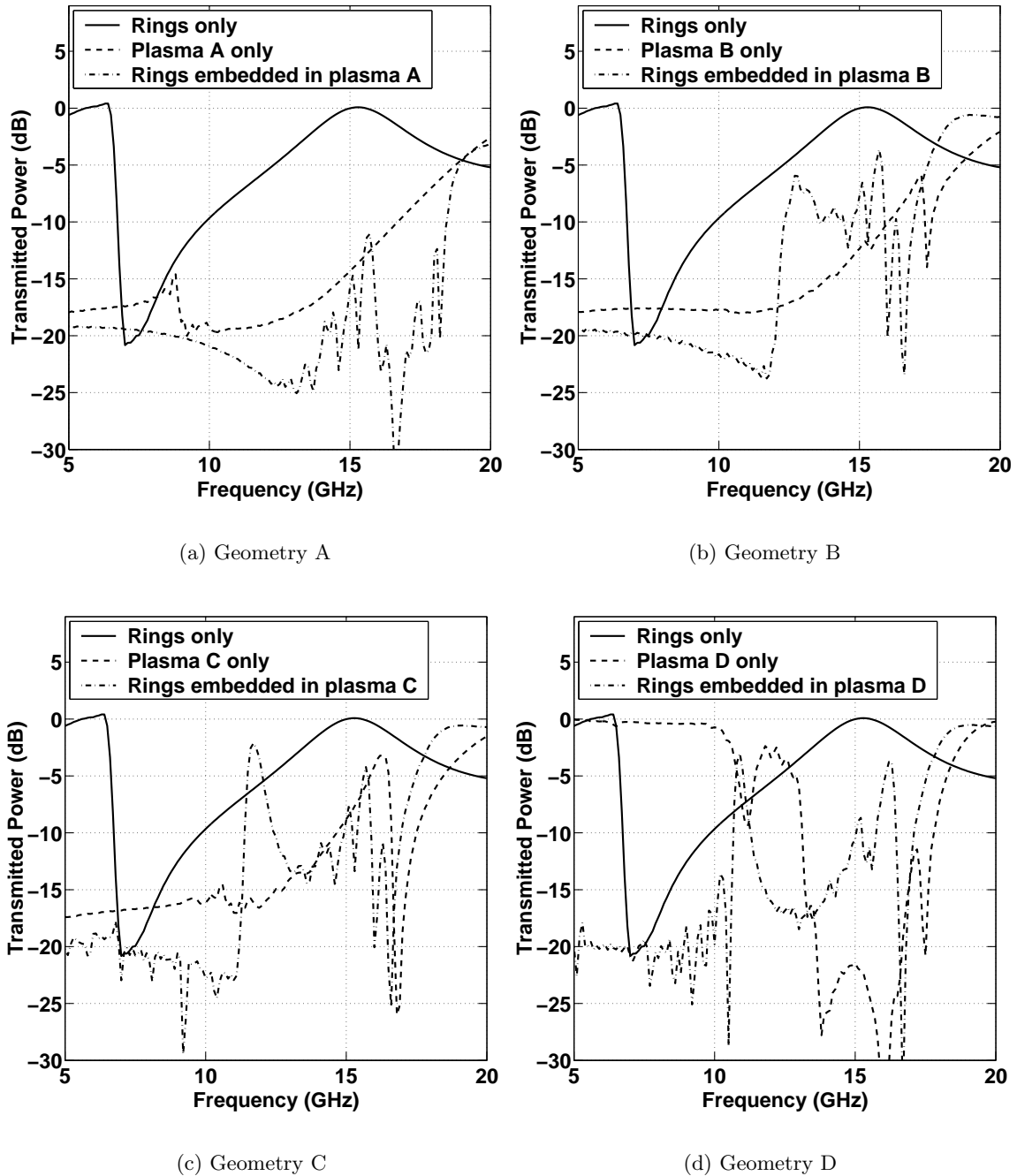
(d) Geometry D

Figure 3-23: Transmission for adjacent split-rings embedded in homogeneous electric plasma medium with various shaped gaps (geometries $A - D$ from Fig. 3-22).
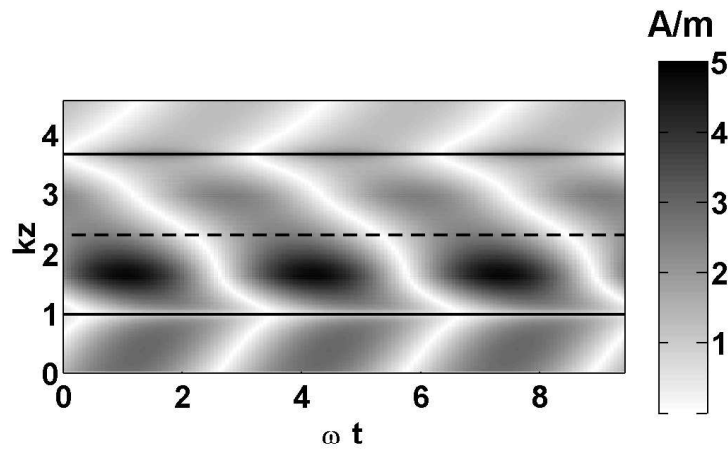
(a) Geometry B at 12.7 GHz
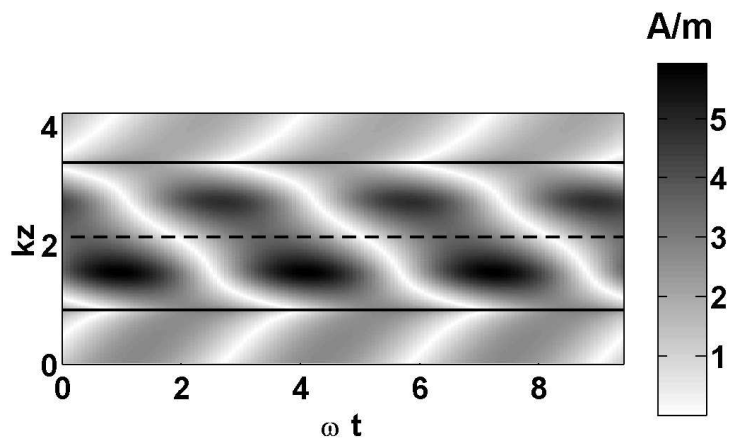
(b) Geometry C at 11.7 GHz

Figure 3-24: Space-time plots of FDTD simulated H-field magnitude of SRRs embedded in modified plasma background medium. The spatial position shown is a cut taken at the boundary of the unit cell, along the $\hat{y}$ direction. Retrieved parameters are: (geom b) $A = 1.23 - i0.01, B = -0.07 + i0.24, n = -1.22 + i0.06$ (geom c) $A = 1.71 + i0.07, B = 0.14 + i0.14, n = -1.40 + i0.06$.
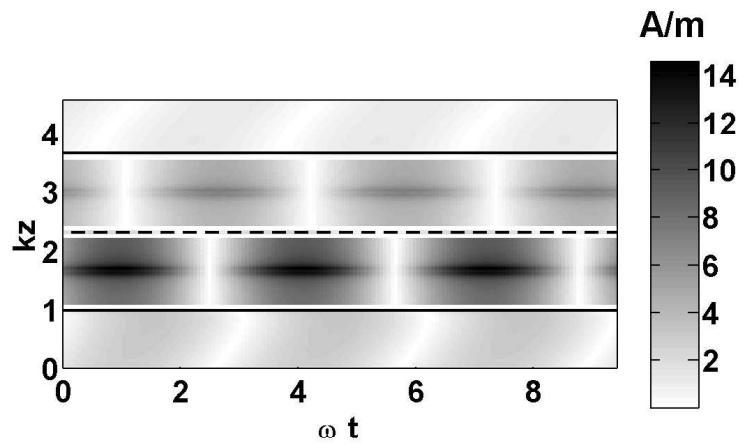
(a) Geometry B at 12.7 GHz
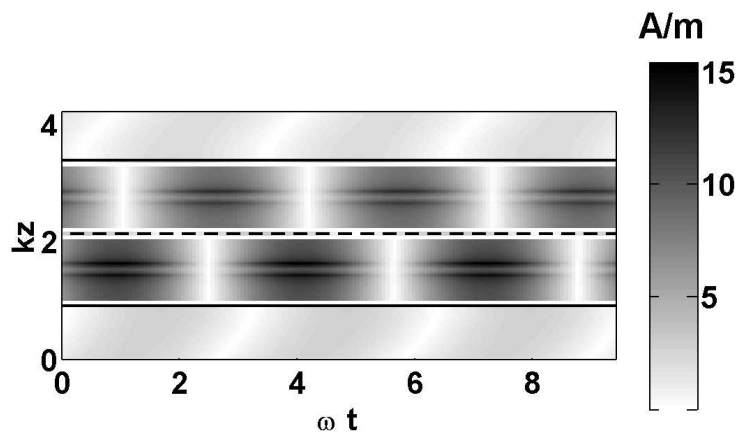
(b) Geometry C at 11.7 GHz

Figure 3-25: Space-time plots of FDTD simulated *H*-field magnitude of SRRs embedded in modified plasma background medium. The spatial position shown is a cut taken through the center of the unit cell along the $\hat{y}$ direction.

3.4 Retrieval of effective permittivity and permeability from S-parameters

Still, the above methods do not give the exact values of the permittivity and permeability. They merely give an estimate of the operating frequencies. In order to better characterize the metamaterial, one method that has been used is to calculate the average field values inside the metamaterial [16]. A similar method based on tracking the phase has also be used to characterize the index of refraction of a metamaterial [81]. Both of these methods rely on knowledge of the electromagnetic field distribution inside the metamaterial, and thus are most easily implemented using full-wave numerical simulations. The disadvantage of the methods is that they cannot easily be implemented in an experimental setup. On the other hand, S-parameter data, which can be used for permittivity and permeability extraction, can be readily determined both experimentally and numerically.

Furthermore, being able to more precisely characterize a metamaterial in terms of its bulk material properties is useful since in most cases it is computationally intensive, or completely unfeasible to model a large collection of SRR/rod unit cells, which would typically be required in application of the metamaterials. Knowledge of the effective permittivity and permeability would allow for devices that use LH media to be designed more easily such as with the two applications considered in this thesis.

Various methods to retrieve the permittivity and permeability using complex valued reflection (S_{11}) and transmission (S_{21}) coefficients have been developed. One of these methods is to parametrically fit the S-parameter measurement data to known permittivity and permeability models. For the case of rod/SRR metamaterials, Shelby *et al* used this approach to extract effective permittivities and permeabilities using the Drude and Lorentz models, respectively, [4, 15]. However, because the parametric fitting method makes explicit assumptions about the form of the permittivity and permeability, methods that directly retrieve the permittivity and permeability have also been applied to the case of rod/SRR metamaterials [76].

In this section, the direct retrieval of the index of refraction and impedance from numerically generated S-parameter data will be used to characterized two typical left-handed metamaterials. In order to apply the retrieval method, the geometries must be of infinite extent in the two directions perpendicular to the direction of propagation. Such geometries can be modeled numerically by using periodic boundary conditions, as implemented in the FDTD and MoM techniques used in this work. Experimentally, these types of geometries can be realized by surrounding the a finite sized slab with microwave absorbing material or by using a single-mode waveguide configuration.

3.4.1 Formulation

The retrieval method used in this work is based on the approach used by Smith *et al* in [76]. The formulation begins by deriving the reflection and transmission coefficients for a planar slab geometry. Here it is assumed that the incident wave is TE polarized with a propagation factor of the form, e^{ikz}, *i.e.*, normal incidence. Under this form, the fields in the three regions take the form,

$$E_{0x} = e^{ik_0 z} + Re^{-ik_0 z} \tag{3.21}$$

$$H_{0y} = \frac{k_0}{\omega \mu_0} \left[e^{ik_0 z} - Re^{-ik_0 z} \right] \tag{3.22}$$

$$E_{1x} = Ae^{ik_1 z} + Be^{-ik_1 z} \tag{3.23}$$

$$H_{1y} = \frac{k_1}{\omega \mu_1} \left[e^{ik_1 z} - Re^{-ik_1 z} \right] \tag{3.24}$$

$$E_{2x} = Te^{ik_0 z} \tag{3.25}$$

$$H_{2y} = T\frac{k_0}{\omega \mu_0} e^{ik_0 z} \tag{3.26}$$

where it assumed that the material parameters of the incident and transmission region are both given by ϵ_0 and μ_0 whereas the slab is characterized by ϵ_1 and μ_1. Letting the slab boundaries be at $z = 0$ and $z = d$, and employing the boundary conditions yields the following equations,

$$1 + R = A + B \tag{3.27}$$

$$1 - R = \eta_n(A - B) \tag{3.28}$$

$$Ae^{ink_0d} + Be^{-ink_0d} = Te^{ik_0d} \tag{3.29}$$

$$Ae^{ink_0d} - Be^{-ink_0d} = \frac{1}{\eta_n}Te^{ik_0d} \tag{3.30}$$

where the normalized impedance is defined as,

$$\eta_n = \frac{\eta_1}{\eta_0} = \sqrt{\frac{\epsilon_0\mu_1}{\epsilon_1\mu_0}} \tag{3.31}$$

and the index of refraction of the slab is defined as,

$$n = \frac{\sqrt{\epsilon_1\mu_1}}{\sqrt{\epsilon_0\mu_0}}. \tag{3.32}$$

Elimination of the A and B coefficients leads to the following equations for R and T,

$$2R = \left[\frac{1}{2}(1 - \eta_n)\left(1 + \frac{1}{\eta_n}\right)e^{ink_0d} + \frac{1}{2}(1 + \eta_n)\left(1 - \frac{1}{\eta_n}\right)e^{-ink_0d}\right]Te^{ik_0d} \tag{3.33}$$

$$2 = \left[\frac{1}{2}(1 + \eta_n)\left(1 + \frac{1}{\eta_n}\right)e^{ink_0d} + \frac{1}{2}(1 - \eta_n)\left(1 - \frac{1}{\eta_n}\right)e^{-ink_0d}\right]Te^{ik_0d}. \tag{3.34}$$

Finally, solving for R and T yields the following,

$$\frac{1}{S_{21}} = \left[\cos(nk_0d) - \frac{i}{2}\left(\eta_n + \frac{1}{\eta_n}\right)\sin(nk_0d)\right] \tag{3.35a}$$

$$\frac{S_{11}}{S_{21}} = -\frac{i}{2}\left(\eta_n - \frac{1}{\eta_n}\right)\sin(nk_0d) \tag{3.35b}$$

where the S-parameters are defined in terms of the reflection and transmission coefficients as,

$$S_{11} = R \tag{3.36}$$

$$S_{21} = Te^{ik_0d} \tag{3.37}$$

In the retrieval process employed in this section, the material parameters of the medium are obtained by inverting (3.35) in terms of S_{11} and S_{21} as follows,

$$\eta_n = \pm\sqrt{\frac{(1+S_{11})^2 - S_{21}^2}{(1-S_{11})^2 - S_{21}^2}} \tag{3.38}$$

$$\text{Im}(n) = \pm\text{Im}\left(\frac{\cos^{-1}\left(\frac{1}{2S_{21}}[1-(S_{11}^2 - S_{21}^2)]\right)}{k_0d}\right) \tag{3.39a}$$

$$\text{Re}(n) = \pm\text{Re}\left(\frac{\cos^{-1}\left(\frac{1}{2S_{21}}[1-(S_{11}^2 - S_{21}^2)]\right)}{k_0d}\right) + \frac{2\pi m}{k_0d}, \tag{3.39b}$$

where m is a unknown integer corresponding to the number of cycles a wave goes through in the slab. Note that in the above formulation it was assumed that the S-parameters are defined based on an incident wave that has a positively propagating wavefront. If the S-parameters are obtained from an incident wave that has a negatively propagating wavefront, the above formulation can be used under the transformation,

$$R_+ = R_- e^{i2k_0d} \tag{3.40}$$

$$T_+ = T_- \tag{3.41}$$

where $R_\pm$ and $T_\pm$ represent the forward and backward propagating reflection and transmission coefficients, respectively. Once the impedance and index of refraction have been

retrieved, the relative permittivity and permeability of the slab can be directly calculated by $\epsilon_{1r} = n/\eta_n$ and $\mu_{1r} = n\eta_n$.

One of the difficulties in extracting the index of refraction using (3.39) is determining the correct value of m to use. The integer variable m roughly corresponds to the thickness of the slab in terms of wavelengths. The problem is of course that the wavelength is not known ahead of time, making m an additional unknown variable. An even more difficult problem is that for frequencies near the resonance, the effective wavelength becomes much smaller than the dimensions of the metamaterial, which is inconsistent with the effective medium concept. For this reason, extraction results near the resonant frequency can not be fully trusted. Luckily, left-handed behavior occurs just beyond this frequency where the effective wavelengths retrieved are more consistent with the effective medium concept.

In order to determine the correct branch, m, to chose, many methods have been employed by various authors [76, 82, 83]. One commonality of these approaches is that one assumes that $m = 0$ for the lowest frequency of interest. This assumption generally holds true assuming the thickness of the slab is very small, typically on the order of one unit cell. The subsequent values of m are then chosen such that difference between the real part of the index of refraction at one frequency and the next is minimized. However, as expected and as will be shown in detail in following subsection, in regions of high variation (*e.g.,* near resonances), this approach is not always successful. Yet, another method for determining the value of m is to use S-parameter data for slabs of different thicknesses. The method makes use of the fact that while each slab thickness will have its own corresponding value of m, the index of refraction retrieved for each case should be the same. Combining the data from the different slab lengths allows the ambiguity to be removed to some extent.

3.4.2   Validation and effects of noise on retrieval method

In order to validate the method outlined above, a simple analytic case is considered. Using the Drude model for the permittivity and the Lorentz model for the permeability, the S-parameters are analytically calculated. The method described above is then used to attempt

to retrieve the original values of ϵ and μ. Fig. 3-26 shows an example of successfully retrieved material parameters.

Despite the success with the simple this example, it is possible for the retrieval method to fail. In particular, depending on the sampling rate of the S-parameters, it is possible that the incorrect branch, m, is chosen. Table 3.1 shows the effect of the sampling rate on the ability to correctly retrieve ϵ and μ when μ takes follows the Lorentz model as listed in (3.2). Using the Lorentz model for the permeability, the S-parameters were analytically calculated over the frequency band 5 GHz to 20 GHz using various sampling rates for a slab that is 5 mm thick. As can be seen in the table, in general for successful retrieval, the sampling rate needs to be on the order of the damping frequency. However, the sampling rate also depends on the separation between the resonant and plasma frequencies of the permeability.

Another difficultly in correctly retrieving the permittivity and permeability is the sensitivity of the algorithm. As discussed in reference [84], it is difficult to extract the index of refraction at frequencies where the S_{11} parameter is nearly zero. This is due to the fact that the impedance, η varies rapidly at these frequencies and thus a slight distortion or presence of noise in the S-parameters can lead to inaccurate results. To illustrate this effect, two types of distortion are considered. The first is an additive Gaussian white noise, while the second is a 5-element low pass filter. Fig. 3-27 shows the original and noisy S-parameters for the first type of distortion. As can be seen, the noise distorts the retrieved material parameters, but does not destroy the general trends. However, it was empirically determined that if the variance of the noise is greater than 0.02 that the retrieval method would tend to fail because of the difficultly in accurately tracking the value of m. The second type of distortion illustrated in Fig. 3-28 gives an example of S-parameters that have been low-pass filtered. Note that, although the S-parameters "appear" noise-free, the small amount of distortion near the nulls inhibits the ability to correctly retrieve the S-parameters. In particular, the method is most sensitive to the distortion occurring at the resonant frequency of the permeability where the impedance is very large. As seen in Fig. 3-28(b), this distortion creates an

(a) Index of refraction

(b) Impedance

(c) Permittivity
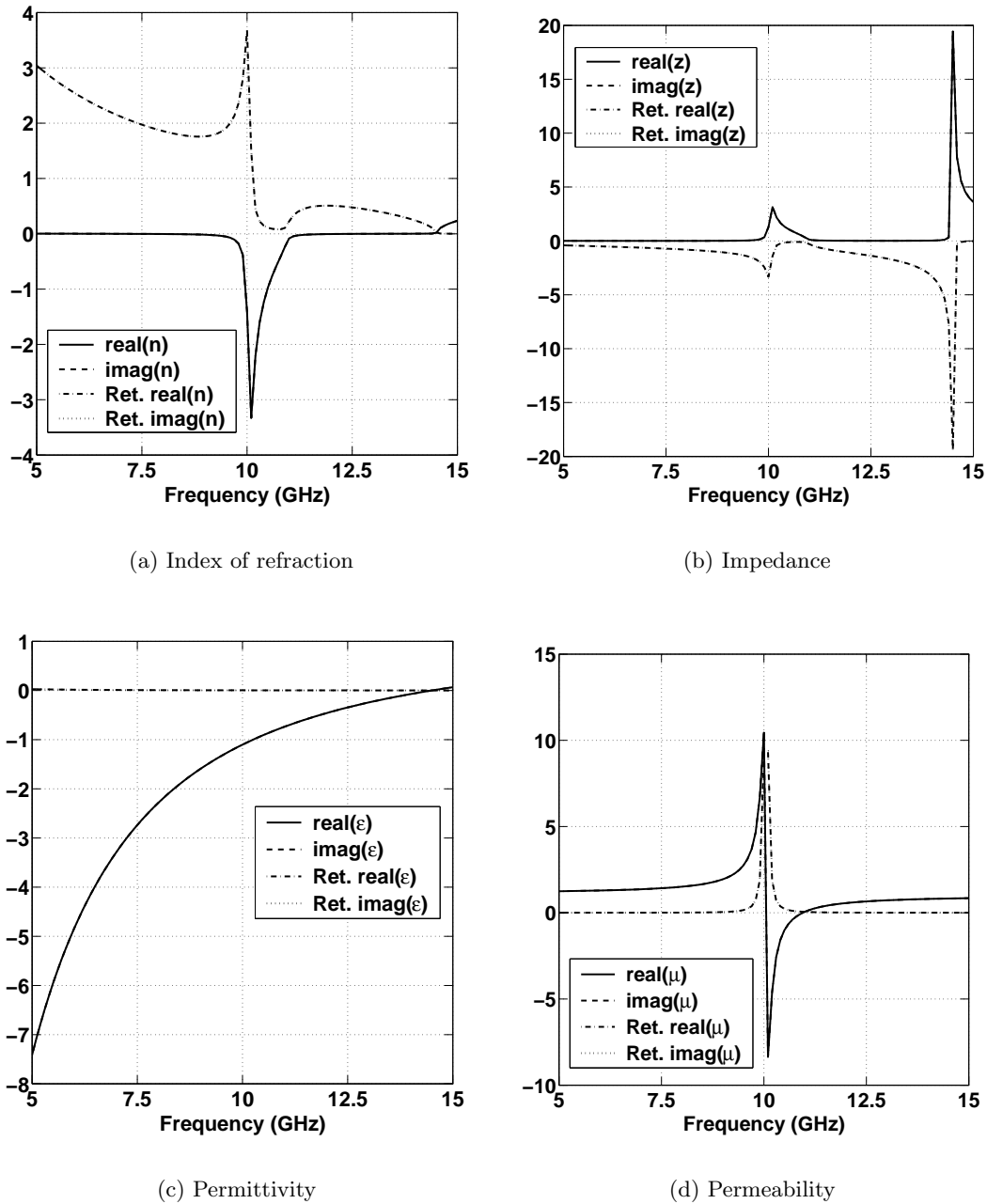
(d) Permeability

Figure 3-26: Retrieved material parameters from analytically calculated S-parameters, which were calculated for a slab that is 5 mm thick with a permittivity that follows the Drude model and a permeability that follows the Lorentz model. $f_{ep} = 14.5$ GHz, $\gamma_e = 100 MHz$, $f_{mo} = 10.05$ GHz, $f_{mp} = 10.95$ GHz, $\gamma_m = 100 MHz$.

	Frequency sampling rate				
μ **Resonant characteristics** ($f_0 = 10$ GHz)	500 MHz	250 MHz	100 MHz	50 MHz	10 MHz
$\gamma = 50$ MHz, $f_p = 10.5$ GHz	×	×	×	✓	✓
$\gamma = 50$ MHz, $f_p = 11.0$ GHz	×	×	×	×	✓
$\gamma = 50$ MHz, $f_p = 12.0$ GHz	×	×	×	×	✓
$\gamma = 100$ MHz, $f_p = 10.5$ GHz	✓	✓	✓	✓	✓
$\gamma = 100$ MHz, $f_p = 11.0$ GHz	×	×	✓	✓	✓
$\gamma = 100$ MHz, $f_p = 12.0$ GHz	×	×	×	✓	✓
$\gamma = 200$ MHz, $f_p = 10.5$ GHz	✓	✓	✓	✓	✓
$\gamma = 200$ MHz, $f_p = 11.0$ GHz	✓	✓	✓	✓	✓
$\gamma = 200$ MHz, $f_p = 12.0$ GHz	✓	✓	✓	✓	✓

Table 3.1: Effect of sampling rate on the ability to correctly retrieve ϵ of μ when μ takes a resonant form. Using the Lorentz model for the permeability, S-parameters were analytically calculated and sampled from 5 GHz to 20 GHz. Check-marks (✓) indicate cases when the retrieval method was successful in automatically recovering the correct values of ϵ and μ. X-marks indicate regions where the branch cuts (m) determined were incorrect. The results shown are similar whether the permittivity is constant or follows the Drude model with a plasma frequency higher than the plasma frequency of the permeability.

artificial anti-resonance in the permittivity. Although this effect is relatively small in this example, in the examples using the S-parameters of numerically simulated metamaterials, this type of effect has been observed to be stronger. Because there has been some question as to whether observation of this anti-resonance effect implies anything extraordinary or unique about the bulk-material properties of these metamaterials, it is important to keep in mind the sensitivity of the method.
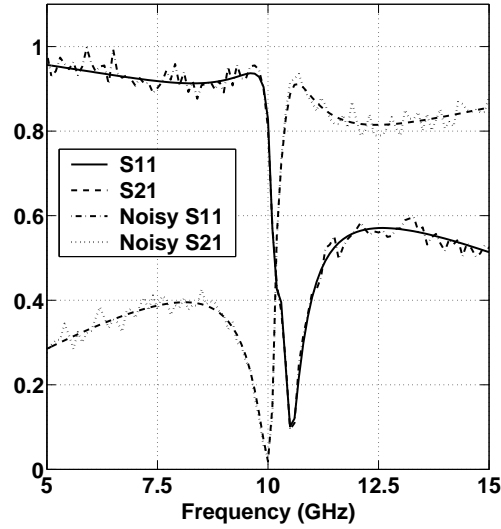
(a) Index of refraction
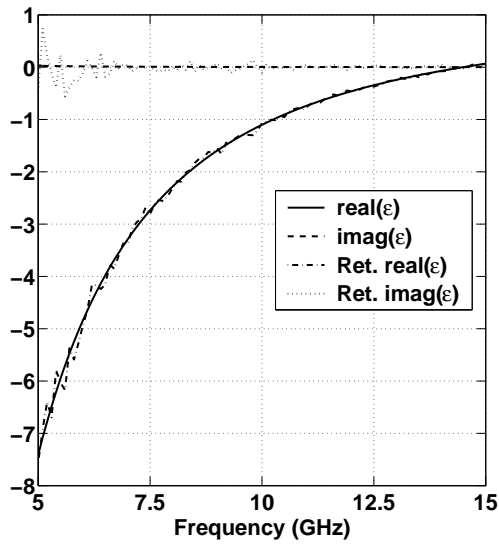
(b) Permittivity
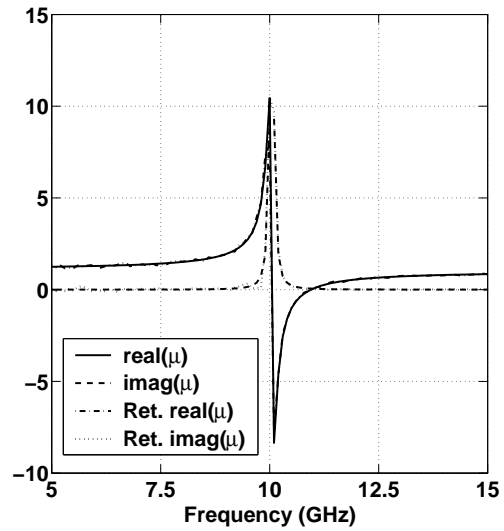
(c) Permeability

Figure 3-27: Retrieved material parameters from analytically calculated S-parameters that were distorted by the presence of zero-mean complex Gaussian white noise with a variance of 0.02. *S*-parameters calculated for a slab that is 5 mm thick with a permittivity that follows the Drude model and a permeability that follows the Lorentz model. $f_{ep} = 14.5$ GHz, $\gamma_e = 100$ MHz, $f_{mo} = 10.05$ GHz, $f_{mp} = 10.95$ GHz, $\gamma_m = 100$ MHz.
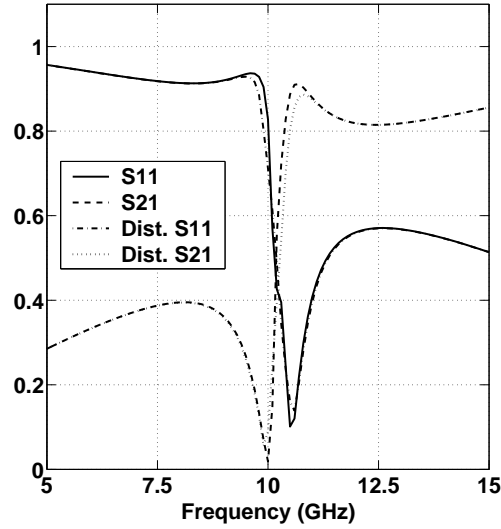
(a) Index of refraction
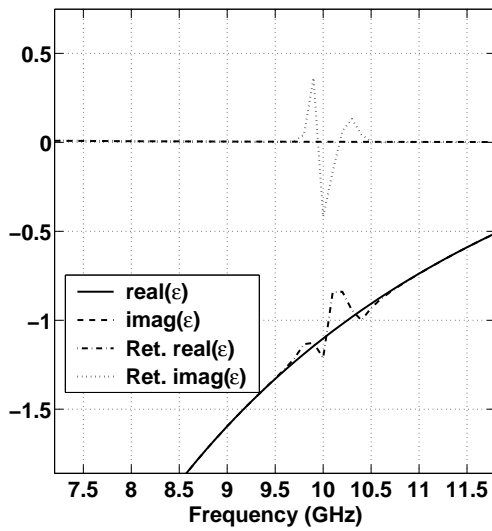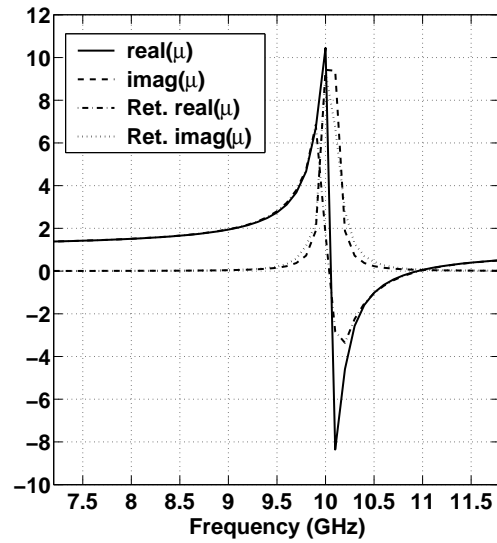
(b) Permittivity

(c) Permeability

Figure 3-28: Retrieved material parameters from analytically calculated S-parameters that were distorted by applying a 5-element low pass filter. S-parameters calculated for a slab that is 5 mm thick with a permittivity that follows the Drude model and a permeability that follows the Lorentz model. $f_{ep} = 14.5$ GHz, $\gamma_e = 100$ MHz, $f_{mo} = 10.05$ GHz, $f_{mp} = 10.95$ GHz, $\gamma_m = 100$ MHz.

3.4.3 Retrieval using numerically generated S-parameters of metamaterials

After validating and illustrating some of the potential pitfalls in the retrieval process, the method will now be used on the S-parameter data of some numerically simulated metamaterials. In the following, two types of metamaterials will be explored, the first based on the concentric SRR design and the second based on the adjacent ring design. In each case, the material parameters for both a single layer structure as well a multilayer structure will be retrieved and compared. As will be shown, because of the sensitivity of the retrieval process, it is difficult to retrieve from multilayer S-parameter data; however, in many cases, knowledge of the single layer S-parameters is enough to characterize the behavior of a particular metamaterial.

Double rod and concentric ring design

The first metamaterial to be investigated here is based on the design published by Parazzoli *et al* of The Boeing Company [32]. The unit cell of their design, shown in Fig. 3-29, consists of two rods for each set of concentric rings. Although a similar design using only one set of rods was shown to have left-handed properties [4], it was placed inside a waveguide, and according to one theory [85] the gap formed between the rods and waveguide plates made the rods resonant increasing their effective density, which in turn allowed the permittivity to be negative over a wider range of frequencies. In constrast, the design shown in Fig. 3-29 operates in freespace, and so it needs the extra rod to raise the electric plasma frequency high enough for the regions of negative permittivity to overlap with regions of negative permeability.

In order to calculate the S-parameters for an infinitely wide slab, a three-dimensional FD-TD periodic code was used. The structure is assumed periodic along the electric and magnetic field direction, and finite along the direction of propagation. In the direction of propagation, the slab is a single layer. As usual, the incident electric field was aligned
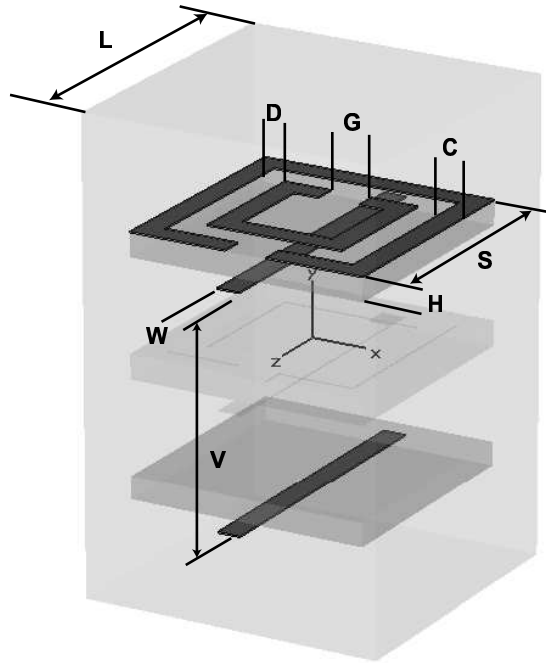
Figure 3-29: Geometry of double rod and concentric split-rings metamaterial taken from reference [32]. Geometry was simulated using a 3D periodic FDTD code. $C = 0.025$ cm, $D = 0.030$ cm, $G = 0.046$ cm, $H = 0.0254$ cm, $L = 0.33$ cm, $S = 0.263$ cm, $W = 0.025$ cm, $V = 0.255$ cm.

with the rod and the magnetic field with the axis of the SRR. The results are shown in Fig. 3-30. For this structure, it can be seen the S_{21} parameter reaches a minimum near 11.5 GHz, which likely corresponds to the resonant frequency of the SRR. Just beyond this frequency, a small passband is observed, which possibly corresponds to the region where the permittivity and permeability are simultaneously negative. Applying the retrieval method to this complex S-parameter data, the index of refraction and impedance (from which ϵ and μ can be derived) of the structure were calculated. Fig. 3-31 shows the retrieved material parameters for this 1-layer structure. From these results, it was found that the index of refraction is negative between 12 GHz and 13 GHz. Note the presence of the anti-resonance effect in the permittivity just below 12 GHz. Still, the general shape and trend of the
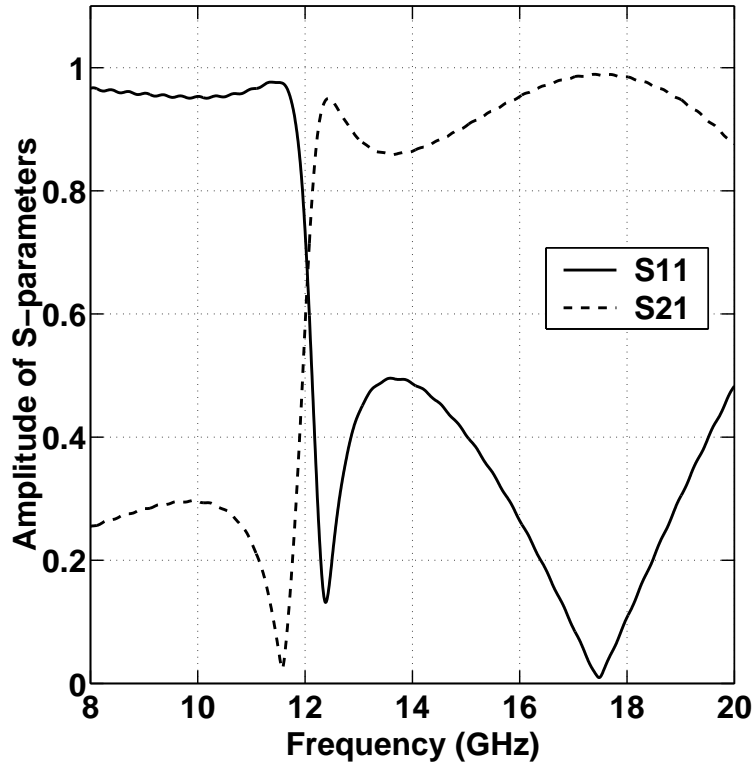
Figure 3-30: S-parameters for 1-layer double rod and concentric split-rings metamaterial. S-parameters results courtesy of X. Chen.

retrieved permittivity and permeability match the analytic Drude and Lorentz methods.

The next set of results were obtained by using the transfer matrix formalism [83, 86]. In this method, the scattering matrix for a single layer metamaterial is cascaded with itself multiple times from which the S-parameters of a multi-layer metamaterial are obtained. The main advantage of this approach is that it speeds up the computation time since only a single layer of the metamaterial structure needs to be numerically modeled. For example, Fig. 3-32 shows the 3-layer *S*-parameter results based on the transfer matrix formalism. Compared to the 1-layer *S*-parameters note the presence of a more pronounced transmission band, which is due to the increased level of absorption occurring outside the left-handed frequency band. Applying retrieval method on the 3-layer *S*-parameters, the parameters found, shown in Fig. 3-33, are practically identical to those retrieved from the 1-layer result.
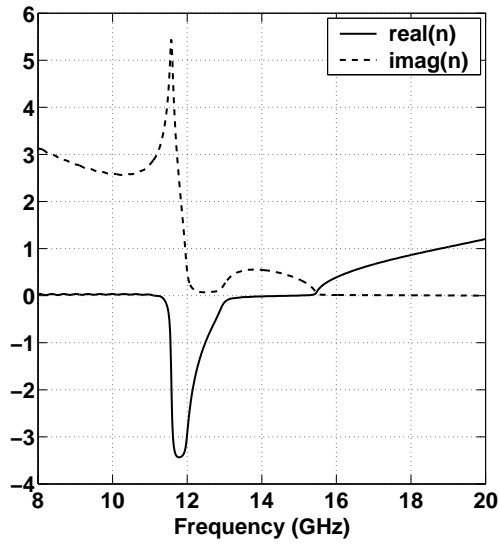
(a) Index of refraction
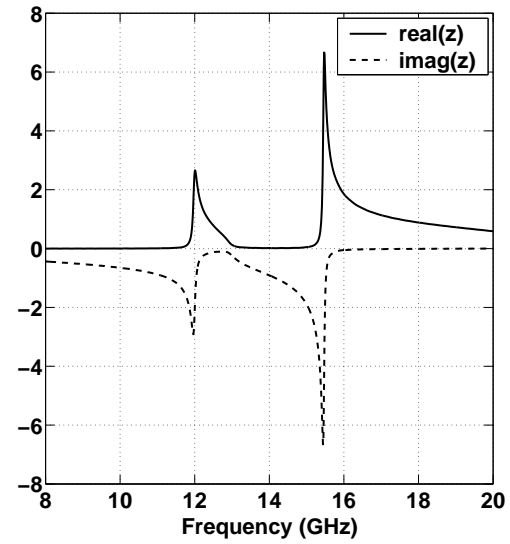
(b) Impedance
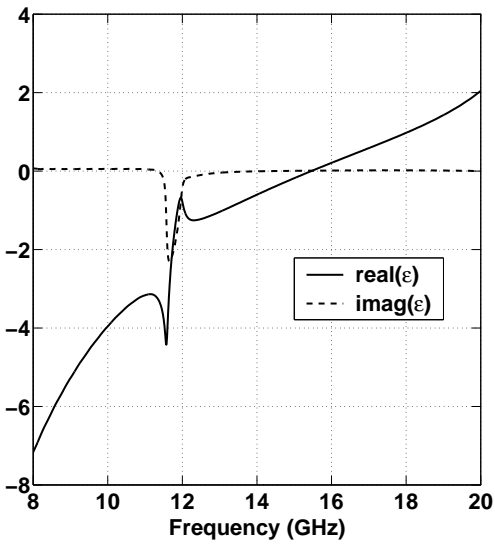
(c) Permittivity
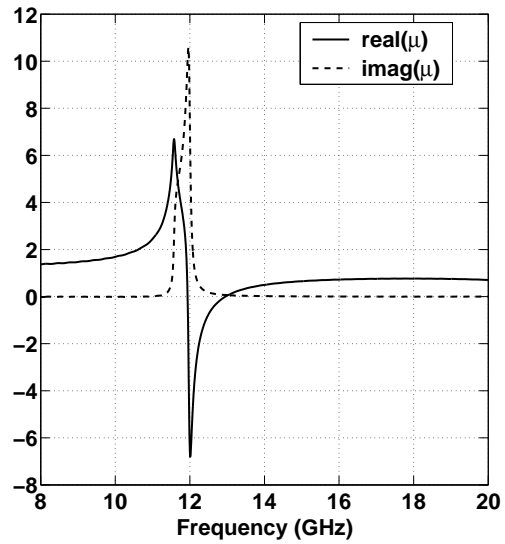
(d) Permeability

Figure 3-31: Retrieved material parameters for 1-layer double rod-concentric ring metamaterial.
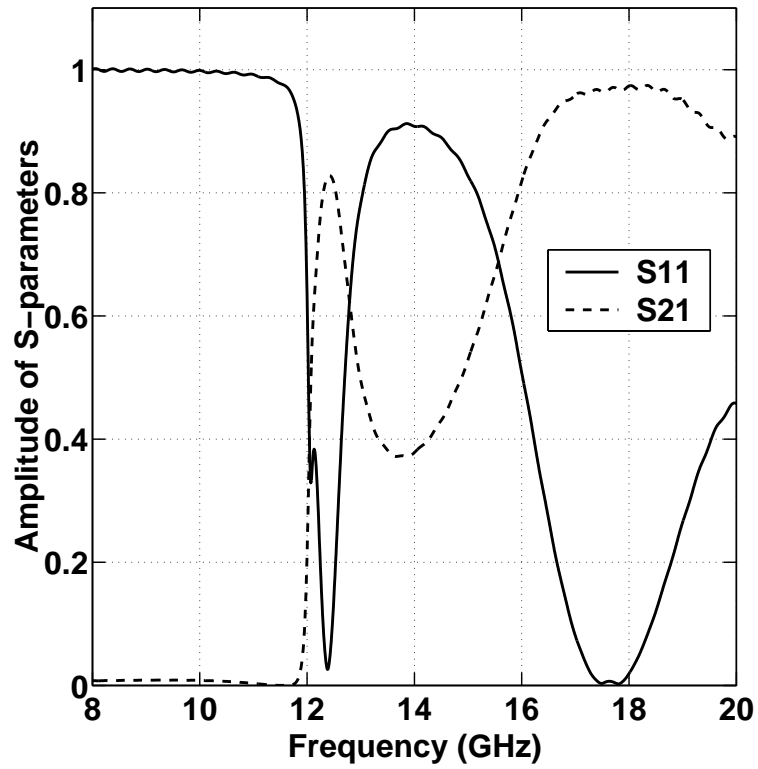
Figure 3-32: *S*-parameters for 3-layer double rod-concentric ring metamaterial obtained via the transfer matrix formalism. *S*-parameters results courtesy of X. Chen.
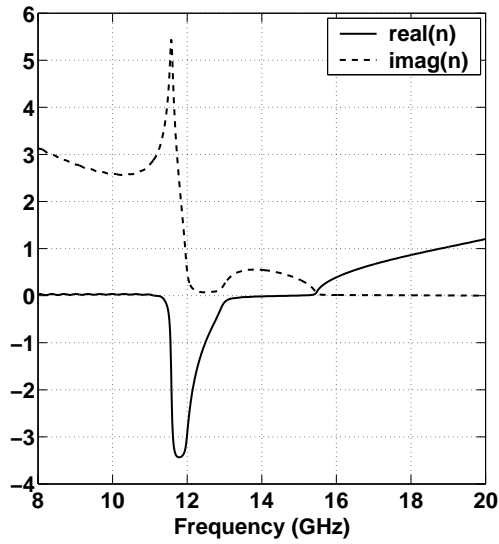
(a) Index of refraction
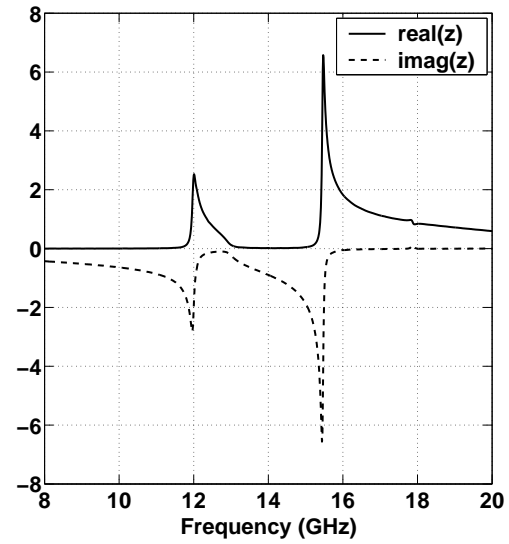
(b) Impedance
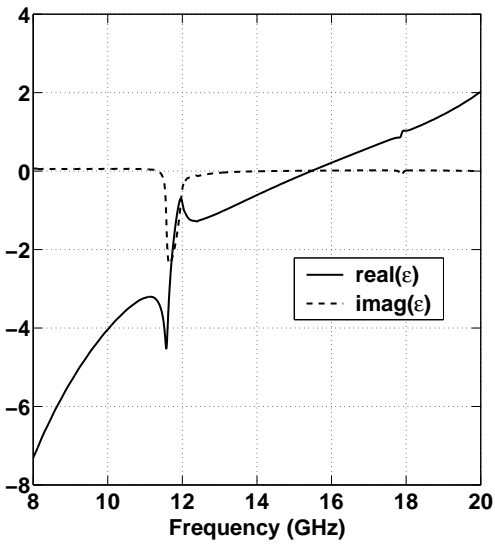
(c) Permittivity
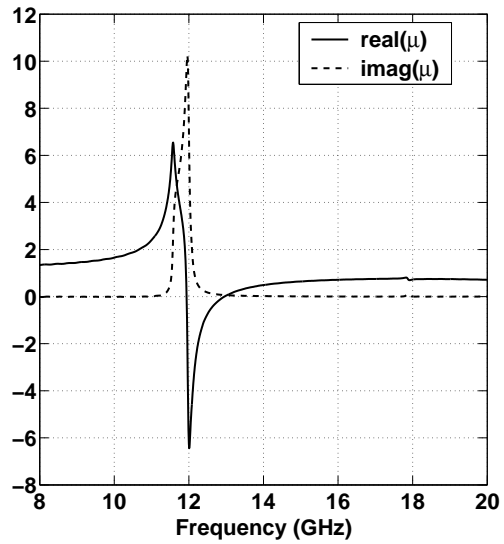
(d) Permeability

Figure 3-33: Retrieved material parameters for 3-layer double rod-concentric ring metamaterial.

Rod and adjacent ring design

One of the disadvantage of the transfer matrix method is that it can build in certain assumptions on the behavior of structure, which may bias the retrieval process. In the next example, the S-parameters of numerically simulated 1-layer and 2-layer metamaterials will used to independently compute the material parameters for comparison. For this example, the rod and adjacent ring metamaterial design shown in Fig. 3-34(a) will be investigated. For these examples, a periodic method of moments code was used to generated the S-parameter results shown in Fig. 3-34 [75]. Based on the presence of the transmission band near 14 GHz, it is possible that the metamaterial is left-handed at this frequency, which is confirmed upon retrieval. Note the retrieval process also shows that the real part of the index of refraction is negative near 12.5 GHz; however, in this frequency band, the imaginary part of the index of refraction is relatively large making to reach any definitive conclusions on the data. Nevertheless beyond 13 GHz through approximately 14.5 GHz, the index of refraction has been found to be negative. In additional, it should be noted that the index of refraction shown is just one possible solution. Because of the unknown branch numbers m, this solution found is of course non-unique; however, based on comparison with the analytic models, it is the most reasonable one.

Next, the 2-layer structure as shown in Fig. 3-35(a) was simulated using the method of moments. For this data, the retrieved index of refraction, shown in Fig. 3-35(b), appears to be a distorted form of the index of refraction retrieved from the 1-layer data. To check whether this is possibly due to the distortion of the S-parameters, the 1-layer index of refraction data was used to analytically calculate the S-parameters for the 2-layer structure. Fig. 3-35(c) shows the comparison between the two results where it is seen that the curves match quite well except near the nulls and local maximum just below 14 GHz.

Still, in the 2-layer as well as the 1-layer, the question of whether the correct choice of m was made remains. One possible method to help verify this choice is to use the phase-tracking method described in the previous section. To do this, a spatial cut along the z
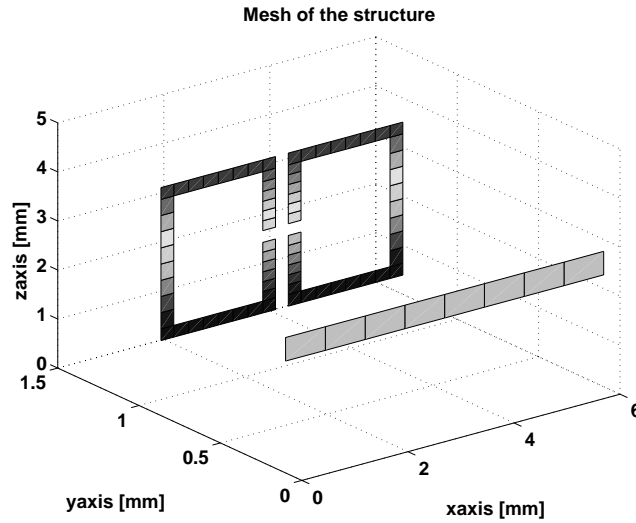
(a) Mesh of 1 layer geometry
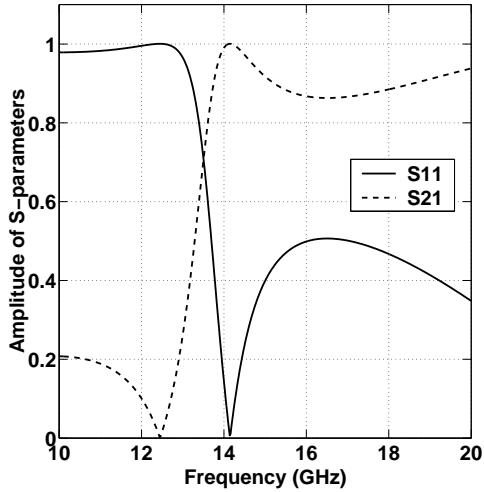
(b) S-parameters
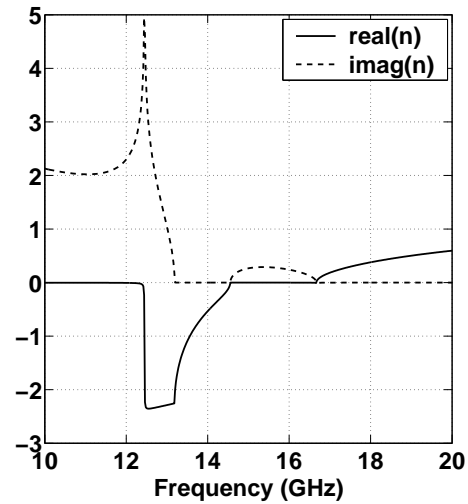
(c) Retrieved index of refraction

Figure 3-34: S-parameters and retrieved index of refraction for 1 layer 3D adjacent ring design with rods. Details of the structures are: ring/rod separation 1 mm, rod thickness of 0.48 mm, and the lattice constants are $a_x = 6$ mm, $a_y = 3$ mm, and $a_z = 5.08$ mm. Incident e-field is assumed to be $\overline{E} = \hat{x}e^{ikz}$. Mesh and MoM S-parameters simulation results courtesy of T. M. Grzegorczyk.
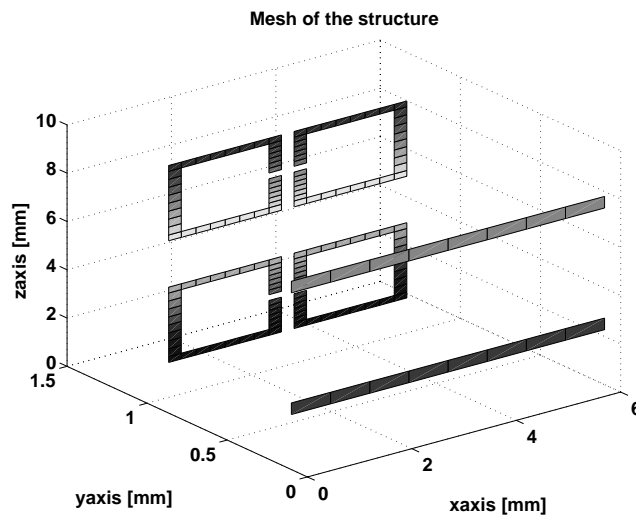
(a) Mesh of 2 layer geometry
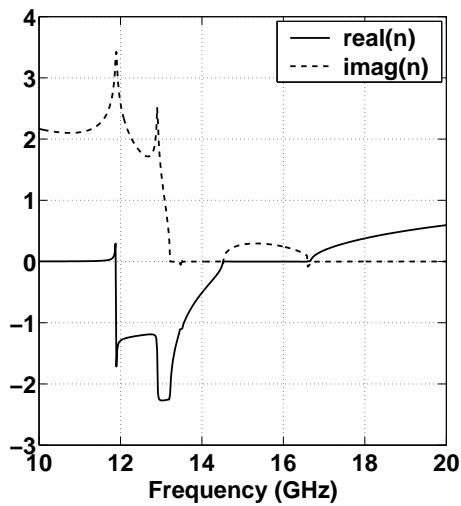
(b) Retrieved index of refraction
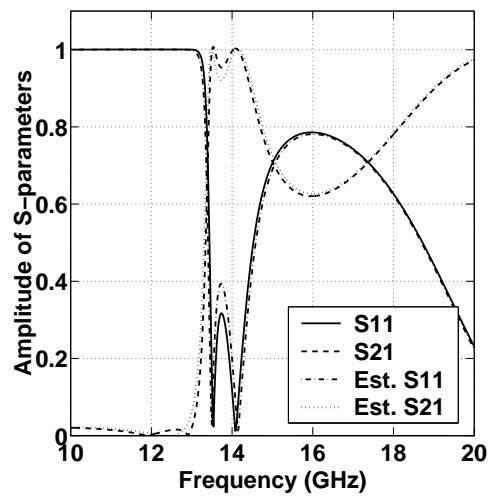
(c) Comparison of S-parameters

Figure 3-35: Retrieved index of refraction for the 2 layer 3D adjacent ring design with rods shown in (a). Figure (c) compares the MoM calculated S-parameters for this 2 layer structure with those analytically calculated using the material parameters retrieved for the 1 layer structure shown in Fig. 3-34. Mesh and MoM S-parameters simulation results courtesy of T. M. Grzegorczyk.

direction for which the fields are the most uniform is needed. For this purpose, it was found that the cut taken at the point $x = 5.95$ mm and $y = 5.95$ mm yielded the most uniform field. Using this spatial data, the index of refraction and coefficients of the forward/backward waves were determined across the entire band of frequencies. Fig. 3-36 shows the retrieved values, where is it seen that the index of refraction is indeed negative approximately between 13 GHz and 14 GHz. The method also produces an index of refraction which approximately matches that found using the S-parameter method except near the resonant region. In this region, the coefficients at the frequencies corresponding to the resonance are unusually large indicating the method's inability to accurately capture the field behavior at these frequencies.

(a) Index of refraction   (b) A/B coefficients
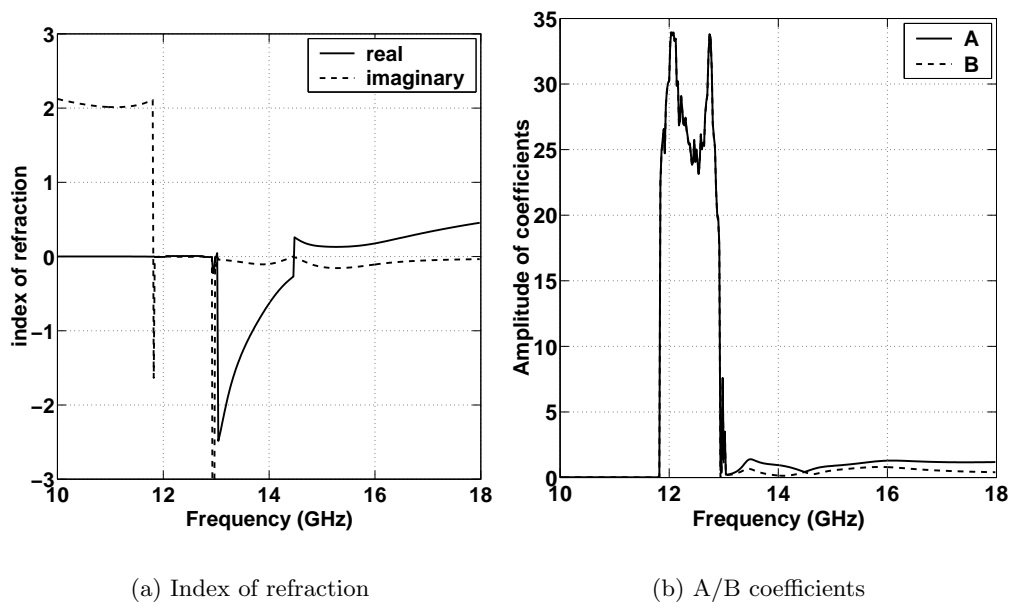
Figure 3-36: Index of refraction retrieved by phase-tracking for 2-layer adjacent ring design with rod.

3.5   Summary

In this chapter, various tools for understanding and characterizing left-handed metamaterials were presented. FD-TD simulations of propagation through periodic slabs of rod and split-ring metamaterials were used to compute the reflection and transmission coefficients. These results were compared to analytic results, and shown to agree well in the case of the rods and approximately in the case of the split-rings. Next, through numerical simulations an understanding of the mechanisms needed for the generation of left-handed properties as presented. In particular, it is shown that a rod metamaterial embedded in a homogeneous magnetic plasma medium cannot function as a left-handed metamaterial nor can a split-ring metamaterial that is embedded in a homogeneous electric plasma medium. This result, termed the "problem of left-handed materials" by Pokrovsky and Efros [20] implies that in combining the rods and split-rings together to form a left-handed metamaterials, it is essential that there be regions of within the metamaterial that are right-handed; however, the overall material can in general still effectively be treated as a left-handed material. The specific regions within the metamaterial that need a right-handed medium background were isolated, and upon removing the background plasma media from these areas, left-handed properties were demonstrated using a modified form of the phase-tracking method. This method allows for the extraction of the bulk index of refraction from the field distribution within the metamaterial. In addition to the phase-tracking retrieval method, a more precise retrieval method that utilizes the complex S-parameter results has been investigated. Using this method, and S-parameters results from three-dimensional FD-TD and MoM simulations, it has been shown that metamaterials composed of rods and split-rings can be characterized by a negative permittivity and a negative permeability.

Chapter 4

Radar-absorbing left-handed metamaterials

4.1 Introduction

With the development of radar during World War II, it became possible to readily detect enemy aircraft; however, at the same time it increased the likelihood of ally aircraft being detected by enemies. Hence, the field of stealth technology was born wherein engineers and scientists have attempted to design coatings known as radar absorbing materials (RAM) to make aircraft and other objects invisible to radar energy. Today, RAM are used in many other applications besides stealth technology such as in anechoic chambers, shielding from electromagnetic interference in high speed electronic circuits, and noise suppression in cellular phones [87].

In the past, there have been a number of different types of radar absorbing materials. Initially, RAM were designed to have RCS reduction capabilities only about a narrow frequency band. Some of these RAM designs such as the Salisbury screen and Dallenbach layers worked by using a quarter-wave transformer configuration in which a resistive layer of a certain thickness was placed over the conducting surface [87]. In order to increase band-

145

width of RCS reduction, multilayer approaches have been used such as Jaumann absorbers, which use a series of Salisbury screens where the resultant bandwidth is proportional to the number of layers [87].

In the above methods, materials were one of the limiting factors in the development of RAM designs. The materials often suffered from bulkiness, lack of durability, and were often anisotropic providing RCS reduction for only a limited range of angles and polarizations. One class of materials that helped alleviate some of these problems are chiral media, which are characterized as a bi-anisotropic medium [59]. The chirality parameter of the medium, often denoted by the symbol, κ, is a measure of the cross coupling between the electric and magnetic fields as well as the handedness of the medium [87]. Due to the additional degree of freedom provided by chirality, absorbers developed using the methodology of Salisbury screens and Dallenbach layers showed increased absorption over wider frequency bands [88, 89].

Still, the search for an ideal absorbers was not met. The need for ideal absorbers was especially needed for various computational electromagnetic techniques such as the Finite Difference-Time Domain method [78], where waves are propagated inside a finite computational domain to model the scattering or radiation of various EM systems. In 1994, such an ideal absorber was developed which was termed the perfectly matched layer (PML) [90]; however, the technique involved a non-physical splitting of the fields in order to provide an all angle and all polarization impedance matched medium that was still able to absorbing incoming waves. The derivation of the original PML was for Cartesian coordinate systems; however, a more general approach based on a complex coordinate stretching [91, 92] was also developed which enabled derivation of PML for arbitrary coordinates systems such as cylindrical or spherical [93]. Still, all of these techniques required the use of non-Maxwellian media, which, while well-suited for numerical simulations, could not be applied to physical problems such as RCS reduction. The problem of creating a Maxwellian (*e.g.*, physical) perfectly matched layer has since then been tackled by a number of researchers who have used specially crafted anisotropic materials to create media which are perfectly
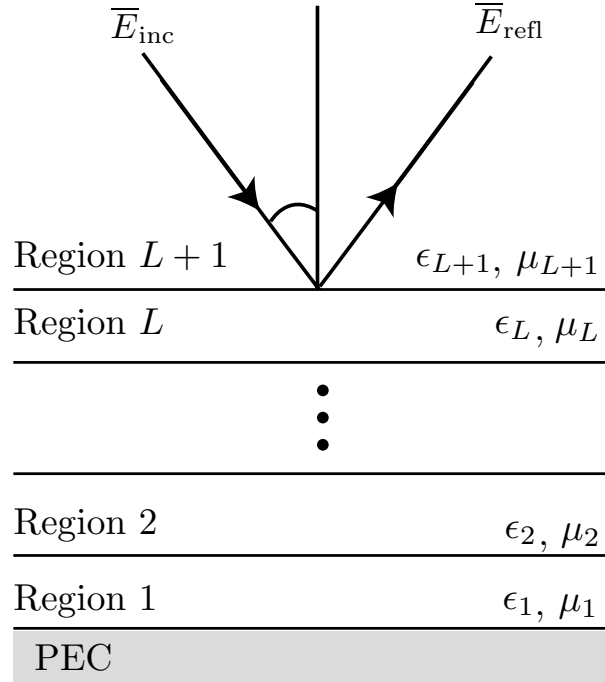
Figure 4-1: Multilayer planar geometry over a perfectly electrically conducting (PEC) ground plane. Genetic algorithms are used to determine the appropriate materials and layer thicknesses to minimize the reflected power over a given frequency band and angular swath.

matched [94–96], although some of these have active components.

In this chapter, the use rod and split-ring metamaterials as radar absorbers will be investigated. The advantage of using metamaterials is that frequency dispersion of their permittivity and permeability can be controlled to some extent, which make metamaterials candidates for the design of new radar absorbing materials. Because of the large number of unknown parameters and nonlinear aspects of the problem, genetic algorithms (GA) will be used to synthesize a multilayer RAM configuration (see Fig. 4-1). Genetic algorithms are a class of the stochastic optimization techniques which attempt to find the global maximum of some objective function by employing randomness or diversity in much the same way natural selection is believed to occur [97]. Such approaches have been used in the past for the development of right-handed radar absorbers [98, 99], and it is the purpose of this

chapter to determine how left-handed metamaterials compare to conventional lossy right-handed materials as absorbers.

4.2   Ideal absorbers

Before exploring the use of metamaterials as radar absorbers, it is useful to review the criterion for perfect absorbers. Here, the discussion is limited those perfect absorbers constructed of materials that obey Maxwell's equation, and could potentially be realized. In other words, numerical absorbers, such as the perfectly-matched layer [90] are not discussed.

4.2.1   Criterion for a perfect EM absorber at normal incidence

At normal incidence, the half-space reflection coefficient for a TE polarized incident wave is given by [59],

$$R = \frac{\eta_1 - \eta_0}{\eta_1 + \eta_0} \tag{4.1}$$

where η_ℓ is the impedance in region ℓ defined as,

$$\eta_\ell = \sqrt{\frac{\mu_\ell}{\epsilon_\ell}}. \tag{4.2}$$

Hence, the requirement for $R = 0$ can be satisfied under the condition that the impedances are equal to each other. For a medium-freespace configuration this requirements can be alternatively expressed as,

$$\eta_1 = \sqrt{\frac{\mu_{1r}}{\epsilon_{1r}}} = 1 \tag{4.3}$$

where μ_{1r} and ϵ_{1r} are the relative permittivity and permeability of the medium.

Under this condition, the amount of absorption depends solely on the magnitude of the imaginary parts of the permittivity and permeability and the thickness of the slab. Consider
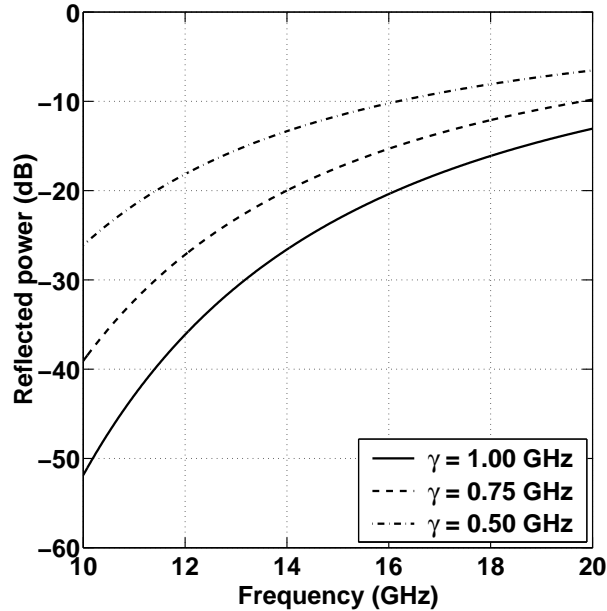
Figure 4-2: Reflected power versus frequency at normal incidence for an absorber that is 4 mm thick constructed of a material whose permittivity and permittivity both follow the Drude model with $f_p = 60$ GHz and a damping frequency of γ.

for example, an ideal metamaterial constructed out of electrically conductive rods crossed with magnetically conductive rods. Although, such a metamaterial has not been built (and may not be possible to build), such a medium would have be characterized by a permittivity and a permeability that each followed the Drude model (see eq. 3.1). If the periodicity of the electric rods and magnetic rods were arranged to be equal in both directions, then the two plasma frequencies would line up and the impedance of the medium would be unity for all frequencies.

The reflected power versus frequency for normal incidence for this type of ideal metamaterial in shown in Fig. 4-2. In the plot, the results for three different damping frequencies are plotted. The metamaterial is assumed to have one layer ($L = 1$) which is 4 mm thick and is backed by a perfectly electrically conducting (PEC) ground plane. As can be seen, depending on the damping frequency, which controls the amount of absorption in the medium, the amount of reflected power varies from a minimum of -50 dB to -25 dB at 10 GHz. Of

course the amount of power reflected can further be reduced by increasing the thickness of the layer.

4.2.2   Criterion for a perfect EM absorber for all incidences

Unfortunately, matching the impedance of the medium to that of freespace will not reduce the reflected power for non-normal incidences. In order minimize the reflection across all angles, a special type of anisotropic medium is needed. Such a medium as been described in [94] and [96]. For comparison with LH media absorbers, the conditions for zero reflection are reviewed here.

The formulation begins by assuming material tensors of the form,

$$\bar{\bar{\epsilon}} \ = \ \epsilon_0 \bar{\bar{\Lambda}} \tag{4.4}$$

$$\bar{\bar{\mu}} \ = \ \mu_0 \bar{\bar{\Lambda}} \tag{4.5}$$

where $\bar{\bar{\Lambda}}$ is of the form,

$$\bar{\bar{\Lambda}} = \begin{pmatrix} \lambda_x & 0 & 0 \\ 0 & \lambda_y & 0 \\ 0 & 0 & \lambda_z \end{pmatrix}. \tag{4.6}$$

The first step in determining the reflection coefficient will be to obtain the dispersion relation for such a medium. To obtain it, a transformation to the kDB domain performed [59]. For simplicity waves will be assumed to propagate only in the xz plane such that without loss of generality, the azimuthal angle can be fixed as $\phi = 0$.

Applying the kDB transformation yields the following reduced matrix form of Maxwell's

equations,

$$\frac{1}{\epsilon_0} \begin{pmatrix} \lambda_{11} & 0 \\ 0 & \lambda_{22} \end{pmatrix} \begin{pmatrix} D_1 \\ D_2 \end{pmatrix} = \begin{pmatrix} 0 & u \\ -u & 0 \end{pmatrix} \begin{pmatrix} B_1 \\ B_2 \end{pmatrix} \tag{4.7}$$

$$\frac{1}{\mu_0} \begin{pmatrix} \lambda_{11} & 0 \\ 0 & \lambda_{22} \end{pmatrix} \begin{pmatrix} B_1 \\ B_2 \end{pmatrix} = \begin{pmatrix} 0 & -u \\ u & 0 \end{pmatrix} \begin{pmatrix} D_1 \\ D_2 \end{pmatrix} \tag{4.8}$$

where $u = \omega/k$ and

$$\lambda_{11} = \frac{1}{\lambda_y} \tag{4.9}$$

$$\lambda_{22} = \frac{1}{\lambda_x} \cos^2 \theta + \frac{1}{\lambda_z} \sin^2 \theta. \tag{4.10}$$

Expanding out and eliminating the B fields yields,

$$\begin{pmatrix} c_0^2 \lambda_{11} - u^2 \lambda_{22}^{-1} & 0 \\ 0 & c_0^2 \lambda_{22} - u^2 \lambda_{11}^{-1} \end{pmatrix} \begin{pmatrix} D_1 \\ D_2 \end{pmatrix} = \begin{pmatrix} 0 \\ 0 \end{pmatrix} \tag{4.11}$$

where c_0 is the speed of light in free space. From this matrix, it is seen that there exists a double eigenvalue; hence, the characteristic waves obey the same dispersion relationship, namely,

$$u^2 = c_0^2 \lambda_{11} \lambda_{22} \tag{4.12}$$

which is equivalent to the following form,

$$\lambda_x k_x^2 + \lambda_z k_z^2 = \omega^2 \mu_0 \epsilon_0 \lambda_x \lambda_y \lambda_z \tag{4.13}$$

where $k^2 = k_x^2 + k_z^2$. Next, to solve for the reflection coefficients, phase-matching and boundary conditions are used. Assuming a TE polarized incident field, with the electric

field in the $\hat{y}$ direction, the electromagnetic fields take the form,

$$\overline{E}_0 \quad = \quad \hat{y}E_0 e^{\mathrm{i}k_x x - \mathrm{i}k_{0z}z} + \hat{y}RE_0 e^{\mathrm{i}k_x x + \mathrm{i}k_{0z}z} \tag{4.14}$$

$$\overline{H}_0 \quad = \quad \frac{E_0}{\omega\mu_0}\left[\hat{z}k_x + \hat{x}k_{0z}\right]e^{\mathrm{i}k_x x - \mathrm{i}k_{0z}z} + \frac{RE_0}{\omega\mu_0}\left[\hat{z}k_x - \hat{x}k_{0z}\right]e^{\mathrm{i}k_x x + \mathrm{i}k_{0z}z} \tag{4.15}$$

for region 0, and in region 1, which is anisotropic, the fields take the form,

$$\overline{E}_1 \quad = \quad \hat{y}TE_0 e^{\mathrm{i}k_x x - \mathrm{i}k_{1z}z} \tag{4.16}$$

$$\overline{H}_1 \quad = \quad \frac{TE_0}{\omega\mu_0}\left[\hat{z}\frac{k_x}{\lambda_z} + \hat{x}\frac{k_{1z}}{\lambda_x}\right]e^{\mathrm{i}k_x x - \mathrm{i}k_{1z}z}. \tag{4.17}$$

Matching the tangential field components at the boundary yields the following solution for R and T,

$$R = \frac{1 - p_{01}}{1 + p_{01}} \qquad T = \frac{2}{1 + p_{01}} \tag{4.18}$$

where

$$p_{01} \quad = \quad \frac{k_{1z}}{\lambda_x k_{0z}} = \frac{1}{\lambda_x \cos\theta_i}\sqrt{\lambda_x\lambda_y - \frac{\lambda_x}{\lambda_z}\sin^2\theta_i} \tag{4.19}$$

Thus from (4.19), we can see that if we set $\lambda_x = \lambda_y$ and $\lambda_y = 1/\lambda_z$ that $p_{01} = 1$, which means that $R = 0$ for all angles so that the incident wave is fully transmitted. Furthermore, if the imaginary part of $\lambda_x > 0$, then the transmitted wave will decay as it propagates through the medium. The rate of decay is related to the k_{1z} term, and can be determined through the dispersion relation as,

$$k_{1z} \quad = \quad \lambda_x\sqrt{\omega^2\mu_0\epsilon_0 - k_x^2} = \lambda_x k_{0z} \tag{4.20}$$

$$\tag{4.21}$$

Then, letting $\lambda_x = 1 + \mathrm{i}\gamma$ and assuming that $k_{0z} = k_0\cos\theta_i$, means that fields inside
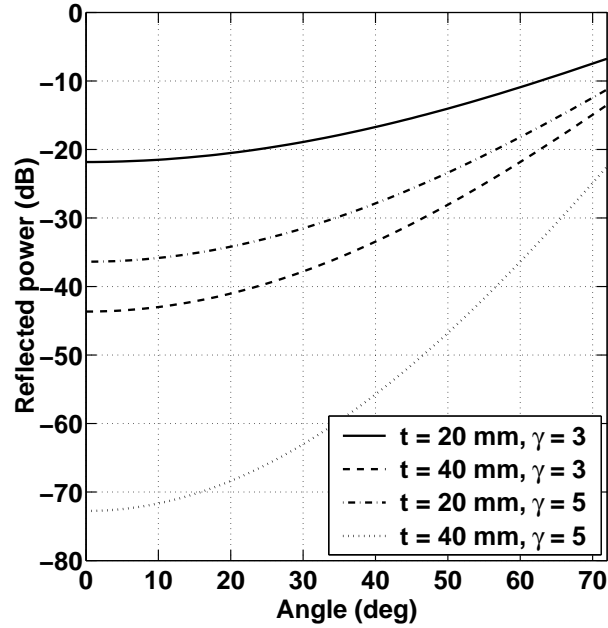
Figure 4-3: Reflected power versus angle at 10 GHz for an ideal absorber. $\lambda_x = \lambda_y = 1 + i\gamma$, $\lambda_z = 1/\lambda_x$.

the medium will exponentially decay at the rate of γk_{0z}. Hence, the larger the value of γ, the higher absorption achieved whereas larger incident angles, θ_i will lead to lower absorption. In a finite slab configuration that is backed by a PEC ground plane, the rate of decay in conjunction with the layer's thickness will determine the minimum possible reflection coefficient. Fig. 4-3 illustrates this effect for the combinations of two different slab thicknesses and two different values of γ.

4.3   Designing absorbing left-handed metamaterials

In the following sections, a genetic algorithm (GA) will be used to design a multi-layered radar absorbing material (RAM) that uses left-handed metamaterials. For comparison, designs based on conventional lossy right-handed materials will also be synthesized using a GA. The designs synthesized will attempt to minimize the reflection coefficient over a given

frequency bandwidth and/or a given angular swath. In order to be able to feasibly use a GA to synthesize the RAM configuration, it is necessary to use the bulk media assumption for characterizing the metamaterials. As discussed in the Chapter 3, the principle models used are the Drude and Lorentz media models (see eqns. 3.1 and 3.2).

4.3.1   Genetic Algorithms

Genetic algorithms are a class of stochastic optimization techniques which are used for finding the global extrema of an objective function. Before describing how GAs will be applied to the problem of reflection coefficient reduction, it is useful to review some of the terminology and concepts associated with genetic algorithms.

As described in detail in [97], a genetic algorithm works by employing diversity schemes based on Darwinian natural selection to determine a set of parameters which maximize the objective function of interest. In the vernacular of GA, each parameter of the objective function is referred to as a *gene*, and the set of all parameters comprising one trial solution is known as a *chromosome*. A given set of trial solutions is collectively known as the *population* of the current *generation*. Members of the current generation, or the *parents* are used to generate the *children* or *offspring* of the next generation. As illustrated in Fig. 4-4, the genetic algorithm begins by randomly initializing a large population of individuals. Individuals from the current population are then selected and used to generate the next generation.

The selection schemes for which individuals are allowed to procreate vary but are all based on the *fitness* level of the individuals, which is a measure of the individual's goodness (*i.e.*, ability to maximize the objective function). One of these methods, known as *tournament selection*, involves the random selection of N members of the current population who compete with each other. The one with the highest fitness level is chosen to be a parent of the next generation. All N members are then returned to the population. This process is repeated until a sufficient number of parents have been selected. Since members are allowed to compete in more than one tournament, it is possible, especially in the later
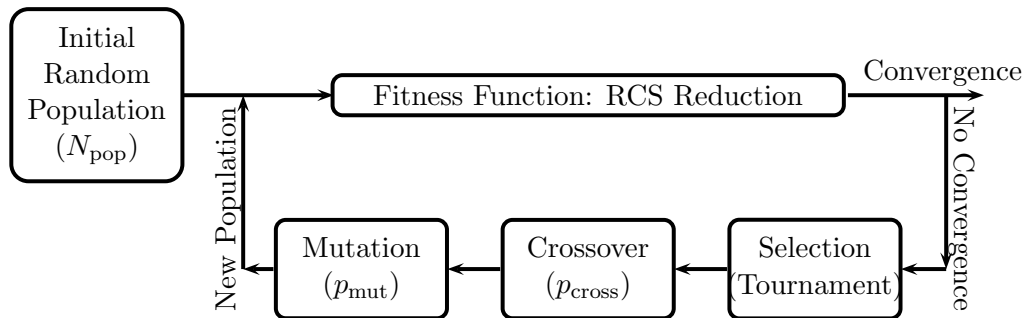
Figure 4-4: Genetic algorithm flowchart for RCS reduction

stages of the evolution process, for one member of the current population to be a parent of multiple children in the next generation.

Once two parents have been selected, they produce two offspring using the principles of *crossover* and *mutation*. Crossover is the process of combining the genetic information of the two parents into the two children, and occurs with a probability, p_{cross}, typically between 0.5 and 0.7. In particular, a crossover site on the chromosome is chosen randomly, and the genes proceeding the crossover site of the first parent and genes after the crossover site of the second parent form the chromosome of the first child. The second child then receives the remainder of the genetic information. If crossover does not occur, the children of the next generation will be clones of the parents. Mutation, which promotes diversity thereby preventing convergence to a local maximum, is the process of randomly changing the value of one gene on each child's chromosome, and occurs with probability, p_{mut}, typically less than 0.1.

The objective function used in this chapter will be a measure of the coating's ability to reduce the radar cross section (RCS) over a given angular swath and frequency band. The choice of objective function will influence the type of solutions found. One possible choice,

which is used in [99], is given by

$$F = \sum_{\theta} \sum_{f} \left[\text{RCS}_{\text{conductor}}^{(\text{dB})}(\theta, f) - \text{RCS}_{\text{coated}}^{(\text{dB})}(\theta, f) \right] \tag{4.22}$$

where $\text{RCS}_{\text{conductor}}^{(\text{dB})}$ is the normalized radar cross section (RCS) of an uncoated conducting surface and $\text{RCS}_{\text{coated}}^{(\text{dB})}$ is the normalized RCS of the coated surface. Essentially, the mean RCS over the given range of frequencies and angles is minimized. As will be discussed in more detail later in this chapter, the parameters over which the function F is minimized include the number of layers, the material type of each layer, and the thickness of each layer.

While the objective function in (4.22) will yield viable solutions, it does not give preference to any specific angles or frequencies within the swath or band of interest. In some cases, it is advantageous to be able to place a deeper null at one frequency or angle while at the same time making the other values as low as possible. For this purpose, the optimizations performed will be done using the following scoring scheme,

$$\text{SCORE} = 100 \left[w_1 I + w_2 G + w_3 BW + w_4 RCS \right] \tag{4.23}$$

where I is the index goal score, G is the dB goal score, BW is the bandwidth score, RCS is the RCS score, and w_i are weights to emphasize the relative importance of each category. Note that, unless otherwise stated, each category will be equally weighted, *i.e.*, $w_i = 0.25$. Each of the scores are designed to range from 0 to 1, with 1 being the optimal solution. For example, the RCS score is defined as

$$\text{RCS} = \frac{0.01}{0.01 + \overline{\text{RCS}}} \tag{4.24}$$

such that a mean RCS of zero yields a value of 1. The index and dB goal scores are defined using the objective functions shown in Fig. 4-5. The index goal objective function reflects

how close the minimum reflection coefficient over the band or swath of interest occurs at the desired frequency or angle. The weights are chosen such that plus or minus deviations are penalized equally. The dB goal reflects how close the minimum value of reflected power over the frequency band or angular swath is to the desired value. The weights are chosen such that solutions where the minimum value of reflected power is smaller than the desired amount are less penalized than those where the minimum value is over the desired amount. Finally the bandwidth score is defined as the percentage of the band or angular swath that is below a certain threshold value.

Although the objective function described above attempts to place a lower bound on the minimum value of the RCS over the given band, this allows solutions to be more fairly compared. For example, consider two different solutions whose mean RCS values are similar. In the first solution, one particular frequency has a very sharp null but the RCS at other frequencies is relatively high. In the second solution, the minimum RCS is higher than the null of solution one, but the solution maintains values close to this minimum throughout the band. The question then becomes, which solution is better? The simple answer is of course that it depends on the specific application. In this work, bandwidth will be emphasized more than deep nulls. The scoring scheme described above reflects this desire in that solutions with wider bands are promoted more than solutions with deep nulls.

One advantage in using a GA is that constraints such as the range of possible thicknesses, and the types of materials are easily incorporated by appropriate choice of the trial solution encoding scheme. In the scheme used in this work, the parameters for a trial solution are encoded by representing each member of the population with a binary string. For multi-layered RAM design, information about the material type and thickness for each layer can be encoded in binary as follows,

$$L_j = M_j T_j = \left[m_j^1 m_j^2 \dots m_j^{N_{mb}} \right] \left[t_j^1 t_j^2 \dots t_j^{N_{tb}} \right] \tag{4.25}$$

where the m_j bits represent the different parameters needed to characterize the material, and
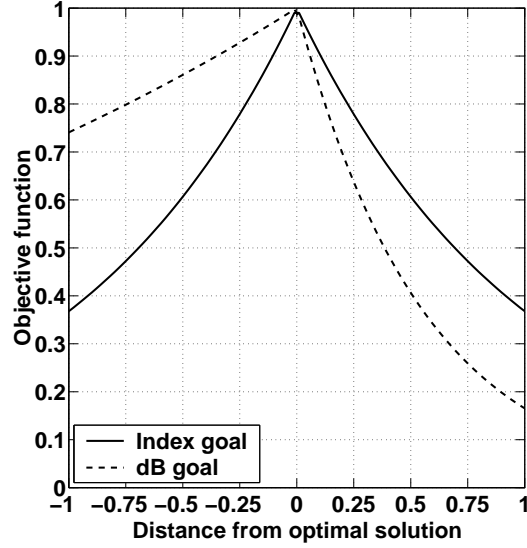
Figure 4-5: Objective functions for the index goal and the dB goal.

t_j represents a quantized version of the thickness. For example, if the range of thicknesses varies from a to b, the binary representation, t_j can be converted to a thickness value by,

$$t = a + \frac{t_j}{2^{N_{tb}} - 1}(b - a).$$ (4.26)

In previous work [98, 99], the m_j bits were used to represent the ID of a material that was taken from a database of materials available for incorporation into the RAM. However, in this chapter, part of the m_j bits will used to determine the class of the material, and remainder will be used to determine the parameters for that particular class. More details are given in Section 4.3.2. Additionally, in this work, the number of layers is chosen prior to the optimization, so that the total chromosome for one trial solution takes the form,

$$R = [L_1 L_2 \ldots L_{N_l}]$$ (4.27)

where N_l is the number of layers.

In running the genetic algorithm, there are many factors that will influence the conver-

gence and success of the method such as the initial population size, N_{pop}, or the probabilities of crossover and mutation. In previous work, it has been empirically observed that the initial population size should vary linearly with the number of bits needed to represent one chromosome [98]. For this work, the population size will in general be chosen according to the rule of thumb, $N_{pop} = \max[50, 1.5N_{bits}]$. Additionally, using the probabilities $p_{cross} = 0.7$ and $p_{mut} = 0.1$ have been been found to work well and have been employed in all the examples presented in this chapter.

4.3.2 Material selection

In using the GA schemes described above, it is necessary to define a class of materials, which can be used in the design of a multi-layered radar absorber. In this chapter, both left-handed metamaterials and generic right-handed lossy materials will be used in the design process.

The class of left-handed metamaterials will be represented by using the Drude and Lorentz bulk media models. In the following, the class labeled "rods" will refer to a medium whose permittivity follows the Drude model and whose permeability is μ_o. Second, the class labeled "rings" will refer to a medium whose permeability follows the Lorentz model and whose permittivity is ϵ_o. Finally, the class "rods and rings," is the combination of the above two classes, *i.e.*, Drude for permittivity and Lorentz for permeability. Table 4.1 lists these three classes as well as the range of parameters that will be used in designing a radar absorber. Following the binary encoding scheme described above, 2 bits will be used to determine the class and 10 bits will be used in the quantization of each parameter. For the choice of class, because with 2 bits there are four possibilities, the class of rods and rings will correspond both the binary strings '10' and '11'. Also, for first two classes, there are fewer parameters than in the last class, so in the binary string some of the bits will be unused when the "rods" only or "rings" only class is used. Depending on the choice of parameters, the resulting Drude/Lorentz media may or may not be left-handed. In either case, the parameters determined represent the specifications for the design of a rod/ring metamaterial. In some cases, the parameters determined may not be able to be realized;

however, because of the stochastic nature of genetic algorithms, it is usually possible to find many potential solutions some of which may be realizable.

For comparison purposes, a set of right-handed materials, taken from references [98,99], will also be used in the design of radar absorbers. The four different classes of materials and their associated parameters are listed in Table 4.2. Although these materials are fictitious, they are representative of a number of materials used in practice [98]. The first class of these right-handed materials listed are lossless dielectrics, which are materials with a lossless permittivity that is independent of frequency. The next two classes of materials are lossy magnetics and lossy dielectrics. Each of these materials are specified through their permeability/permittivity at 1 GHz along with the decay coefficients α and β. In addition, the magnetic materials have a frequency independent permittivity while the dielectric materials have a frequency independent permeability. An example of the permeability for a magnetic material is shown in Fig. 4-6(a). Finally, the last class of right-handed materials is lossy magnetics with a relaxation type characteristic. These are specified by their real permeability at $f = 0$, and by the frequency, f_m at which their imaginary part peaks. An example of the permeability for this type of material is shown in Fig. 4-6(b).

(a) Lossy magnetic

(b) Relaxation-type magnetic
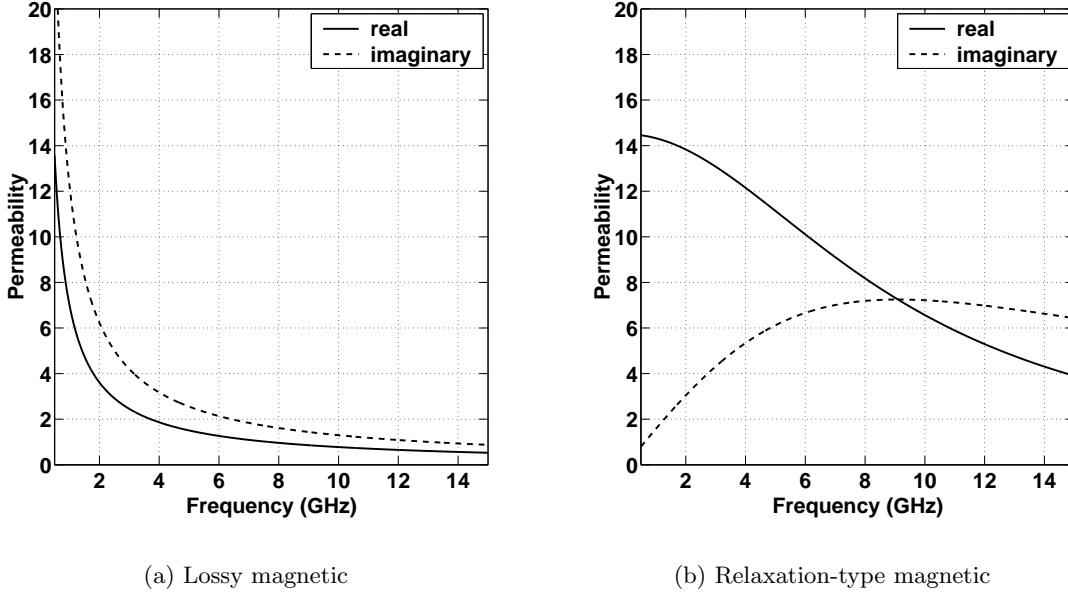
Figure 4-6: Example of the permeability for two classes of right-handed materials used in the design of RAMs. Magnetic: $\mu_r = 7$, $\mu_i = 12.25$, $\alpha = 0.955$, and $\beta = 0.975$. Relaxation-type: $\mu_m = 14.5$, $f_m = 9.1$.

Class	Permittivity Model	Permeability Model	Parameter Ranges
Rods	$\epsilon = 1 - \dfrac{f_{ep}^2}{f^2 + \mathrm{i}f\gamma_e}$	$\mu = 1$	$f_{ep} \sim [1, 30]$, $\gamma_e \sim [0.001, 5]$
Rings	$\epsilon = 1$	$\mu = 1 - \dfrac{f_{mp}^2 - f_{mo}^2}{f^2 - f_{mo}^2 + \mathrm{i}f\gamma_m}$	$f_{mo} \sim [1, 30]$, $f_{mp} \sim f_{mo} + [0.1, 5]$, $\gamma_m \sim [0.001, 5]$
Rods and rings	$\epsilon = 1 - \dfrac{f_{ep}^2}{f^2 + \mathrm{i}f\gamma_e}$	$\mu = 1 - \dfrac{f_{mp}^2 - f_{mo}^2}{f^2 - f_{mo}^2 + \mathrm{i}f\gamma_m}$	$f_{ep} \sim [1, 30]$, $\gamma_e \sim [0.001, 5]$, $f_{mo} \sim [1, 30]$, $f_{mp} \sim f_{mo} + [0.1, 5]$, $\gamma_m \sim [0.001, 5]$

Table 4.1: List of LH metamaterials used in designing absorbers. The three classes of materials shown are based on conventional models for LH metamaterials composed of metallic rods and rings. Frequencies are listed in GHz.

Class	Permittivity Model	Permeability Model	Parameter Ranges
Lossless dielectric	$\epsilon = \epsilon_r$	$\mu = 1$	$\epsilon_r \sim [1, 15]$
Lossy magnetic	$\epsilon = \epsilon_r$	$\mu = \dfrac{\mu_r}{f^\alpha} + \mathrm{i}\dfrac{\mu_i}{f^\beta}$	$\epsilon_r \sim [1, 15]$, $\mu_r \sim [1, 15]$, $\mu_i \sim [1, 15]$, $\alpha \sim [0, 1]$, $\beta \sim [0, 1]$
Lossy dielectric	$\epsilon = \dfrac{\epsilon_r}{f^\alpha} + \mathrm{i}\dfrac{\epsilon_i}{f^\beta}$	$\mu = 1$	$\epsilon_r \sim [1, 15]$, $\epsilon_i \sim [1, 15]$, $\alpha \sim [0, 1]$, $\beta \sim [0, 1]$
Relaxation-type magnetic	$\epsilon = \epsilon_r$	$\mu = \dfrac{\mu_m(f_m^2 + \mathrm{i}f_m f)}{f^2 + f_m^2}$	$\epsilon_r \sim [1, 15]$, $\mu_m \sim [1, 15]$, $f_m \sim [1, 30]$

Table 4.2: List of right-handed material used in designing absorbers. The materials listed are generic right-handed lossy materials taken from [98]. Frequencies are listed in GHz.

4.3.3 Minimization over frequency bandwidth

After defining the set of available materials, the use of genetic algorithms to design a two layer radar absorber will be investigated. In this section, the goal of the optimization will be to minimize the reflection coefficient for normal incidence over the frequency band from 8 GHz to 12 GHz. The scoring scheme described in (4.23) will be used as the objective function of the genetic algorithms. To obtain the score, the band is sampled at 21 frequencies. For the examples presented here, the optimization parameter ranges and goals are as follows,

1. Optimization parameter ranges

    a. Frequency band: 8 – 12 GHz

    b. Incident angles: $\theta = 0$.

    c. Layer thicknesses: 0.01 – 0.20 cm.

2. Optimization goals

    a. Index goal: 10 GHz

    b. dB goal: -30 dB

    c. threshold: -20 dB

Upon revisiting the ideal solution shown in Fig. 4-3, a goal of -30 dB at 10 GHz is quite conservative; however, the challenge in the design will be to maintain that level of absorption over the entire frequency band.

Use of LH metamaterials

The first example will be to attempt to meet the above goals using the Drude and Lorentz metamaterial models. For this example, and the remaining in the chapter, the genetic algorithm was run several times yielding a variety of different solution with varying levels of success. In most cases, the final score achieved were quite similar; however, for some runs the final score was significantly lower than the others. For this reason, and because

GAs are a stochastic method, it is important to run the optimization several times in order avoid outlier solutions. Fig. 4-7 shows the reflected power achieved over the band for four different metamaterials solutions found. The corresponding material parameters are listed in Table 4.3. In each case, the index goal and dB goal were met, but the bandwidth goal was not met. For each case, there is a large degree of asymmetry present, which is due in part to inherent nature of the Drude and Lorentz models. For example, the permittivity and permeability for the two layers of the first solution are shown in Fig. 4-8. Because of the Drude model, the loss in the permittivity will always be largest on the lower part of the frequency band; however, the main contributor to the absorption is due to the resonance in the Lorentz model. For the example shown, the imaginary part is largest for the lower frequencies, which is apparent in the reflection power plot.

Use of RH lossy materials

For comparison purposes, the same optimization parameters and goals were run using the set of right-handed lossy materials. As with the metamaterial section, the GA was run several times to increase the chances of identifying and removing any outlier solutions. Fig. 4-9 shows the reflected power achieved over the band for two different solutions found. The corresponding material parameters are listed in Table 4.4. In each case, the index goal, dB goal, and bandwidth goal were met. Additionally, in constrast to the metamaterials solutions, the level of absorption about the center frequency is relatively symmetric. This symmetry noting that in the solution, many of the layers found were of the magnetic relaxation-type, with f_m frequencies well outside the frequency band of interest. Because these frequencies are well outside the band of interest, the magnitude of the imaginary part of the permeability in the 8–12 GHz frequency is relatively constant, which leads to the more symmetric reflection reduction solutions. Thus, for optimization over widebands, this set of right-handed materials is better than the set of LH metamaterials used. It should be noted that the right-handed materials also have the unfair advantage of in general being more lossy than left-handed metamaterials.

Metamaterial (LH) solution #1: score = 74.74

Layer	Layer thickness (cm)	Material Class	Parameter Values
1	0.175484	Rods & Rings	$f_{ep} = 9.56305$, $f_{mo} = 6.8651$, $f_{mp} = 11.9358$, $\gamma_e = 3.84264$, $\gamma_m = 2.31772$
2	0.144839	Rods & Rings	$f_{ep} = 12.7595$, $f_{mo} = 9.91496$, $f_{mp} = 14.751$, $\gamma_e = 2.59142$, $\gamma_m = 3.72534$

Metamaterial (LH) solution #2: score = 72.72

| 1 | 0.126452 | Rings only | $f_{mo} = 7.68622$, $f_{mp} = 10.5233$, $\gamma_m = 0.621723$ |
| 2 | 0.200000 | Rings only | $f_{mo} = 9.97361$, $f_{mp} = 13.7784$, $\gamma_m = 4.99611$ |

Metamaterial (LH) solution #3: score = 71.29

| 1 | 0.101935 | Rings only | $f_{mo} = 8.50733$, $f_{mp} = 13.5291$, $\gamma_m = 1.81429$ |
| 2 | 0.193871 | Rods & Rings | $f_{ep} = 30.0323$, $f_{mo} = 10.0029$, $f_{mp} = 15.0541$, $\gamma_e = 1.20823$, $\gamma_m = 3.09973$ |

Metamaterial (LH) solution #4: score = 64.42

| 1 | 0.028387 | Rings only | $f_{mo} = 11.5572$, $f_{mp} = 16.3297$, $\gamma_m = 1.49171$ |
| 2 | 0.150968 | Rings only | $f_{mo} = 9.44575$, $f_{mp} = 13.7246$, $\gamma_m = 2.85535$ |

Table 4.3: Metamaterial parameters for four RAM designs. Goal = -30 dB, threshold = -20 dB. Corresponding reflected power results shown in Fig. 4-7.

Lossy RH solution #1: score = 94.68

Layer	Layer thickness (cm)	Material Class	Parameter Values
1	0.052903	Relaxation-type	$\epsilon_r = 10.3695,$ $\mu_m = 12.3050,$ $f_m = 19.8067$
2	0.108065	Relaxation-type	$\epsilon_r = 11.9091,$ $\mu_m = 10.9413,$ $f_m = 4.32287$

Lossy RH solution #2: score = 91.48

Layer	Layer thickness (cm)	Material Class	Parameter Values
1	0.016129	Relaxation-type	$\epsilon_r = 12.5103,$ $\mu_m = 15.7947,$ $f_m = 18.3111$
2	0.040645	Lossy magnetic	$\epsilon_r = 9.84164,$ $\mu_r = 2.71554,$ $\mu_i = 15.6334,$ $\alpha = 0.774194,$ $\beta = 0.218964$

Table 4.4: Lossy RH material parameters for two GA designs. Score = 91.48. Goal = -30 dB, threshold = -20 dB. Corresponding reflected power results shown in Fig. 4-9.
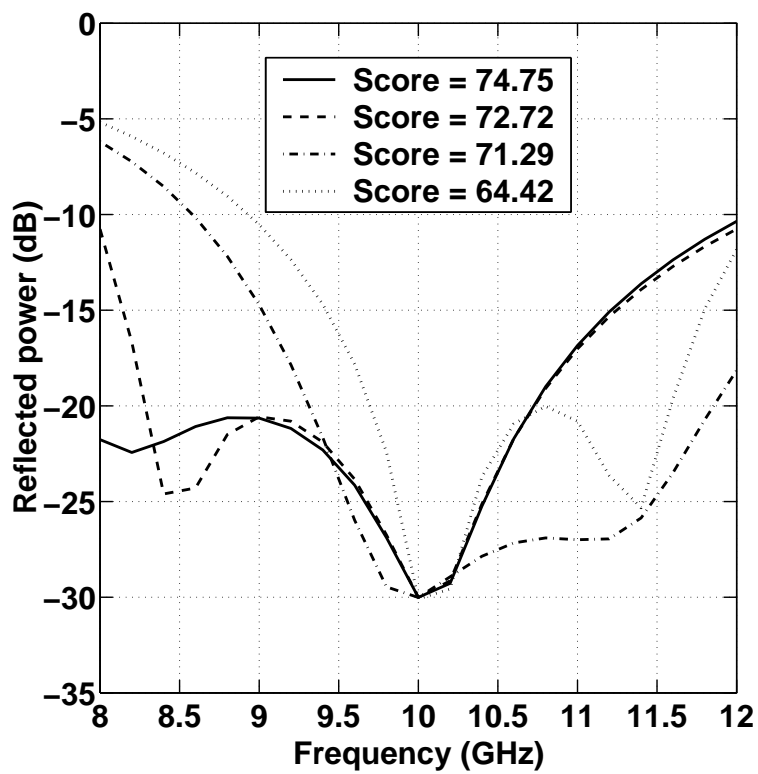
Figure 4-7: Reflected power versus frequency for 2-layer RAM designed using LH meta-materials only. Some typical solutions shown in the plot. Goal = -30 dB, Level = 10 dB. Material parameters are listed in Table 4.3.

(a) Permittivity
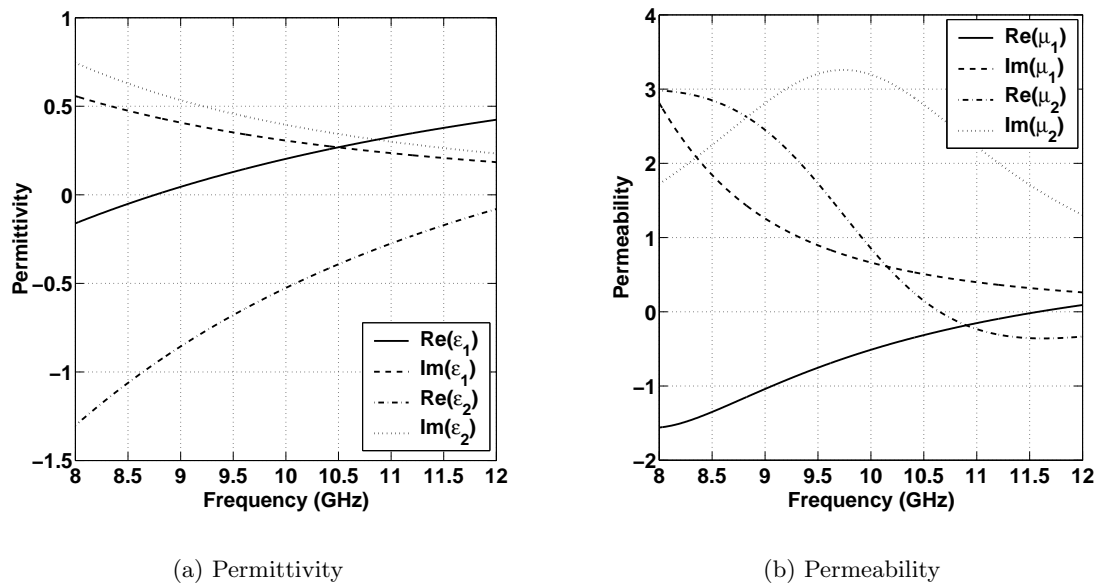
(b) Permeability

Figure 4-8: Permittivity and permeability over frequency band 8–12 GHz for metamaterial (LH) solution #1 as listed in Table 4.3.
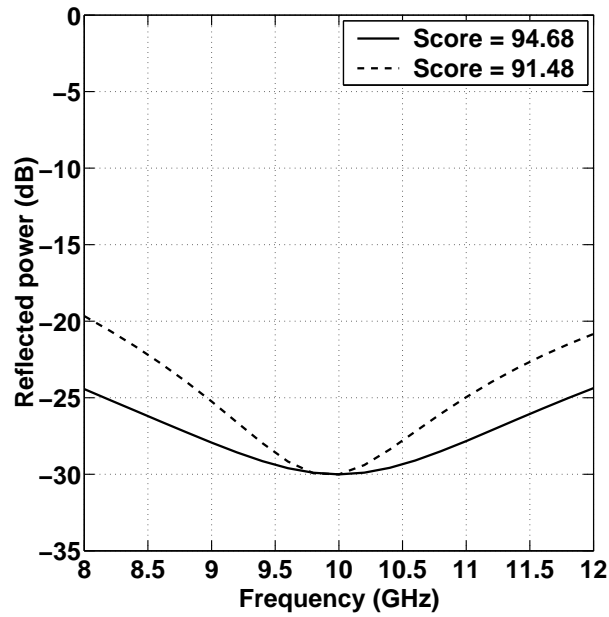
Figure 4-9: Reflected power versus frequency for 2-layer RAM designed using only lossy RH materials. Two GA generated designs are shown. Goal = -30 dB, threshold = -20 dB. Materials parameters are listed in Table 4.4.

4.3.4   Minimization over angular swath

Next, the use of genetic algorithms to design a two layer radar absorber that can minimize the reflection coefficient over a range of incident angles for a single frequency will be investigated. The scoring scheme described in (4.23) will be used as the objective function of the genetic algorithms. To obtain the score, the range of angles is sampled every two degrees. For the examples presented here, the optimization parameter ranges and goals and are as follows,

1. Optimization parameter ranges

   a. Frequency band: 10 GHz

   b. Incident angles: $\theta = 0° - 60°$.

   c. Layer thicknesses: $0.01 - 0.20$ cm.

2. Optimization goals

   a. Index goal: $\theta = 0°$

   b. dB goal: -30 dB

   c. threshold: -20 dB

As before a goal of -30 dB at 10 GHz is quite conservative for normal incidence; however, the challenge in this design will be to maintain that level of absorption over the entire angular swath. In addition, note that the ideal solution used an anisotropic medium with gain properties whereas in the following, the materials are restricted to being isotropic as well as passive.

Direct determination of ϵ and μ

The first example will be to attempt to meet the above goals by directly determining the necessary values for the permittivity and permeability. In directly solving the binary encoding scheme of the GA has been altered such that for each layer there are four unknown

Figure 4-10: Reflected power versus angle at 10 GHz for 2-layer RAM designed using either RH media only, LH media only, or RH and LH media. Goal = -30 dB, threshold = -20 dB. Materials parameters listed in Table 4.5.

material parameters, which are the real and imaginary parts of ϵ and μ. In the following examples, these parameters are restricted as follows:

1. RH only: $0.05 < \Re\{\epsilon, \mu\} < 5$, $\quad 0 < \Im\{\epsilon, \mu\} < 5$

2. LH only: $-5 < \Re\{\epsilon, \mu\} < -0.05$, $\quad 0 < \Im\{\epsilon, \mu\} < 5$

3. RH and LH: $-5 < \Re\{\epsilon, \mu\} < 5$, $\quad 0 < \Im\{\epsilon, \mu\} < 5$

Fig. 4-10 shows the minimization of the reflected power achieved over the range of angles for the different cases listed above. The corresponding material parameters are listed in Table 4.5. For each case, the index goal, dB goal were met, and swath goals were met. The achievable results seem not to depend on the sign of the real part of the permittivity and permeability so much as the magnitude of the imaginary part. Hence, for the present example, there are no advantages to using left-handed media versus right-handed media.

RH solution

Layer	Layer thickness (cm)	Permittivity	Permeability
1	0.0774	$3.5387 + \mathrm{i}1.5200$	$4.2258 + \mathrm{i}1.2561$
2	0.2529	$3.5000 + \mathrm{i}3.7488$	$2.3823 + \mathrm{i}4.2278$

LH solution

1	0.1816	$-4.9129 + \mathrm{i}3.5924$	$-3.2823 + \mathrm{i}1.0313$
2	0.2223	$-0.0500 + \mathrm{i}2.4927$	$-1.8113 + \mathrm{i}1.1095$

LH and RH solution

1	0.1755	$-0.8574 + \mathrm{i}4.7654$	$-1.2042 + \mathrm{i}4.9658$
2	0.2039	$4.3307 + \mathrm{i}3.4311$	$-0.4177 + \mathrm{i}3.5044$

Table 4.5: Permittivity and permeability values found for results shown in Fig. 4-10. Note that for this example, the range of possible thicknesses used was 0.01 cm – 0.32 cm.

Choosing the material parameters

In the previous example, it was seen how appropriate choice of the permittivity and permeability can reduce the reflection coefficient over a wide range of angles. In the following example, the exercise will be repeated, but instead using the GA to find the values of ϵ and μ, the GA will be used to find specific types of materials that can achieve the same type of results. For this example, three different types of solution will be presented. The first will utilize only right-handed materials, the second only left-handed materials, and the third will utilize a combination of a RH media and a LH media. Fig. 4-11 shows the minimization of the reflected power achieved over the range of angles for the different cases listed above. The corresponding material parameters are listed in Table 4.6. For each case, the index goal, the dB goal, and the swath goals were met.

RH solution: score = 71.98

Layer	Layer thickness (cm)	Material Class	Parameter Values
1	0.034516	Relaxation-type	$\epsilon_r = 9.02053$, $\mu_m = 7.97947$, $f_m = 28.2525$
2	0.059032	Relaxation-type	$\epsilon_r = 13.1994$, $\mu_m = 15.0323$, $f_m = 4.73343$

Metamaterial (LH) solution: score = 73.84

Layer	Layer thickness (cm)	Material Class	Parameter Values
1	0.200000	Rings only	$f_{mo} = 16.4839$, $f_{mp} = 19.8341$, $\gamma_m = 2.77226$
2	0.132581	Rods & rings	$f_{ep} = 6.95308$, $f_{mo} = 9.65103$, $f_{mp} = 13.0159$, $\gamma_e = 2.45457$, $\gamma_m = 1.66767$

RH and Metamaterial (LH) solution: score = 71.87

Layer	Layer thickness (cm)	Material Class	Parameter Values
1	0.010000	Rods only	$f_{ep} = 16.5425$, $\gamma_e = 2.82114$
2	0.071290	Lossy magnetic	$\epsilon_r = 3.88856$, $\mu_r = 3.09677$, $\mu_i = 14.0352$, $\alpha = 0.753666$, $\beta = 0.312805$

Table 4.6: Material parameters for select solutions. Goal = -30 dB, threshold = -20 dB. Corresponding reflected power results shown in Fig. 4-11.

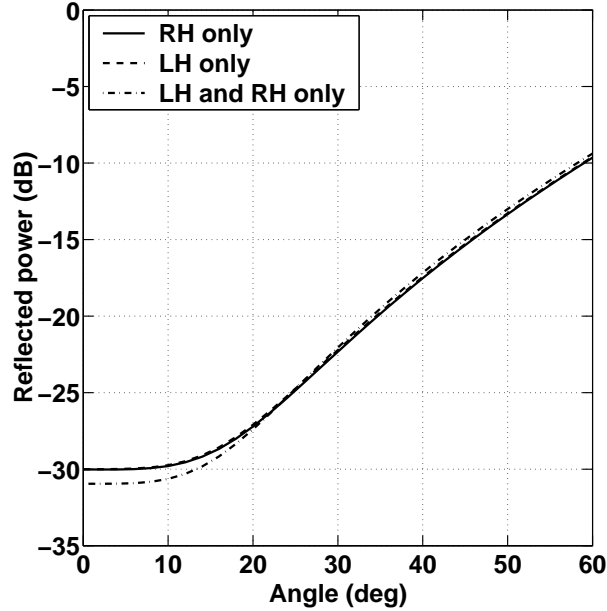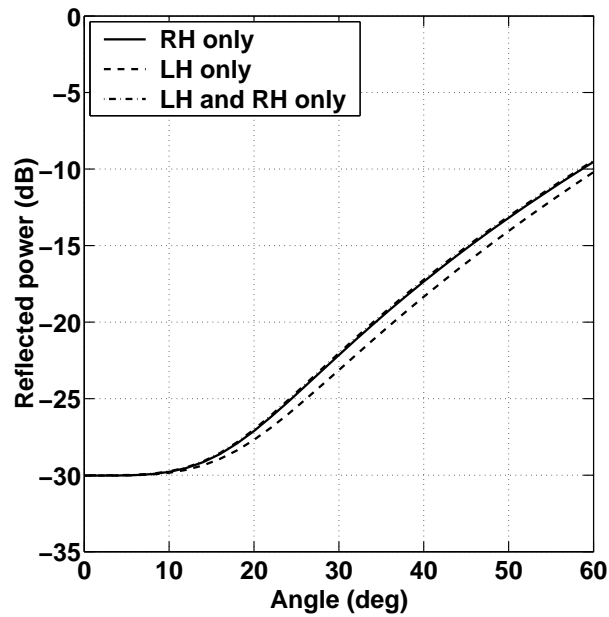Figure 4-11: Reflected power versus angle at 10 GHz for 2-layer RAM designed either RH only, LH only, or RH and LH. parameters found are in terms of actual material model parameters rather than just specific values of ϵ and μ. Shown are typical results after several GA runs. Goal = -30 dB, threshold = -20 dB. Materials parameters listed in Table 4.6.

4.3.5 Minimization over frequency and angle simultaneously

The obvious next question is can these materials be used to achieve similar types of results over both angle and frequency band. In this section, a few examples that achieve this goal will be presented. In generating these results, a modified scoring scheme was used in order to minimize over frequency and angle. This modified version essentially averages the scores achieved along frequency for each angle and along angle for each frequency. For example, if the frequency-angle space was sampled at 5 frequencies by 20 angles, a total of 5 angular swaths and 20 frequency scores would be averaged. In this work, when minimizing over frequency and angle, the goal will be to place the deepest null at one specific frequency and angle, *e.g.*, 10 GHz and 0°. Thus, in order to promote a solution of this form, rather than directly averaging the scores, a weighting system is employed. For the following examples, the weights are designed using a Hamming window that is centered at the frequency or angle of interest. The following example will illustrate an optimal solution for this scoring scheme. Note that in this example, the band of frequencies sampled is half as wide as previously considered, ranging from 9 GHz to 11 GHz. Also, the angular swath has been reduce to the range 0 to 30 degrees.

The result shown in Fig. 4-12, which was designed using right-handed materials, is the type of solution expected under the scoring scheme described above. The corresponding material parameters are listed in Table 4.7. Note that the smallest amount of reflection approximately occurs at 10 GHz and 0°. Also note that for a given frequency and for increasingly larger angles, the amount of reflection increases, whereas at a given angle, the amount of reflection increase as the frequency departs from the center frequency of 10 GHz.

On the other hand, the solution obtained using only left-handed metamaterials does not follow this prescription very well. The corresponding material parameters are listed in Table 4.8. For small angles, the solution obtained, shown in Fig. 4-13, has the smallest reflected power around 10 GHz in agreement with the desired results; however, outside
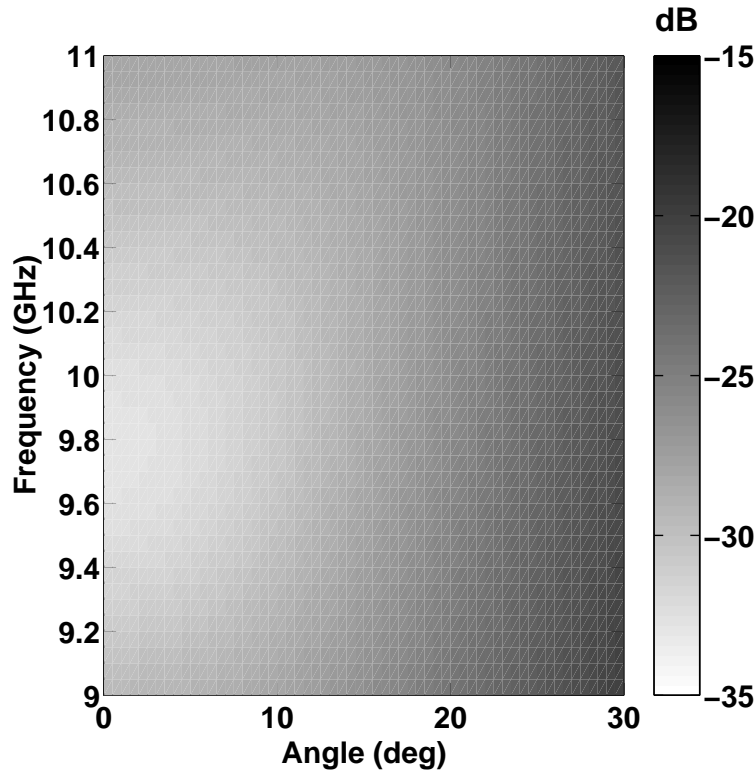
Figure 4-12: RH only minimization over frequency and angle. The score is based on Frequency band from 9 to 11 GHz, and angular swath from 0 to 30 degrees. Objective scored by sampling at 5 frequencies for each angle which were sampled every 2 degrees. Score = 91.44.

the narrowband surrounding the center frequency, particularly in the lower frequencies, the solution has a smaller reflected power at angles much larger than zero degrees. Hence, while the solution obtained may be useful for some applications, it did not achieve the desired specifications.

The final example shown uses a combination of a right-handed material and metamaterial. The corresponding material parameters are listed in Table 4.9. The score obtained for the results shown in Fig. 4-14 is comparable to the score obtained for the purely right-handed medium solution.

Layer	Layer thickness (cm)	Material Class	Parameter Values
1	0.065161	Lossy magnetic	$\epsilon_r = 3.91789$, $\mu_r = 8.1261$, $\mu_i = 13.6833$, $\alpha = 0.204301$, $\beta = 0.529814$
2	0.193871	Relaxation-type	$\epsilon_r = 10.4868$, $\mu_m = 9.31378$, $f_m = 5.23196$

Table 4.7: RH media only. Material parameters for best solution out of 5 GA runs. Score = 91.44. Goal = -30 dB, threshold = -20 dB. Corresponding reflected power results shown in Fig. 4-12.

Layer	Layer thickness (cm)	Material Class	Parameter Values
1	0.138710	Rings only	$f_{mo} = 8.5366$, $f_{mp} = 13.6122$, $\gamma_m = 2.79181$
2	0.083548	Rods & rings	$f_{ep} = 11.5572$, $f_{mo} = 11.4106$, $f_{mp} = 15.2593$, $\gamma_e = 0.0401007$, $\gamma_m = 3.16816$

Table 4.8: LH metamaterials only. Material parameters for best solution out of 5 GA runs. Score = 83.52. Goal = -30 dB, threshold = -20 dB. Corresponding reflected power results shown in Fig. 4-13.
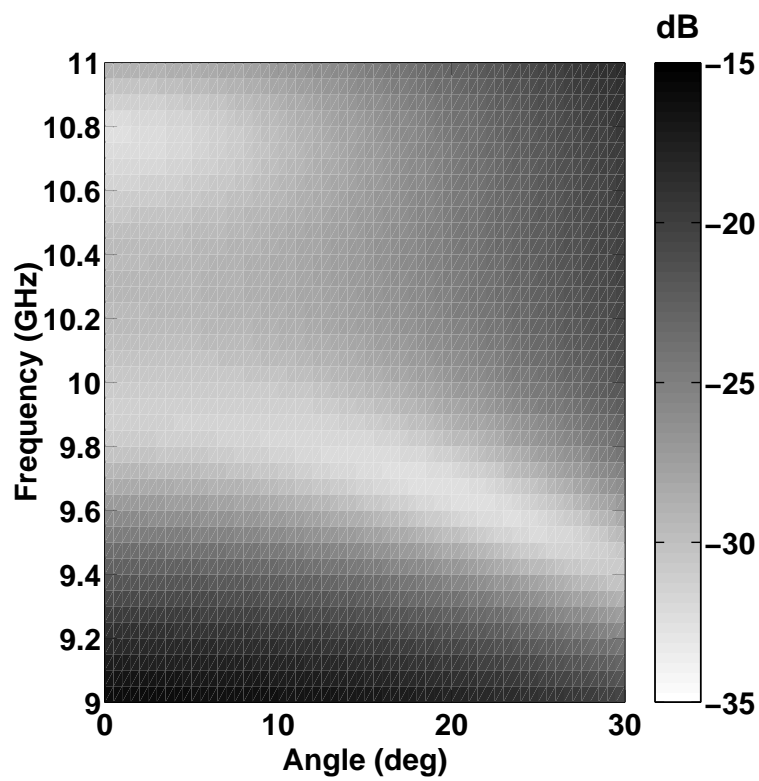
Figure 4-13: Metamaterial only minimization over frequency and angle. Frequency band from 9 to 11 GHz, and angular swath from 0 to 30 degrees. Objective scored by sampling at 5 frequencies per angle, and 16 angles per frequency. Score = 83.52.
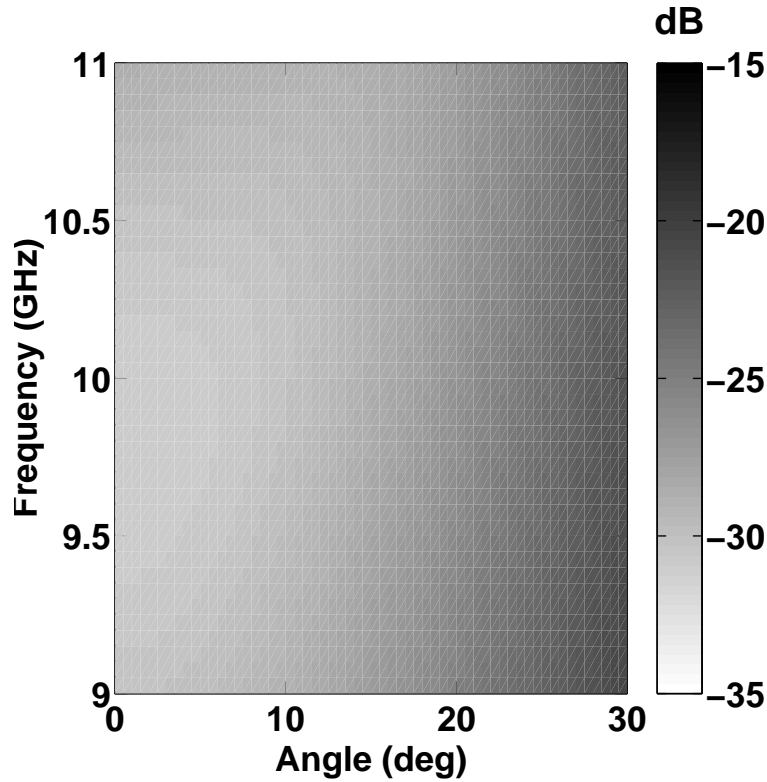
Figure 4-14: RH Lossy and Metamaterial minimization over frequency and angle. Frequency band from 9 to 11 GHz, and angular swath from 0 to 30 degrees. Objective scored by sampling at 5 frequencies per angle, and 16 angles per frequency. Score = 91.16.

Layer	Layer thickness (cm)	Material Class	Parameter Values
1	0.114194	Relaxation-type	$\epsilon_r = 4.26979$, $\mu_m = 13.5367$, $f_m = 2.82727$
2	0.108065	Rods & rings	$f_{ep} = 14.1378$, $f_{mo} = 5.2522$, $f_{mp} = 9.5262$, $\gamma_e = 0.0401007$, $\gamma_m = 2.49367$

Table 4.9: RH and MTM. Material parameters for best solution out of 5 GA runs. Score = 91.16. Goal = -30 dB, threshold = -20 dB. Corresponding reflected power results shown in Fig. 4-14.

4.4   Summary

In summary, this chapter has discussed the potential of using left-handed metamaterials as radar absorbers. In order to design the multilayer (2 layers for the above examples) coating, the use of genetic algorithms was employed. The unknown parameters were the class of material, the parameters of the particular class, and the layer thickness. For comparison, a set of generic right-handed absorbers were also used to generate radar absorbing coatings. The GAs attempted to minimize the reflection coefficient over a given frequency band at normal incidence, or a given angular swath at a fixed frequency, or both simultaneously. For each type, it was found that while left-handed metamaterials generally could be used as radar absorbers, the effective bandwidth over which they are viable is much smaller than those designs achieved using conventional right-handed absorbers. However, in the case of minimizing over a given angular swath, left-handed materials performed similarly to the right-handed materials indicating that the sign of the real part of the permittivity and permeability is not as crucial as the magnitude of the imaginary part. Yet despite these drawbacks, metamaterials offer an alternative to conventional radar absorbers. In general, in terms of applications, the main advantage provided by metamaterials today is that they are scalable and light-weight. In other words, they can easily be redesigned to operate at different wavelengths, and because they are mostly air filled they are light-weight, and would be well-suited to applications that are constrained by weight such as space-based applications.

Chapter 5

A wideband directive antenna using left-handed metamaterials

5.1 Introduction

One potentially useful property of metamaterials that possess left-handed properties at some frequencies is that, because they are frequency dispersive, the real part of their index of refraction can vary from negative to zero to positive. Thus, if an antenna source, placed inside a metamaterial substrate, radiates at a frequency where the index of refraction is approximately zero, then by Snell's law all the source rays emitted from inside the substrate will be transmitted into free-space at an angle close to the normal of the slab, *i.e.*, creating a highly directive antenna (see Fig. 5-1).

Recently, Enoch *et al* [100] have constructed an antenna based on this concept by embedding a monopole inside a substrate made of periodically arranged metallic rods. Enoch *et al* measured one such antenna configuration to have a half-power beamwidth of about $\Delta\theta_1 = 8.9°$ in the H plane and $\Delta\theta = 12.5°$ in the E plane at the single frequency of 14.5 GHz [100]. The narrowband characteristic of the substrate can be understood by noting that the rods behave similarly to an electric plasma medium [2], which has an index of
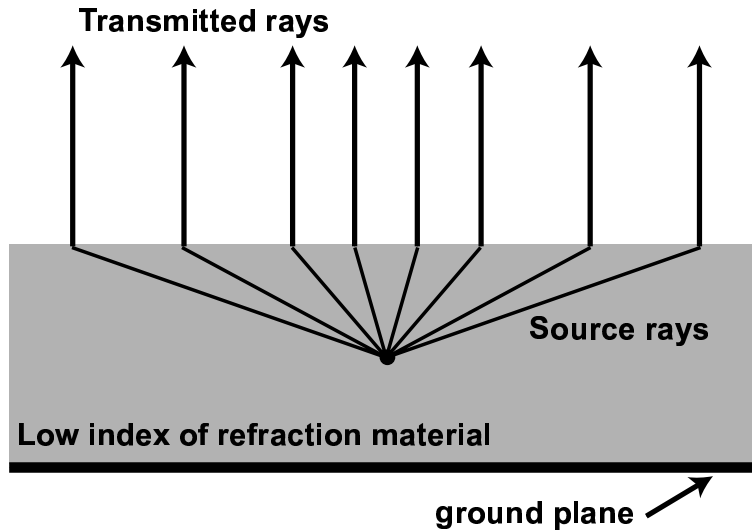
Figure 5-1: Directive antenna concept. By Snell's law, if a source is embedded in a substrate that has a small index of refraction compared to air, its source rays will be transmitted near the normal of the substrate.

refraction that is approximately zero only near the plasma frequency.

Other recent directive antenna designs, based on photonic band gap structures [101–103] have also been limited by a narrow operating bandwidth. In these approaches, a structure, which has a band gap at the operating frequency of interest is created. A defect is then placed in the structure by removing one or more of the periodic elements creating a Fabry-Perot resonator, which with a source placed inside it will emit a highly narrow beam. Still, because the cavity was only resonant for a specific frequency, this PBG design had a high directivity over a narrow frequency band.

In the previous two examples, the high directivity of the antennas was only maintained over a narrowband, which limited their use. In this chapter, the potential of metamaterials to improve the bandwidth over which a narrow beamwidth can be achieved is examined. As in [100], narrow beamwidth is achieved by embedding a source inside a low index of refraction material; however, rather than engineer the index of refraction by only adjusting the substrate's electrical properties (ϵ), the ability to adjust its magnetic properties (μ) will

also exploited. In particular, in the Chapter 3 it was shown how a periodic arrangement of rods can effect the permittivity and a periodic arrangement of split-rings can control the permeability. It was seen that the permittivity and permeability were negative for a range of frequencies, and equal to zero at their respective plasma frequencies. Thus, an antenna embedded in such a substrate would radiate with a narrow beamwidth at these two frequencies. In fact though, as will be shown, it is possible to adjust these plasma frequencies such that a narrow beamwidth can be achieved over a relatively wide bandwidth. For the studies in this chapter, the Drude and Lorentz bulk media models for the permittivity and permeability, respectively, will be used (see eqns. 3.1 and 3.2).

In addition, because the substrate will have a low index of refraction, the advantages of using a perfect magnetic conductor (PMC) ground plane versus a perfect electric conductor (PEC) ground plane will be examined. As will be shown, PMC ground planes yield larger gains and in fact narrower beamwidths due to its imaging properties. It should be noted that although PMC surfaces are only a mathematical construct, it is possible to create an artificial PMC by using a composite high-impedance ground plane [104].

5.2 Formulation

The configuration under study, shown in Fig. 5-2, is an infinite linear antenna placed at $z = 0$ inside of homogeneous slab of thickness $d_1 + d_2$, which is backed by either a PMC or PEC ground plane located at $z = -d_2$. To determine the radiation pattern, the two-dimensional Green's function is used. The general solution for the electric field in region ℓ, $\overline{E}_\ell = \hat{x} E_{\ell x}$, is [59],

$$E_{\ell x} = \int_{-\infty}^{\infty} dk_y \left[A_\ell e^{ik_{\ell z} z} + B_\ell e^{-ik_{\ell z} z} \right] e^{ik_y y}, \tag{5.1}$$

where A_ℓ and B_ℓ are the expansion coefficients. Since the source is located inside region 1, they can be written as, $A_0 = TE_{lin}$, $B_0 = 0$, $A_{1+} = \alpha_1 + E_{lin}$, $B_{1+} = \beta_1$ $A_{1-} = \alpha_1$,
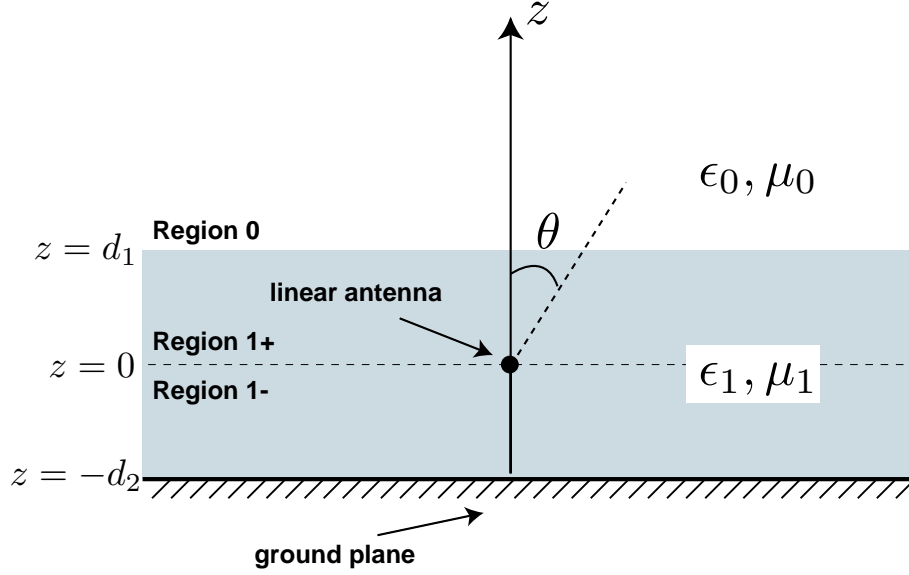
Figure 5-2: Geometry for directive emission studies.

$B_{1-} = \beta_1 + E_{lin}$ where $1+$ refers to the region inside the slab above the source $(0 < z < d_1)$, and $1-$ refers to the region below $(-d_2 < z < 0)$, and E_{lin} is the source term given by,

$$E_{lin} = -\frac{\omega \mu_1 I}{4\pi k_{1z}}. \tag{5.2}$$

The unknown coefficients are found by enforcing the boundary conditions at $z = d_1$ and $z = -d_2$. Note that, of course, the boundary condition at $z = -d_2$ depends on the type of ground plane. In the case of a PEC, $E_{1x}(z = -d_2) = 0$ whereas for a PMC, $H_{1y}(z = -d_2) = 0$. For example, the T coefficient is,

$$T = \left(\frac{2}{1 + p_{10}^{TE}}\right) \frac{e^{ik_{1z}d_1} \pm e^{ik_{1z}(2d_2+d_1)}}{1 \mp R_{10}e^{i2k_{1z}(d_2+d_1)}} e^{-ik_{0z}d_1}, \tag{5.3}$$

where

$$p_{10}^{TE} = \frac{\mu_1 k_{0z}}{\mu_0 k_{1z}} \tag{5.4}$$

$$R_{10}^{TE} = \frac{1 - p_{10}^{TE}}{1 + p_{10}^{TE}}, \tag{5.5}$$

and where the upper sign refers to the PMC case and the lower to the PEC case.

The radiation pattern is determined by approximating the integral in (5.1) by using far-field assumptions as follows,

$$
\begin{aligned}
E_{0x} &= \int_{-\infty}^{\infty} dk_y \left[TE_{lin} \right] e^{ik_{0z}z} e^{ik_y y} \\
&\approx f(k_{yo}) \int_{-\infty}^{\infty} dk_y e^{ikr} \exp\left[\frac{-ir}{2k \cos^2 \theta} (k_y - k_{yo})^2 \right] \\
&= f(k_{yo}) \frac{e^{ikr - i\pi/4}}{\sqrt{r}} \sqrt{2\pi k} \cos \theta \tag{5.6}
\end{aligned}
$$

where $k_{yo} = k_0 \sin \theta$ is the stationary phase point and $f(k_{yo}) = T(k_{yo}) E_{lin}(k_{yo})$.

5.3 Ideal substrates

Before exploring the use of metamaterials, it is useful to understand the radiation pattern of a source embedded in an ideal low-index of refraction medium. In the following sections, fixed values of ϵ and μ are chosen in order to study the effects of ground plane type, anisotropy, and substrate geometry.

5.3.1 Effects of the groundplane: PEC *vs.* PMC

The formulation given in the previous section was developed for the case where the ground plane is either a perfect electric conductor (PEC) or a perfect magnetic conductor (PMC). From image theory, it is well known that a horizontally or tangentially oriented source over a PEC ground plane is equivalent to having two sources of *opposite* sign (*i.e.*, out of phase)

placed at mirror locations. On the other hand, a horizontal source over a PMC ground plane is equivalent to having two sources of the *same* sign (*i.e.*, in phase).

For many applications, the distinction between PEC and PMC ground planes is not important since the electrical distance between the source and image is relatively large. However, for the current application, the source will be embedded in a low index of refraction medium whose wavelength is relatively large compared to the source-ground plane separation, meaning that the source and its image are electrically close. In the case of a tangential source above a PEC ground plane, because the source and image are out of phase, destructive interference occurs, and the gain of the antenna is reduced. In constrast, with a PMC ground plane, the source and image will be in phase and the antenna will have a larger gain.

To illustrate the effect of the ground plane with a specific example, consider the ideal case of a material that is isotropic and non-dispersive with $\epsilon_1(\omega) = 0.01$ and $\mu_1(\omega) = 1$. Fig. 5-3 shows the radiation pattern as a function of frequency of a source embedded in a substrate over a PEC and PMC ground plane. As can be seen, both radiation patters are highly directive; however, the radiated power of the PMC system is several decibels higher.

In order to more precisely quantify the performance of the overall antenna, the half-power beamwidth (HPBW) and peak power (or gain) of the system are calculated. The peak power or gain of the system is the measure as the strength of the main lobe with respect to an isotropic radiator. The HPBW of the system is defined as the angular swath over which the antenna maintains a power level greater than or equal to the peak power. Note that for certain radiation patterns, some of which will be encountered later in Section 5.4, the HPBW cannot be defined because the main lobe is not centered at $\theta = 0°$. For the radiation patterns shown above in Fig. 5-3, Fig. 5-4 shows the corresponding HPBW and peak power versus frequency.

The peak power of the PMC system is near 6 dB $(10 \log(1+1)^2)$, which corresponds to the nearly complete constructive interference of the source and image. On the other hand, the PEC power level is quite low, although increasing as a function of frequency as the source

(a) Radiation Pattern for PEC

(b) Radiation Pattern for PMC
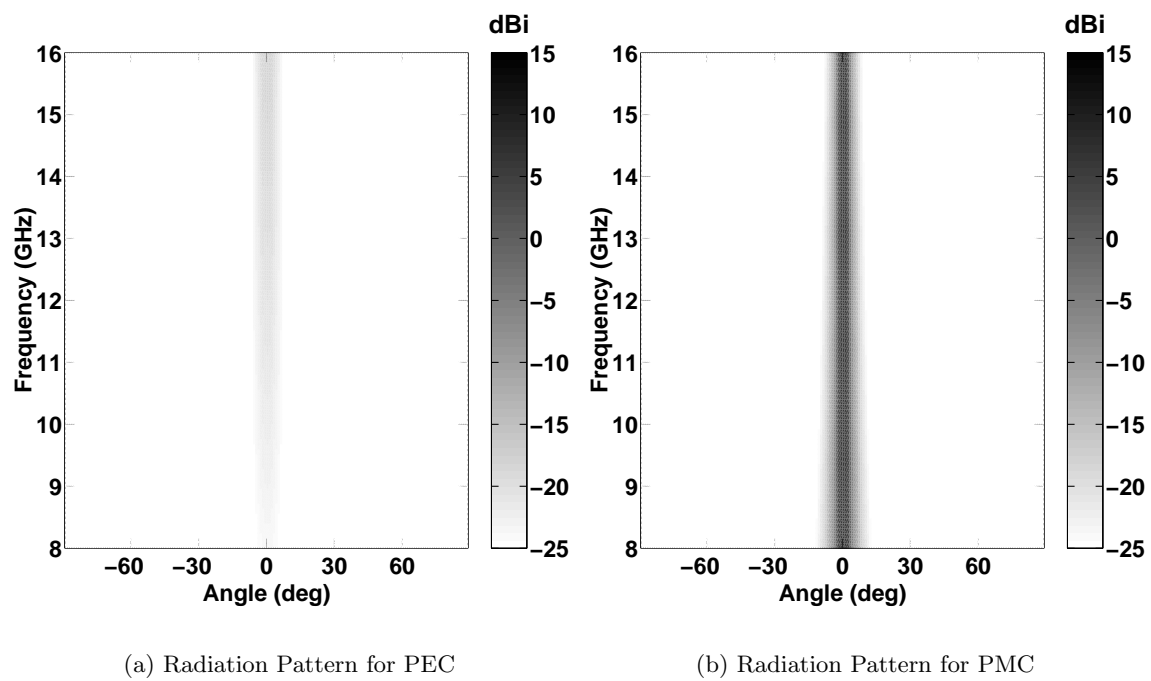
Figure 5-3: Antenna radiation properties for ideal isotropic medium with a constant relative permittivity of $\epsilon_{r1} = 0.01$ and a constant relative permeability of $\mu_{r1} = 0.01$. Slab is 4 cm thick and the source is equidistant from the ground plane and air-media interface.

(a) Half-power beamwidth   (b) Peak power
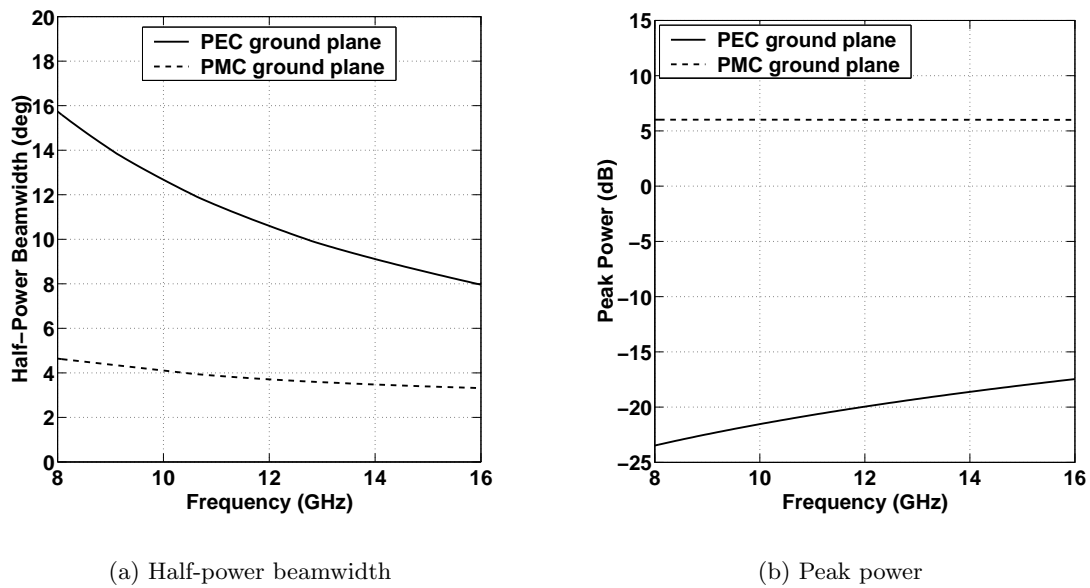
Figure 5-4: Antenna radiation properties for ideal isotropic medium with a constant relative permittivity of $\epsilon_{r1} = 0.01$ and a constant relative permeability of $\mu_{r1} = 0.01$. Slab is 4 cm thick and the source is equidistant from the ground plane and air-media interface.

and image become electrically further apart. In addition, the beamwidth for the PMC is better than that of the PEC system. This is due to the fact that the distinction between the PMC and PEC systems becomes less apparent for the rapidly attenuating source evanescent waves. Specifically the transmission coefficient for large k_{1z} can be approximated as follows,

$$T \sim \left(\frac{2}{1 + p_{10}^{TE}} \right) e^{ik_{1z}d_1} e^{-ik_{0z}d_1}, \tag{5.7}$$

where there is no distinction between PEC and PMC ground planes. The better beamwidth results from the fact that there is less destructive interference for the PMC system and thus a higher peak; however, this higher peak must roll off faster than the the smaller peak of the PEC system in order that they reach the same power level for the transmission angles corresponding to the large k_{1z} components of the source inside the substrate.

5.3.2   Effects of anisotropy

In the previous examples, the ideal substrates considered were isotropic. Although, in this chapter, all calculations are performed under the bulk media assumption, it is important to note that it is possible to engineer metamaterials with these properties. However, in practice metamaterials are often anisotropic, so it is important to understand effects of anisotropy on the radiation properties of a source embedded in such a material. In particular, the rods are known to affect the component of the permittivity tensor corresponding to their lengthwise orientation, whereas as the rings are known to affect the component corresponding to the direction of their central axis [2, 3].

As in Chapter 2, the model used for representing the anisotropy of the rod and split-ring resonator metamaterials will be frequency dispersive material tensors of the form,

$$\overline{\overline{\epsilon}}(\omega) = \begin{pmatrix} \epsilon_x(\omega) & 0 & 0 \\ 0 & \epsilon_y(\omega) & 0 \\ 0 & 0 & \epsilon_z(\omega) \end{pmatrix} \quad \overline{\overline{\mu}}(\omega) = \begin{pmatrix} \mu_x(\omega) & 0 & 0 \\ 0 & \mu_y(\omega) & 0 \\ 0 & 0 & \mu_z(\omega) \end{pmatrix}. \tag{5.8}$$

In general, the dispersion relation of an anisotropic medium can be determined by solving the following equation [59],

$$\det\left[\overline{k}\times\overline{\overline{I}}\cdot\overline{\overline{\mu}}^{-1}\cdot\overline{k}\times\overline{\overline{I}}+\omega^2\overline{\overline{\epsilon}}\right]=0, \tag{5.9}$$

where $\overline{k}$ and $\overline{\overline{I}}$ are the three-dimensional wave vector and unity matrix, respectively. Assuming that the electric field is polarized along the $\hat{y}$ direction, the dispersion relation above can be simplified as,

$$k_z^2=\epsilon_y\mu_x\omega^2-\frac{\mu_x}{\mu_z}k_y^2, \tag{5.10}$$

where k_y and k_z are the two non-zero k components of a wave polarized along the y direction with a spatial cutoff frequency of $k_{cy}=\omega\sqrt{\epsilon_y\mu_z}$.

The formulation for determining the radiation pattern of a source embedded in an anisotropic medium is very similar to the isotropic formulation. In order to use the formulation given in the previous section, it is only necessary to use the appropriate dispersion relation, *i.e.*, eq. (5.10), to calculate k_{1z}, and to change the form of p_{10}^{TE} and R_{10}^{TE} as follows,

$$p_{10}^{TE} = \frac{\mu_{1y}k_{0z}}{\mu_0 k_{1z}} \tag{5.11}$$

$$R_{10}^{TE} = \frac{1-p_{10}^{TE}}{1+p_{10}^{TE}}, \tag{5.12}$$

where the μ_{1y} term in the numerator of p_{10}^{TE} has replaced the previous term, μ_1, given in the isotropic case.

Before preceding to calculate radiation patterns, it is helpful to consider how the individual plane wave components of the source will be transmitted from the substrate into freespace. By phase-matching, a particular k_{1z} component and its corresponding transmis-

sion angle into region 0 are related by,

$$k_0 \sin \theta_0 = k_1 \sin \theta_1 = \sqrt{k_1^2 - k_{1z}^2} \tag{5.13}$$

where k_1 is the wavenumber of the substrate. For the moment, consider the case when the permittivity (ϵ_1) and permeability (μ_1) of the substrate are both positive and purely real, and possibly less than those of free space. Under these assumptions, propagating waves inside the slab, which correspond to purely real k_{1z}, will all translate to propagating waves in region 0. In addition, due the source, there will also be evanescent waves present in region 1. Due to a critical-angle type effect, some of these waves, for which k_{1z} is purely imaginary, will also translate to propagating waves in region 0. However because the quantity k_{1z}^2 is negative, the term on left-hand side of (5.13) will be larger than k_1 meaning the angle of transmitted propagating waves corresponding to imaginary k_{1z} will be larger than those that correspond to real k_{1z}. This fact is illustrated for four different anisotropic media in Fig. 5-5. In each of the four cases, the components of the permittivity and permeability tensors are ideally assumed to take on either the values 1 or 0.1. As can be seen, the angle at which transmitted waves begin to be due to the evanescent waves of the source depends on which components are equal to 0.1. In particular, the angle depends on the spatial cutoff frequency of the medium, k_{cy}, which for a TE polarized wave depends only on the ϵ_{1y} and μ_{1z} components.

In the ideal case, if all the evanescent waves are suppressed (*i.e., not transmitted*), the the value of μ_{1x} does not matter. However, because the value of μ_{1x} affects the slope of k_{1z}, as can be seen in (5.10), it is actually advantageous in terms of beamwidth to use an anisotropic substrate with only the ϵ_{1y} and μ_{1z} components being small. This is due to the fact that evanescent waves inside this medium are attenuated more rapidly than in any of the other three media.

So far, only media with positive values of ϵ and μ have been considered; however, in the construction of metamaterials with rods and SRR, it is possible that at some frequencies
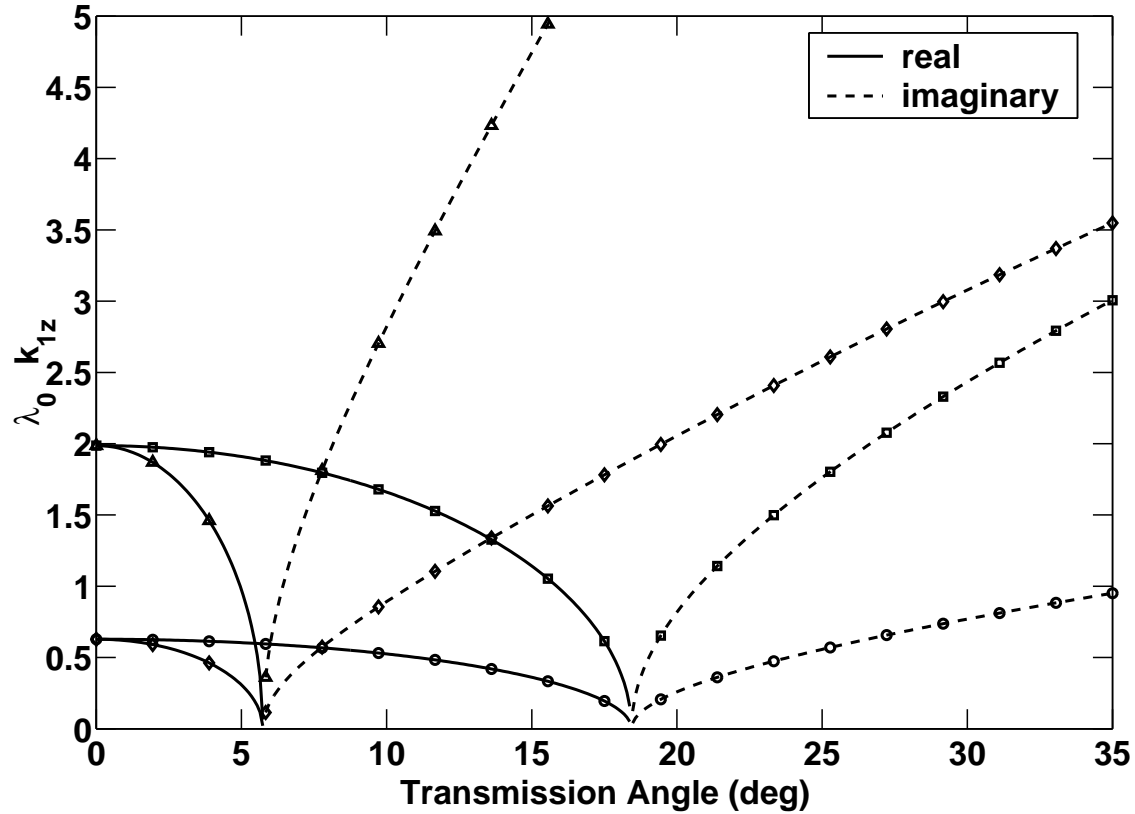
Figure 5-5: Relation between k_{1z} and the transmission angle into free space for four different anisotropic substrates. Permittivity and permeability tensor components are given as:
$\square$: $\epsilon_y = 0.1$, $\mu_y = \mu_z = 1$, $\diamond$: $\epsilon_y = \mu_y = \mu_z = 0.1$, $\circ$: $\epsilon_y = \mu_y = 0.1$, $\mu_z = 1$, $\triangle$: $\epsilon_y = \mu_z = 0.1$, $\mu_y = 1$.

in the band of interest that either the permittivity or permeability will take on small but negative values. This sign change will affect the dispersion relation, and potentially destroy the directive properties of the substrate. For example, consider the case when $\epsilon'_y = 0.1$, $\mu'_z = -0.1$, $\mu'_y = 1$. At first glance, this case is similar to the best case depicted in Fig. 5-5, where the evanescent waves are attenuated the most rapidly. However, further examination reveals that the far-field pattern is highly oscillatory and contains two spikes just beyond the normal direction. The angle of the spikes correspond to the spatial cutoff frequency for this medium, where it happens that transmission coefficient is largest. Fortunately, as shown in
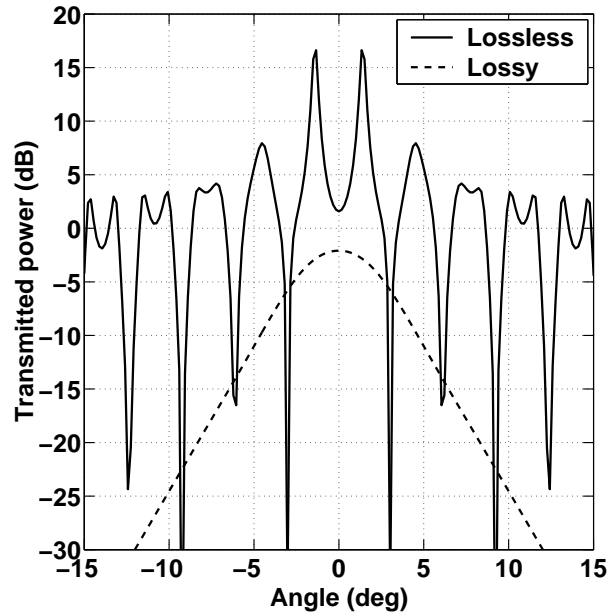
Figure 5-6: Radiation pattern for a source operating at 14 GHz that is embedded in the center of a 4 cm thick anisotropic substrate over a PEC groundplane. Loss helps eliminate spikes due to the large transmission coefficient of the evanescent waves. Real parts of the permittivity and permeability tensor components are: $\epsilon_y' = 0.1$, $\mu_z' = -0.1$, $\mu_y' = 1$. For the lossy case, the imaginary parts are, $\epsilon_y'' = \mu_z'' = 0.05$.

Fig. 5-6, introduction of a small amount of loss alleviates this problem by smoothing out the oscillations and removing the spikes, albeit at the cost of gain and beamwidth.

Still, there are many other combinations to consider. Tables 5.1 and 5.2 list each of these different possibilities for the cases of a PEC or PMC ground plane. For some combinations, the half-power beamwidth is left undefined (–) because the main lobe of the radiation pattern is not centered at $\theta = 0$. In many of these cases, the reason it is undefined is because there are two main lobes that are due to the spikes-type effect discussed above. As before, introduction of a small loss component somewhat removes this problem, but the resulting beamwidths are usually larger.

$\Delta = 0.01$, $\epsilon''_y = \mu''_x = \mu''_z = 0$					$\Delta = 0.01$, $\epsilon''_y = \mu''_x = \mu''_z = 0.05$				
ϵ'_y	μ'_x	μ'_z	HPBW	Gain	ϵ'_y	μ'_x	μ'_z	HPBW	Gain
Δ	1	Δ	1.61	1.58	Δ	1	Δ	4.57	-2.42
$-\Delta$	1	Δ	1.78	-1.48	$-\Delta$	1	Δ	5.00	-4.32
1	Δ	Δ	6.43	-11.12	Δ	1	$-\Delta$	5.38	-2.42
$-\Delta$	$-\Delta$	$-\Delta$	9.08	-18.62	$-\Delta$	1	$-\Delta$	6.07	-4.32
Δ	Δ	Δ	9.08	-18.62	1	1	$-\Delta$	9.97	-5.03
Δ	$-\Delta$	$-\Delta$	9.12	-18.73	Δ	Δ	Δ	10.98	-9.44
$-\Delta$	Δ	Δ	9.12	-18.73	$-\Delta$	$-\Delta$	$-\Delta$	10.98	-9.44
1	$-\Delta$	$-\Delta$	10.93	-23.11	$-\Delta$	Δ	Δ	10.99	-9.49
Δ	1	1	16.11	1.58	Δ	$-\Delta$	$-\Delta$	10.99	-9.49
$-\Delta$	1	1	17.87	-1.48	1	1	Δ	11.16	-5.03
1	Δ	1	53.79	-11.12	Δ	Δ	$-\Delta$	11.21	-9.44
Δ	Δ	1	65.84	-18.62	$-\Delta$	$-\Delta$	Δ	11.21	-9.44
$-\Delta$	Δ	1	65.99	-18.73	$-\Delta$	Δ	$-\Delta$	11.27	-9.49
1	$-\Delta$	1	121.91	-23.11	Δ	$-\Delta$	Δ	11.27	-9.49
Δ	$-\Delta$	1	139.39	-18.50	1	Δ	$-\Delta$	15.53	-15.03
$-\Delta$	$-\Delta$	1	139.87	-18.37	1	$-\Delta$	$-\Delta$	16.49	-17.06
1	1	1	–	–	1	Δ	Δ	17.52	-15.03
1	1	Δ	–	–	1	$-\Delta$	Δ	19.22	-17.06
1	1	$-\Delta$	–	–	Δ	1	1	20.19	-2.42
1	Δ	$-\Delta$	–	–	$-\Delta$	1	1	20.64	-4.32
1	$-\Delta$	Δ	–	–	$-\Delta$	Δ	1	64.85	-9.49
Δ	1	$-\Delta$	–	–	Δ	Δ	1	65.89	-9.44
Δ	Δ	$-\Delta$	–	–	$-\Delta$	$-\Delta$	1	77.53	-9.44
Δ	$-\Delta$	Δ	–	–	Δ	$-\Delta$	1	79.22	-9.49
$-\Delta$	1	$-\Delta$	–	–	1	1	1	–	–
$-\Delta$	Δ	$-\Delta$	–	–	1	Δ	1	–	–
$-\Delta$	$-\Delta$	Δ	–	–	1	$-\Delta$	1	–	–

Table 5.1: Ranking according to beamwidth of 27 different possible combinations of an anisotropic substrate over a PEC groundplane for a source operating at 14 GHz that is embedded in the center of a 4 cm thick substrate. Both lossless (left) and lossy (right) substrates are considered.

$\Delta = 0.01$, $\epsilon''_y = \mu''_x = \mu''_z = 0$						$\Delta = 0.01$, $\epsilon''_y = \mu''_x = \mu''_z = 0.05$				
ϵ'_y	μ'_x	μ'_z	HPBW	Gain		ϵ'_y	μ'_x	μ'_z	HPBW	Gain
Δ	1	Δ	0.71	12.43		Δ	1	Δ	4.42	-3.37
$-\Delta$	1	Δ	1.29	2.44		$-\Delta$	1	Δ	4.45	-4.25
Δ	$-\Delta$	$-\Delta$	3.10	5.92		Δ	1	$-\Delta$	4.76	-3.37
$-\Delta$	Δ	Δ	3.10	5.92		$-\Delta$	1	$-\Delta$	5.01	-4.25
$-\Delta$	$-\Delta$	Δ	3.24	6.01		$-\Delta$	Δ	Δ	5.71	1.25
Δ	Δ	$-\Delta$	3.24	6.01		Δ	$-\Delta$	$-\Delta$	5.71	1.25
$-\Delta$	$-\Delta$	$-\Delta$	3.46	6.03		Δ	Δ	$-\Delta$	5.71	1.28
Δ	Δ	Δ	3.46	6.03		$-\Delta$	$-\Delta$	Δ	5.71	1.28
$-\Delta$	Δ	$-\Delta$	3.62	6.03		Δ	Δ	Δ	5.76	1.28
Δ	$-\Delta$	Δ	3.62	6.03		$-\Delta$	$-\Delta$	$-\Delta$	5.76	1.28
Δ	1	1	7.05	12.43		$-\Delta$	Δ	$-\Delta$	5.79	1.25
1	$-\Delta$	$-\Delta$	7.12	-15.92		Δ	$-\Delta$	Δ	5.79	1.25
$-\Delta$	1	1	12.80	2.44		1	1	Δ	7.08	0.58
$-\Delta$	Δ	1	30.76	5.92		1	1	$-\Delta$	7.37	0.58
1	1	$-\Delta$	31.68	6.02		1	$-\Delta$	$-\Delta$	18.12	-17.37
$-\Delta$	$-\Delta$	1	32.04	6.01		1	Δ	$-\Delta$	18.32	-16.61
Δ	Δ	1	34.42	6.03		1	Δ	Δ	21.72	-16.61
Δ	$-\Delta$	1	35.86	6.03		$-\Delta$	1	1	21.76	-4.25
1	1	1	150.52	6.02		1	$-\Delta$	Δ	22.03	-17.37
1	1	Δ	–	–		Δ	1	1	24.42	-3.37
1	Δ	1	–	–		$-\Delta$	Δ	1	36.26	1.25
1	Δ	Δ	–	–		$-\Delta$	$-\Delta$	1	37.14	1.28
1	Δ	$-\Delta$	–	–		Δ	Δ	1	39.39	1.28
1	$-\Delta$	1	–	–		Δ	$-\Delta$	1	40.48	1.25
1	$-\Delta$	Δ	–	–		1	1	1	104.96	0.58
Δ	1	$-\Delta$	–	–		1	Δ	1	–	–
$-\Delta$	1	$-\Delta$	–	–		1	$-\Delta$	1	–	–

Table 5.2: Ranking according to beamwidth of 27 different possible combinations of an anisotropic substrate over a PMC groundplane for a source operating at 14 GHz that is embedded in the center of a 4 cm thick substrate. Both lossless (left) and lossy (right) substrates are considered.

5.3.3   Effect of substrate geometry

In this section, the effect of the substrate geometry will be examined. Specifically, the effect of the thickness and source position within the substrate will be considered. As discussed in the previous section, the larger the percentage of evanescent waves transmitted, the larger the beamwidth will be. Because the substrate thickness and source position directly affect this percentage, it is important to quantify to what extent.

As discussed previously, ideally, all of the evanescent waves would be completely suppressed and not transmitted from the source through the substrate into freespace. In this case, only the propagating waves, which can be confined to a small range of transmitted angles by appropriate choice of material parameters, would be present. On the other hand, if they are not suppressed, the evanescent waves that are transmitted from region 1 to region 0 become propagating waves that span the entire range of angles, which affects the radiation pattern.

In practice, the evanescent waves can only be partially suppressed. The rate at which the evanescent waves decay inside the substrate depends on the k_{1z} component and locations of the substrate surface and the ground plane, d_1 and d_2, with respect to the source position. It is expected that a thicker substrate will have a higher suppression of evanescent waves since the source waves have a longer distance over which to decay before they emerge into freespace as a propagating wave.

To more precisely illustrate this phenomena, the half-power beamwidth and peak power are calculated for an isotropic substrate with a relative permittivity of $\epsilon_{r1} = 0.01$ and a constant relative permeability of $\mu_{r1} = 0.01$. As shown in Fig. 5-7, the substrate thickness is varied from 2 cm to 10 cm with the source being equidistant from the ground plane and air-media interface. Comparing the results a PEC ground plane and a PMC ground plane, it is apparent that the thicker substrate significantly improves the beamwidth of the PEC system, whereas it only moderately improves that of the PMC system. The explanation for this is that as the source is pushed further away from the ground plane, the destructive

(a) Half-power beamwidth
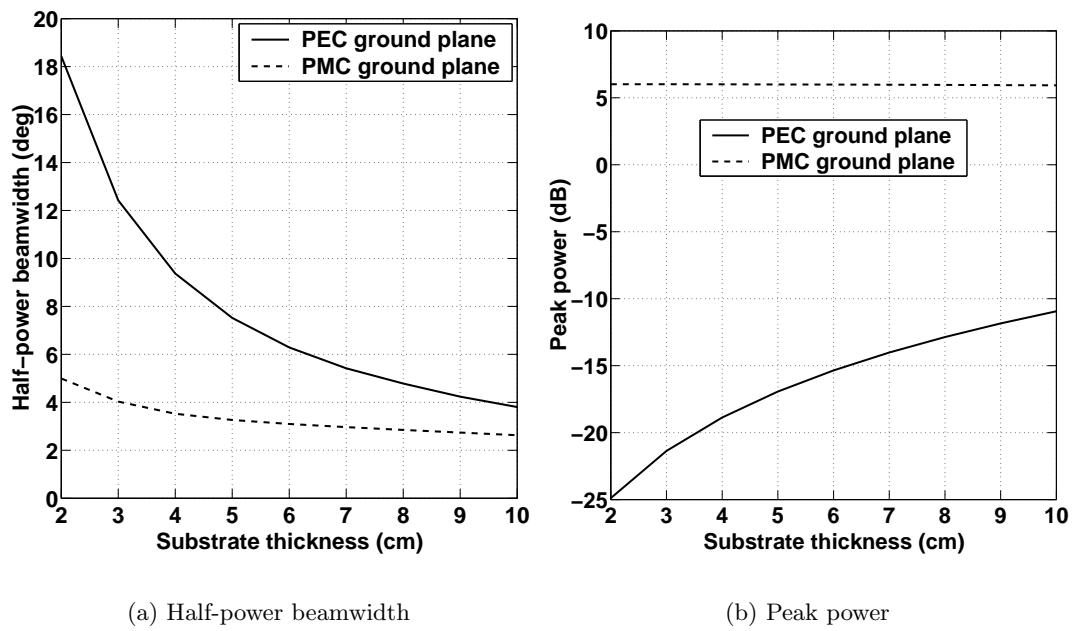
(b) Peak power

Figure 5-7: Effect of substrate thickness for an ideal isotropic medium. Half-power beamwidth and peak power at 14.0 GHz calculated for a substrate with a relative permittivity of $\epsilon_{r1} = 0.01$ and a constant relative permeability of $\mu_{r1} = 0.01$. For every substrate thickness, the source is placed equidistant from the ground plane and air-media interface.

interference effects of the PEC system become less drastic allowing the peak power to reach a larger value. Then, as described above, because the peak power is higher, it will roll off faster yielding a better beamwidth. On the other hand, the beamwidth of the PMC system does not improve significantly because it is already near optimal performance for the smallest substrate thickness considered. A smaller beamwidth would require confining the propagating waves of the source to a tighter range of transmission angle, which is affected by the substrate's material parameters rather than its thickness.

Next, the effects of anisotropy and loss in combination with substrate thickness are presented is Fig. 5-8. In each case, the four different types of anisotropic substrates whose dispersion relations are shown in Fig. 5-5 are considered. When varying the substrate thickness as in Fig. 5-8, the source is placed at the center of the substrate. The results show that for increasing substrate thickness, the resulting beamwidth decreases, which as before is due to the decay of the evanescent waves. One interesting result apparent in the lossless versus lossy cases is that the beamwidth of cases B and A approach the same value when the substrate thickness is 10 cm. Under the argument that the thicker substrate suppresses more of the evanescent waves, this result is inconsistent. However, as in Fig. 5-6, the larger beamwidth than expected in case B is due to the high transmission coefficient at the spatial cutoff frequency of the medium. As before, though, introduction of loss removes the large spikes. In Fig. 5-8(b), it can clearly be seen that the medium in case B yields a better beamwidth than the medium in case A.

Finally, the last geometrical feature considered is the effect of the source position within the substrate. Based on the argument presented for the previous cases, it is reasonable to expect that for a given substrate thickness, the system will perform better in terms of beamwidth when the source is as far away from the surface as possible. Indeed, this is what has been found and is illustrated in Fig. 5-9. The closer the source is to the surface of the substrate, the worse the resulting beamwidth is. As with the substrate thickness effect, this is due to the evanescent waves that are being transmitted. When the source is located further away from the surface, the evanescent waves decay to a larger extent before

emerging as propagating waves.
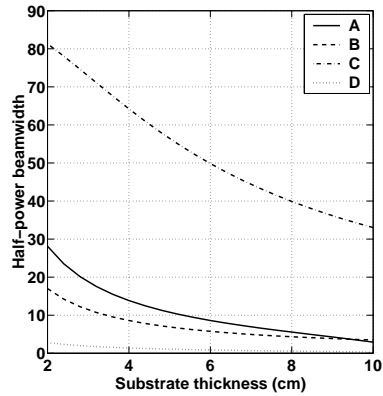
(a) Lossless substrate over
PEC ground plane
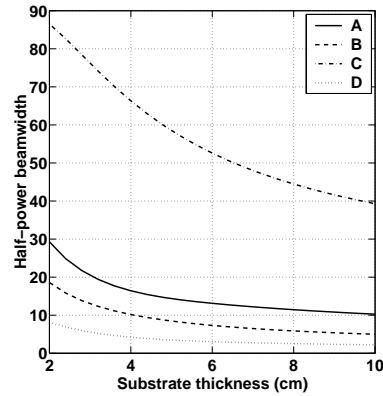
(b) Lossy substrate over PEC
ground plane

Figure 5-8: Effect of substrate thickness with anisotropic substrates. Half-power beamwidth
at 14.0 GHz calculated for source embedded in the center of the substrate. Real parts
of permittivity and permeability are given as follows: A: $\epsilon_y = 0.01$, $\mu_x = \mu_z = 1$ B:
$\epsilon_y = \mu_x = \mu_z = 0.01$ C: $\epsilon_y = \mu_x = 0.01$, $\mu_z = 1$ D: $\epsilon_y = \mu_z = 0.01$, $\mu_x = 1$. For figure (b),
the imaginary component for each component is 0.05.
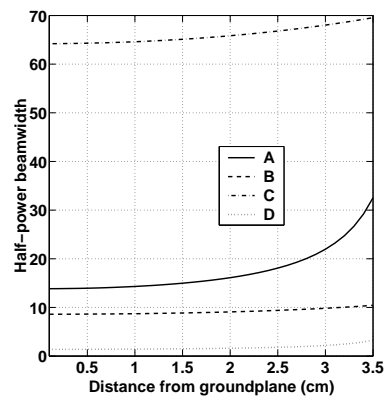
(a) Lossless substrate over PEC ground plane
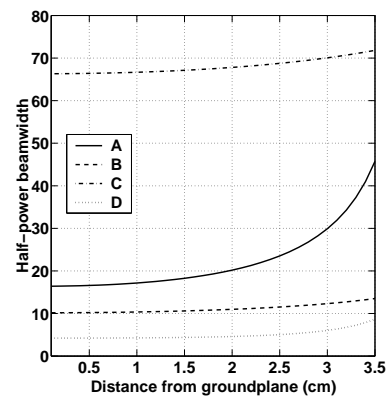
(b) Lossy substrate over PEC ground plane

Figure 5-9: Effect of source position within an anisotropic substrate. Half-power beamwidth at 14.0 GHz calculated for a substrate that is 4 cm thick. Real parts of permittivity and permeability are given as follows: A: $\epsilon_y = 0.01$, $\mu_x = \mu_z = 1$ B: $\epsilon_y = \mu_x = \mu_z = 0.01$ C: $\epsilon_y = \mu_x = 0.01$, $\mu_z = 1$ D: $\epsilon_y = \mu_z = 0.01$, $\mu_x = 1$. For figure (b), the imaginary component for each component is 0.05.

5.4 Metamaterial substrates

In the previous section, the emphasis has been on achieving a small beamwidth at a single frequency by adjusting the ground plane, the anisotropy of the substrate, and the geometrical configuration. In this section, however, the emphasis will be on obtaining a good beamwidth over a wideband. To this end, the Drude and Lorentz bulk media models will be used to access the performance of an antenna system built with a source embedded in a metamaterial based substrate. Both isotropic and anisotropic metamaterial models will be considered. In addition, the trade-offs between bandwidth, beamwidth, and gain performance will be addressed.

Metamaterial models

As discussed in the introduction, narrow beamwidths were achieved previously at a single frequency by controlling only the substrate electrical properties. In order to achieve a narrow beamwidth over a wideband, the approach taken here is to use a material that exhibits both electric and magnetic properties. In particular, left-handed metamaterials, which can be tuned to operate at specified frequencies through geometrical scaling will be investigated.

As discussed in Chapter 3, typically left-handed metamaterials constructed using rods and split-rings are characterized using the Drude [27] and Lorentz bulk media models [4]. In this chapter, these models will be used for the permittivity and permeability, respectively. Again, these relations are given by,

$$\epsilon_r = 1 - \frac{\omega_{ep}^2}{\omega^2 + i\gamma_e\omega} \tag{5.14}$$

and

$$\mu_r = 1 - \frac{\omega_{mp}^2 - \omega_{mo}^2}{\omega^2 - \omega_{mo}^2 + i\gamma_m\omega}. \tag{5.15}$$

where ω_{ep} ($\omega = 2\pi f$) and γ_e are the electric plasma and damping frequencies, and ω_{mo}, ω_{mp}, and γ_m are the magnetic resonance, plasma, and damping frequencies, respectively. One example of these models is shown in Fig. 5-10. For these particular parameters, it is seen that the index of refraction will be approximately zero at f_{mp} and f_{ep}, and remains relatively small between these two frequencies.

As will be shown in the following examples, the index of refraction, and hence the radiation properties of the substrate, can be tuned to yield narrow beamwidths over a specified bandwidth. The extent of the bandwidth will determine the beamwidth sizes that are achievable.
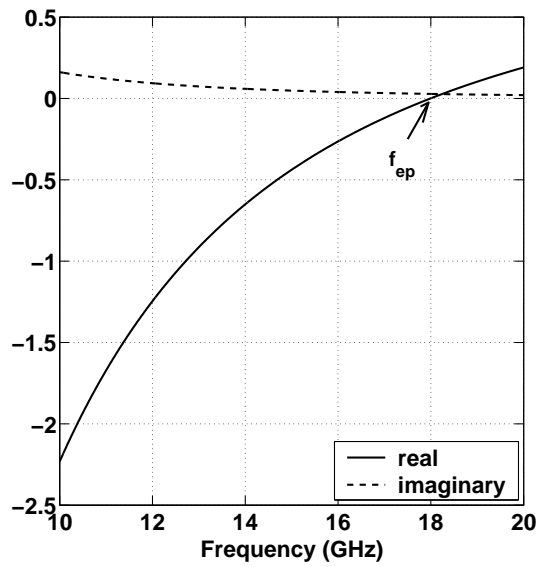
(a) Permittivity model
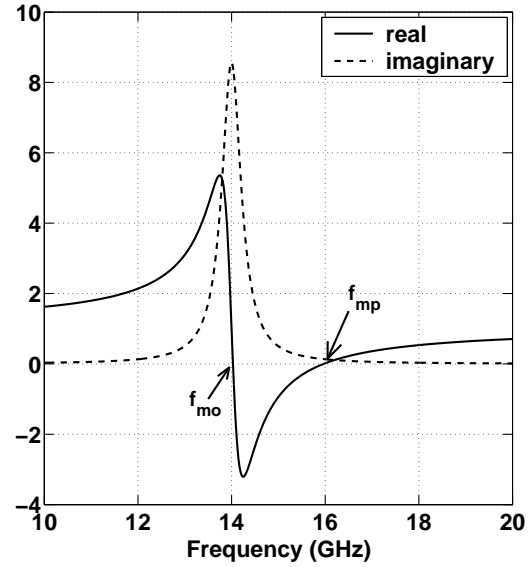
(b) Permeability model
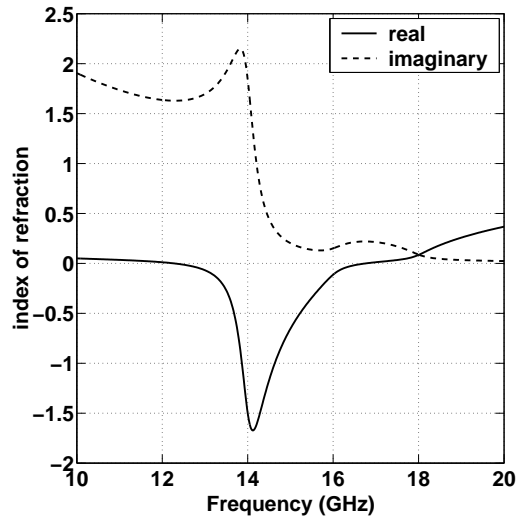
(c) Index of refraction

Figure 5-10: Example of typical left-handed metamaterial dispersion models. Permittivity is characterized by the Drude model: $f_p = 18$ GHz, $\Gamma = 0.5$ GHz. Permeability is characterized by the Lorentz: $f_o = 14$ GHz, $f_p = 16$ GHz, $\Gamma = 0.5$ GHz. Note, damping frequencies are exaggerated for the purposes of illustration.

5.4.1   Isotropic substrates

Isotropic rods-only metamaterial

To begin, Fig. 5-11 shows the radiation pattern and corresponding corresponding beamwidth and peak power for a substrate that is characterized by the bulk media model for a rods-only metamaterial. The plasma frequency of the medium was chosen to be 13.5 GHz, which corresponds to a lattice constant of 6.045 mm × 5.8 mm [105]. Similar to the results reported by Enoch *et al* in [100], it is found that the beamwidth is minimum at a frequency slightly above the plasma frequency of the medium. Above the plasma frequency, as the index of refraction increases, the main lobe diverges into two separate lobes (visible as the "U" shaped pattern in Fig. 5-11(a) and Fig. 5-11(b)), thereby destroying the directivity properties of the antenna system. Hence, a small beamwidth is only achieved over a relatively narrow band, in this case between 13.5 GHz and 14 GHz, depending on the type of ground plane.

Isotropic rings-only metamaterial

The other component typically used in left-handed metamaterials is the split-ring resonator. In Fig. 5-12, the radiation pattern and corresponding corresponding beamwidth and peak power for a substrate that is characterized by the bulk media model for a rings-only metamaterial. The resonant and plasma frequencies of the medium were chosen to match those found in [4] for concentric split-ring resonator design. From the radiation plots shown in figures 5-12(a) and 5-12(b), it can be seen that region of good beamwidth is near the plasma frequency of the medium, around 11 GHz. Above 11 GHz, the "U" shaped pattern that appeared in the case of the rods-only medium is also present in this case, albeit the "U" shape is much wider. The change in width can be attributed to the fact that just beyond the plasma frequency, the permeability under the Lorentz medium model increases more rapidly than under the Drude medium model.
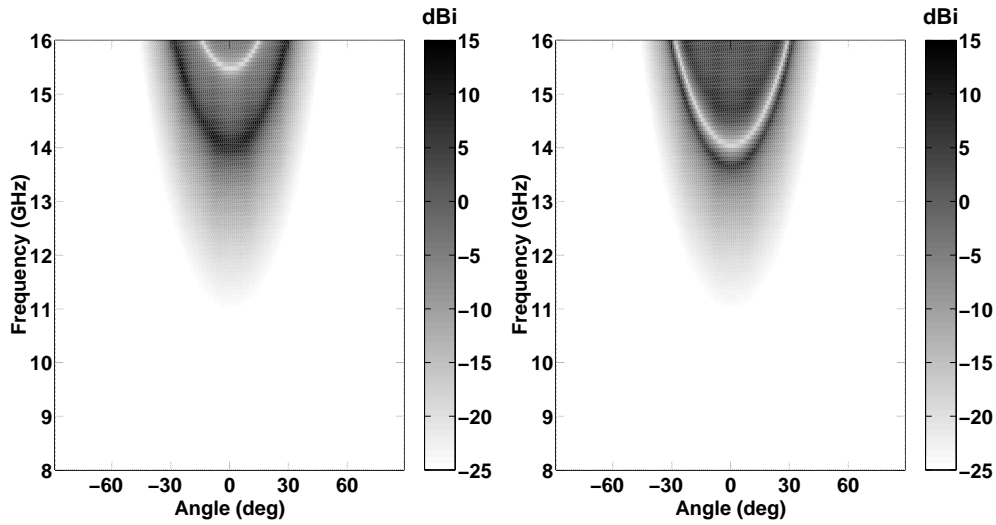
(a) Radiation Pattern for PEC

(b) Radiation Pattern for PMC
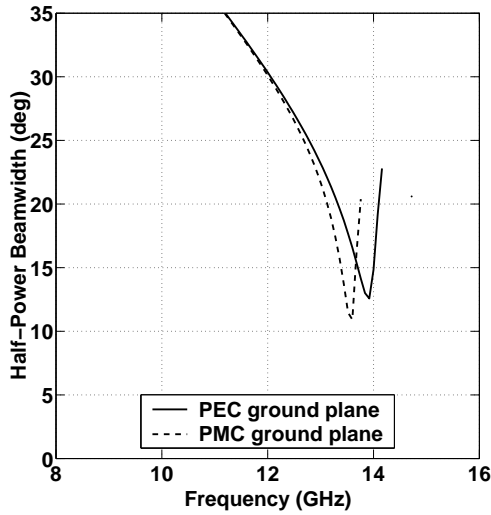
(c) Half-power beamwidth

(d) Peak power

Figure 5-11: Antenna radiation properties for isotropic medium with a permittivity that follows the Drude model with $f_{ep} = 13.5$ GHz and $\gamma_e = 0.1$ GHz, and a free-space permeability. Slab is 4 cm thick and the source is equidistant from the ground plane and air-media interface.

(a) Radiation Pattern for PEC

(b) Radiation Pattern for PMC

(c) Half-power beamwidth

(d) Peak power

Figure 5-12: Antenna radiation properties for isotropic medium with a free-space permittivity, and a permeability that follows the Lorentz model with $f_{mo} = 10$ GHz, $f_{mp} = 10.5$ GHz, and $\gamma_m = 0.1$ GHz. Slab is 4 cm thick and the source is equidistant from the ground plane and air-media interface.

Isotropic rods and rings metamaterial

In the previous two cases, narrowband performance was achieved, and in order to get a wider band of operation, the above two metamaterials can be combined. In the following results, the permittivity and permeability follow the same Drude and Lorentz media models used for generating the previous two results. Fig. 5-13 shows the resulting radiation pattern, beamwidth, and peak power. From the radiation patterns, it can be seen that the combination has yielded a band of frequencies between the resonant and plasma frequency of the rings for which the medium is left-handed. In this band, because of the large index of refraction, the resulting beamwidth is relatively large. On the other hand, in constrast to the rings-only medium, the band of frequencies (roughly 2 GHz) above the plasma frequency of the rings and below the plasma frequency rods now has one main lobe centered about $\theta = 0$. Although in this case the beamwidth is now definable, it is rather large except near the plasma frequency of the rods. Furthermore, the gain of the system in this frequency range is smaller than the gain in the region of operation for the rods-only or rings-only design.

In order to improve upon the previous results, it is important to note that one of the problems hindering the performance is that the permeability varies rapidly near the resonant frequency. In the above case, because the plasma frequency of the rings was so close to the resonant frequency, the value of μ increased at such a rate that it product of μ and ϵ remained relatively large. One simple approach to alleviate this situation would be to decrease the plasma frequency of the rods to a value closer to the plasma frequency of the rings; however, the bandwidth of the system would suffer. A better solution is to increase the separation between the resonant and plasma frequency of the rings. By increasing the separation, the rate at which the permeability changes would be lower allowing for a larger band where the product of ϵ and μ is small. Such a case is considered in Fig. 5-14, where the substrate is characterized as an isotropic medium with a permittivity that follows the Drude model with $f_{ep} = 15.0$ GHz and $\gamma_e = 0.1$ GHz, and a permeability that follows the
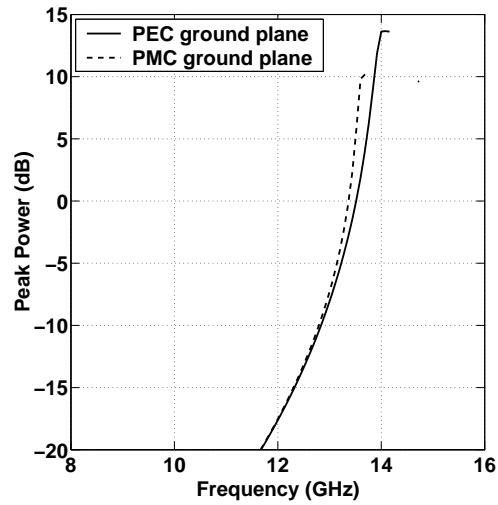
(a) Radiation Pattern for PEC
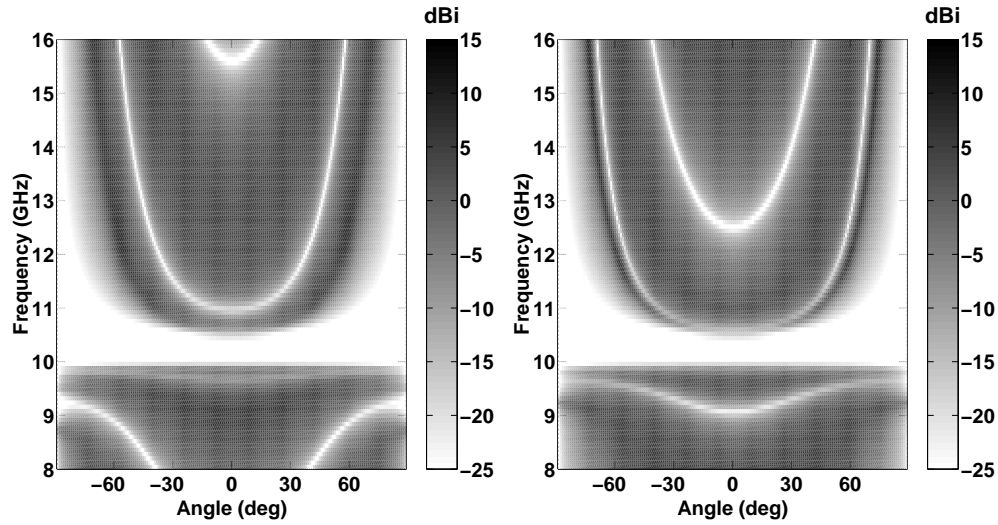

(b) Radiation Pattern for PMC
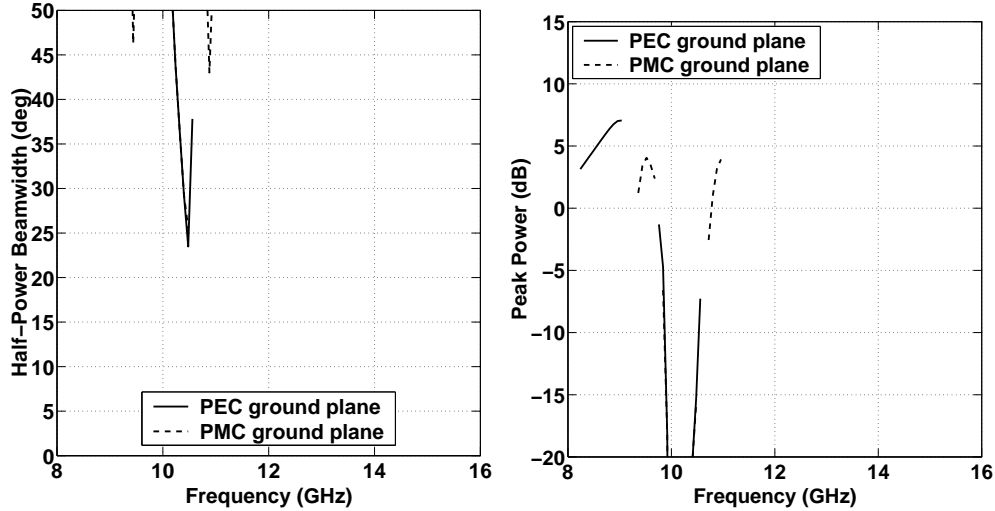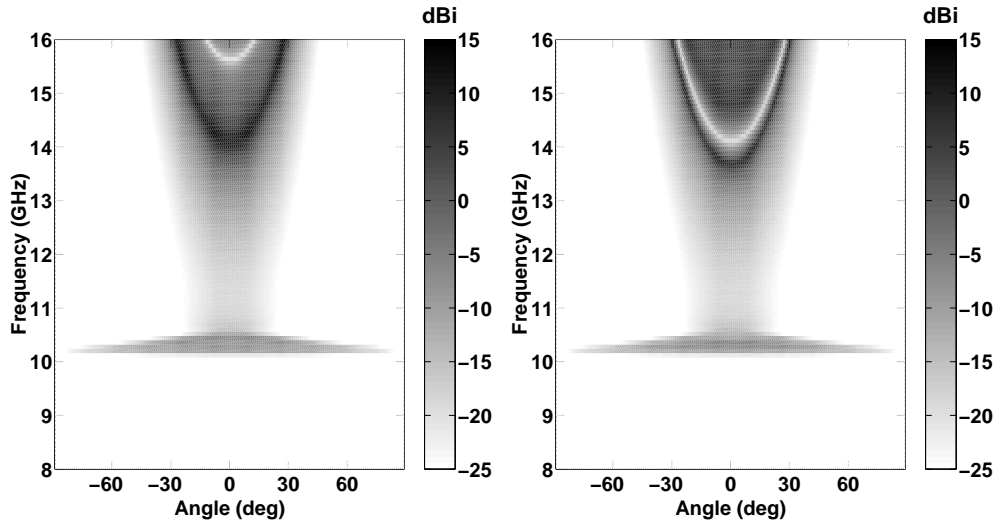

(c) Half-power beamwidth

(d) Peak power

Figure 5-13: Antenna radiation properties for isotropic medium with a permittivity that follows the Drude model with $f_{ep} = 13.5$ GHz and $\gamma_e = 0.1$ GHz, and a permeability that follows the Lorentz model with $f_{mo} = 10.0$ GHz, $f_{mp} = 10.5$ GHz, and $\gamma_m = 0.1$ GHz. Slab is 4 cm thick and the source is equidistant from the ground plane and air-media interface.
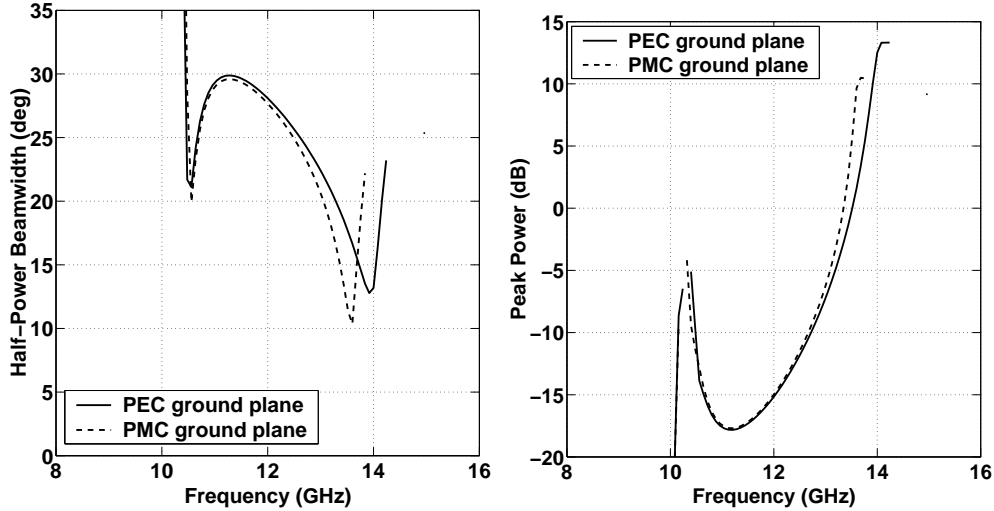
Lorentz model with $f_{mo} = 9.0$ GHz, $f_{mp} = 13.0$ GHz, and $\gamma_m = 0.1$ GHz. As can be seen, in addition to achieving a lower beamwidth over a 2 GHz band, the gain of the system for the frequencies of interest is larger compared to the results of Fig. 5-13.

(a) Radiation Pattern for PEC

(b) Radiation Pattern for PMC

(c) Half-power beamwidth

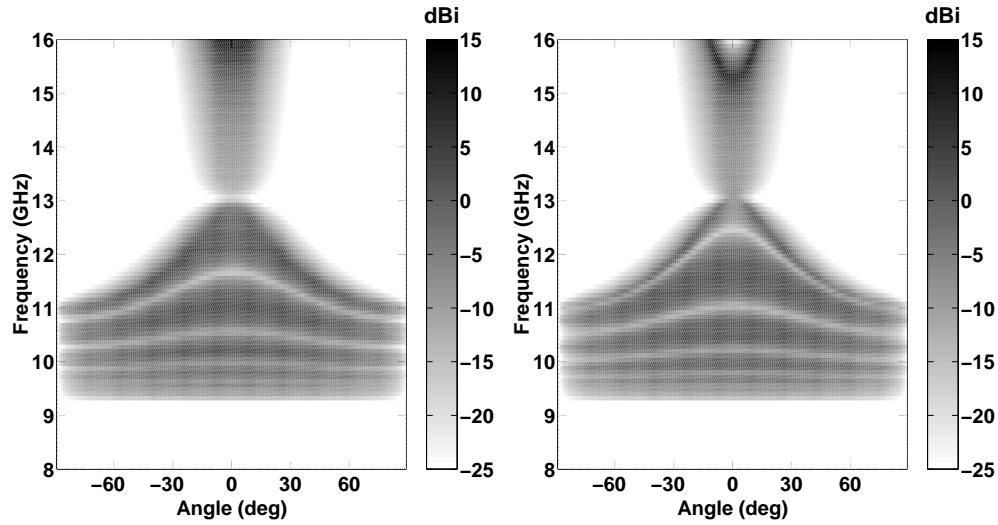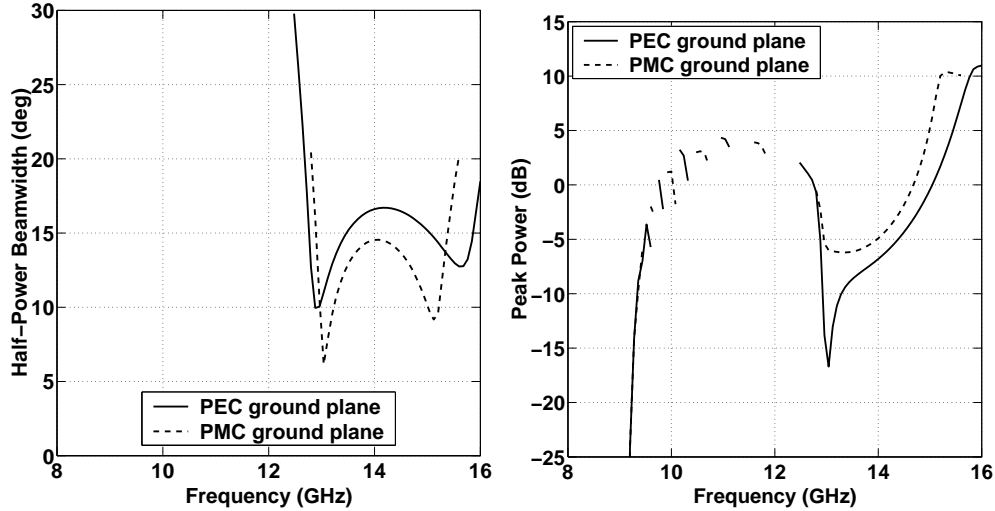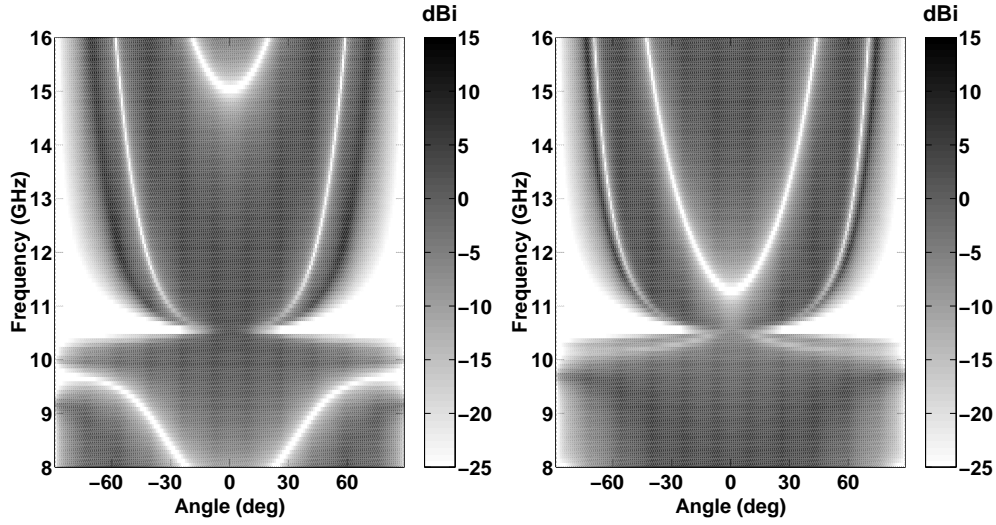
(d) Peak power

Figure 5-14: Antenna radiation properties for isotropic medium with a permittivity that follows the Drude model with $f_{ep} = 15.0$ GHz and $\gamma_e = 0.1$ GHz, and a permeability that follows the Lorentz model with $f_{mo} = 9.0$ GHz, $f_{mp} = 13.0$ GHz, and $\gamma_m = 0.1$ GHz. Slab is 4 cm thick and the source is equidistant from the ground plane and air-media interface.

5.4.2   Anisotropic substrates

Each of the designs considered in the previous section, although considered to be isotropic, can be approximately realized using a combination of rods and split-rings. Assuming the source approximates a line source, the rods need only be oriented along the direction parallel to the line source. However, to achieve the isotropic results, split-rings are needed in two perpendicular directions. Experimentally, this 3D metamaterial has been built and successfully measured to have isotropic-like left-handed properties for a single polarization. The drawback of these designs is that they are often difficult to fabricate and sometimes lack mechanical stability. A 2D design, in which rings and rods could be printed on individual layers and stacked is considerably easier to fabricate and is more stable. As an added benefit, as discussed in Section 5.3.2, it was seen that a certain class of anisotropic medium achieves a better beamwidth than its isotropic counterpart. Hence, in this section, the anisotropic counterparts of the metamaterial results presented in the previous section will be examined.

The first geometry to consider is a 2D rings-only geometry in which the $\hat{z}\hat{z}$ component of the permeability tensor is characterized by the Lorentz medium model while the other components remain equal to that of freespace. Fig. 5-15 shows the radiation pattern assuming the parameters of the ring design given in [4]. Comparing these results to those of its isotropic counterpart shown in Fig. 5-12, the same general shape appears. However, the gap between the resonant and plasma frequency is less apparent and the beamwidth in this region is approximately ten to fifteen degrees smaller. In addition, the gain of the system is higher; however, note that as will be seen in the following result, this additional gain is not maintained when the rods are introduced. Regardless, the lower beamwidth of the 2D ring design at its plasma frequency gives hope that an overall better beamwidth over a wide band can be achieved.

As in the previous section, in order to improve upon the previous results, it is necessary to increase the separation between the resonant and plasma frequency of the rings. By

(a) Radiation Pattern for PEC

(b) Radiation Pattern for PMC
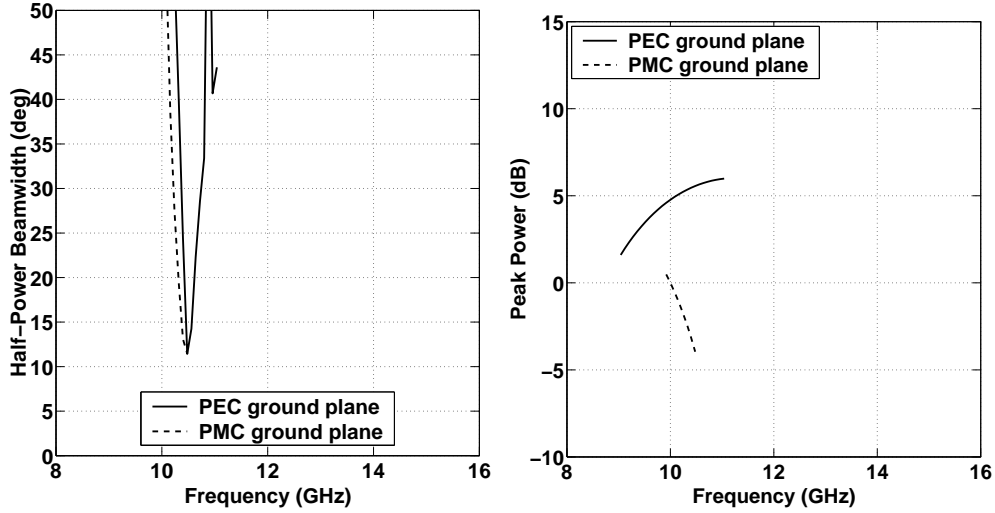
(c) Half-power beamwidth

(d) Peak power

Figure 5-15: Antenna radiation properties for isotropic medium with a free-space per-mittivity, and an *anisotropic* (μ_z only) permeability that follows the Lorentz model with $f_{mo} = 10.0$ GHz, $f_{mp} = 10.5$ GHz, and $\gamma_m = 0.1$ GHz. Slab is 4 cm thick and the source is equidistant from the ground plane and air-media interface.

adopting the same parameters used for the Drude and Lorentz media models in Fig. 5-14, the radiation pattern of the 2D counterpart of that 3D design is calculated and shown in Fig. 5-16. As with the 3D design, the band of operation is shifted to be between 13 GHz and 15 GHz. While the resulting beamwidth has improved by approximately 5°, it is done so at the expense of gain.

It should be noted that the gain can be improved by effectively reducing the bandwidth of the system. Other slight improvements could be achieved by reducing the inherent loss of the rings and rods by lowering the damping frequency. Still, in all cases, there is a trade-off between bandwidth and gain. In addition to the improved beamwidth of the 2D design, it is also a much simpler design to fabricate.
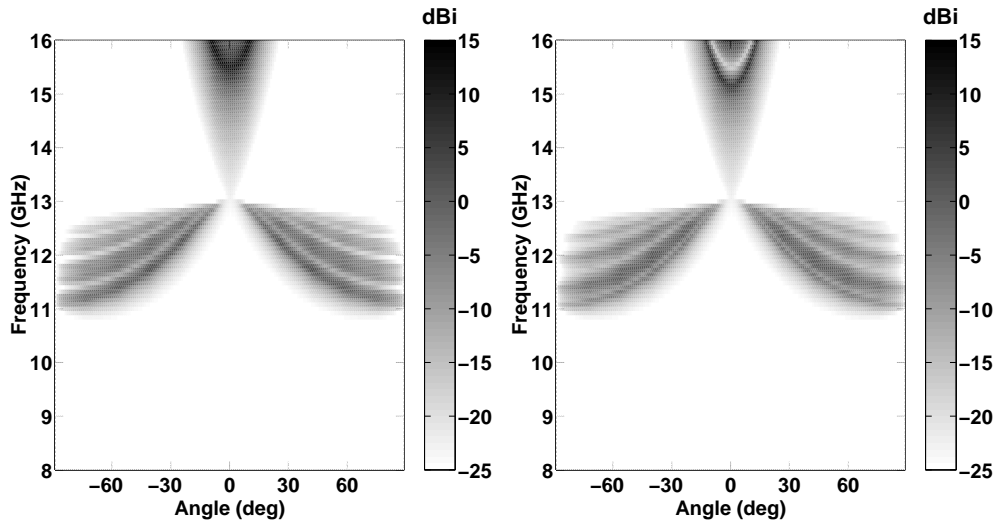
(a) Radiation Pattern for PEC

(b) Radiation Pattern for PMC
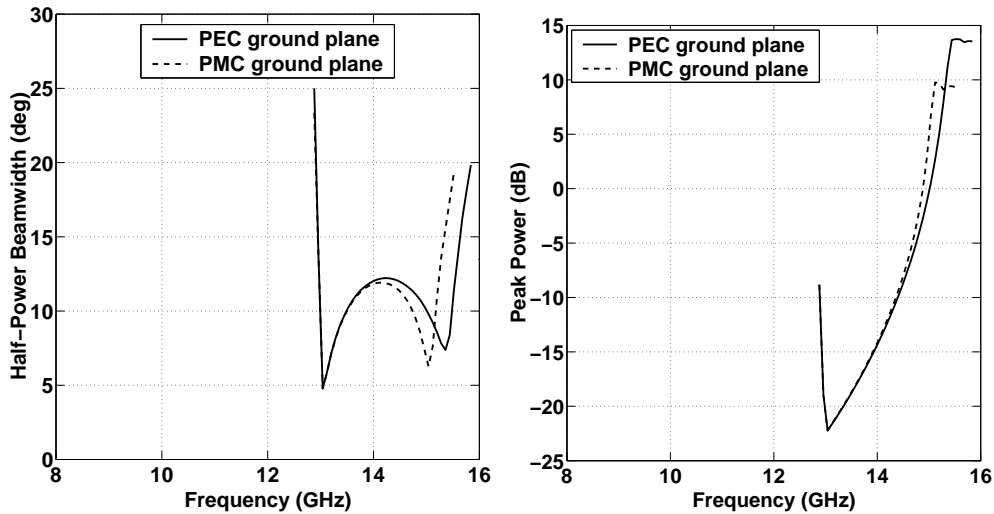
(c) Half-power beamwidth

(d) Peak power

Figure 5-16: Antenna radiation properties for anisotropic medium with a permittivity (ϵ_y) that follows the Drude model with $f_{ep} = 15.0$ GHz and $\gamma_e = 0.1$ GHz, and a permeability (μ_z) that follows the Lorentz model with $f_{mo} = 9.0$ GHz, $f_{ep} = 13.0$ GHz, and $\gamma_m = 0.1$ GHz. Slab is 4 cm thick and the source is equidistant from the ground plane and air-media interface.

5.5   Summary

In this chapter, the application of metamaterials in the design of a light-weight directive antenna substrate has been studied. It was seen that by Snell's law, if a source is embedded in a substrate that has a small index of refraction compared to air, its source rays will be transmitted near the normal of the substrate. In the past, antennas have been designed using this concept; however, they have been limited to narrowband operation. However, it was shown here that the use of left-handed metamaterials, which have frequency dispersive magnetic and electric properties, can be used to design a wideband directive antenna. The higher bandwidth results from the flexibility of achieving an index of refraction that is exactly zero at the plasma frequency of the rods and at the plasma frequency of the rings. The extent of the bandwidth will be approximately the frequency separation between the two plasma frequencies. Furthermore, the role that anisotropy can play in controlling the beamwidth was discussed. It was shown that certain anisotropic metamaterials, which in practice are simpler to fabricate, will actually perform better in terms of beamwidth than their isotropic counterparts. Finally, some of the performance trade-offs between beamwidth, gain, and substrate thickness were discussed.

Chapter 6

Conclusion

In this thesis, the theory and application of left-handed materials has been investigated. Theoretically, two approaches have been taken to understand these materials: macroscopic and microscopic. In the macroscopic approach, effective permittivities and permeabilities were used to study such phenomena as propagation, radiation, and scattering from what was termed left-handed media. While this approach yielded many valuable insights in the fundamental phenomena and potential applications, it did not teach us how to physically realize material with such properties. This is where the microscopic approach came into play. In this approach, the physically realizable metamaterials that have been shown to exhibit left-handed properties were modeled using exact numerical electromagnetic solvers. The motivation for using both of these approaches was to try to develop a more complete understanding of left-handed materials.

In chapter 2, the propagation, radiation, and scattering properties of homogeneous left-handed media were examined. Propagation was studied by analyzing the transmission of a multi-frequency signal from a right-handed medium into a frequency dispersive left-handed medium. The radiation properties of left-handed media were studied by examining in detail the perfect lens concept originally proposed by Pendry [25]. Next, as an example of the scattering properties of left-handed media, the scattering by spheres composed of LH media

was investigated. Finally, as was pointed out more specifically in chapter 3, most current metamaterials designs are anisotropic, and so in the final section, some of the basic principles of propagation and scattering from planarly layered anisotropic media were considered.

Although in each of these studies, the basic analytic tools used, such as Green's function analysis and Mie theory, are already known in the field, it was necessary to re-derive their formulations for the specific case of left-handed media in order to understand the consequences of simultaneous negative permittivity and permeability. As shown in this thesis, many of the usual intuitive principles used in electromagnetics are actually reversed in the case of left-handed media.

Because of some of these non-intuitive principles, the theoretical existence of some of the left-handed properties, such as a negative index of refraction, were disputed. As discussed in chapter 2, the authors of [19] claimed that dispersion and causality constraints prohibited waves from refracting at negative angles. However, as was shown, this confusion came about due to the generation of an interference pattern whose apparent direction of propagation was different from the actual direction of power flow. While the theory presented in this thesis gave an explanation for this confusion, many in the field have demanded more experimental proof of left-handed behavior.

Because homogeneous left-handed media, such as those studied in this thesis, do not exist, one must turn to left-handed metamaterials for an experimental demonstration. Such a demonstration was performed at a recent DARPA workshop of metamaterials by S. Schultz of the University of California at San Diego. In his demonstration, Schultz used a prism shaped block of a metamaterial, previously shown to have left-handed properties for at least one frequency, to refract a microwave beam that had been modulated by a audio signal. The receiving antenna was placed at an angle that corresponded to a negative index of refraction. Now if the receiving antenna is able to properly receive the audio signal, which has non-zero bandwidth (approximately 45 MHz), then the experiment would show that dispersion does not prohibit left-handed behavior. Fortunately, in agreement with theoretical results, the entire bandwidth of the audio signal was refracted in a left-handed manner.

Whereas in Chapter 2, homogeneous left-handed media were explored, Chapter 3, investigated the physical realization of LH media in terms of metamaterials. In order to understand the physical mechanisms and to be able to characterize metamaterials, a few different tools were implemented. With each of these tools, the metamaterials in a slab configuration were numerical modeled by using periodic finite difference-time domain (FD-TD) or the method of moments (MoM).

Before beginning with the numerical characterization tools, the analytical models for the effective permittivity and permeability were presented. The Drude and Lorentz models were introduced as typical examples of how to characterize the dispersion of the metamaterials. Generally, the rods were modeled using a Drude medium while the split-ring resonators were modeled by a Lorentz medium. Using numerical simulations, it was shown that the rods generally behaved according to the analytic models while the rings only compared favorably to their analytic model near the resonance, although it was found that the S-parameter results of the adjacent ring design more closely matched those predicted by its analytic theory.

Next, the nature of the field distribution within the vicinity of the metamaterial was explored by separately embedding the rods and SRR in background homogeneous plasma media and looking for left-handed properties. In the case of the rods, it was found, in agreement with the theoretical prediction in reference [20], that the space immediately surrounding the rods cannot not be a negative permeability medium. Transmission and eventual confirmation of left-handed properties were only found once the magnetic plasma immediately surrounding the rods was removed. Similarly, in the case of the SRR, it was found that the background plasma in between the regions of strong capacitance needed to be removed in order for the hybrid metamaterial-homogeneous material to behave in a left-handed manner. These effects can be explained by noting that a negative permittivity converts capacitative effects into inductive effects whereas a negative permeability converts inductive effects into capacitative effects. By removing the homogeneous background plasma in these key areas, the negative permittivity of the rods and the negative permeability of

the rings was restored.

Despite the advantages of using the hybrid approach to understand the behavior of the rods and SRRs, it is of course necessary to combine the two to show that together they do indeed operate as a left-handed metamaterial. In addition to numerical simulations, it is important to have experimental proof of left-handed behavior. Because it is impractical to measure the field inside the metamaterial, the method of retrieving the permittivity and permeability from the complex S-parameters was studied. The idea of characterizing materials based on their S-parameters is of course not a new concept and has been studied in the past. However, in the case of left-handed metamaterials composed of rods and SRRs, the retrieval is complicated by the resonant behavior of the metamaterials for two reasons. First, the resonant behavior makes it difficult to accurately calculate the S-parameters, which in turn because of the sensitivity of the method makes it difficult to determine the permittivity and permeability. Second, the resonant behavior made it difficult to determine the correct branch cut for use in calculation of the real part of the index of refraction.

Still, as seen in the final example of the adjacent ring with rods design, by using a combination of the phase-tracking and retrieval method, a better estimation of the actual material parameters can be obtained. The phase-tracking method allows one to obtain an estimate of the value of the real part of the index of refraction, while the retrieval from S-parameter method allows a more precise calculation of the index refraction. The ambiguity of the branch cut choice was reduced by utilizing the phase-tracking results.

Finally, in the last two chapters, two potential applications of left-handed metamaterials were explored. The first application considered was how to use left-handed metamaterials as radar absorbers. The motivation behind this work was to investigate the potential benefits of being able to design an absorber with materials that have negative permittivity and/or negative permeability. In designing the coatings, a genetic algorithm optimization method was used to determine the parameters of the Drude and Lorentz models, which were used to characterize the current generation of left-handed metamaterials. For single frequency applications, it was found that there is no advantages to using right-handed

versus left-handed materials. On the other hand, for wideband applications, it seen that the sharp resonance of the Lorentz models limits the maximum bandwidth achievable. Despite these drawbacks, metamaterials do have the advantage of being light-weight and frequency tunable. Thus, for applications requiring light-weight coatings, left-handed metamaterials offer a viable alternative.

The second application investigated was the use metamaterials in the design of a light-weight directive antenna substrate. It is well known that by Snell's law, if a source is embedded in a substrate that has a small index of refraction compared to air, its source rays are transmitted near the normal of the substrate. It was shown in Chapter 5 that left-handed metamaterials, which possess frequency dispersive magnetic and electric properties, can be used to design a wideband directive antenna. It was also seen that the role that anisotropy plays in controlling the beamwidth is very important. It was shown that certain anisotropic metamaterials, which in practice are simpler to fabricate, will actually perform better in terms of beamwidth than their isotropic counterparts. In conjunction, the performance trade-offs between beamwidth, gain, and substrate thickness were discussed. Although not discussed in great detail, the fact that metamaterials are extremely light-weight is actually one of the most significant advantages of using metamaterials in new antenna designs. These types of antennas would be useful for example in space-based applications where weight is very crucial.

Future work includes further study of the effects of different numbers of layers on the overall effective permittivity and permeability of a given metamaterial. Future experimental work includes producing a solid-state version of left-handed metamaterials. This would enable its applicability to a much wider range of applications. For example, realistic radar absorber applications require the ability to make very thin layers of a specific thickness. Unfortunately, current metamaterials are very bulky, and are therefore not directly applicable to this field. Other work includes further study of the periodic nature of metamaterials. Is the periodicity an essential feature? Can isotropic left-handed materials be designed by using a random collection of some unit design much in the same way chiral materials were

realized? In general, in the opinion of the author, in order for metamaterials to become more commonplace in modern engineering applications, stable and robust designs are needed.

Bibliography

[1] V. G. Veselago. The electrodynamics of substances with simultaneously negative values of ϵ and μ. *Sov. Phys. Usp.*, 10:509, 1968.

[2] J. B. Pendry, A. J. Holden, W. J. Stewart, and I. Youngs. Extremely low frequency plasmons in metallic mesostructures. *Phys. Rev. Lett.*, 76:4773, 1996.

[3] J. B. Pendry, A. J. Holden, D. J. Robbins, and W. J. Stewart. Magnetism from conductors and enhanced nonlinear phenomena. *IEEE Trans. Microwave Theory Tech.*, 47:2075, 1999.

[4] R. A. Shelby, D. R. Smith, and S. Schultz. Experimental verification of a negative index of refraction. *Science*, 77:292, 2001.

[5] D. R. Smith, W. J. Padilla, D. C. Vier, S. C. Nemat-Nasser, and S. Schultz. Composite medium with simultaneously negative permeability and permittivity. *Phys. Rev. Lett.*, 84:4184, 2000.

[6] J. B. Pendry, A. J. Holden, D. J. Robbins, and W. J. Stewart. Low frequency plasmons in thin-wire structures. *Journal of Physics: Condensed Matter*, 10:4785–4809, 1998.

[7] P. Gay-Balmaz and O. J. F. Martin. Electromagnetic resonances in individual and coupled split-ring resonators. *J. Appl. Phys.*, 92(5):2929–2936, 2002.

[8] P. Gay-Balmaz and O. J. F. Martin. Efficient isotropic magnetic resonators. *Appl. Phys. Lett.*, 81(5):939–941, 2002.

[9] J. B. Pendry and S. O'Brien. Very-low-frequency magnetic plasma. *Journal of Physics: Condensed Matter*, 14:7409–7416, 2002.

[10] S. O'Brien and J. B. Pendry. Magnetic activity at infrared frequencies in structured metallic photonic crystals. *Journal of Physics: Condensed Matter*, 14:6383–6394, 2002.

[11] R. Marques, F. Medina, and R. Rafii-El-Idrissi. Role of bianisotropy in negative permeability and left-handed metamaterials. *Phys. Rev. B*, 65:144440, 2002.

[12] R. Marques, F. Medina, and R. Rafii-El-Idrissi. Comparative analysis of edge- and broadside- coupled split ring resonators for metamaterial design – theory and experiements. *IEEE Trans. Antennas Propagat.*, 51(10):2572–81, 2003.

[13] C. R. Simovski and S. L. He. Frequency range and explicit expressions for negative permittivity and permeability for an isotropic medium formed by a lattice of perfectly conducting omega particles. *Phys. Lett. A*, 311:254, 2003.

[14] M. M. I. Saadoun and N. Engheta. A reciprocal phase shifter using novel pseudochirla or Omega medium. *Microwave Opt. Technol. Lett.*, 5(4):184–188, 1992.

[15] R. A. Shelby, D. R. Smith, S. C. Nemat-Nasser, and S. Schultz. Microwave transmission through a two-dimensional, isotropic, left-handed metamaterial. *Appl. Phys. Lett.*, 78(4):489, 2001.

[16] D. R. Smith, D. C. Vier, N. Kroll, and S. Schultz. Direct calculation of permeability and permittivity for a left-handed metamaterial. *Appl. Phys. Lett.*, 77:2246, 2000.

[17] D. R. Smith and N. Kroll. Negative refractive index in left-handed materials. *Phys. Rev. Lett.*, 85:2933, 2000.

[18] N. Garcia and M. Nieto-Vesperinas. Is there an experimental verification of a negative index of refraction yet? *Optics Letters*, 27:885, 2002.

[19] P. M. Valanju, R. M. Walser, and A. P. Valanju. Wave refraction in negative-index media: Always positive and very inhomogeneous. *Phys. Rev. Lett.*, 88:187401, 2002.

[20] A. L. Pokrovsky and A. L. Efros. Electrodynamics of metallic photonic crystals and the problem of left-handed materials. *Phys. Rev. Lett.*, 89:093901, 2002.

[21] N. Garcia and M. Nieto-Vesperinas. Left-handed materials do not make a perfect lens. *Phys. Rev. Lett.*, 88:207403, 2002.

[22] D. R. Smith, D. Schurig, and J. B. Pendry. Negative refraction of modulated electro-magnetic waves. *Appl. Phys. Lett.*, 81(15):2713–2715, 2002.

[23] J. Pacheco, T. M. Grzegorczyk, B.-I. Wu, Y. Zhang, and J. A. Kong. Power propagation in homogeneous isotropic frequency dispersive left-handed media. *Phys. Rev. Lett.*, 89:257401, 2002.

[24] S. Foteinopoulou, E. N. Economou, and C. M. Soukoulis. Refraction in media with a negative refractive index. *Phys. Rev. Lett.*, 90:107402, 2003.

[25] J. B. Pendry. Negative refraction makes a perfect lens. *Phys. Rev. Lett.*, 85:3966, 2000.

[26] G. Gomez-Santos. Universal features of the time evolution of evanescent modes in a left-handed perfect lens. *Phys. Rev. Lett.*, 90:077401, 2003.

[27] R. Ziolkowski and E. Heyman. Wave propagation in media having negative permittivity and permeability. *Phys. Rev. E*, 64:056625, 2001.

[28] J. Pacheco, C. D. Moss, B.-I. Wu, T. M. Grzegorczyk, Y. Zhang, and J. A. Kong. Theoretical and numerical simulations of propagation through left-handed materials. In *PIERS*, page 359, 2002.

[29] N. Fang and X. Zhang. Imaging properties of a metamaterial superlens. *Appl. Phys. Lett.*, 82:161, 2003.

[30] S. Anantha Ramakrishna, J. B. Pendry, D. Schurig, D. R. Smith, and S. Schultz. The asymmetric lossy near-perfect lens. *Journal of Modern Optics*, 49(10):1747–1762, 2002.

[31] K. Li, J. McLean, R. B. Greegor, C. G Parazzoli, and M. Tanielian. Free-space focused-beam characterization of left-handed materials. *Appl. Phys. Lett.*, 82(15):2535–2537, 2003.

[32] C. G Parazzoli, R. B. Greegor, K. Li, B. E. C. Koltenbah, and M. Tanielian. Experimental verification and simulation of negative index of refraction using Snell's law. *Phys. Rev. Lett.*, 90:107401, 2003.

[33] A. A. Houck, J. B. Brock, and I. L. Chuang. Experimental observations of a left-handed material that obeys Snell's law. *Phys. Rev. Lett.*, 90:137401, 2003.

[34] L. Ran, X. Zhang, K. Chen, T. M. Grzegorczyk, and J. A. Kong. Experimental verification of NRI properties of various Rods/SRRs configurations. In *PIERS*, page 252, Singapore, January 2003.

[35] J. A. Kong, B.-I. Wu, and Y. Zhang. Lateral displacement of a Gaussian beam reflected from a grounded slab with negative permittivity and permeability. *Appl. Phys. Lett.*, 80:2084, 2002.

[36] J. A. Kong, B.-I. Wu, and Y. Zhang. A unique lateral displacement of a Gaussian beam transmitted through a slab with negative permittivity and permeability. *Microwave Opt. Technol. Lett.*, 33(2):136–139, April 2002.

[37] C. Caloz, C.-C. Chang, and T. Itoh. Full-wave verification of the fundamental properties of left-handed materials in waveguide configurations. *J. Appl. Phys.*, 90(11):5483–5486, 2001.

[38] J. Gerardin and A. Lakhtakia. Negative index of refraction and distributed Bragg reflectors. *Microwave Opt. Technol. Lett.*, 34(6):409–411, 2002.

[39] R. W. Ziolkowski. Double negative metamaterial design, experiments, and applications. In *IEEE Antennas Propagat. Int. Symp.*, volume 1, pages 396–9, June 2002.

[40] R. B. Greegor, C. G Parazzoli, K. Li, and M. Tanielian. Origin of dissipative losses in negative index of refraction materials. *Appl. Phys. Lett.*, 82(14):2356–2358, 2003.

[41] G. V. Eleftheriades, A. K. Iyer, A. Grbic, and O. Siddiqui. Negative refractive index metamaterials based on L-C loaded transmission lines. In *PIERS*, page 354, 2002.

[42] I. S. Nefedov and S. A. Tretyakov. Theoretical study of waveguiding structures containing backward-wave materials. In *URSI XXVIIth General Assembly*, page 1074, August 2002.

[43] A. K. Iyer and G. V. Eleftheriades. Negative refractive index metamaterials supporting 2-D waves. In *IEEE MTT-S Int. Microwave Symp. Digest*, volume 2, pages 1067–1070, June 2002.

[44] A. Grbic and G. V. Eleftheriades. Growing evanescent waves in negative-refractive-index transmission-line media. *Appl. Phys. Lett.*, 82(12):1815–17, 2003.

[45] A. Grbic and G. V. Eleftheriades. Experimental verification of backward-wave radiation from a negative refractive index metamaterial. *J. Appl. Phys.*, 92(10):5930–5935, 2002.

[46] G. V. Eleftheriades, A. K. Iyer, and P. C. Kremer. Planar negative refractive index media using periodically L-C loaded transmission lines. *IEEE Trans. Microwave Theory Tech.*, 50(12):2702–2712, 2002.

[47] M. Notomi. Theory of light propagation in strongly modulated photonic crystals: Refraction like behavior in the vicinity of the photonic band gap. *Phys. Rev. B*, 62:10696, 2000.

[48] C. Luo, S. G. Johnson, J. D. Joannopoulos, and J. B. Pendry. All-angle negative refraction without negative effective index. *Phys. Rev. B*, 65:201104, 2002.

[49] G. Shvets. Photonic approach to making a material with a negative index of refraction. *Phys. Rev. B*, 67:035109, 2003.

[50] J. D. Joannopoulos, R. D. Meade, and J. N. Winn. *Photonic Crystals: Molding the Flow of Light.* Princeton University Press, Princeton, New Jersey, 1995.

[51] J. B. Pendry and S. Anantha Ramakrishna. Near-field lenses in two dimensions. *Journal of Physics: Condensed Matter*, 14:8463–8479, 2002.

[52] I. V. Lindell, S. A. Tretyakov, K. I. Nikoskinen, and S. Ilvonen. BW media–media with negative parameters, capable of supporting backward waves. *Microwave Opt. Technol. Lett.*, 31(2):129–133, 2001.

[53] B.-I. Wu, T. M. Grzegorczyk, Y. Zhang, and J. A. Kong. Guided modes with imaginary transverse wave number in a slab waveguide with negative permittivity and permeability. *J. Appl. Phys.*, 93(11):9386–9388, 2003.

[54] J. Lu, T. M. Grzegorczyk, Y. Zhang, J. Pacheco, B.-I. Wu, and J. A. Kong. Čerenkov radiation in materials with negative permittivity and permeability. *Optics Express*, 11(7):723–734, 2003.

[55] R. W. Ziolkowski. Superluminal transmission of information through an electromagnetic metamaterial. *Phys. Rev. E*, 63:046604, 2001.

[56] N. Engheta. An idea for thin subwavelength cavity resonators using metamaterials with negative permittivity and permeability. *IEEE Antennas and Wireless Propagation Letters*, 1(1):10–13, 2002.

[57] L. D. Landau, E. M. Lifshitz, and L. P. Pitaevskii. *Electrodynamics of Continuous Media.* Pergamon Press, New York, 1984.

[58] L. Brillouin. *Wave Propagation and Group Velocity.* Academic Press, New York, 1960.

[59] J. A. Kong. *Electromagnetic Wave Theory.* EMW Publishing, Cambridge, Massachusetts, 2000.

[60] Y. Zhang, T. M. Grzegorczyk, and J. A. Kong. Electromagnetic wave interaction with stratified negative isotropic media. *PIER*, 35:1–52, 2002.

[61] J. A. Kong. Electromagnetic wave interaction with stratified negative isotropic media. *PIER*, 35:1–52, 2002.

[62] R. W. Ziolkowski. Causality and double-negative metamaterials. *Phys. Rev. E*, 68:026615, 2003.

[63] J. Pacheco, B. E. Barrowes, and J. A. Kong. Electromagnetic scattering by canonical objects composed of left-handed materials. In *PIERS*, page 453, 2002.

[64] R. Ruppin. Intensity distribution inside scatterers with negative-real permittivity and permeability. *Microwave Opt. Technol. Lett.*, 36(3):150–154, 2003.

[65] R. Ruppin. Extinction properties of a sphere with negative permittivity and permeability. *Solid State Communications*, 116:411–415, 2000.

[66] A. N. Lagarkov and V. N. Kisel. Electrodynamic properties of simple bodies made of materials with negative permeability and negative permittivity. *Doklady Physics*, 377:40–43, 2001.

[67] V. Kuzmiak and A. A. Maradudin. Scattering properties of a cylinder fabricated from a left-handed material. *Phys. Rev. B*, 66:045116, 2002.

[68] L. Hu and S. T. Chui. Characteristics of electromagnetic wave propagation in uniaxially anisotropic left-handed materials. *Phys. Rev. B*, 66:085108, 2002.

[69] D. R. Smith and D. Schurig. Electromagnetic wave propagation in media with indefinite permittivity and permeability tensors. *Phys. Rev. Lett.*, 90:077405, 2003.

[70] D. Schurig and D. R. Smith. Spatial filtering using media with indefinite permittivity and permeability tensors. *Appl. Phys. Lett.*, 82(14):2215–2217, 2003.

[71] M. K. Kärkkäinen. Numerical study of wave propagation in uniaxially anisotropic lorentzian backward-wave slabs. *Phys. Rev. E*, 68:026602, 2003.

[72] D. R. Smith. Negative refraction in indefinite media. *preprint*, 2003.

[73] W. C. Chew. *Waves and Fields in Inhomogeneous Media*. IEEE Press, 1995.

[74] P. Markos and C. M. Soukoulis. Absorption losses in periodic arrays of thin metallic wires. *Optics Letters*, 28(10), 2003.

[75] T. M. Grzegorczyk, C. D. Moss, and J. A. Kong. New ring resonator for the design of left-handed materials at microwave frequencies. *PIERS*, page 286, 2003.

[76] D. R. Smith, S. Schultz, P. Markos, and C. M. Soukoulis. Determination of effective permittivity and permeability of metamaterials from reflection and transmission coefficients. *Phys. Rev. B*, 65:195104, 2002.

[77] J. L. Young and R. O. Nelson. A summary and systematic analysis of FDTD algorithms for linearly dispersive media. *IEEE Trans. Antennas Propagat. Magazine*, 43(1):61–77, February 2001.

[78] Allen Taflove. *The Finite-Difference Time-Domain Method*. Artech House, 1995.

[79] Allen Taflove. Review of the formulation and applications of the finite-difference time-domain method for numerical modeling of electromagnetic wave interactions with arbitrary structures. *Wave Motion*, 10:547–582, 1988.

[80] N. Engheta. private communication, October 2003.

[81] C. D. Moss, T. M. Grzegorczyk, Y. Zhang, and J. A. Kong. Numerical studies of left handed metamaterials. *PIER*, 35:315–334, 2002.

[82] C. Parazzoli. private communication, November 2002.

[83] P. Markos and C. M. Soukoulis. Numerical studies of left-handed materials and arrays of split ring resonators. *Phys. Rev. E*, 65:036622, 2002.

[84] R. W. Ziolkowski. Design, fabrication, and testing of double negative metamaterials. *IEEE Trans. Antennas Propagat.*, 51(7):1516–1529, July 2003.

[85] D. R. Smith. private communication, July 2002.

[86] J. B. Pendry and P. M. Bell. Transfer matrix techniques for electromagnetic waves. In C. M. Soukoulis, editor, *Photonic Band Gap Materials*, volume 315 of *NATO ASI Series E: Applied Sciences*, pages 203–228. Kluwer Academic Publishers, 1996.

[87] K. J. Vinoy and R. M. Jha. *Radar Absorbing Materials: From theory to design and characterization.* Kluwer Academic Publishers, Norwell, Masschusetts, 1996.

[88] D. L. Jaggard and N. Engheta. Chirosorb^{TM} as an invisible medium. *Electron. Lett.*, 25(3):173–4, February 1989.

[89] D. L. Jaggard and N. Engheta. Chiroshield: A Salisbury/Dallenbach shield alternative. *Electron. Lett.*, 26(17):1332–4, August 1990.

[90] Jean-Pierre Berenger. A perfectly matched layer for the absorption of electromagnetic waves. *Journal of Computational Physics*, 114:185–200, 1994.

[91] Weng Cho Chew and William H. Weedon. A 3D perfectly matched medium from modified Maxwell's equations with stretched coordinates. *Microwave Opt. Technol. Lett.*, 7(13):599–604, September 1994.

[92] W. C. Chew, J. M. Jin, and E. Michielssen. Complex coordinate stretching as a generalized absorbing boundary condition. *Microwave Opt. Technol. Lett.*, 15(6):363–369, August 1997.

[93] F. L. Teixeira and W. C. Chew. PML-FDTD in cylindrical and spherical grids. *IEEE Microwave and Guided Wave Letters*, 7(9):285–287, September 1997.

[94] Z. S. Sacks, D. M. Kingsland, R. Lee, and J.-F. Lee. A perfectly matched anisotropic absorber for use as an absorbing boundary condition. *IEEE Trans. Antennas Propagat.*, 43(12):1460–1463, December 1995.

[95] F. L. Teixeira and W. C. Chew. Systematic derivation of anisotropic PML absorbing media in cylindrical and spherical coordinates. *IEEE Microwave and Guided Wave Letters*, 7(11):371–373, November 1997.

[96] R. W. Ziolokowski. The design of Maxwellian absorbers for numerical boundary conditions and for practical applications using engineered artificial materials. *IEEE Trans. Antennas Propagat.*, 45(4):656–671, April 1997.

[97] Y. Rahmant-Samii and E. Michielssen. *Electromagnetic Optimization by Genetic Algorithms*. Wiley, New York, 1999.

[98] E. Michielssen, J.-M. Sajer, S. Ranjithan, and R. Mittra. Design of lightweight, broadband microwave absorbers using genetic algorithms. *IEEE Trans. Microwave Theory Tech.*, 41(67):1024–1031, Juny/July 1993.

[99] H. Mosallaei and Y. Rahmat-Samii. RCS reduction of canonical targets using genetic algorithm synthesized RAM. *IEEE Trans. Antennas Propagat.*, 48(10):1594–1606, October 2000.

[100] S. Enoch, G. Tayeb, P. Sabouroux, N. Guerin, and P. Vincent. A metamaterial for directive emission. *Phys. Rev. Lett.*, 89:213902, 2002.

[101] B. Gralak, S. Enoch, and G. Tayeb. Anomalous refractive properties of photonic crystals. *J. Opt. Soc. Am A*, 17(6):1012–1020, 2000.

[102] B. Temelkuran, M. Bayindir, and E. Ozbay. Photonic crystal-based resonant antenna with a very high directivity. *J. Appl. Phys.*, 87(1):603, 2000.

[103] M. Thèvenot, C. Cheype, A. Reineix, and B. Jecko. Directive photonic-bandgap antennas. *IEEE Trans. Microwave Theory Tech.*, 47(11):2115–2122, Novemeber 1999.

[104] D. Sievenpiper, L. Zhang, R. F. Jimenez Broas, N. G. Alexopólous, and E. Yablonovitch. High-impedance electromagnetic surfaces with a forbidden frequency band. *IEEE Trans. Microwave Theory Tech.*, 47(11):2059–2074, 1999.

[105] W. Wang, B.-I. Wu, J. Pacheco, T. M. Grzegorczyk, and J. A. Kong. Metamaterial as a substrate for antenna design. *PIERS*, page 295, 2003.

Biographical note

Joe Pacheco, Jr. was born in San Antonio, Texas on July 4, 1978.

He received the Bachelor of Science degree in Electrical Science and Engineering with a Minor in Music from the Massachusetts Institute of Technology, Cambridge, Massachusetts, in 2000, and the Master of Engineering degree in Electrical Engineering and Computer Science from the Massachusetts Institute of Technology, Cambridge, Massachusetts, in 2000.

As an undergraduate, he participated in the EECS department's VI-A co-op program at the M.I.T. Lincoln Laboratory, Lexington, Massachusetts from 1997-2000, where he worked on the problem of radar cross section prediction using finite difference techniques in the Systems and Analysis group. Since 2000, he has been affiliated with the Center for Electromagnetic Theory and Applications, within the Research Laboratory of Electronics at the Massachusetts Institute of Technology, Cambridge, Massachusetts, where he worked on problems related to left-handed metamaterials as well as radar based imaging and detection problems. He was a TA in the EECS department of MIT during the Spring 2001 semester for the undergraduate course 6.014: Electrodynamics.

Joe Pacheco, Jr. is an alumnus of the Texas Academy of Mathematics and Science (1994-1996). He was a member of the administrative committee for the Progress in Electromagnetics Symposium (2000-2003). He is a member of the Eta Kappa Nu Association (since 1999), and a Student Member of the IEEE (since 2002). He was the recipient of the IEEE Microwave Theory and Techniques Society 2003 Graduate Fellowship Award.